Characterisation of Imperfections in Single Crystals of High Purity Synthetic Quartz

by

Keith Beveridge Hutton M.Sc.

Thesis presented for the degree of Doctor of Philosophy

Department of Pure and Applied Chemistry

University of Strathclyde

February 1990

Abstract

The work described in this thesis is a study of imperfections in high purity, low dislocation content synthetic quartz single crystals which are grown on a commercial scale by the General Electric Company. Hydrogen and metal ion impurities in quartz were studied using low temperature transmission Fourier Transform Infrared Spectroscopy, (FTIR). Incorporation of impurities in quartz was investigated using crystals which were doped with Al, Fe, Cr, Co, Ti, P, Cu and K. Orientation of hydroxyl impurities was determined using polarised infrared spectroscopy. Deuterated quartz crystals were grown and studied as analogues to high purity crystals. X-ray diffraction topography was used to evaluate crystal quality and to perform a study of quartz which had been treated by electrodiffusion, or sweeping. Crystal lattice strain and sweeping damage was studied using double crystal topography at the Synchrotron Radiation Source, (SRS), at the Daresbury Laboratory.

Metal ion impurities were shown to incorporate interstitially into quartz crystals. The only exceptions were aluminium and iron, which incorporated substitutionally. All the impurities studied introduced hydrogen impurities such as hydroxyl ions and water molecules into quartz. A relationship between impurity concentration and hydrogen content was clearly indicated. The 3200 cm-1 broad absorption band characteristic of impure and fast grown synthetic quartz was strongly implicated as being due to interstitially incorporated water molecules. The major hydrogen impurities in quartz were sodium hydroxide molecules which were preferentially aligned along the X, Y and Z growth axes. Hydroxyl ions were not incorporated directly from the growth solution.

Sweeping was shown to induce the formation of a negative space charge in treated quartz which gave rise to inhomogeneous lattice strain. The strain was gradually relieved upon prolonged exposure to x-rays. A mechanism for the production and relief of lattice strain has been proposed. Sweeping produced surface damage on mechanically polished crystals but not on those treated by chemical polishing using hydrofluoric acid. No further detrimental effects of sweeping were observed.

Double crystal topographic studies revealed two possible bulk defects in Quartz. The first of these was a previously unreported planar defect parallel to the X-Y plane of quartz. The second was possibly a planar defect associated with the cellular growth cells in the (00.1) growth sector of quartz. The validity of these observations was put in doubt by the possibility of defect projection from the silicon monochromator which had been used in double crystal studies.

Contents

Page

List of Figures

Chapter 1.

Page

Chapter 2.

Page

Page

List of Tables

Chapter 1.

Chapter 2.

Acknowledgements

I would like to convey my sincere gratitude to my supervisors Dr. D. B. Sheen and Dr. R. T. Bailey and also to Prof. J. N. Sherwood for suggestions of project topics and for their encouragement and guidance throughout this work. I would also like to express my appreciation to Dr. D. F. Croxall, my supervisor at the General Electric Company's Hirst Research Centre in Wembley, for his invaluable assistance in every aspect of quartz crystal growth and his constructive discussions and advice. I also thank Dr. Croxall for providing many crystal samples which were essential for this work. My gratitude and thanks also go to Miss Barbara Lukjaniec of Lancaster University for her advice and numerous helpful suggestions throughout the course of this project. I also thank Dr. C. Cramer and Dr. A. Pearson for their help and assistance in the production of the photographs which appear in this thesis.

Dedication

This thesis is dedicated to my parents Thomas and Anna Hutton, for their unwavering support and encouragement throughout my life and especially during the lengthy period of my education.

Chapter 1. Introduction

Chapter 1. Introduction

1.1 Forms of Silicon Dioxide

Silicon dioxide exists in a number of different polymorphs[1,2], the most common of which is known as low or α-quartz. This polymorph is thermodynamically stable at room temperature and pressure and the term quartz normally refers to this form only. The other modifications of silicon dioxide are given in table 1.1. α-Quartz can be converted into any of the other silicon dioxide forms by increasing temperature and pressure (see fig. 1.1). At atmospheric pressure quartz is stable up to a temperature of 573°C after which the structure undergoes a rapid displacive inversion to the ß-quartz modification. This change is reversible and the α-quartz structure is regained when the temperature falls below the inversion point. On heating, ß-quartz can persist at temperatures above 870°C up to its melting point somewhere below 1670°C . However the presence of fluxing or of mineralising agents produces a slow reconstructive structural inversion at 870°C which results in the formation of high-tridymite. This form can exist in a metastable state when cooled below this inversion temperature. High-tridymite undergoes two displacive inversions at 163°C and 117°C to produce the middle and low tridymite forms respectively. The latter tridymite form can exist in a metastable state at room temperatures. However, if no fluxing agents are present and the ß-quartz modification reaches its melting point, the cristobalite modification normally crystallises out when

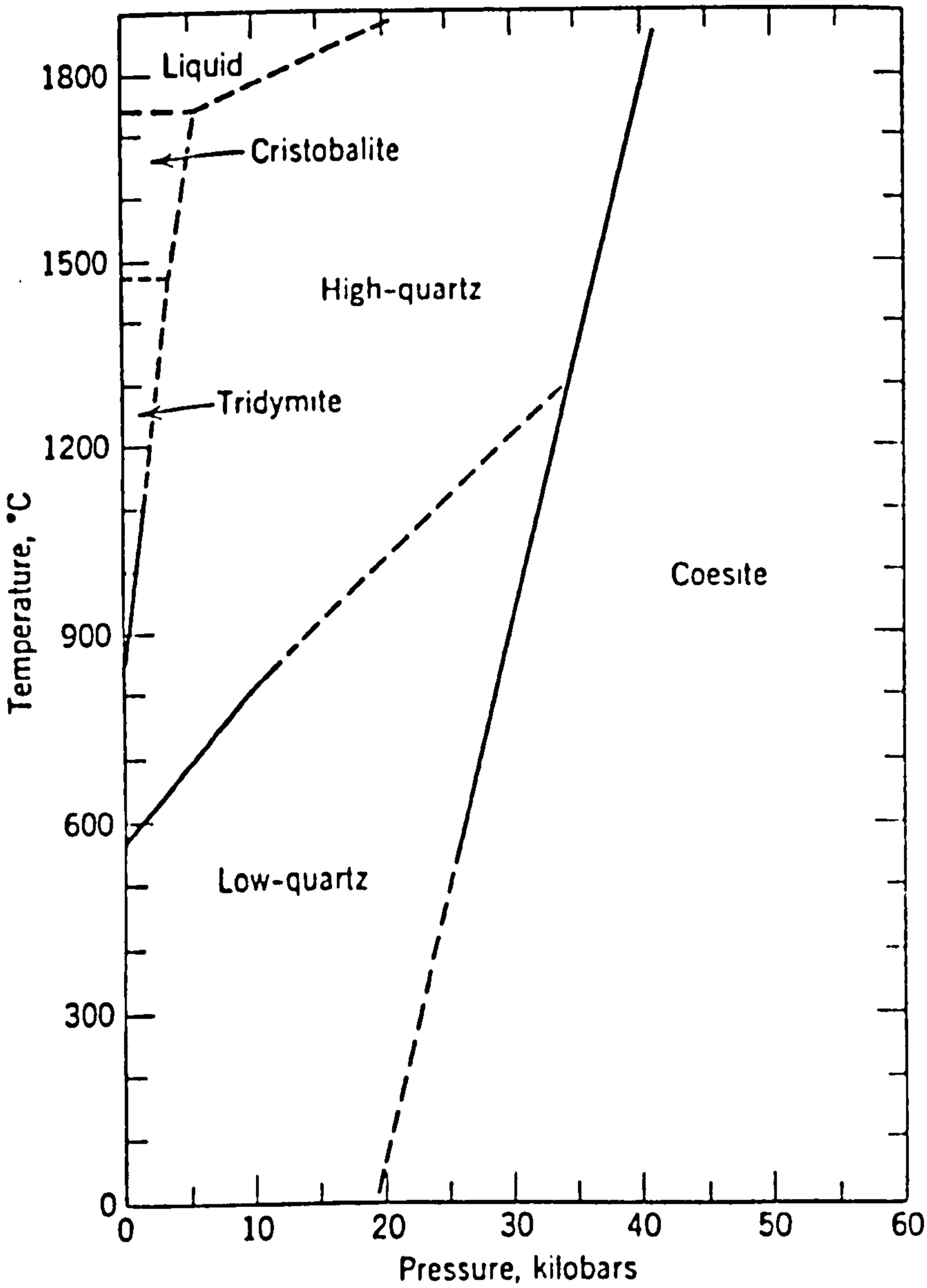

Fig. 1.1 Temperature and Pressure Relationships of SiO_2 Polymorphs

(From Ref.2)

Table 1.1 Polymorphs of Silica

Name	Thermal Stability Range at 1 atm.
α-Quartz	Below 573 °C
ß-Quartz	573 - 870 °C
Low-tridymite	Below 117 °C
Middle-tridymite	117 - 163 °C
High-tridymite	163 - 1470 °C
	(stable 870 - 1470 °C)
Low-cristobalite	Below 200 °C
High-cristobalite	200 - 1720 °C
	(stable 1470 - 1720 °C)

temperatures fall back below 1723°C. This form is stable at temperatures between 1470°C and 1723°C but high-tridymite can be formed via a slow constructive inversion below 1470°C. If this fails to happen, cristoblite undergoes a displacive inversion at temperatures below 267°C to become the low-cristobalite modification. This form of silicon dioxide can exist in a metastable state at room temperatures. At temperatures above 1720°C and atmospheric pressure, liquid silica is formed. This phase does not crystallise easily and is more readily supercooled to a glass which is known as vitreous silica, silica glass or quartz glass. This devitrifies after prolonged heating at around 1000°C to form cristobalite.

1.2 Uses of Quartz Crystals

The quartz crystal is an important component used in modern electronic technology. It is a product of the discovery of piezoelectricity in 1880 by Jacques and Pierre Curie. The definition of this property is " the electric polarisation produced by mechanical strain in crystals belonging to certain crystal classes[3]". The electronics industry utilises the converse of this effect by applying a polarising electric field across a quartz crystal. The mechanical strain which this produces causes the crystal to vibrate at a specific frequency which is dependent on the strength of the applied field and the direction it is applied across. As a consequence, vibrating quartz elements can be

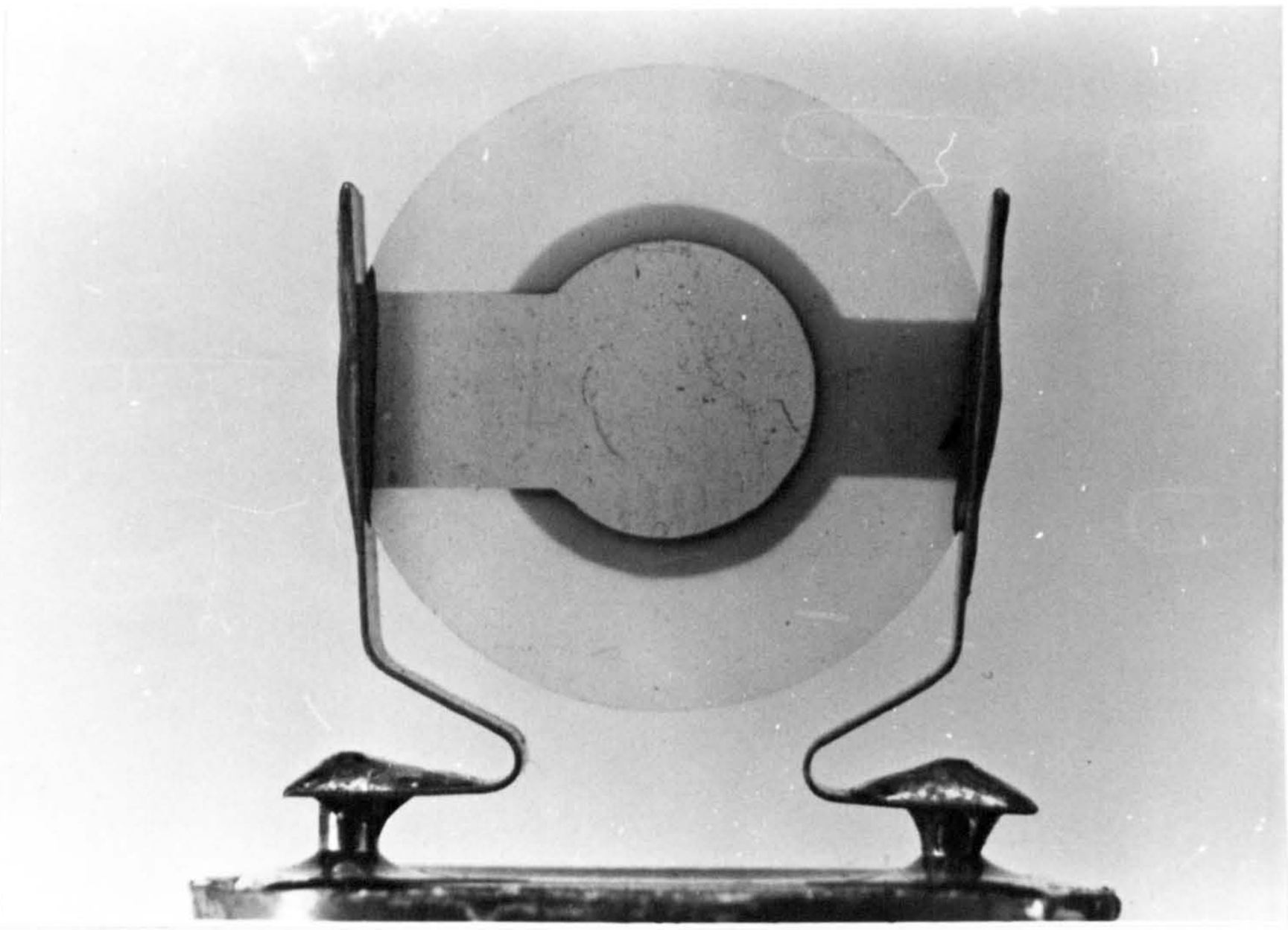

Fig. 1. 2 Quartz Crystal Oscillator

used to mark off equal intervals of time with great precision[4]. The most familiar application of quartz is that of a timing element in clocks, watches, computers and microprocessors. However the most important application of this property is the incorporation of quartz crystal units in oscillator circuits[3-6], which are used to control and manage frequencies in virtually all communication systems ranging from mundane applications such as portable radios up to the more sophisticated needs of professional telecommunications and satellite navigation (see fig. 1.2). These devices can operate over the whole range of the radio frequency spectrum from 15kHz to 100GHz and oscillator circuits are essential to provide the highly accurate frequency control that is necessary to avoid interference between transmitters operating in adjacent channels or even in the same geographical areas[5]. However, only crystals of exceptional quality can be used for these arduous applications. Until recently, only naturally grown quartz has possessed the high degree of crystalline perfection required. Unfortunately, reserves of high quality natural crystals are finite and in recent years the availability of suitable material has been severely restricted, particularly by Brazil, the major source of natural quartz. However, recent breakthroughs at the General Electric Company's Hirst Research Laboratories have resulted in the development of a commercial process capable of producing synthetic crystals of a quality approaching that of the best naturally grown quartz[7]. This

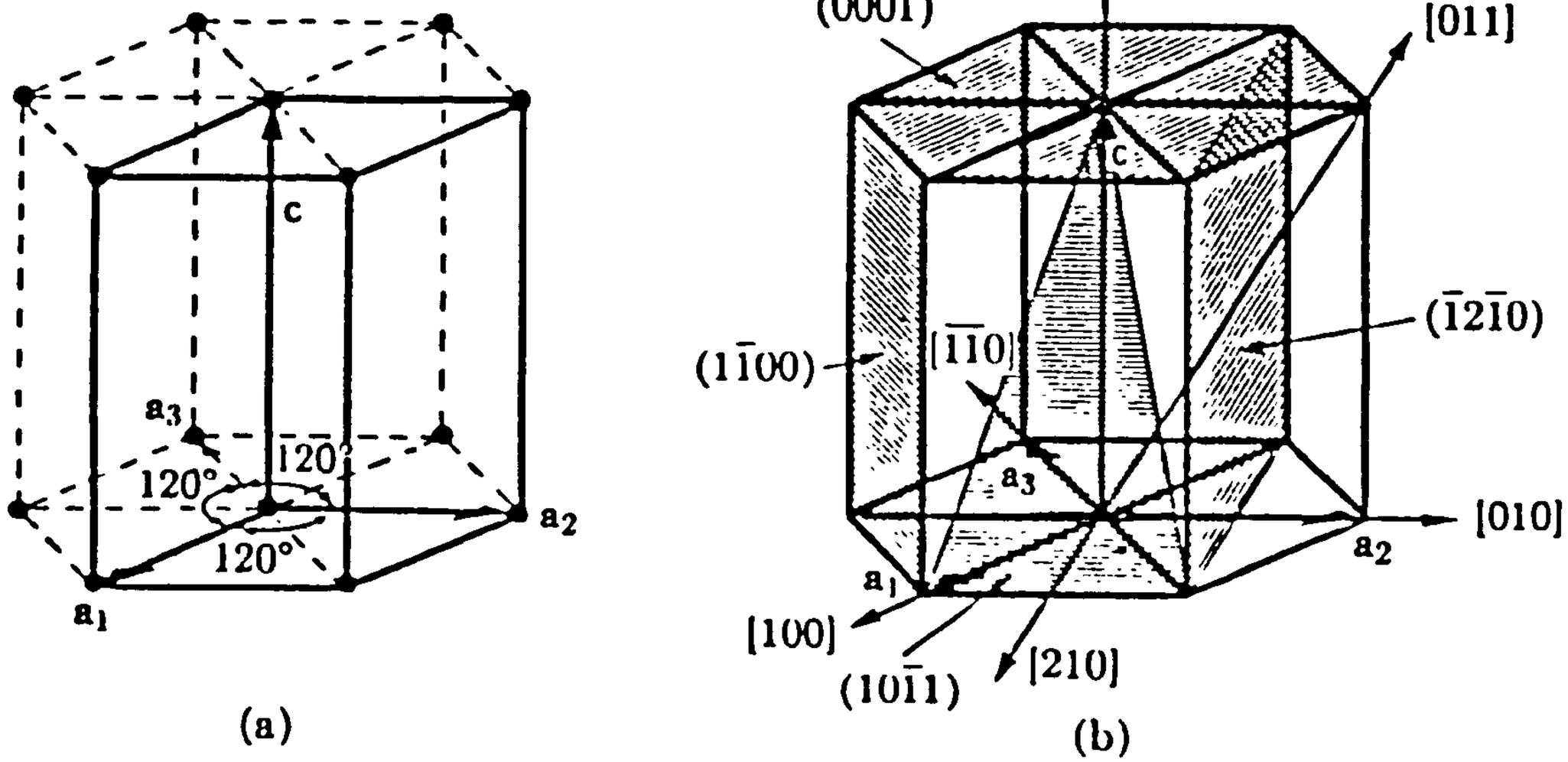

Fig. 1.3 (a) The hexagonal unit cell (heavy lines) and (b) indices of planes and directions.

(From Ref.10)

thesis details an extensive assessment of structural aspects of this material and attempts to compare these features with those of conventionally produced synthetic quartz crystals.

1.3 Symmetry, Morphology and Structure of α-Quartz

Quartz crystallises in class (32) of the rhombohedral or trigonal system but is conventionally described using a non-primitive hexagonal unit cell instead of a rhombohedral cell[2] (see fig. 1.3). The hexagonal cell is composed of one triad axis of three-fold symmetry with three diad axes of two fold symmetry lying in a perpendicular plane. The diad axes are separated from each other by angles of 120°. The unit cell possesses neither a plane nor a centre of symmetry.

By convention, the description of the morphology of a natural quartz crystal given by Weiss[8] is the accepted standard (see fig. 1.4a). Synthetically produced crystals show a similar morphology but exhibit several facets not usually present in natural crystals (see fig. 1.4b). Both types of quartz are enantiomorphous which means that, structurally speaking, crystals can belong to one of two enantiomorphous space groups. Enantiomorphism is a term used to describe the relationship between two identical but non-superimposable objects such as mirror images. The two forms which quartz can assume are known as right and left-handed quartz. The assignment of which form is present in a crystal is made using polarised light[9]. Quartz is doubly refractive because of the two structural forms and rotates the plane of polarised

Fig. 1.4 Quartz Crystal Morphology

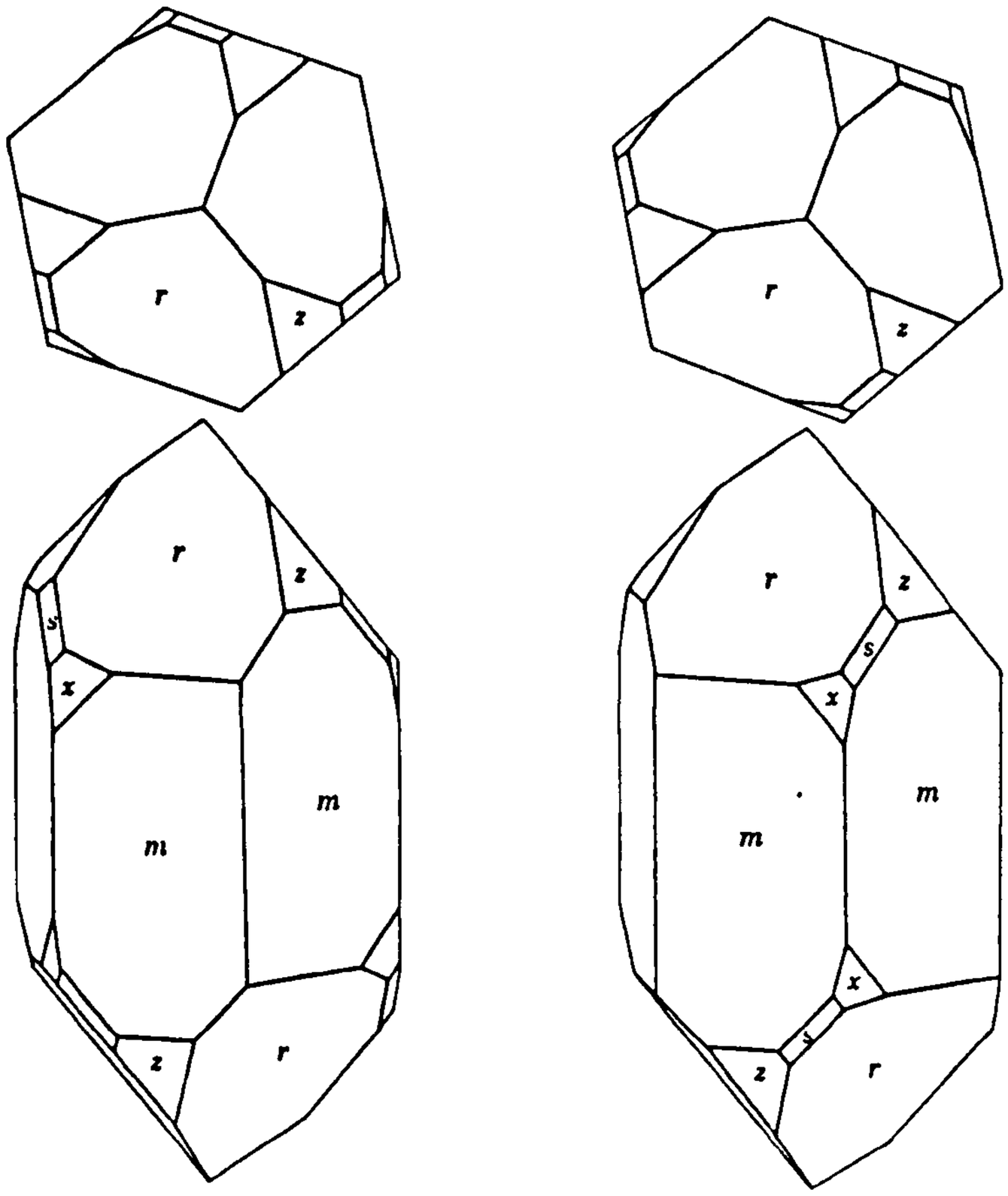

a) Natural Quartz

(From Ref. 2)

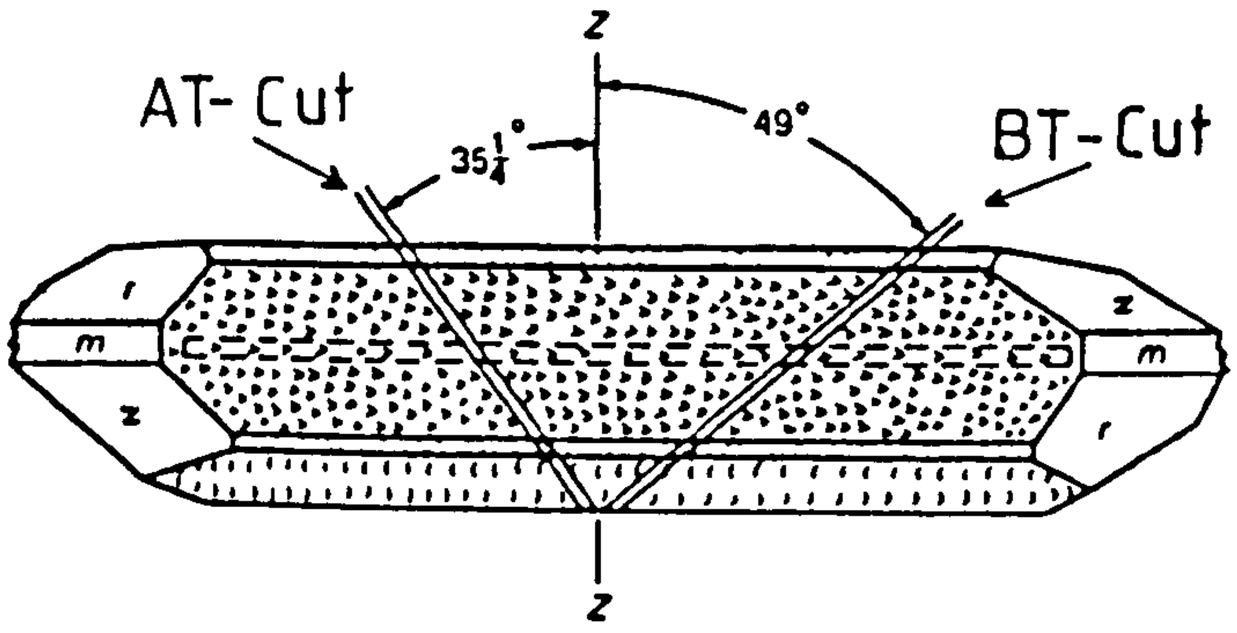

b) Synthetic Quartz

Table 1.2 Important Facets of Quartz Crystals

Symbol	Name	Index of Plane Family
r	Major Rhombohedron	{ 10.1 }
z	Minor Rhombohedron	{ 01.1 }
x	Positive Trigonal Trapezohedron	{ 51.1 }
s	Trigonal Pyramid	{ 11.1 }
m	Prism	{ 10.0 }

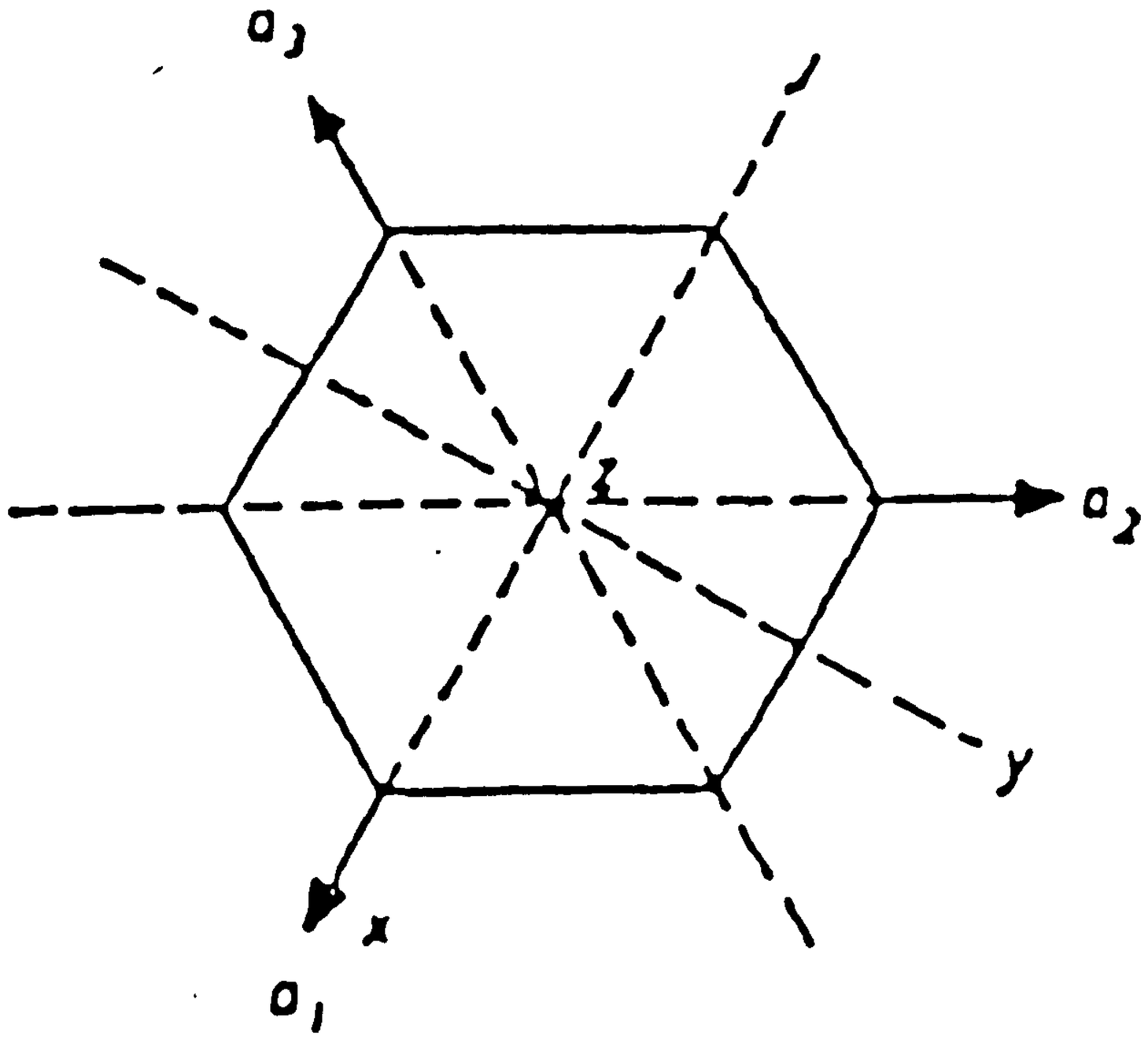

a_1, a_2, a_3, c - Crystallographic Axes

X, Y, Z - Piezoelectric and Growth Axes

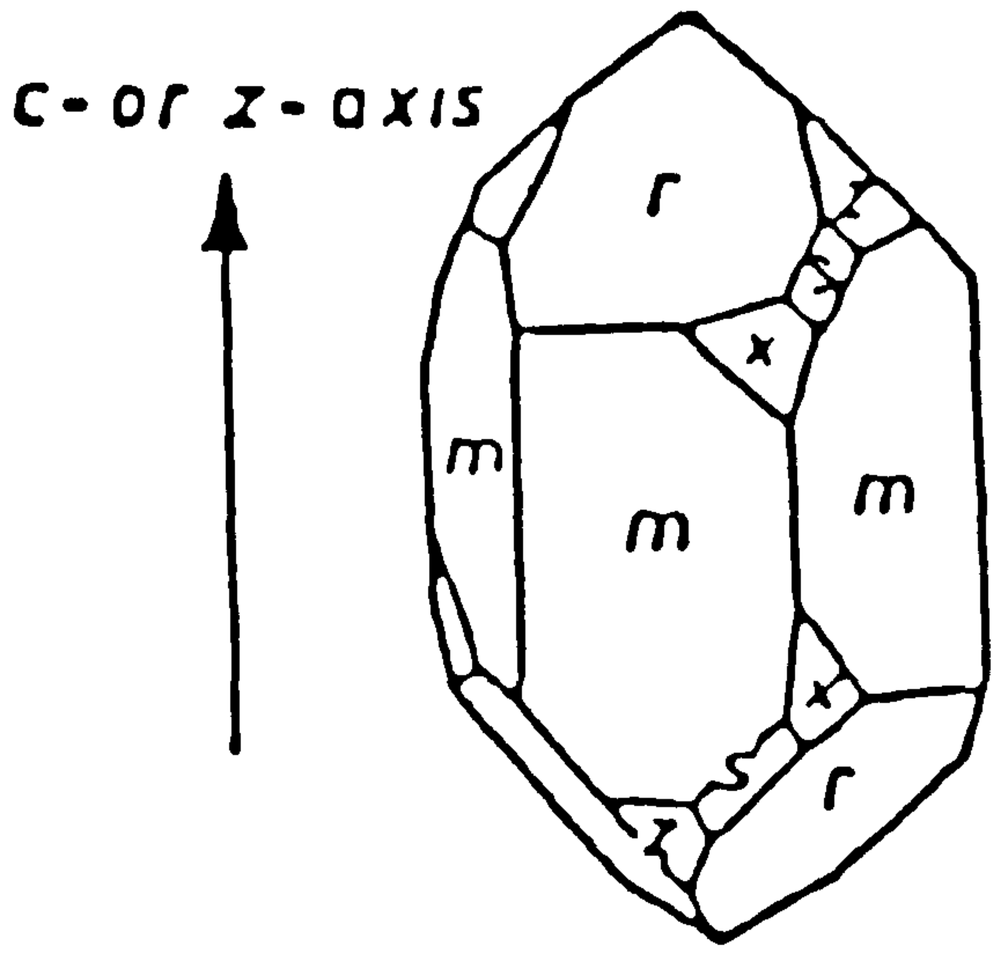

Fig. 1.5 Crystallographic and Piezoelectric Axial Systems of Quartz Crystals (From Ref.52)

light clockwise for right-handed and anti-clockwise for left-handed quartz. Structurally, right-handed quartz belongs to the $P3_12$ space group whereas structurally left-handed quartz belongs to the $P3_22$ space group.

Polarised light is only rotated if it is parallel to the optical axis of the quartz crystal. This is an example of a crystal property which is dependent on direction. Other properties such as the piezoelectric effect are also directionally dependent. Therefore in order to give a complete description it is necessary to be able to index directions and planes in a crystal. Quartz is indexed using two sets of reference directions known as the crystallographic and piezoelectric axes respectively. Crystallographic axes are usually described using the Miller-Bravais indexing system[10] and are coincident with the symmetry axes (see fig. 1.5). The axial system consists of a vertical Z-axis, also known as the C-axis[11], which is coincident with the triad symmetry axis and three horizontal X-axes which make angles of 120° to each other. These axes are also denoted as the a_1 ,a_2 and a_3 axes and coincide with the three axes of binary symmetry[11]. These axes form a coordinate system which can be used for indexing atom planes in a crystal. Any atom plane can be described from the interception points it makes with each of the four coordinate axes. Where a plane is parallel to an axis it is presumed to intersect it at infinity. Indexing of quartz crystal planes is carried out with respect to a primitive hexagonal unit cell. Where a plane intercepts a coordinate

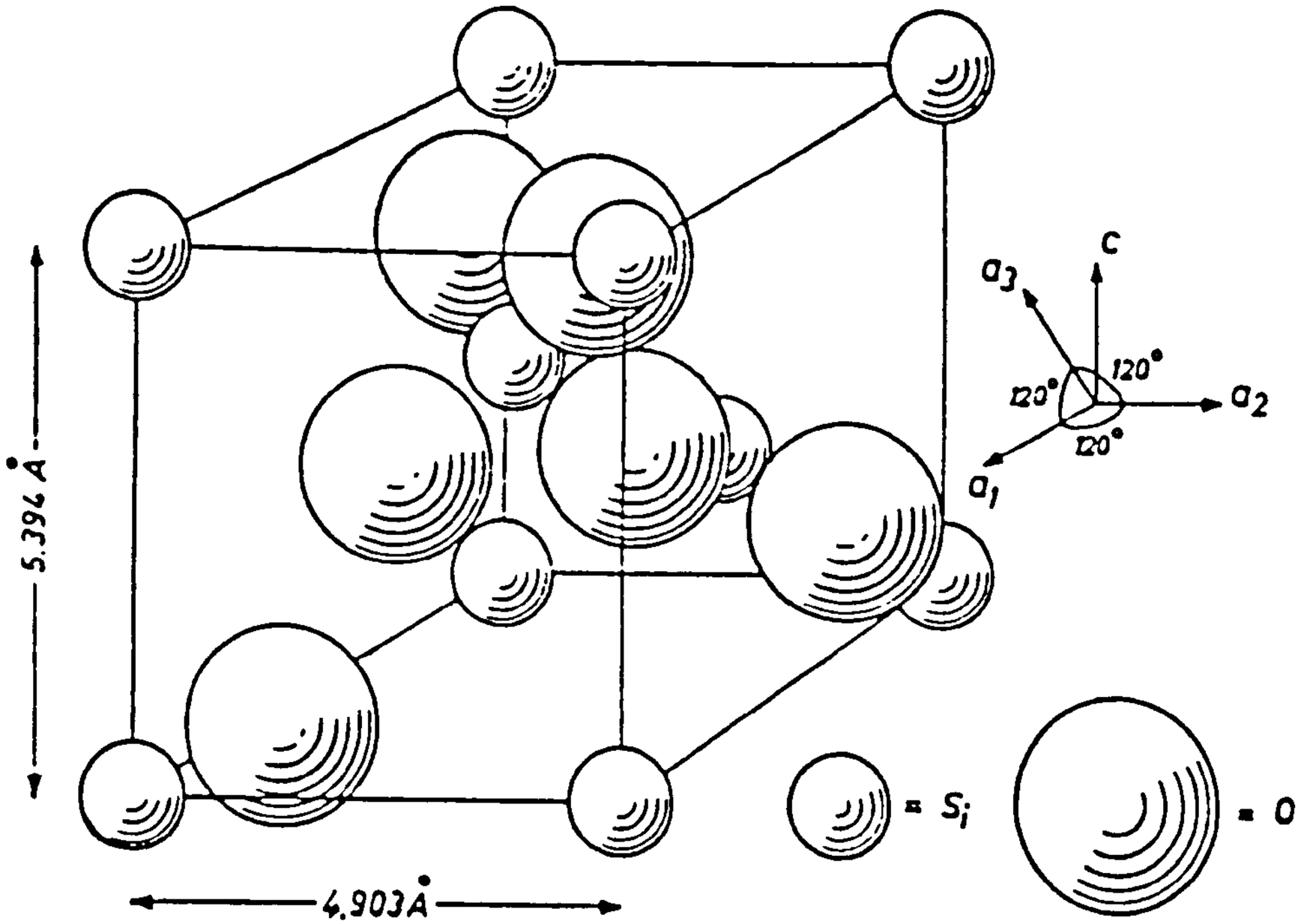

Fig. 1.6 Atom Positions in the Quartz Unit Cell
(From Ref.52)

axis at a unit cell boundary, the corresponding index is unity and interception points between the cell origin and a boundary are denoted by fractions of one. To eliminate non-integer terms, the reciprocal of intercepts is used for indexing. The resultant four number index is then divided by the lowest integer value to give the lowest index for that crystal plane. Directions in a crystal are described by four basic vectors following the a_1, a_2, a_3 and C-axes. Again unit cell boundaries represent unity conditions. Examples of indexed planes and directions are illustrated in figure 1.3. However, a convention exists which simplifies the indexing system. It is based on the fact that the sum of the first three indices is always zero. Therefore, if the first two indices are known then the third can be easily worked out. In practice the third number of the index is denoted by a dot, eg. the (2-1-1 0) plane can also be represented as (2-1.0). The indices of important quartz crystal faces are given in table 1.2 and illustrated in figure 1.4.

Two additional sets of axes are used in reference to the piezoelectric properties of quartz. The earliest of these defines two sets of axes, one for each structural hand of quartz[12], which are made up of three orthogonal directions X, Y and Z. The Z-direction of the piezoelectric axes coincides with that of the C-direction in the crystallographic axes for both structural hands. The later convention adopts the right handed convention for both right and left-handed quartz[13]. Therefore, the X and Y directions are reversed for right-

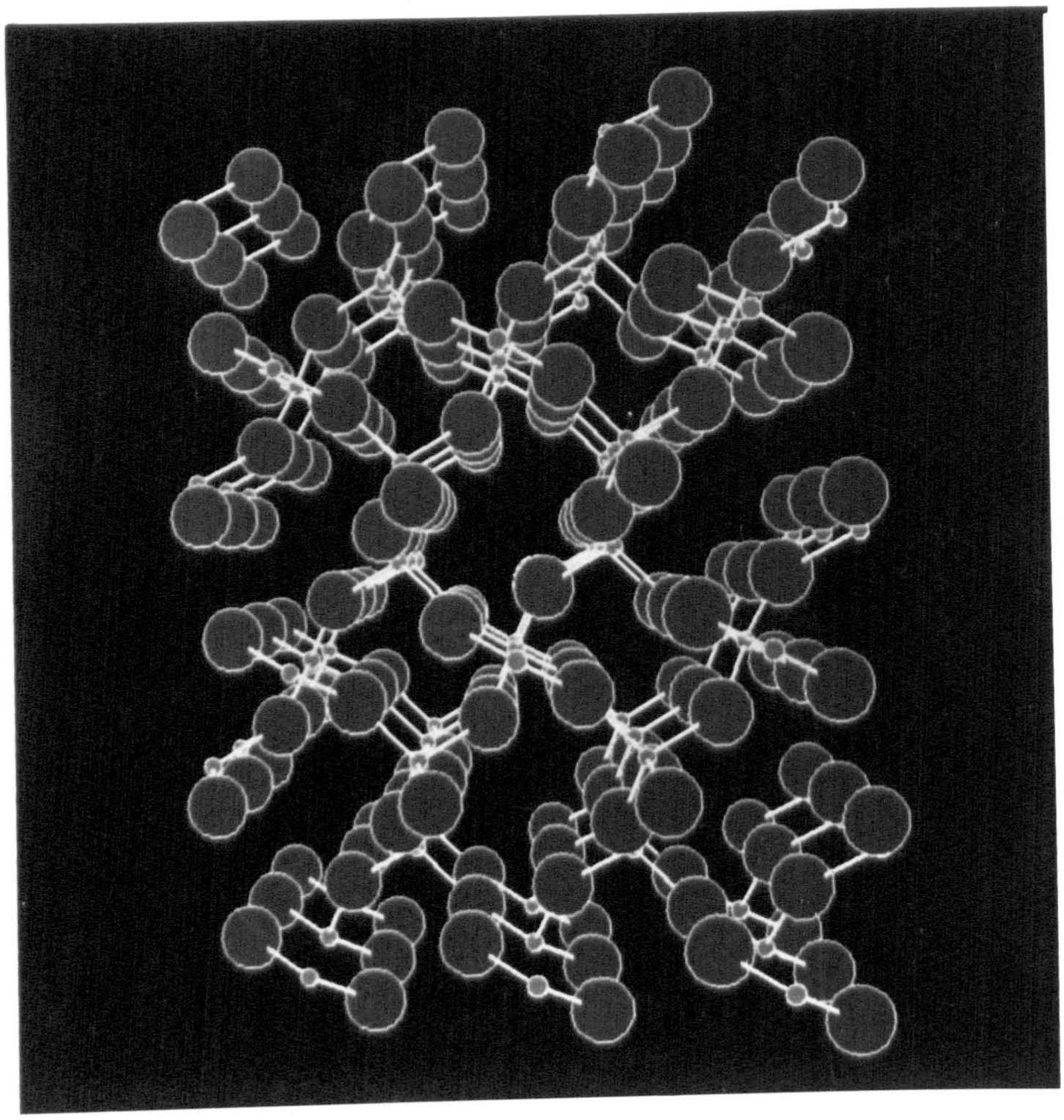

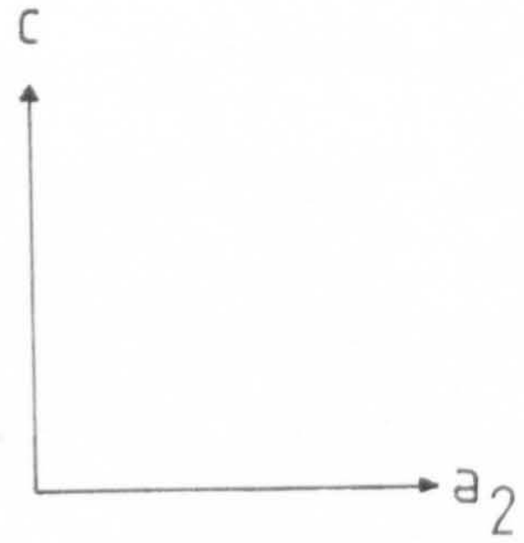

Fig. 1.7 Quartz Crystal Structure Parallel to the [001]

Direction

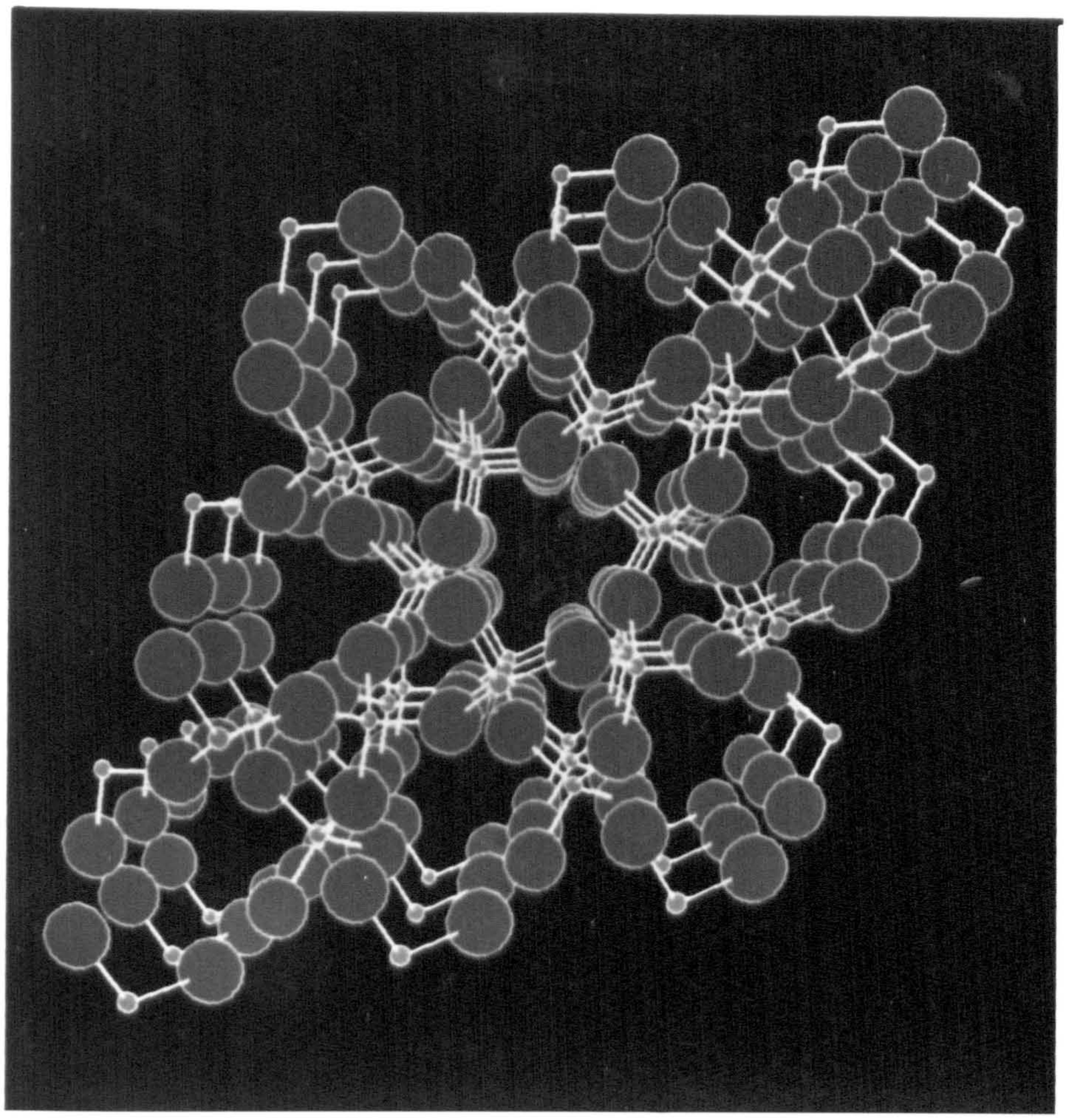

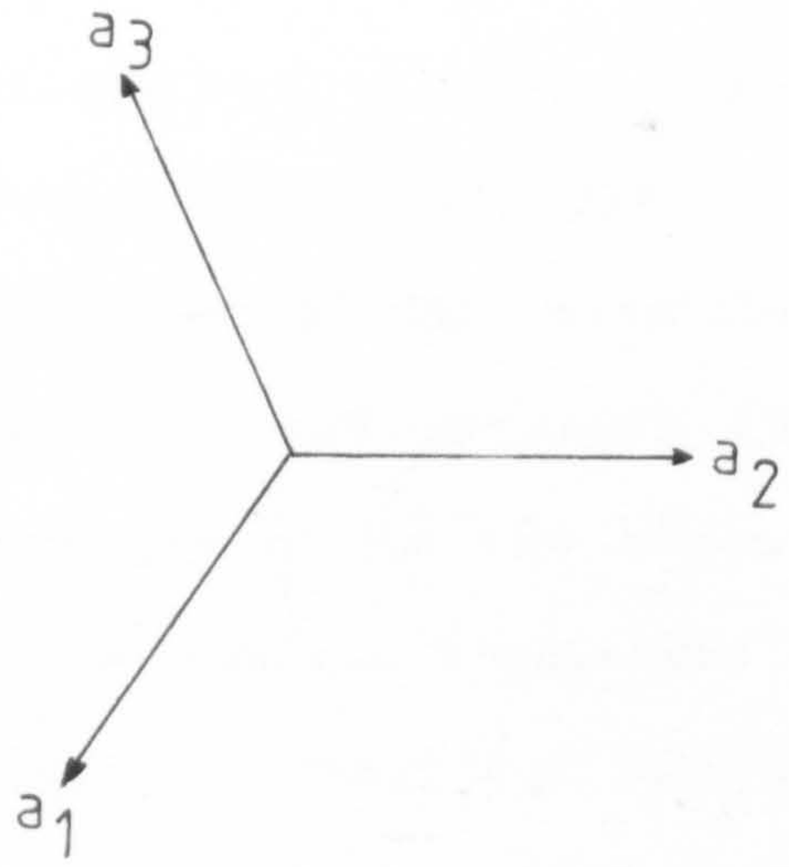

Fig. 1.8 Crystal Structure Showing C-Channels

handed quartz with respect to the earlier convention (see fig. 1.4). This convention has the advantage that these axes are identical to the three quartz growth directions X, Y and Z and so will be used in this thesis for describing piezoelectric and growth axes.

The crystal structure of quartz is rather complicated[2,14,15]. The unit cell contains three silicon and six oxygen atoms which are arranged as helixes in the [00.1] direction (see fig. 1.6 and 1.7). Open tunnels parallel to the C-axis known as C-channels are formed between these spirals (see fig. 1.8). The structure is sufficiently open to accommodate neutral particles of up to 1.4Å radii without significant lattice distortion.

1.4 Growth of Natural Quartz Crystals

Silicon dioxide in both crystalline and amorphous forms is an essential component of igneous rocks[16]. As such it is one of the major constituents of the Earth's crust. Igneous rocks originate from the fused mass known as magma which is found below this crust. Magma can be considered to be a solution of many elements kept molten by the extremes of heat and pressure found in this environment. Each component in the magma is free to circulate and under the correct conditions formation of minerals can take place. In order for this to happen the fluidity of the magma has to be sufficiently high for individual mineral elements to come together. Mineral

crystallisation will therefore be dependent on the chemical composition of the magma. The presence of certain substances known as mineralisers, such as water vapour and carbon dioxide, increases magma fluidity and promotes mineral formation. In the case of quartz formation these substances are essential. Crystalline quartz is most commonly found in pegmatite dykes and vein mineral deposits.

Pegmatite dykes[16] are formed during the final cooling and solidification of igneous rocks and are most commonly found in granites. Cracks form as the cooling rocks contract allowing fluid material to be forced into the fissures by external pressure. As the magma further cools, minerals crystallise out releasing large amounts of water vapour. The fluid that is forced into the fissures will contain more water than in the original magma composition. As a result, even though the composition of minerals in the pegmatite is the same as the igneous rocks which surround it, they are not deposited in the same order. Typical pegmatites are composed of crystals of quartz feldspar and mica whereas the surrounding magma produces igneous rocks such as granite. The varied composition of fissure fluids means that quartz is grown in the presence of many elements foreign to its structure and as a consequence crystals taken from this source tend to have high impurity levels.

Vein mineral deposits[16,17] are also formed in rock fissures but by different mechanisms than those described

for pegmatites. Veins consist of fissures or cavities in the rocks that make up the Earth's crust. Vein mineral deposits are formed when a vein is filled with water at depths where the high pressure and temperature conditions cause water to become an efficient leaching agent of minerals. Water circulates through openings in the fissure dissolving constituents in the rock and carrying them with it. When a suitable pathway is available, this fluid rises out of the fissures. The drop in temperature and pressure as the fluid rises causes minerals to crystallise out of the solution. When a vein is completely filled with minerals the resultant deposit is called a mineral vein. Where filling is incomplete the vein is usually lined with crystallised minerals. This is known as a replacement deposit because minerals formed in this way were originally present in another part of the rock wall[18]. These deposits are commonly found in water soluble rocks such as sandstone. The selective leaching of water ensures that quartz crystals found in these deposits are of a considerably higher purity than those found in pegmatite dykes.

1.5 Growth of Synthetic Quartz Crystals

All the modern processes used for the growth of large single crystals of synthetic Quartz have been developed from the pioneer work carried out by Spezia[19] at the turn

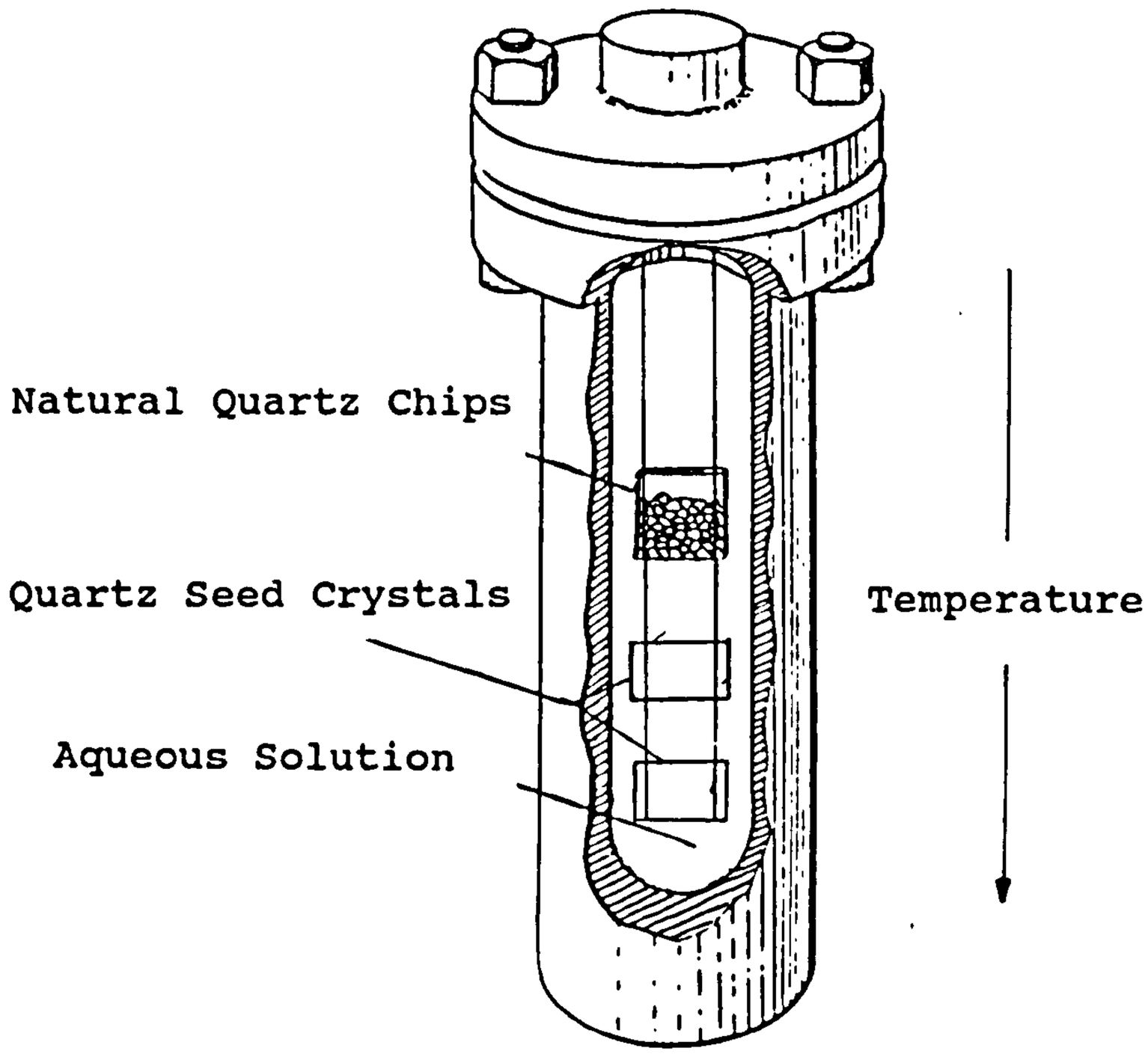

Fig. 1.9 Spezia's Crystal Growth Set-Up

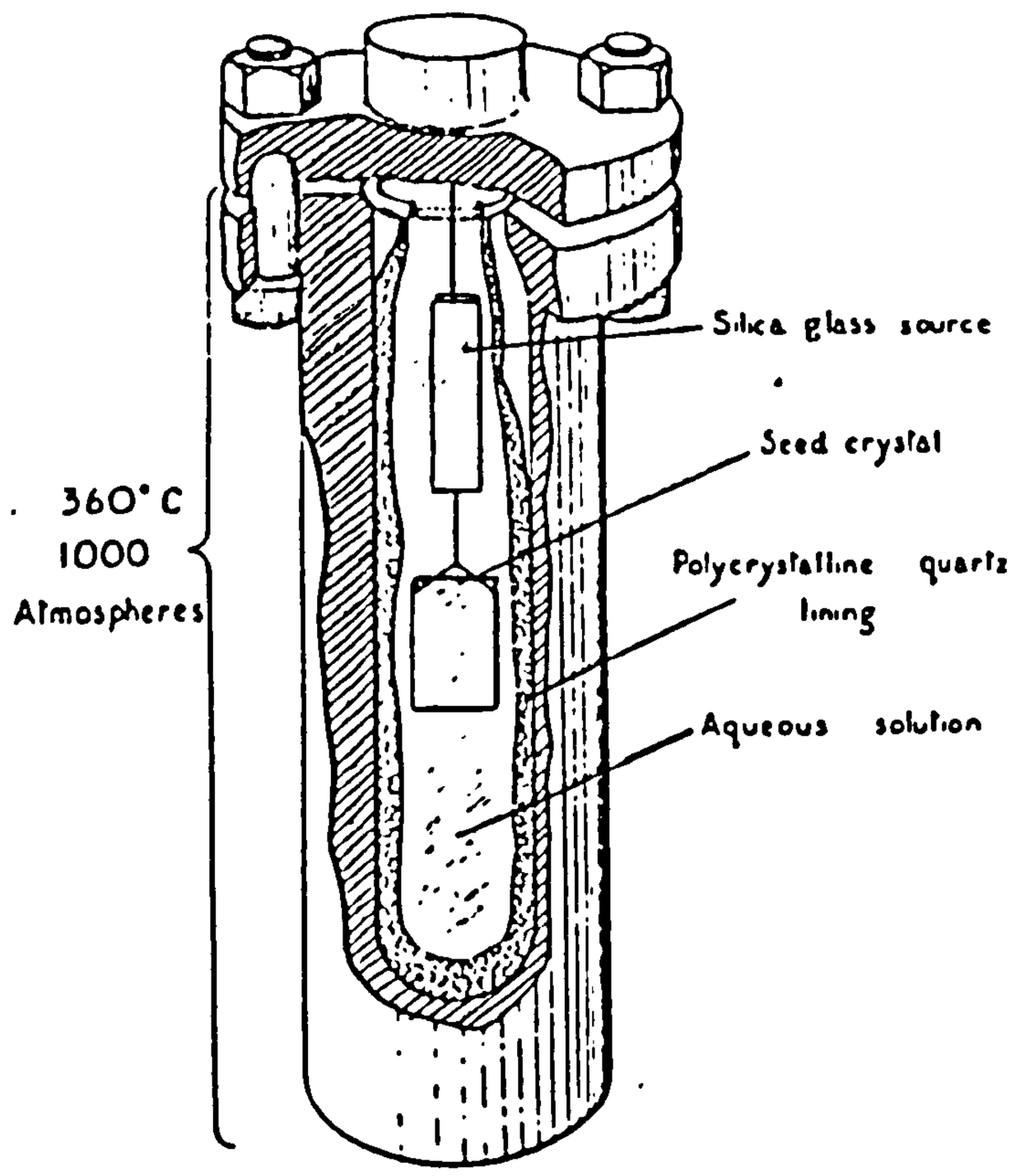

Fig. 1.10 Nacken's Isothermal Crystal Growth Set-up (From Ref. 33)

of the century. That author was the first to successfully grow a large single crystal using a hydrothermal growth technique. The word hydrothermal is used in this context to describe a reaction which takes place at high temperature and pressure in the presence of water. Spezia's method made use of the fact that Quartz was more soluble in solutions of sodium metasilicate above 300°C than at temperatures below this value. Growth was carried out in a metal vessel, known as an autoclave, which was partially filled with a solution of sodium metasilicate. The form of SiO_2 which provided the source of growth material or nutrient was chips of natural quartz crystals. The chips were suspended in the autoclave using a silver basket under which two truncated quartz seed crystals were situated (see fig. 1.9). When the vessel was heated, the metasilicate solution expanded to fill the growth chamber creating the high pressures necessary to assist the dissolution processes of the nutrient. The top of the autoclave was heated to a higher temperature than the base so that when the nutrient dissolved, the increased density of the solution surrounding the basket resulted in the heavy liquid flowing down past the seed crystals into the cooler area to produce supersaturation of the solution and crystal growth on the seed. After a period of 100 days, the truncated seed crystals had developed complete rhombohedral terminations and had increased in weight by

79% and 97%. Spezia also reported that crystals grown from pure sodium metasilicate solutions were cloudy in appearance but could be produced in a clear form if sodium chloride was added to the growth solution.

Although successful, the slow rate of growth attained discouraged the development of Spezia's procedure until Nacken's[20,21] attempts during World War II. Nacken placed both a silica glass source and a crystalline quartz seed crystal in an autoclave partially filled with sodium metasilicate (see fig. 1.10). He found that as the vessel was heated , the silica nutrient dissolved at a much faster rate than the seed crystal. This rate was sufficient to produce a solution which although only saturated with respect to the vitreous phase was supersaturated with respect to the crystalline phase. As a consequence of this, the temperature gradient employed by Spezia was unnecessary and the autoclave could therefore be heated evenly to produce an isothermal system. Rates of growth of up to 0.5mm per side per day were reported.

Nacken's research ended in 1944 but was carried on by Wooster and Wooster[22], Thomas[23] and others[24]. These workers discovered that although the initial rate of growth was rapid, devitrification of the silica nutrient soon prevented further crystal growth. The high degree of supersaturation which was produced by the nutrient caused spontaneous nucleation of crystals on the walls of the

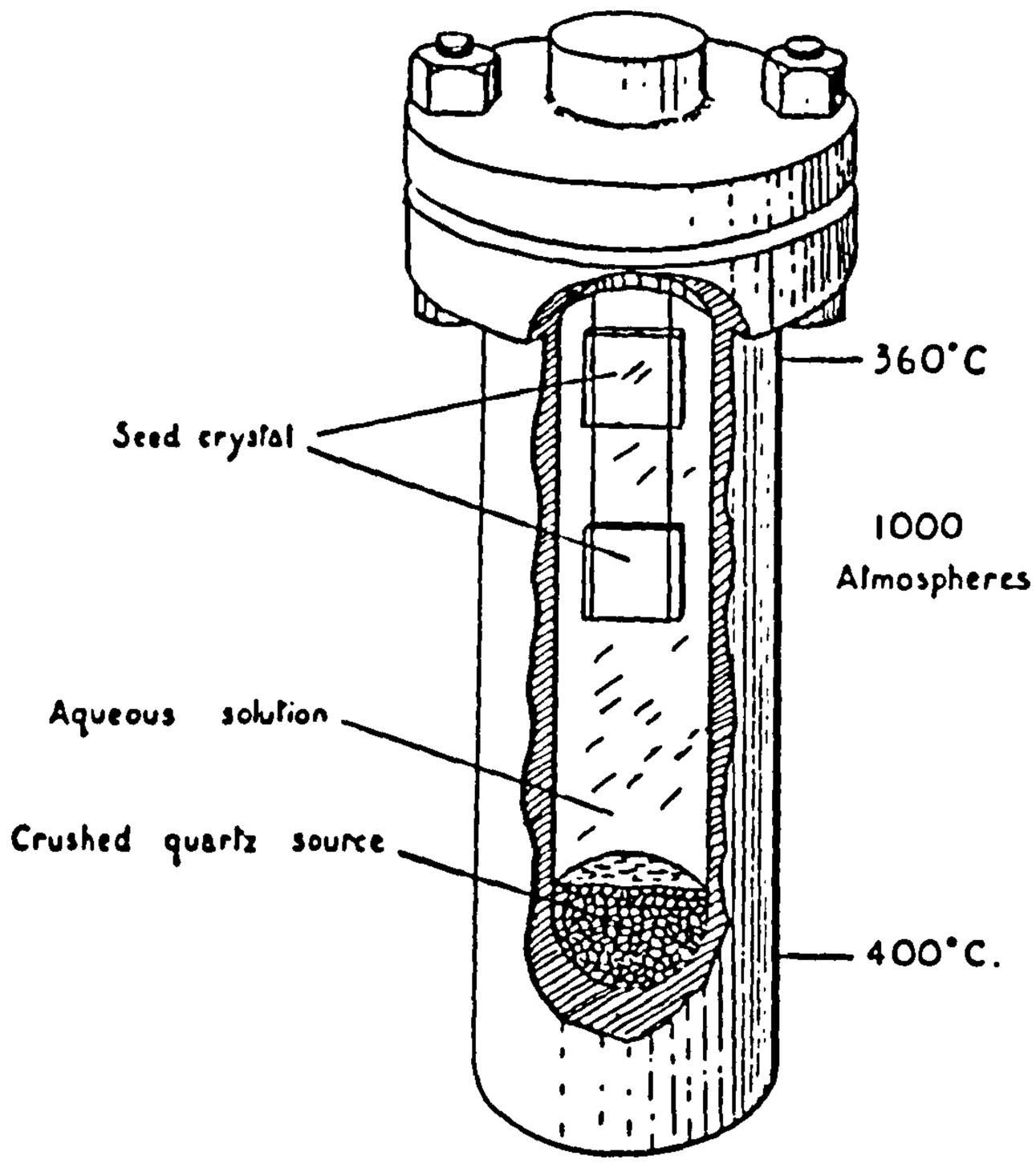

Fig. 1.11 Hale's Growth Set-Up

(From Ref. 33)

autoclave forming a polycrystalline coating (see fig. 1.10). This lining removed most of the material from the growth solution and effectively devitrified the silica source. Increasing the amount of source material only increased the amount of nutrient which devitrified and did not increase the amount of material available for deposition onto the seed. This limited the duration of a crystal growth run to no longer than about a day. Growth of large crystals was only achieved by successively depositing layers of quartz using an autoclave which was continually recharged with fresh nutrient. However, even this proved unsatisfactory as it was discovered that a thin imperfect region was formed during the initial stages of growth between each layer of crystal. The inability of the isothermal method to produce a thick layer of quartz that showed no imperfections, led to a reevaluation of the temperature gradient process used by Spezia.

Hale[25-27] succeeded in growing quartz at a rate which was several times as fast as that reported by Spezia. Spezia's procedure was modified by suspending seed crystals above a crushed natural quartz nutrient in an autoclave partially filled with sodium carbonate solution (see fig. 1.11). The temperature and pressure used were greater than those employed by Spezia and were sufficient to dissolve the nutrient to form a saturated growth solution. The base of the autoclave was heated to

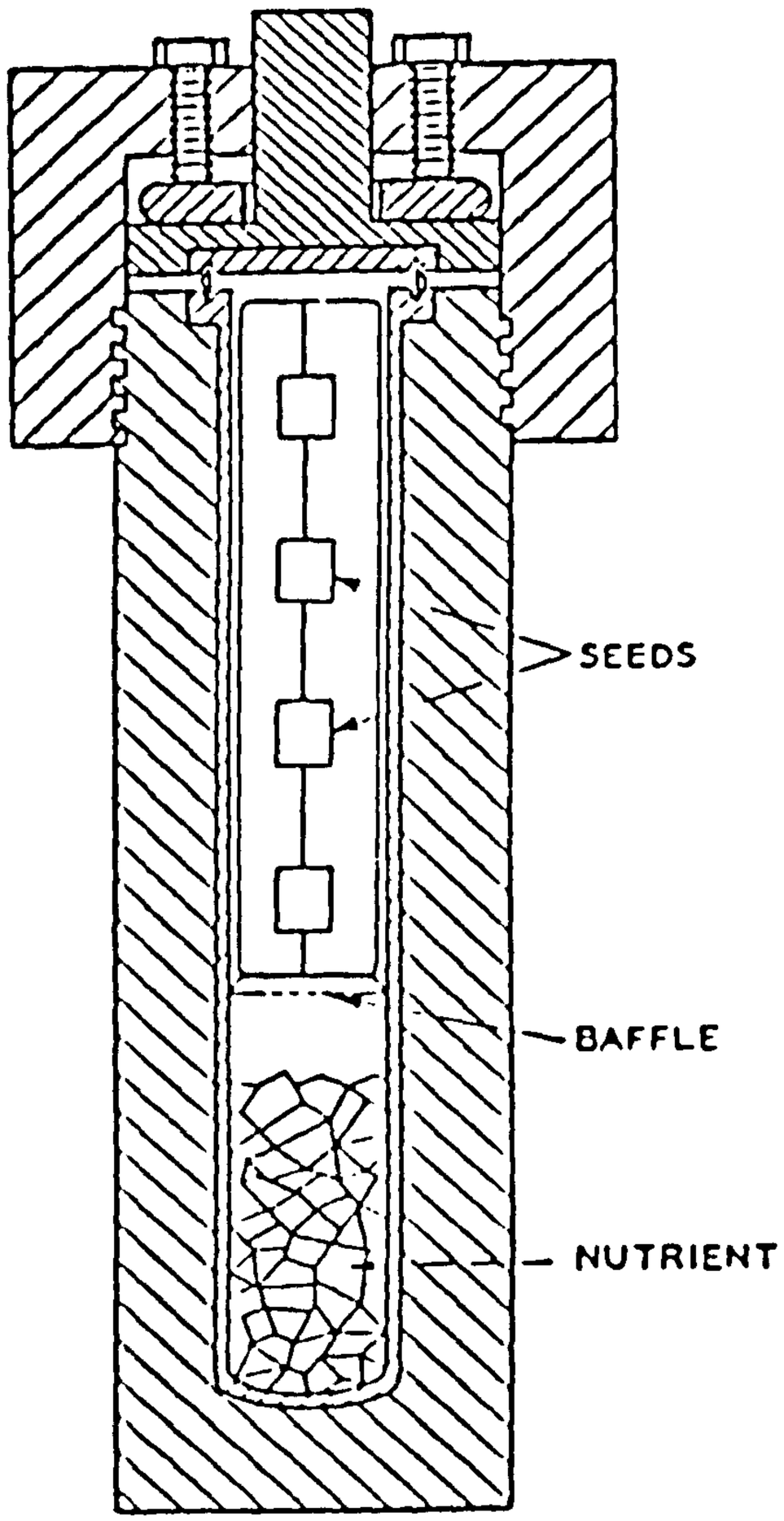

Fig. 1.12 Bueller and Walker's Crystal Growth Set-up

(From Ref. 35)

a higher degree than that of the upper portion where the seeds were suspended. Convection currents transported the saturated solution into this cooler region where the resulting supersaturation of the solution induced deposition of quartz onto the seed crystals. However, several disadvantages were associated with growth from sodium carbonate solutions. Not only did crystals usually have a cloudy appearance, but also spontaneous nucleation could take place at temperatures only 6 to 8°c below the saturation point.

Bueller and Walker[28,29] solved these problems and produced the first commercially viable growth procedure. The method was similar to that of Hale except that a sodium hydroxide solution was employed. Much higher pressures were necessary because of the change in solvent however, grown crystals were clear in appearance and spontaneously formed nuclei did not appear until temperatures dropped to 50 °C below the saturation point. These authors achieved very good crystal yields due to the introduction of a baffle into the autoclave as suggested by Kohman[30] (see fig. 1.12). This effectively divided the autoclave into two nearly isothermal regions, one for dissolution and one for crystallisation. The large isothermal crystallisation zone allowed the simultaneous growth of a number of crystals at approximately uniform rates. The publication of this work was quickly followed by reports from several laboratories

of the successful growth of crystals suitable for piezoelectric device fabrication[31-34].

Once a successful method for growing quartz had been developed, investigations were soon underway to optimise growth conditions and to improve the quality of crystals which could be produced. Laudise and Nielsen[35] tried to deliberately add impurities during growth in order to determine which ions could be incorporated into a growing crystal. They reported that Li^{+}, Ag^{+}, Ge^{4+}, Pb^{4+} and Sn^{4+} were incorporated but that Ca^{2+}, Ti^{4+}, Zr^{4+}, P^{5+} and As^{5+} were not. An interesting observation they reported was that the incorporation of pentavalent ions such as P^{5+} and As^{5+} could not be induced even by their addition in the forms of $AlPO_4$ and $AlAsO_4$ which were isomorphous with quartz. Brown and Thomas investigated the effect of using nutrients which contained high concentrations of aluminium on the growth of quartz[36]. These authors discovered that crystal quality decreased significantly when nutrients with aluminium contents greater than 0.25% w/w were employed. The rate of growth was shown to slow down with increasing aluminium concentration and levels of 2.5% were sufficient to prevent growth entirely. Systematic studies of impurity effects carried out by Flickstein and Schieber[37,38] and Yamashita et al.[39] concluded that, in general, almost all impurities were undesirable. These authors showed that in addition to aluminium, vanadium, gallium, magnesium, germanium and

zinc were growth depressants. Iron, aluminium and magnesium were shown to induce fluid inclusions and seed veil formation.

The source of many impurities is the natural quartz nutrient and several attempts have been made to find a more suitable alternative growth material. Kolb. et al.[40] tried to use amorphous silica despite the earlier history of failure when using this nutrient.The advantages were that high purity glass could be produced which contained very much lower levels of impurities than natural quartz. However, these authors had no more success with the amorphous nutrient than the earlier workers had. Crystal quality was reported to be poor with specimens exhibiting many cracks. Again the problems with spurious nucleation on autoclave walls and devitrification of the nutrient were encountered. This later work did however prompt a study by Baughman, who successfully developed a procedure for using the amorphous nutrient[41]. Although Baughman not did specify growth conditions, the success of his method was probably due to the careful selection of seed material. Instead of the normal basal seed orientation, seeds were cut parallel to the AT orientation[5] (see fig. 1.4b). Crystal growth rates are much slower on this type of seed in comparison to the basal cut[35]. The quality of growth was reported to be comparable with those crystals grown using a crystalline nutrient.

Croxall et al. went a stage further than Baughman by converting high purity silica to a crystalline state before using the material for growth[7]. This was achieved by heating a silica nutrient in an autoclave under normal operating conditions for one day. The devitrified silica was converted into a finely divided crystalline state. After the conversion had taken place, seed crystals were inserted into the autoclave and a normal run was carried out. These authors also took extensive steps to remove all other sources of contamination. The internal surface of the autoclave was coated in gold and the seed supports and baffles were constructed from platinum to prevent impurities from the growth vessel coming into contact with the solution. The solution itself was made up from high purity Aristar grade sodium hydroxide and double deionised water. These procedures combined with careful seed selection and growth conditions, produced the first report of a synthetic crystal which was not only of high purity but which also possessed crystalline perfection similar to that found in naturally grown crystals.

The growth of synthetic crystals possessing high crystalline perfection was not new, although no workers prior to Croxall et al had achieved this property in conjunction with high purity. Gordienko et al.[42] grew and studied dislocation free quartz prepared from basal seed slices cut from a virtually perfect natural crystal but

did not report conditions of growth. Barns et al.[43] successfully grew crystals which were of high crystalline perfection. Both AT cut and basal seed plates were used for growth experiments which were carried out in noble metal lined autoclaves. A loss of growth quality was reported for those runs where a conventional unlined autoclave was used as a control experiment. This loss was attributed to particulate inclusions originating from the deterioration of the autoclave walls under growth conditions. The perfection of the seed crystal and its preparation prior to a growth run was shown to be essential. Any dislocations that were present in the seed were propagated into the growing crystal. This could only be avoided by selection of a dislocation free seed. The procedure employed by Barns et al. consistently produced material which was either completely or at least nearly dislocation free. The purity of their crystals was not reported. The only other report of the production of high purity, low dislocation synthetic crystals was that of Armington and Larkin[44]. They concentrated on reducing aluminium levels and showed that if the nutrient used contained very low levels of impurities, then high purity quartz with aluminium levels in the range reported by Croxall et al. could be obtained even if an unlined autoclave was used. They also reported that if sufficient care was taken with seed selection, then low dislocation content crystals could also be grown using an unlined

autoclave.

Work was also carried out by several workers to find an alternative to the sodium hydroxide and sodium carbonate solvents used commercially. Kopp and co-workers[45,46] successfully produced good quality crystals using a rhodium hydroxide solvent. This had the advantages of eliminating sodium impurities originating from the solvent but resulted in the incorporation of high levels of rhodium into the crystal instead. In all other ways the crystal was comparable in quality with the quartz that was being produced at that time. Hosaka and Taki produced a series of publications which dealt with the usage of pure water[47,48], sodium chloride[48,49] and potassium chloride solvents[48,50]. As would be expected, the rates of growth in pure water solutions were reported to be only one tenth to one hundredth of that observed for alkaline solvents. The sodium content of the crystals produced was much reduced in comparison to those grown conventionally. However, despite growth having taken place in a platinum vessel, the crystals contained high levels of aluminium which originated from the converted fused silica nutrient used. The investigations into growth from sodium and potassium chloride solutions were attempts to produce a growth environment as close as possible to that which occurred in nature. The growth conditions they employed induced a change in the morphology of the crystals which made them more closely

resemble naturally grown quartz. Growth striations on prism faces, which were commonly observed on natural but not synthetic quartz, were reported for the chloride grown crystals. These authors also successfully grew crystals in a heavy water sodium carbonate solution[48]. Growth of deuterated quartz had only been reported previously by King et al.[51] and Kats[52] who used sodium deuteroxide in deuterium oxide as the growth solution.

1.6 Defects in Quartz Crystals

Crystals grown both in nature and synthetically are rarely perfect and usually contain a number of imperfections or defects. These defects can be characterised into four groups according to the area of a crystal they affect, namely : volume (three dimensional) defects; planar (two dimensional) defects; linear (one dimensional) defects and point defects. In the following sections, the importance of a defect will be assessed with regard to what influence it has on the fabrication and performance of a quartz resonator and in particular, those defects common in the high purity crystals studied during this project.

1.6.1 Volume defects

The most important volume defects found in quartz crystals are inclusions. These defects come in two types, namely fluid[53] and particulate[5,43] inclusions. Fluid inclusions arise from the trapping of layers of solution adsorbed onto a crystal surface during growth[53]. This commonly occurs close to the seed and can lead to the formation of a highly imperfect region known as a seed veil which contains many fluid inclusions[5]. A particulate inclusion is formed when a foreign particle at the surface of a crystal is trapped by overgrowth. The major sources of particles arise from autoclave walls

and fittings[43], which are attacked during growth to form a layer of the mineral acmite, $Na_2O \cdot Fe_3O_4 \cdot 4SiO_2$. Parts of the acmite layer can be detached by the rigorous growth environment and incorporated in the growing crystal. However simpler species such as dirt or dust which are present in the autoclave can also form these defects. The boundary between an inclusion and a host crystal is a highly strained region. This strain can sometimes result in the formation of a defect known as a dislocation (see section 1.6.3). Inclusion related defects are common in synthetic crystals, however conditions used for high purity growth produces crystals free from inclusions of any significant size.

1.6.2 Planar Defects

Defects which fall into this class are crystal twins and fault surfaces. A crystal twin is defined as " a geometrical position of intergrowth of one or more crystals of the same species which occurs at a frequency greater than by chance"[2]. That is, the different parts of intergrown crystals are related to each other by a specific geometric relationship as opposed to a random orientation. The commonest types of twins which occur in quartz are optical and electric. These are also known as Brazil and Dauphiné twins, respectively, after the geographic areas where natural crystals displaying each type of defect were originally found. An optical twin

can be considered as both structural hands of quartz occurring in the same crystal. The twinned parts of a crystal are related as by a reflection over a plane of the type {11.0}. It is known as an optical twin because it is detected using properties of the optical axis. As previously discussed (see section 1.3) when polarised light is shone through a quartz sample along the optical axis it is rotated in a direction which corresponds to the structural hand of the crystal. When this light passes through an area of different structural hand the direction of rotation will reverse indicating the presence of an optical twin. This detection procedure requires the preparation of optically clear samples cut at right angles to the optical axis. A more convenient detection technique, which requires no prior sample preparation, is the immersion of a crystal in a liquid which possesses a similar refractive index, such as benzoyl alcohol, followed by an examination of the crystal using an intense polarised light source. If the crystal is tilted at a slight angle to the optical axis, the differences in thickness between the twinned area and the crystal bulk reveals the imperfection as an area of coloured interference lines against a highly ordered uniform background. Electrical twins[2] are related to each other by a rotation of 180° around the C-axis. The polarity of the electrical axes is reversed although the structural hand of twinned areas is the same. These

defects have no distinct boundaries within a crystal and are detected by the use of chemical etching. Due to anisotropy, the rate at which an etchant attacks quartz varies depending on crystal direction. Therefore, because crystal directions are different in twinned areas they will etch at different rates. Consequently, etch pits will form faster in one part of a twin than in the other. Simple inspection of an etched crystal will reveal the boundaries between twinned areas.

A quartz resonator must have no twins present if it is to function correctly. This is a consequence of the anisotropy of the piezoelectric properties of quartz. Crystal vibration always occurs along the piezoelectric axes. When a twin is present, a crystal will vibrate in two different directions, each corresponding to the alignment of the piezoelectric axis with respect to the different crystal regions, resulting in the resonator being damaged. Twins are common defects in natural quartz with only around 2% of crystals being free from this imperfection. However, a resonator can be made from natural crystals if the twinned regions are separated from each other. Twins do not usually occur to any significant extent in synthetic crystals.

Fault surfaces are another type of planar defect with atom planes which have grown slightly out of step with the rest of a crystal. These defects can be detected from a marginal difference in the lattice parameters

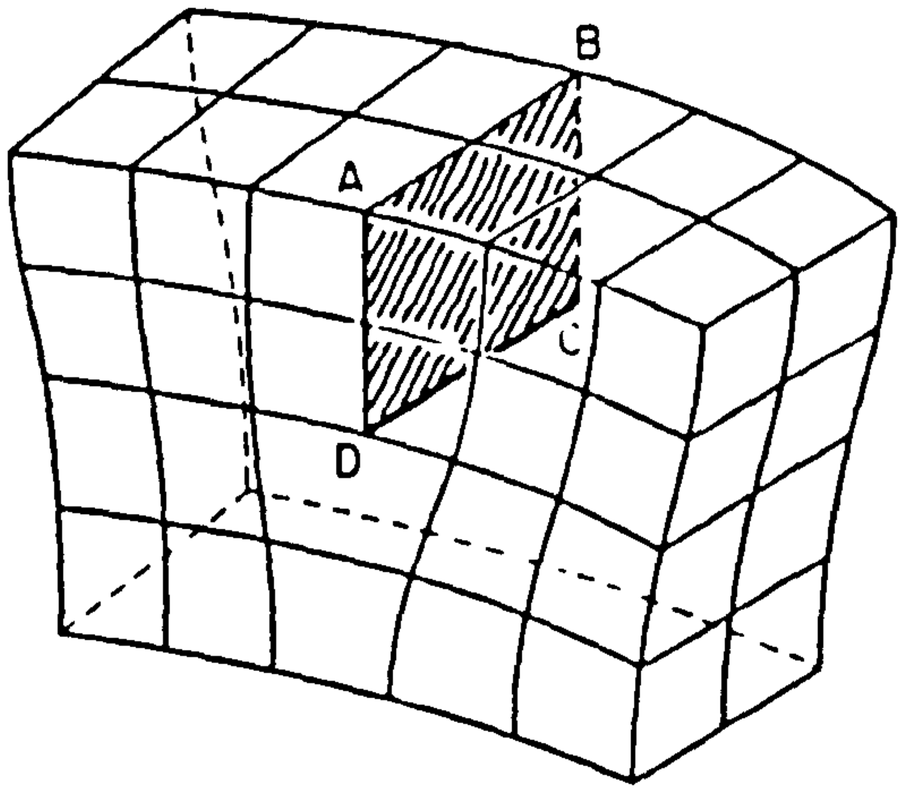

Fig. 1.13 Edge Dislocation

(From Ref. 56)

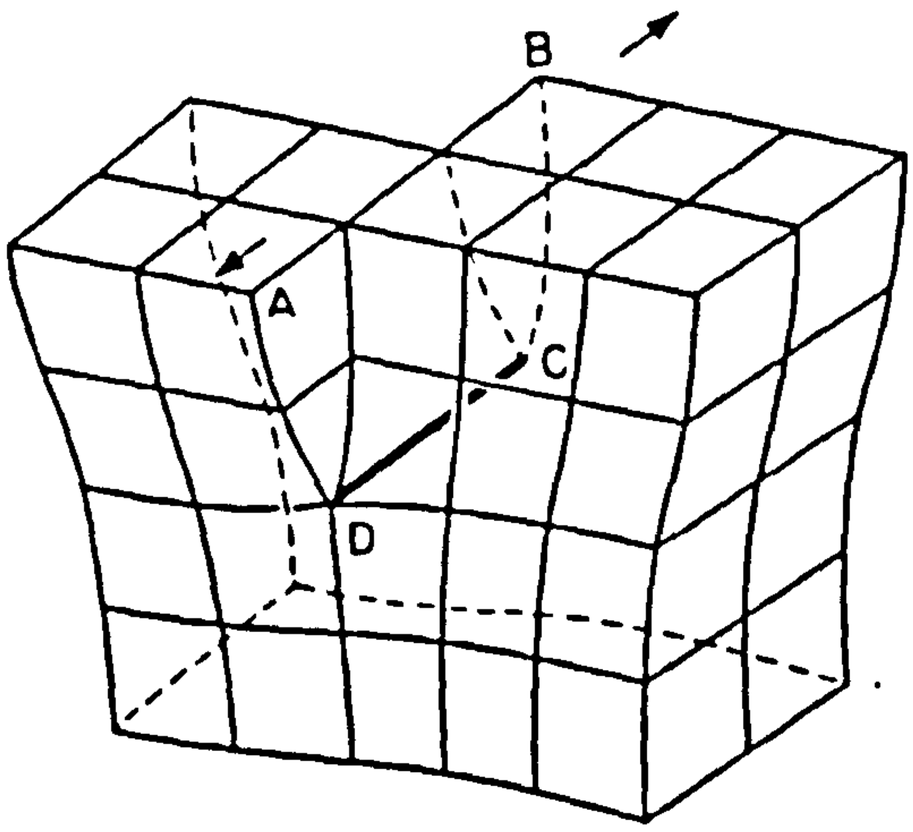

Fig. 1.14 Screw Dislocation

(From Ref. 56)

between the defect and the perfect crystal[54]. These defects are commonly observed at the cellular growth boundaries present in the (00.1) growth sector of synthetic quartz but do not have any detrimental effect on crystal properties.

1.6.3 Linear Defects

The most important linear defects are known as dislocations. There are three types of dislocations, namely of edge, screw and mixed character[55]. An edge dislocation results from the presence of an extra plane of atoms, ABCD, in the crystal lattice (see fig. 1.13), whereas a screw dislocation occurs where one part of a crystal, ABCD, grows out of step with the rest by one lattice spacing (see fig. 1.14). Mixed dislocations exhibit part screw and edge character. The most useful definition of a dislocation is given in terms of a Burgers circuit[56]. This circuit is any atom to atom pathway in a crystal lattice which forms a closed loop around a dislocation (see fig. 1.15). If such a pathway is selected for an imperfect crystal lattice and then the same route followed around a perfect lattice, the result will be non-closure of the circuit in the former case indicating the presence of a dislocation. The vector required to close the circuit is known as the Burgers vector. The different dislocation types are defined by the relationship of the Burgers vector, $\underline{b}$, and the

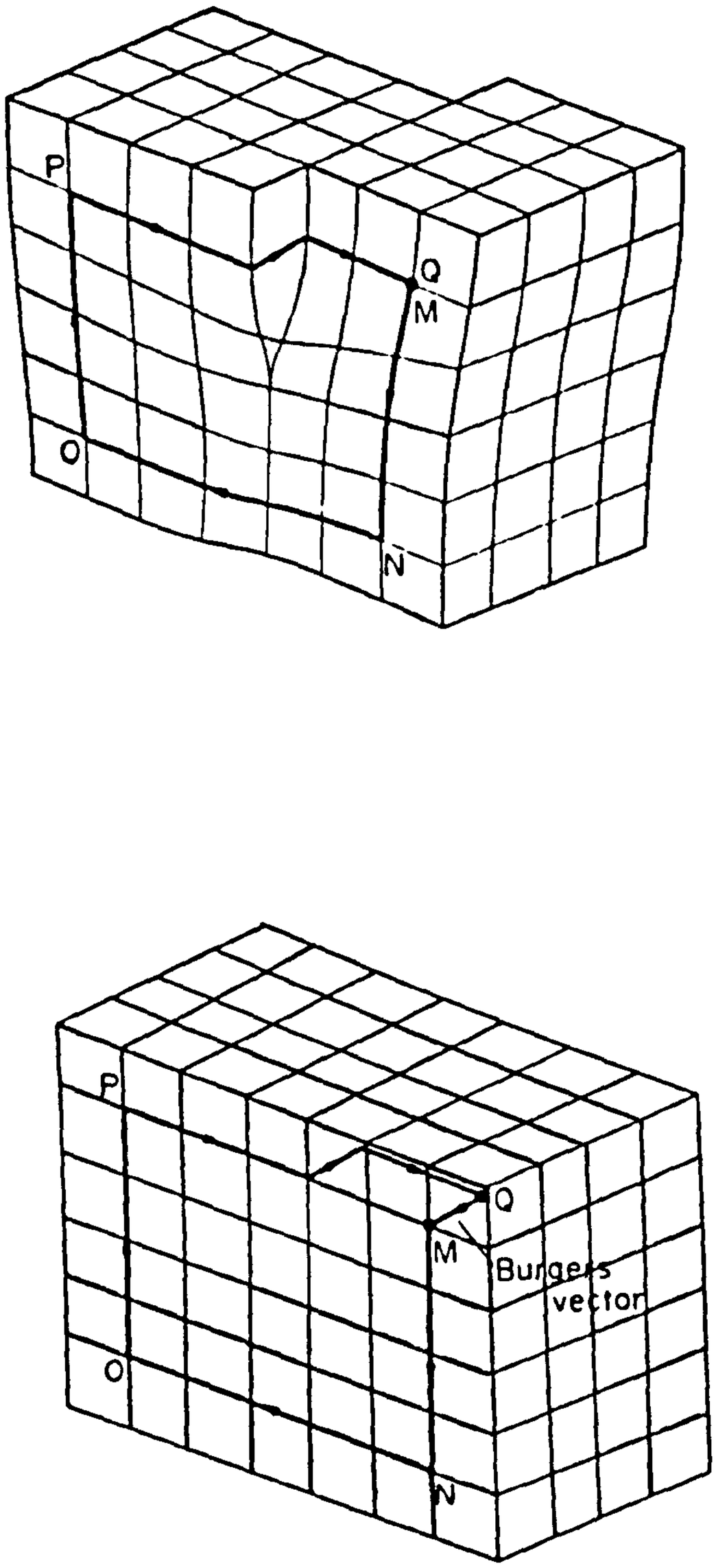

Fig. 1.15 Burgers Circuit
(From Ref. 56)

Table 1.3 Definition of Dislocation Types

Type	Relationship Between Burgers Vector and Dislocation Line Direction
Edge	$\underline{b}$ perpendicular to $\underline{l}$
Screw	$\underline{b}$ parallel to $\underline{l}$
Mixed	some combination of the above relationships

dislocation line direction, $\underline{l}$ (see table 1.3).

Dislocations can be further characterised as originating from either mechanical or growth defects. Mechanical dislocations can be generated in plastic materials either as a means of relieving internal strain or as a result of the application of an applied mechanical shear[56]. However, quartz is a brittle material and does not plastically deform except when water has been incorporated into the crystal lattice[57,58]. Under conditions of high temperature and pressure quartz which contains a high water content plastically deforms via hydrolytic weakening[57]. However, under normal conditions, the main dislocation type encountered in quartz are growth dislocations. As the name implies, these imperfections are generated during the growth process of a crystal. Continuation of dislocations from a seed into a growing crystal are common[43]. Dislocations are also generated during growth in highly strained crystal regions such as in the vicinity of an inclusion[5,53] although the presence of the later defect does not always produce a dislocation.

A common practice for the removal of surface damage on a quartz resonator is chemical polishing using hydrofluoric acid[59,60]. In the case of a perfect crystal, this polish is even across the surface of a resonator. However, the atomic bonds in the core of a dislocation are highly strained and are consequently more reactive

than those in a perfect crystal. This results in preferential etching at emergent defect sites on the surface of a crystal. Dislocation bundles also etch to form tunnels of up to 1μm in diameter[61]. In extreme cases, holes can be formed in the quartz which severely degrade the electrical properties when used as a resonator.

Commercially produced synthetic crystals generally have between 500 and 2000 dislocations per cm^2 in comparison to around 10 dislocations per cm^2 in high purity crystals. Dislocation concentrations in natural single crystals of quartz are generally much less than synthetic quartz and dislocation free crystals are not uncommon.

1.6.4 Point Defects

Lattice vacancies and impurities are commonly found in quartz crystals and are termed point defects. Vacancies as simply missing atoms in a crystal structure. At all temperatures above absolute zero there exists a thermodynamically stable number of vacant lattice sites. When a crystal is grown above ambient temperature and then cooled, there will be a non-equilibrium concentration of vacancies trapped in the crystal. Under the correct conditions, excess vacancies collect together to form a vacancy cluster which can collapse to produce a dislocation loop[56] (see fig. 1.16). However, these

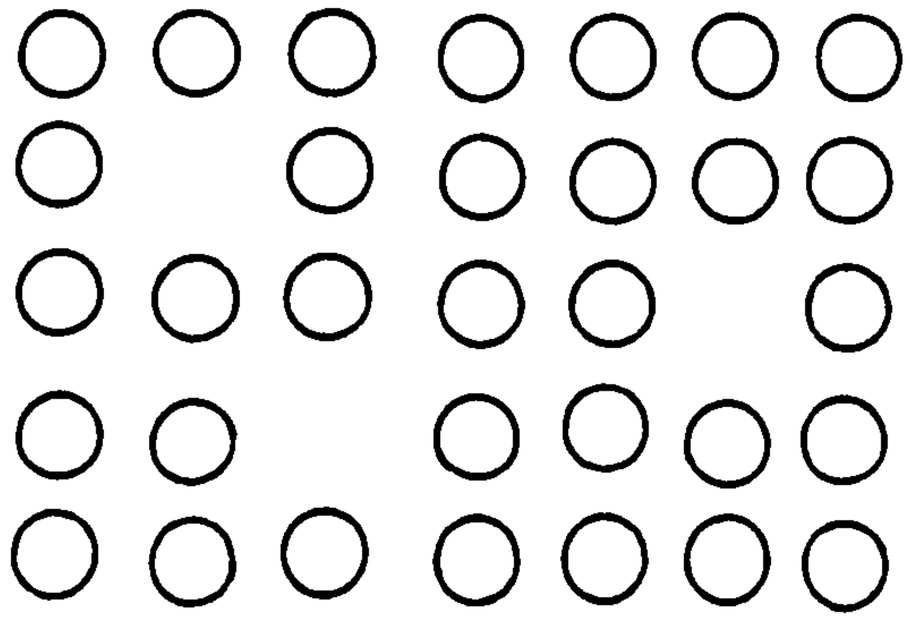

a) Crystal Lattice Vacancies

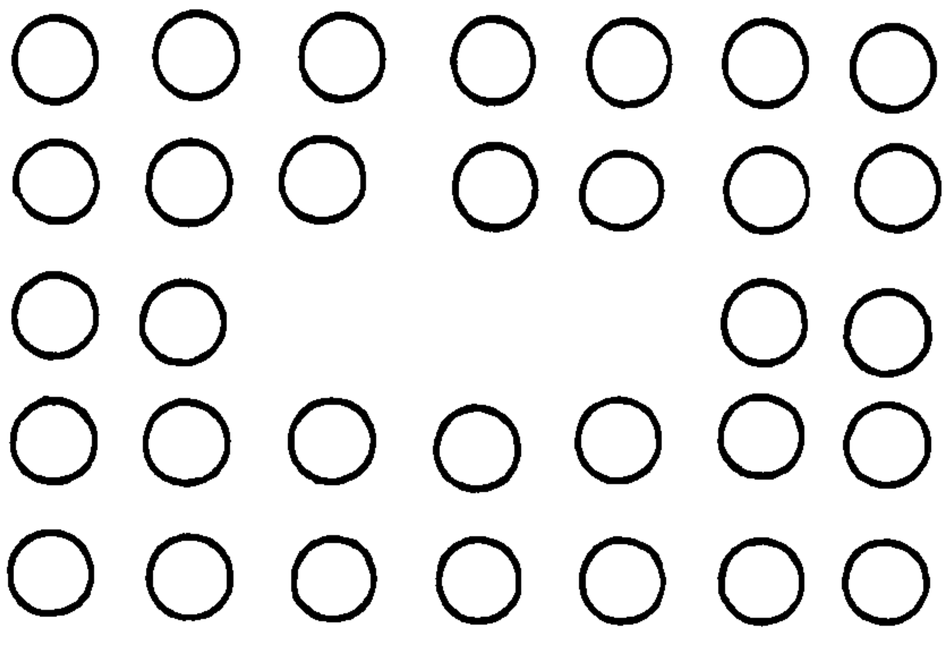

b) Vacancy Cluster Formation

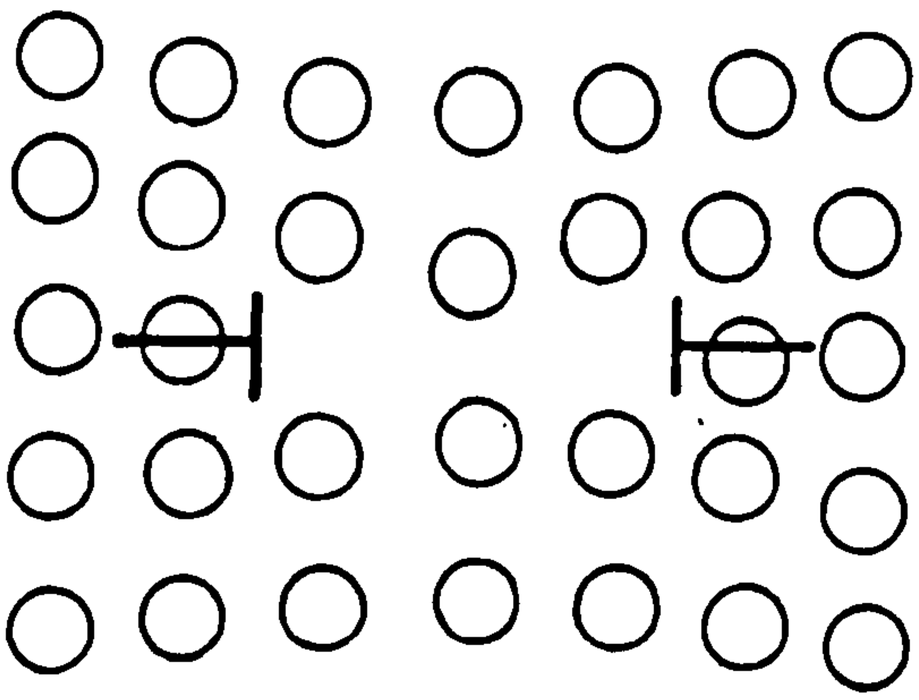

c) Dislocation Loop Formation

Fig. 1.16 Schematic Represention of Crystal Lattice Vacancies

Table 1.4 Effects of Impurities on Synthetic Quartz Growth

Impurity	Source	Effect
Va, Ga, Mg, Ge, Zn	natural quartz nutrient	slows down growth rate
Fe	autoclave walls and fittings	causes inclusion formation and degrades crystal properties
Al	natural quartz nutrient	as for Fe
Mg	natural quartz nutrient	causes inclusion formation

Table 1.5 Impurity Levels in Quartz Crystals

Quartz Type	Source	Impurity Levels (ppm)				
		Li^+	Na^+	K^+	$Al3^+$	$Fe3^+$
Natural clear Quartz[a]	Brazil	165	<3	-	353	<3
Natural smoky Quartz[a]	Ukraine	200	<3	-	189	<3
Amethyst Quartz[a]	NS	112	192	53	28	350
Commercial Quartz[b]	STC	0.7	0.4	-*	1.0	0.02
High Purity Quartz[b]	GEC	-*	-*	-*	0.01	-*

* - Below the limit of detection of 0.005 ppm

a - Figures quoted from Kats (see reference 49)

b - Crystal analysed at GEC Hirst research laboratories using spark source atomic absorption spectrometry

NS - Not specified

STC - Standard Telecommunications and Cables Company

GEC - General Electric Company, Hirst Research Labs

defects more commonly occur as single atom vacancy sites such either an oxygen or a silicon atom is absent from the quartz crystal structure[62-64]. Vacancy related defects are only significant with regard to synthetic quartz if a crystal is heated above 550°C[58].

Impurities consist of single atoms, ions or molecules of any species foreign to a crystal which are incorporated during the growth of a crystal from contaminants present in the growth solution[37,38,52]. The presence of certain impurities can also alter the rate and the quality of a growing crystal (see table 1.4). Typical concentrations of impurities in natural, commercial and high purity quartz are given in table 1.5. Impurities play an important role in etch tunnel formation and in the deterioration of resonator performance under the influence of radiation. Impurities are known to concentrate along the length of a dislocation and, since etch channels are always formed along these defects, the leaching of these impurities by an etchant is thought to be a mechanism for channel formation[65]. More important is the effect of impurities on the radiation response of quartz resonators. Under normal conditions, the vibrational frequency of a resonator is very stable. However, this frequency can be significantly altered when a crystal is subjected to ionising radiation. Frequency offsets are thought to be attributable to the migration of radiation induced alkali

metal impurities, such as Na^+ and Li^+, and also to the subsequent changes in material constants produced by the redistribution of defect centres in the crystal[66,67]. The elastic, piezoelectric and dielectric constants of quartz are affected after irradiation. The frequency offset of a resonator increases with the concentration of certain impurities, notably aluminium[68]. Resonators fabricated from commercial and natural quartz are subject to large frequency offsets. High purity crystals are radiation "hard" and are not greatly affected by radiation treatment.

1.7 The Detection and Characterisation of Defects in Quartz Crystals

The following sections review work carried out by researchers in the field of defect characterisation and concentrates on the use of x-ray diffraction methods and infrared spectroscopy. Defect studies involving these two techniques make up the bulk of work carried out during the course of this project. The theory and experimental procedures of x-ray diffraction and infrared spectroscopy are detailed in chapter 2.

1.7.1 X-Ray Diffraction Studies of Quartz Crystals

The first x-ray diffraction image of a quartz crystal defect was reported by Lang in 1959[69]. By performing a study of PendellÖsung fringes observed on diffraction images obtained from a series of specially cut natural quartz samples, Lang detected but could not characterise a planar defect in the bulk of the crystals. Lang also reported the first use of transmission x-ray diffraction topography[70,71], or projection topography as it was also known, to image natural quartz crystal defects[72]. In his publication, Lang reported the observation of short linear features of enhanced intensity on diffraction topographs which he tentatively assigned to dislocation lines. He observed that, when a sample was etched using hydrofluoric acid, tunnels were formed in the crystal

which followed the course of the linear defects. He also reported a band of PendellÖsung interference effects across the centre of a sample crystal which he attributed to the planar defect he had previously reported[69]. In a later publication, Lang also succeeded in detecting Dauphiné and Brazil twins using topography[73]. In comparison with the crystal bulk, Brazil twins produced weaker contrast on x-ray diffraction topographs because of differences in structure factors for a given set of reflection planes. Dauphiné twins on the surface of a crystal could be imaged using reflection topographic methods. Although this did not provide any more information than conventional detection methods using chemical etching, the process did not destroy the crystal surface.

The first major x-ray topographic study of defects in synthetic quartz was that of Spencer and Haruta[74]. They reported that the dominant defects in synthetic quartz were lines of strain which originated at an inclusion, or similar defect site, present on the seed during the hydrothermal growth of crystals. The linear features were shown to change contrast on topographs obtained from different Bragg planes and to etch at a considerably higher rate than perfect regions of the crystal. These authors suggested that alkali metal impurities, found at the cathode edge of a sample which had been subjected to electrolysis[75], were concentrated around the linear

features and enhanced the strain in the crystal which led to increased etch rates at these defect sites. They further postulated that the linear features were dislocations but could not prove this theory.

Lang and Muiscov applied high resolution topographic techniques to conclusively identify the linear features as dislocations[54]. They dealt exclusively with synthetic crystals and reported the detection of a range of crystal defects. The crystals which were studied were considered of good quality and yet were reported to possess dislocation densities of approximately 3000 defects cm^{-2}. The authors observed that the majority of dislocation line directions made an angle of not more that 12° to the C-axis and that exact alignment with the [001] direction was avoided in all cases. They examined sections of the crystal cut from the seed to the crystal surface and observed that on those sections near to the seed, dislocations were randomly distributed in density but as growth proceeded in the C-direction, these defects were observed to concentrate into groups around the boundaries of a polygonal cellular structure. This cellular network reached its maximum development with the formation of the rough final cobbled surface characteristic of synthetic crystals. The boundaries of the cells were shown to be outlined by stacking fault type fringes which resembled parallel horizontal layers. These authors also observed individual growth layers

lying parallel to (00.1) planes at various depths and showed that the surface of the crystal was covered by a thin imperfect layer several microns thick. Previous etching studies carried out by Lang[72], were expanded to confirm that etch pits were formed almost exclusively at dislocation sites. They could find no correlation between the depth of an etch pit and the Burgers vector of its associated dislocation although they showed that a third of dislocations went on to form etch tunnels after prolonged etching.

McClaren et al.[76] followed up this study with an investigation concentrating on the occurrence and nature of dislocations in synthetic crystals. They studied a series of samples which contained dislocation densities ranging from 2000 to 500 defects/cm^{-2}. Synthetic and natural seeds were identified by their high and low dislocation concentrations respectively. Examination of crystal sections, which were cut perpendicular to the (00.1) faces and which contained a seed, revealed that dislocations present in the seed continued into the growing crystal. Topographs of crystals grown from a defect free natural seed showed that dislocations were also produced at the surface of the seed. These grew with the new crystal to form a substructure similar to that observed when a high dislocation synthetic seed crystal was used. The authors also reported a highly strained band next to and parallel with the seed crystal.

This was attributed to bending of the crystal lattice associated with stress relaxation at the intersection of new growth layers with the natural seed. Differences between the lattice parameters of natural and synthetic quartz were responsible for the strain. Similar bands were not observed on topographs of crystals grown from synthetic seeds. The growth layers parallel to the (00.1) faces reported by Lang[72] were again observed except in this study the development of growth cells was shown to disrupt the feature near to the cobbled crystal surface to producing waved layers. McClaren et al. confirmed the concentration of dislocations at cell boundaries and in addition showed that the apex of each cobble on the (00.1) crystal face was the termination point for a dislocation. They took this as an indication that dislocations were involved with the growth mechanism for quartz. The crystals examined in this work had different concentrations of hydrogen impurities. This was used by the authors to tentatively suggest that there was a correlation between dislocation density and the levels of hydrogen impurities with defect levels increasing with the concentration of impurity. The majority of dislocations observed on topographs were characterised as being nearly pure edge in character possessing Burgers vectors lying in the [110] direction.

Homma and Iwata studied the imperfect growth layer near to the cobbled surface of synthetic crystals[77]. They

demonstrated that the layer was in the order of tens of microns thick, nearly ten times the value quoted by Lang and Muiscov[54]. They observed that this imperfect layer could be removed by chemical etching or mechanical polishing. When 600μm of the surface was removed by mechanical polishing, diffraction topographs showed that the crystal interior was homogeneous and of nearly perfect crystal quality. Diffraction studies were complimented by electron probe micro analyser (EMPA) investigations of impurities at the crystal surface. Contrast on topographs showed that impurities, identified by EMPA as aluminium, iron and sodium, were concentrated on the surface in grooves between growth hillocks, suggestive that impurities were concentrated at the cell boundaries. Takagi et al [78] examined the -X growth sector and reported the observation of a cellular growth structure similar to that seen for Z-sector material. Cell walls were in the order of a few microns thick and were shown to exhibit a ten times greater difference in lattice parameter to that of the surrounding material as was reported for Z-sector cells[54].

Dislocations and their relationship to etch tunnels were studied by Iwasaki[61]. This author studied the forming processes of etch channels in the +X, -X and Z growth sectors of synthetic quartz by topographing crystal slices before and after etching with hydrofluoric

acid. Light etching produced very thin tunnels which became progressively thicker with increase in etching time. Tunnels in the X-sectors were observed to widen at a higher rate than those present in the Z-sector to produce ribbon shaped defects approximately 1μm in diameter. Once formed, all tunnels propagated rapidly into the crystal bulk at a rate exceeding 100 μm/hour, a far greater etching rate than for bulk quartz of any crystal cut. Etch tunnels in the +X and -X regions were propagated from the etch pits which were initially formed upon treatment. Although etch pits were formed in the Z-growth region, only a few of these defects produced etch tunnels. The rapid rate of defect formation was attributed to the action of HF vapour on the highly strained cores of dislocations.

As well as conventional topographic techniques, several authors used modified processes to improve the imaging or characterisation of crystal defects. Young and Wagner[79] applied an alternating electric field across AT-cut quartz resonators and obtained diffraction topographs in situ. This was designed to allow the direct examination of oscillation modes of a resonator. However, the applied field also enhanced certain crystal defects in a resonator. These appeared on topographs as distortions in the vibration pattern produced by the oscillating resonator. Characterisation of certain defect types, notably inclusions and surface damage, was

possible by interpretation of individual distortion patterns. Yamashita and Kato[80] expanded this work by applying a static applied field across AT-cut natural and synthetic quartz oscillators. They found that the application of 1500V and higher produced a considerable increase in the contrast of crystal imperfections, particularly those defects pertinent to crystal growth, on diffraction topographs obtained in situ. In this work, the defects were imaged as contrast features and not as vibrational distortion patterns. Growth sector boundaries, growth layers, dislocations and cellular growth boundaries were all clearly visible in the area of a crystal subjected to the applied field. On those areas outside the field's influence or on pre-treatment topographs, growth layers were not observable and much detail was lost with regard to the imaging of the other defect types. Contrast enhancement was observed on topographs of both natural and synthetic oscillators. The phenomenon persisted for several hours after the removal of the electric field but decayed with time until it was no longer noticeable. The changes in contrast were attributed by the authors to the converse piezoelectric effect. The applied field produced electrostriction in the oscillator resulting in the production of inhomogeneous strain which manifested itself at sites of crystal imperfection. Epelboin and Patel used computer simulations to help characterise dislocations observed on

section topographs[81]. They were investigating dislocations reported by Barns et al [43] that were present in low dislocation quartz which did not obey the normal geometrical rules for extinction contrast. This ruled out the normal procedures used for dislocation characterisation and so the authors wrote a computer simulation program capable of generating an image of the section topograph that would be expected if a dislocation possessed a certain Burgers vector. Comparison with experimental section topographs allowed these authors to characterise the Burgers vectors of several dislocations which did not show extinction contrast. Michot et al [82] performed in situ studies of the evolution of fluid inclusions at high temperatures using intense x-rays produced by a synchrotron radiation source. A synthetic crystal was heated to just below the α-ß transition temperature and a series of topographs taken at various temperatures. The inclusions which were examined originated as a result of etch channel formation in the seed followed by subsequent trapping of growth solution once growth took place. The strain in the lattice in the area of an inclusion increased with temperature until decrepitation occurred and the fluid formed a bubble easily observed on the diffraction images. Synchrotron radiation was also used by Zarka and Lin[83] in their investigations into variations of lattice spacings of (00.1) crystal planes. They used a combination of

transmission and plane-wave reflectance topography to assess the distortions present in the Z-growth sector and showed that lattice parameter values varied depending on which growth sector was examined.

Another useful procedure for the detection of small variations in lattice strain is that of double crystal topography. Yoshimura and Kohra[84] used this technique to study lattice distortions around growth sector boundaries in Y-plate samples. Using a non-parallel crystal setting, they observed layered distortions due to two dimensional distributions of impurities called sub-boundaries in the Z-growth sector. Inclinations of lattice planes around growth sector boundaries and sub-boundaries were studied using parallel crystal methods. Inclinations at sector boundaries were attributed to differences in lattice spacings between adjacent sectors and those at sub-boundaries explained by local lattice dilations. The strain observed at each sector boundary was concluded to also be resultant of lattice space differences between growth sectors. In a later publication[85], these double crystal studies were expanded to examine local variations in the (01.0) lattice plane spacings. These were combined with impurity analysis to show that a correlation existed between the concentration of aluminium present in a crystal and the observed lattice strain, with the former increasing in proportion to the content of the latter. A similar correlation for

sodium impurities was suggested but not conclusively proved. From the comparison of variations in the spacing and orientation of the (01.0) plane, these authors deduced the existence of internal stress which they suggested arose from differences in growth cell dimensions in various parts of a crystal. Zarka et al. carried out similar investigations on Y-cut plates of different quartz crystals coming from various industrial sources and arrived at the same conclusions[86].

1.7.2 Infrared Spectroscopic Studies of Quartz Crystals

Many authors have investigated the near infrared absorption spectrum of α-quartz in the 3900-3000 cm^{-1} region. One of the earliest workers in this field, Dreisch[87], showed that a large number of sharp absorption bands were observed in this region if a crystal was cooled to liquid nitrogen temperatures. This group of bands was initially assigned to overtone or combinations of fundamental lattice vibrations[88-90]. However, the validity of this assignment was always in doubt because Dreisch[87] and later Drummond[91] had both reported that the absorption coefficients of the bands varied from crystal to crystal. This apparent failure of Lambert's law was explained by Mitchell and Rigden[92] as a consequence of the band intensities being related to a defect in the crystal lattice as opposed to a proper vibration. They also eliminated the possibility that the

bands were produced by oxygen or silicon lattice vacancies by observing no increase in peak intensities after neutron irradiation. These authors stated that the absorptions were due to either impurities or dislocations. The latter defects were ruled out because no variation in the dichroic ratios of individual peaks were observed for samples taken from different growth sectors which contained very different concentrations of dislocations. Irradiation with x-rays, heat bleaching and annealing in an electric field were shown by Wood[93] to greatly effect the intensity of the bands. Wood assigned a 3580cm^{-1} absorption band as an O-H stretching vibration and suggested that interstitial impurities, Li and Na in particular, played an important role in the formation of infrared active sites. Synthetic quartz infrared spectra were shown to exhibit an intense broad absorption peak centred around 3200 cm^{-1} (see fig.3.6). This peak was similar in appearance to that observed for hydrogen bonded polymeric water, however upon cooling no ice peak materialised thus proving that the absorption was not produced by simple fluid water inclusions. This broad absorption was a characteristic feature of synthetic quartz spectra.

The greatest breakthrough in the assignment of quartz infrared absorption bands came in a study by Kats that remains the classic work in this field[52]. Using a technique developed by King[94], Kats was able to remove or

Table 1.6 Impurity Sensitive Absorption Bands in Natural Quartz Infrared Spectra According to Kats

Impurity	Associated Absorption Band $(cm^{-1})^a$
K^+	3610, 3585, 3578, 3567, 3550, 3538, 3460, 3414
H^+	3590, 3530, 3485, 3462, 3422, 3400, 3305
Li^+	3573, 3520, 3510, 3478, 3440, 3408, 3396
Na^+	3556, 3546, 3534, 3513, 3453, 3400, 3382
Cu^+	3553, 3540, 3514, 3462, 3415
Ag^+	3551, 3535, 3524, 3500, 3454, 3400
Al^{3+}	3371, 3310

a - Frequency values quoted from reference 52

Table 1.7 Fundamental Overtone and Combination Absorption Bands in Quartz Infrared Spectra

Kats' Values $(cm^{-1})^a$
3396
3350
3300
3204
2793
2680
2603
2503
2373
-
2330
2256
2238
2224
2136

a - Frequency values quoted from reference 52

introduce impurities in natural quartz by diffusion induced by electrolysis at high temperatures. He proved conclusively that all of the sharp absorption bands were produced by O-H stretching vibrations by exchanging hydrogen impurities for deuterium and observing the corresponding shifts in frequencies. Kats also used exchanged Na^+, K^+, Li^+, Ag^+ and Cu^+ ions with like impurities in clear natural crystals to assign most of the absorption bands present in quartz to specific impurities (see table 1.6). As a consequence of this he was able to correctly allocate overtone and combination bands associated with fundamental lattice vibrations (see table 1.7). From his observations he concluded that those impurities associated with the majority of peaks in natural quartz were coupled with Al^{3+} ions which had substituted for Si^{4+} in the quartz lattice and required charge compensation. Examination of crystals grown in heavy water showed that absorptions present in the spectra of synthetic quartz were also produced by O-H stretching vibrations. However, several of these bands occurred at frequencies not observed for natural quartz crystals (see table 1.8). These absorptions were unaffected by electrodiffusion and could therefore not be assigned to any specific impurity. From this Kats concluded that hydrogen in synthetic quartz was incorporated into the crystal lattice in a totally different manner to that observed for the natural

Table 1.8 Characteristic Infrared Absorption Bands

Type	Characteristic Absorption Bands Brown and Kahan[a] (cm^{-1})
Natural Quartz	3520
	3508
	3473
	3436
	3427
	3419
	3392
	3383
Natural and Swept Electronic Grade*	3367
	3306
Swept Electronic and Premium** grade	3583
	3441
	3399
	3350

a - Frequency values quoted from reference 98

* - Standard commercial quality quartz crystals

** - Highest quality commercially grown quartz crystals

material.

Levels of O-H species in natural crystals were studied by Bambauer[95,96], who reported that the extinction coefficients of several bands increased linearly with the total O-H content of the examined crystal. Dodd and Fraser[97] carried out electrolysis experiments which verified the conclusions reached by Kats. They showed that Li^+ ions which were incorporated during the growth of synthetic crystals entered sites which differed from those involved when these ions were introduced by electrodiffusion. A concentration of hydrogen bonded O-H species near to the seed of a rapidly grown crystal was reported and the milky appearance characteristic of such crystals was shown to be produced by fluid inclusions which contained structured water. Brown and Kahan[98] characterised types of quartz with regard to their unirradiated infrared spectra (see table 1.8). They demonstrated that the 3306 and 3367cm^{-1} absorptions could be introduced into synthetic quartz, which did not previously show any aluminium associated peaks, by electron irradiation. In the case of high quality quartz samples, the appearance of these peaks was accompanied by significant reductions in the intensities of the original four hydrogen related absorptions. The absence of the Al(H) peaks reported by Kats and their appearance after irradiation led the authors to conclude that substitutional aluminium sites

in untreated synthetic crystals were preferentially compensated by alkali metal ions and not hydrogen impurity ions. They proposed a radiation damage mechanism for quartz which suggested that ionising radiation released alkali and hydrogen impurities, but that the latter were re-trapped at aluminium centres to produce infrared active sites. Chakraborty and Lehmann[99] investigated the distribution of hydroxyl impurities in the Z, +X and -X growth regions of synthetic and natural crystals. The integral absorptions of O-H bands associated with various defects in synthetic quartz samples were found to vary linearly with total O-H concentration. This demonstrated that the hydrogen content of a crystal could be related to the integral of any absorption band in that region. Concentrations of O-H in different growth zones were reported as varying in the order Z < +X << -X. In a later publication[100], these authors compared polarisation ratios of natural and synthetic quartz in order to assign Fe(H) centres to absorption peaks. The material they examined had previously been assessed by Lehmann[101] with Electron Paramagnetic Resonance measurements which suggested that hydrogen compensated iron impurities were present in quartz. Comparison of theoretical direction vectors with polarisation ratios proved that, in the case of synthetic samples, none of the absorptions matched those characteristic of the Fe(H) centre. It was therefore

concluded that iron was probably incorporated interstitially. The broad absorption band characteristic of synthetic quartz was tentatively assigned to water molecules acting as charge compensators to interstitial transition metal impurity ions. Walrafen and Luongo[102] carried out a room temperature polarisation study to determine the orientation of O-H bonds in synthetic crystals. By examining samples cut perpendicular to the three growth directions X, Y and Z, they determined that the O-H bonds were aligned perpendicular to the C-axis. They combined Raman with infrared studies to show that the major hydrogen impurity in quartz was water molecules which were hydrogen bonded in various ways to produce the broad absorption characteristic of synthetic quartz. A sharp absorption at 3589 cm^{-1} was assigned to OH^- ions which were hydrated by a water molecule. Lipson et al [103] carried out a study of X, Y and Z cut crystal slices of high quality crystals at low temperature, 15°K, using unpolarised light. The only significant absorptions observed were those characteristic of synthetic crystals (see table 1.6). Spectra of X and Y slices were identical, however Z-slices were shown to exhibit several differences in comparison with these crystal cuts. In the Z crystal orientation, the 3350 cm^{-1} absorption was barely observable and the intensities of the other peaks were significantly altered. This was accounted for by

polarisation effects. Electrodiffusion in an air atmosphere was shown to produce similar effects to those expected for irradiation but only for samples of premium grade quartz. Hydrogen related absorptions for electronic grade samples were considerably increased in intensity after the treatment in addition to the appearance of aluminium associated bands. This was attributed to the process drawing hydrogen species from the air into the crystal where they formed infrared active sites thereby enhancing the original absorption bands. Haliburton et al[104] used electron spin resonance measurements in combination with infrared studies to conclusively identify the absorptions at 3306 and 3367 cm^{-1} as being produced by $Al\text{-}OH^-$ defect sites. They also confirmed the radiation damage mechanism postulated by Brown and Kahan was correct. Monovalent alkali metal ions, such as Na^+ and Li^+, were shown to be the primary charge compensating species which were only replaced by hydrogen after irradiation or electrodiffusion. Lipson and Kahan[105] demonstrated that absorption peaks depleted upon irradiation were regenerated after electrodiffusion in an air atmosphere. They also reported the possibility of infrared inactive sources of hydrogen citing as evidence the continued growth of $Al\text{-}OH^-$ absorptions even after all other hydrogen related peaks had been removed by irradiation.

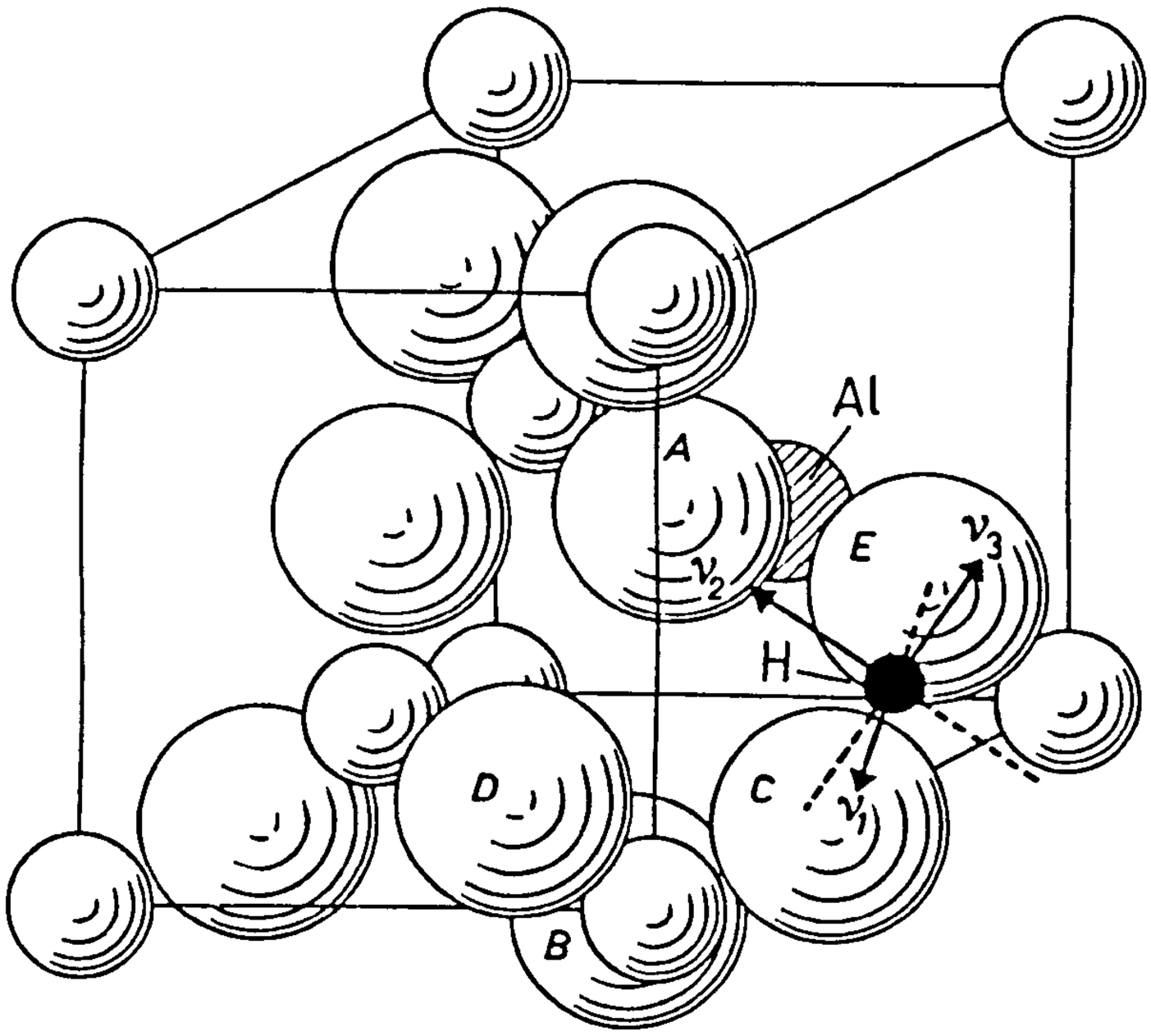

Fig. 1.17 Kats' First Model for Hydrogen in Smokey and Annealed Natural Quartz

(From Ref. 52)

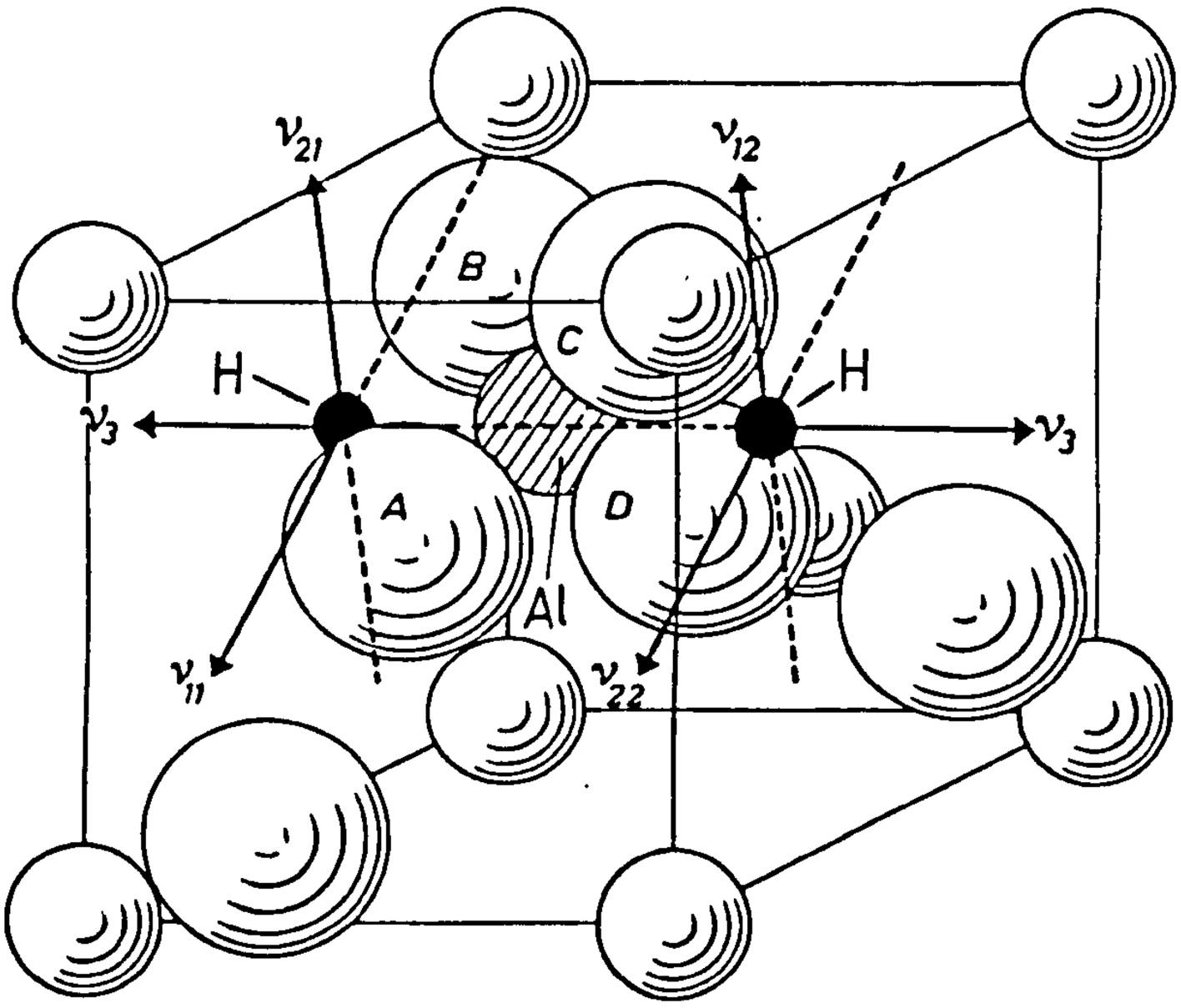

. 1.18 Kats' Second Model for Hydrogen in Smokey and Annealed Natural Quartz

(From Ref. 52)

1.8 Models for the Incorporation of Hydrogen in α-Quartz

The first models to account for hydrogen related absorptions in the 3000-3900 cm^{-1} region of quartz infrared spectra were proposed by Kats[52]. The majority of his models depended on the presence of Al^{3+} ions substituting for Si^{4+}in the crystal lattice. These were charge compensated by alkali metal ions, such as Li^{+}, and hydrogen atoms bonded to adjacent bridging and non-bridging oxygen ions. His first two models accounted for O-H vibrations occurring at 3403, 3311 and 3305 cm^{-1} in the spectra of smokey quartz or clear natural quartz which had been heated above 620°C (see figs. 1.17 and 1.18). For untreated natural crystals he proposed four models, each of which was associated with both alkali metal and hydrogen impurity ions (see figs. 1.19a-d). However although no model was assigned to any specific absorption, he concluded that O-H vibrations which were sensitive to the presence of metal ions (see table 1.6), were due to two or more of the specific configurations shown by these models. He did not report any model for hydrogen in synthetic quartz but did suggest that hydrogen could be present in three forms, namely fluid inclusions, as water molecules positioned interstitially in C-channels or as groups of Si-OH bonds present in localities of disturbed crystal growth. This latter model was originally proposed by Brunner et al[106] to account for hydrolytic weakening in quartz. Brunner et al.

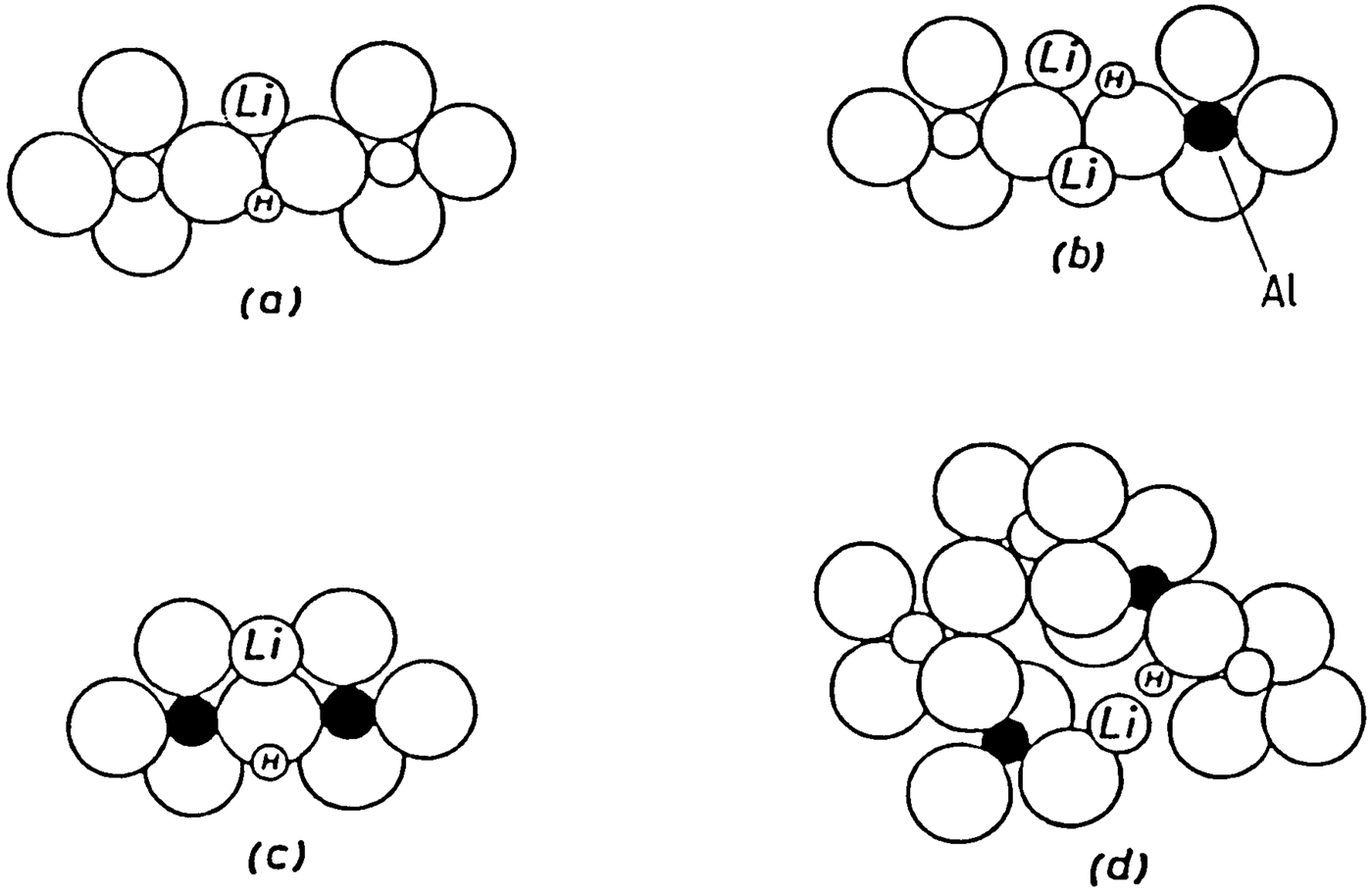

Fig. 1.19 Kats' Models for Alkali Sensitive Hydrogen Impurities in Clear Natural Crystals (From Ref. 52)

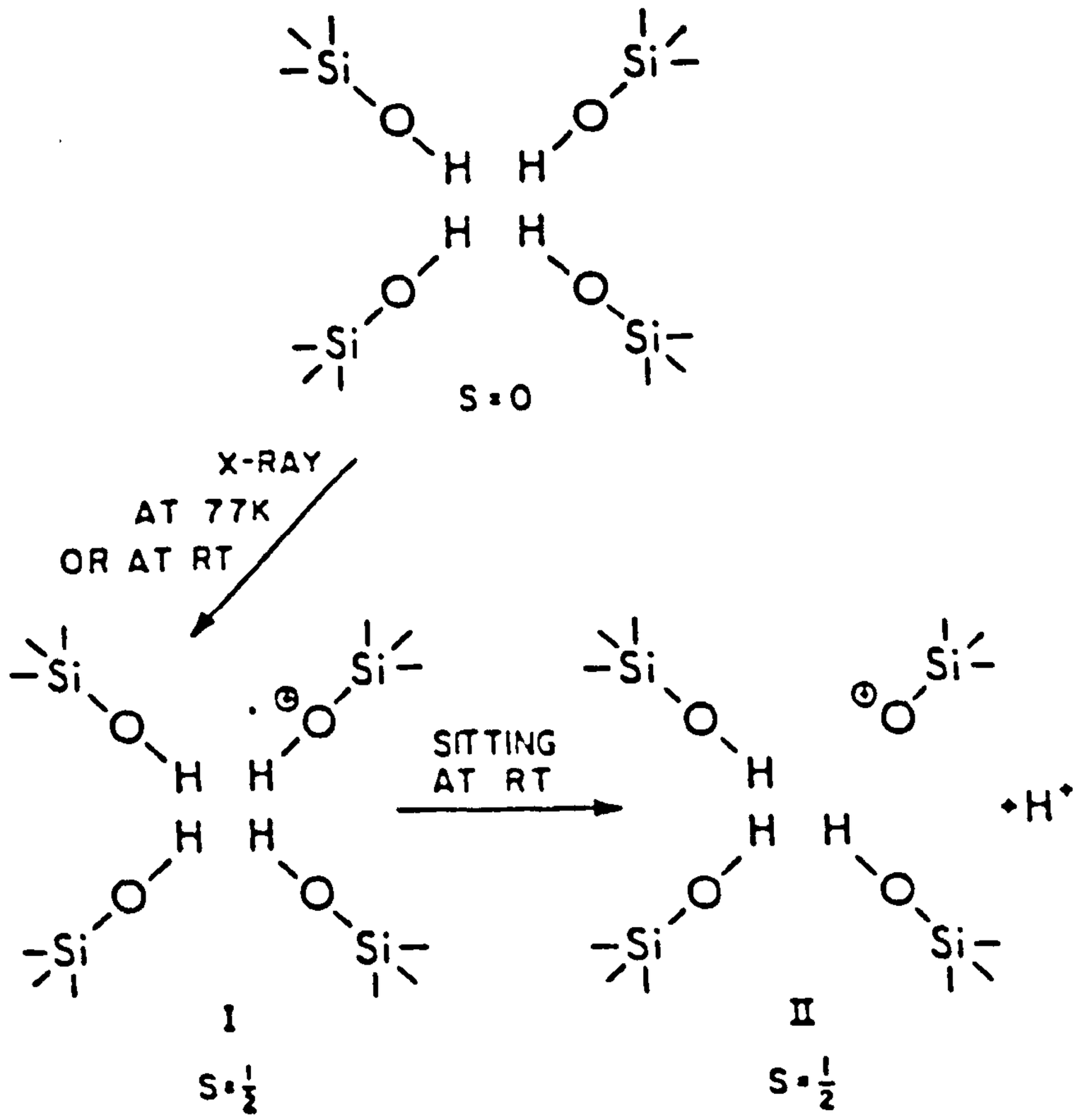

Fig. 1.20 Nuttal and Weil's Silicon Vacancy Defect Model

(From Ref. 108)

proposed that water present in quartz could hydrolyse Si-O bonds to produce Si-OH bonds. Perlson and Weil[107] reported the discovery of atomic hydrogen sites located interstitially between silicon atoms on the twofold symmetry axes in the c-channels. Griggs[57] postulated the presence of mobile water molecules in the core of a dislocation but did not submit a model to account for this behaviour. Nuttall and Weil[108] reported the detection of two hydrogenic trapped hole species using electron paramagnetic resonance (EPR) measurements of irradiated quartz. To explain their observations, Nuttall and Weil adopted Kats proposed model for Si-OH local lattice disturbances (see fig. 1.20). This model accounts for the species observed in irradiated quartz by EPR studies. Halliburton et al [104] proposed models to account for the 3306 and 3367 cm^{-1} absorptions observed on irradiated synthetic and natural quartz infrared spectra. As with Kats' models, their models depended on substitutional Al^{3+} ions being present. In an untreated crystal, Al^{3+} ions are charge compensated by monovalent alkali metal ions, notably Na^{+} and Li^{+} ions, to form $Al\text{-}M^{+}$ centres (see fig. 1.21a). Irradiation induces these metal ions to become mobile and diffuse through the crystal away from aluminium substitutional sites[109]. When no replacement charge compensating species are present, an Al-hole centre is formed. This consists of an electron hole trapped at a non-bonding orbital of an oxygen ion

Fig. 1.21 Aluminium Impurity Defect Models

(From Ref. 109)

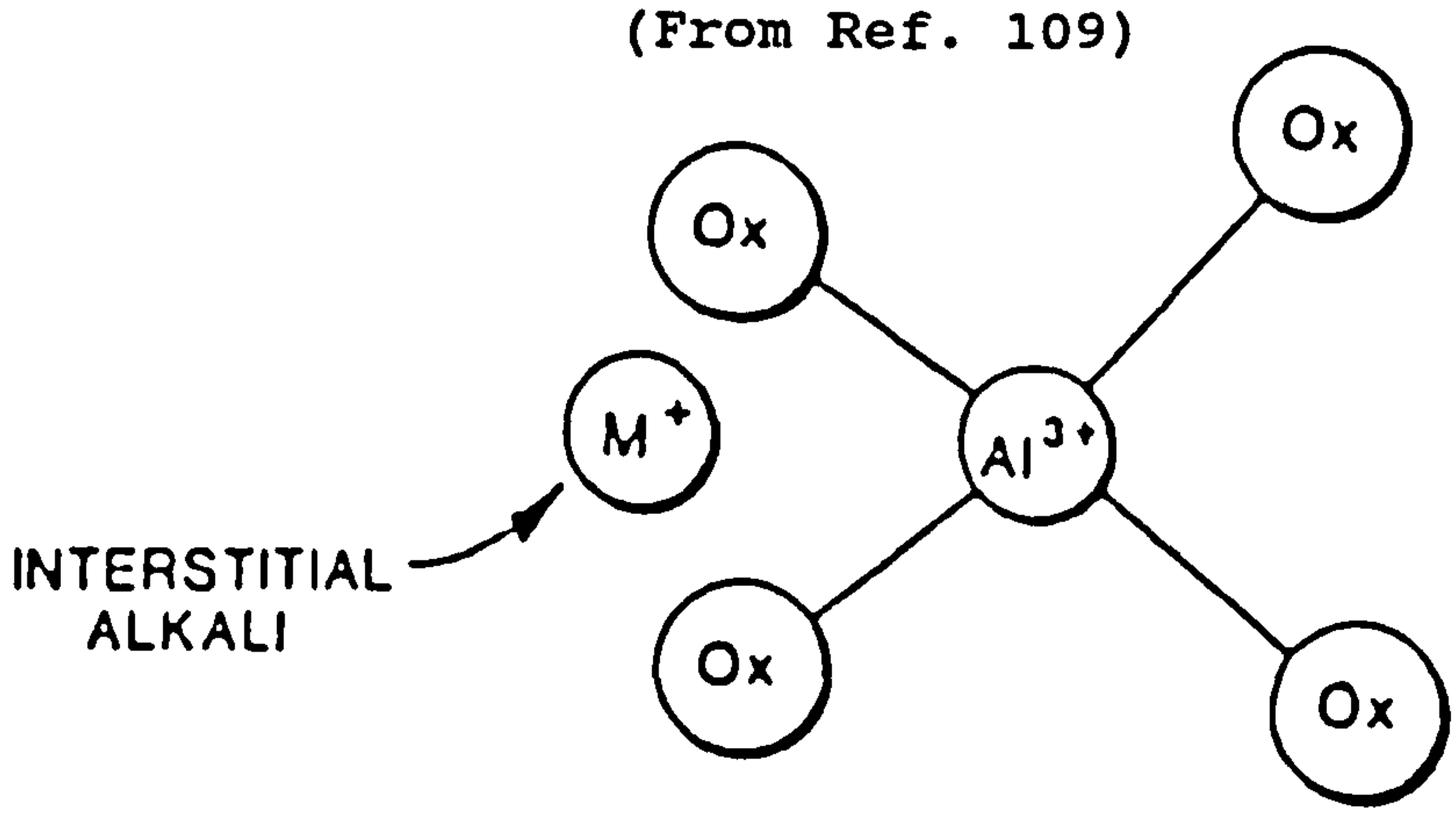

a) Al-M^+ Defect

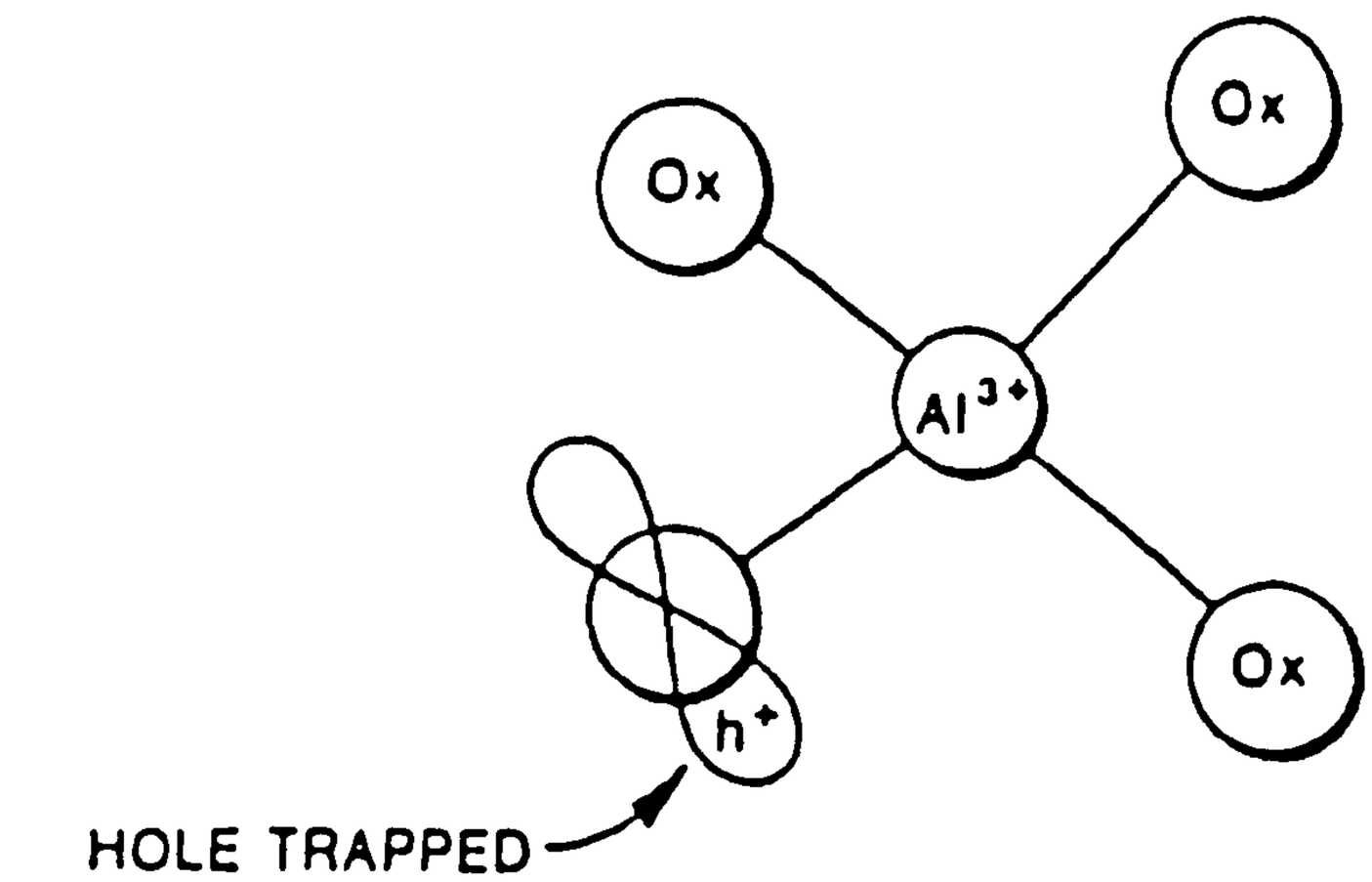

b) Al-Hole Defect

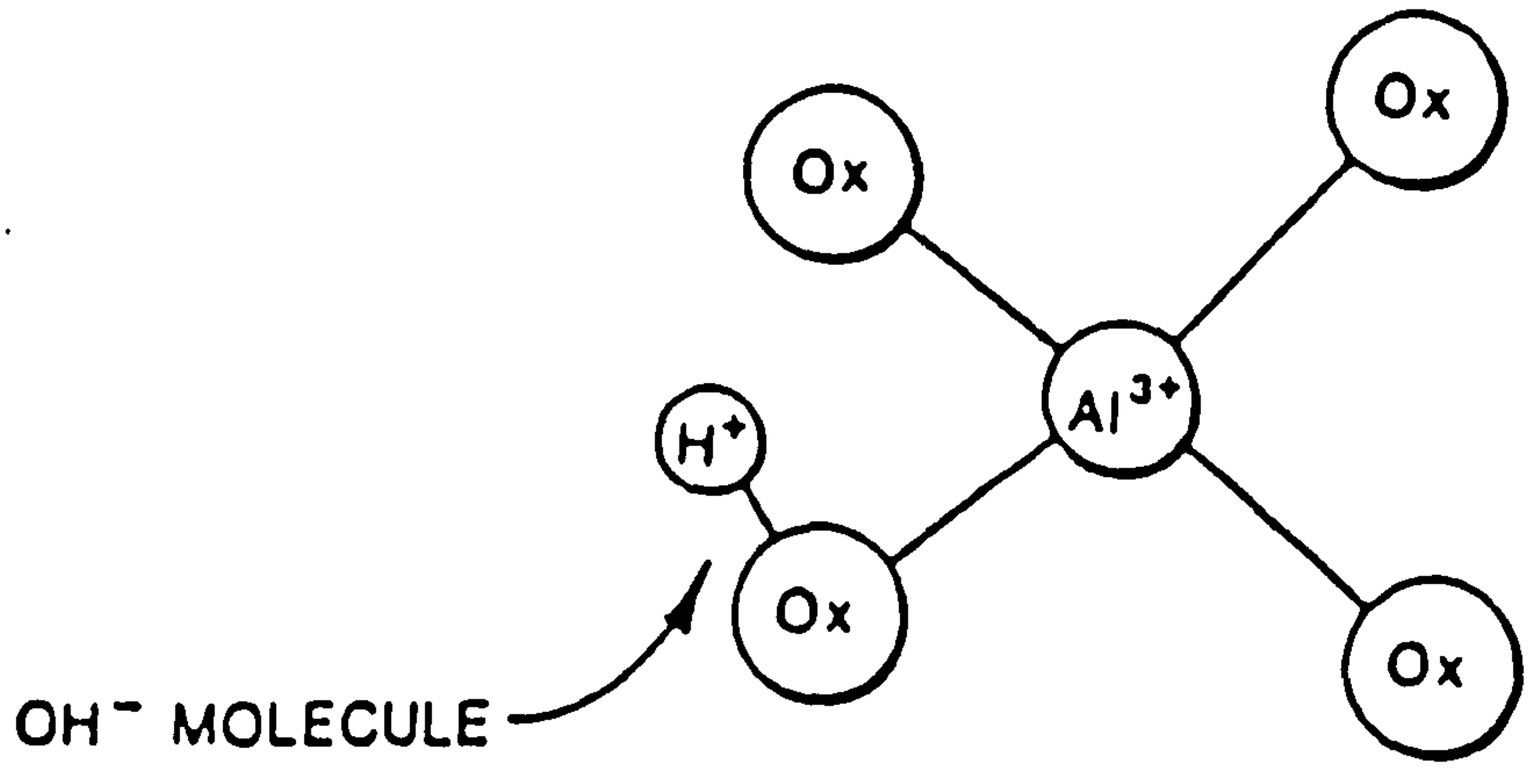

c) Al-OH^- Defect

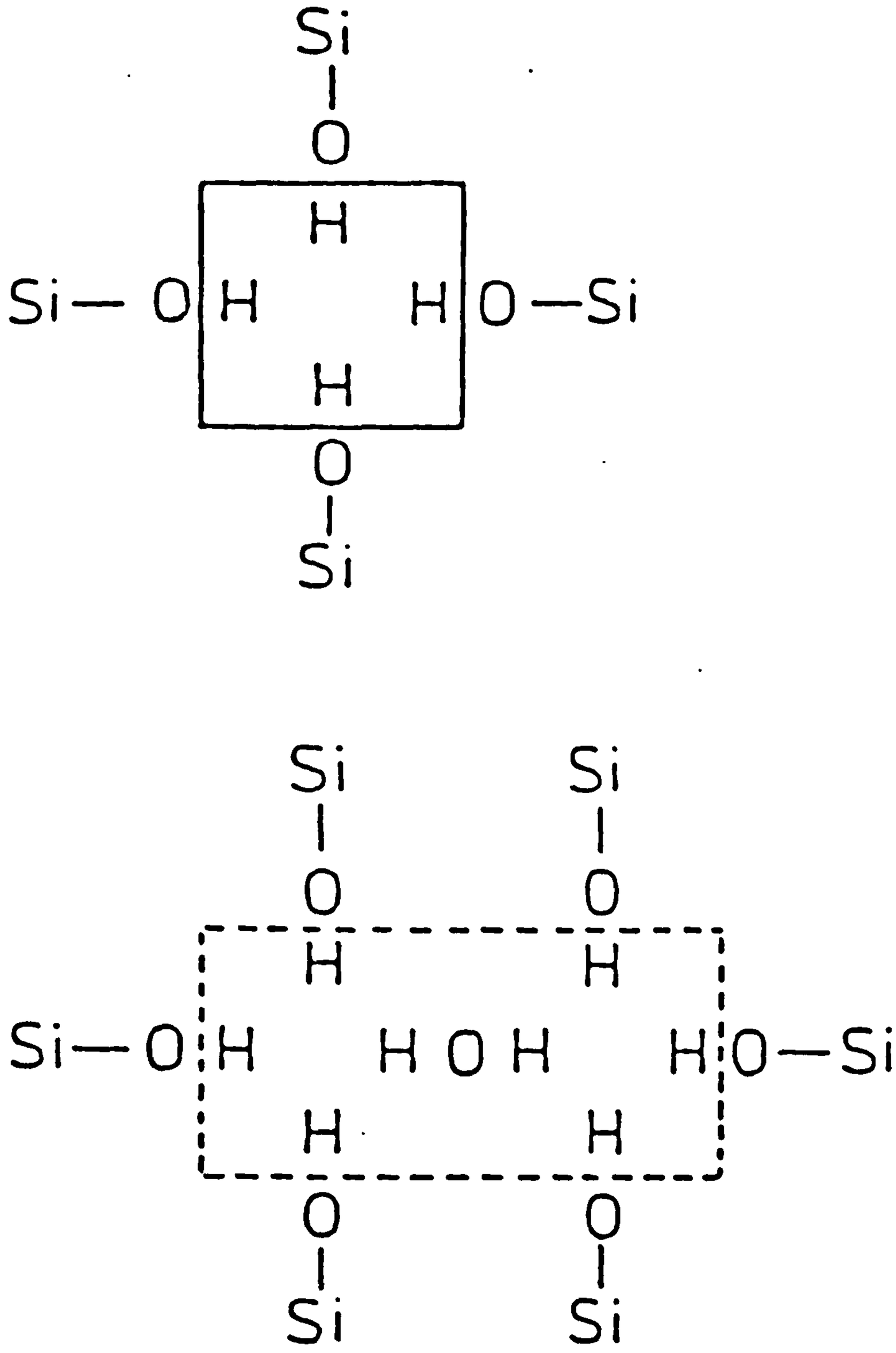

Fig. 1.22 McLaren's Model for Water Incorporation in Quartz (From Ref. 58)

adjacent to an aluminium centre as interpreted by O'Brien[110] (see fig. 1.21b). However, when available, hydrogen ions migrate to aluminium sites to form Al-OH^- centres (see fig. 1.21c). The O-H vibration of this centre gives rise to the two mentioned infrared absorptions. The frequency difference between these peaks is an indication of two different but closely related defect sites. McClaren et al.[58] expanded on Nuttall and Weil's model to provide a mechanism which accounted for fluid bubble formation in annealed quartz samples. They demonstrated that clusters of Si-OH bonds could hold water molecules in the centre of the defect (see fig. 1.22). Aines et al.[111]. carried out a study which specialised in hydrogen speciation in quartz. They concluded from their observations that the major hydrogen impurity in synthetic quartz was molecular water, with hydroxide species being present in much lower concentrations. These authors postulated that groups of between 1-200 water molecules were distributed throughout a typical quartz crystal. These groups of water molecules would still produce a broad hydrogen bonded absorption but would be too small to give rise to an ice peak. Aines et al. were unable to provide any spectroscopic evidence for the presence of Si-OH groups which consequently shed doubt on Brunners' defect model and those systems which depended upon it. The most recent model for hydrogen in quartz was proposed by Stenina[112]. This author postulated

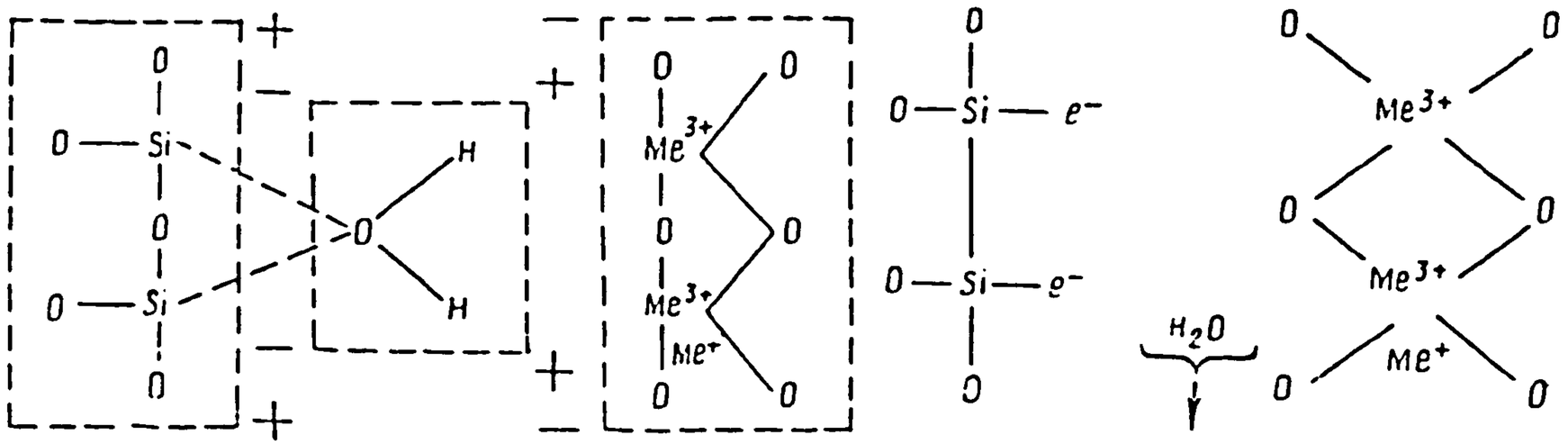

Fig. 1.23 Stenina's Model for Water Incorporation in Quartz
(From Ref. 112)

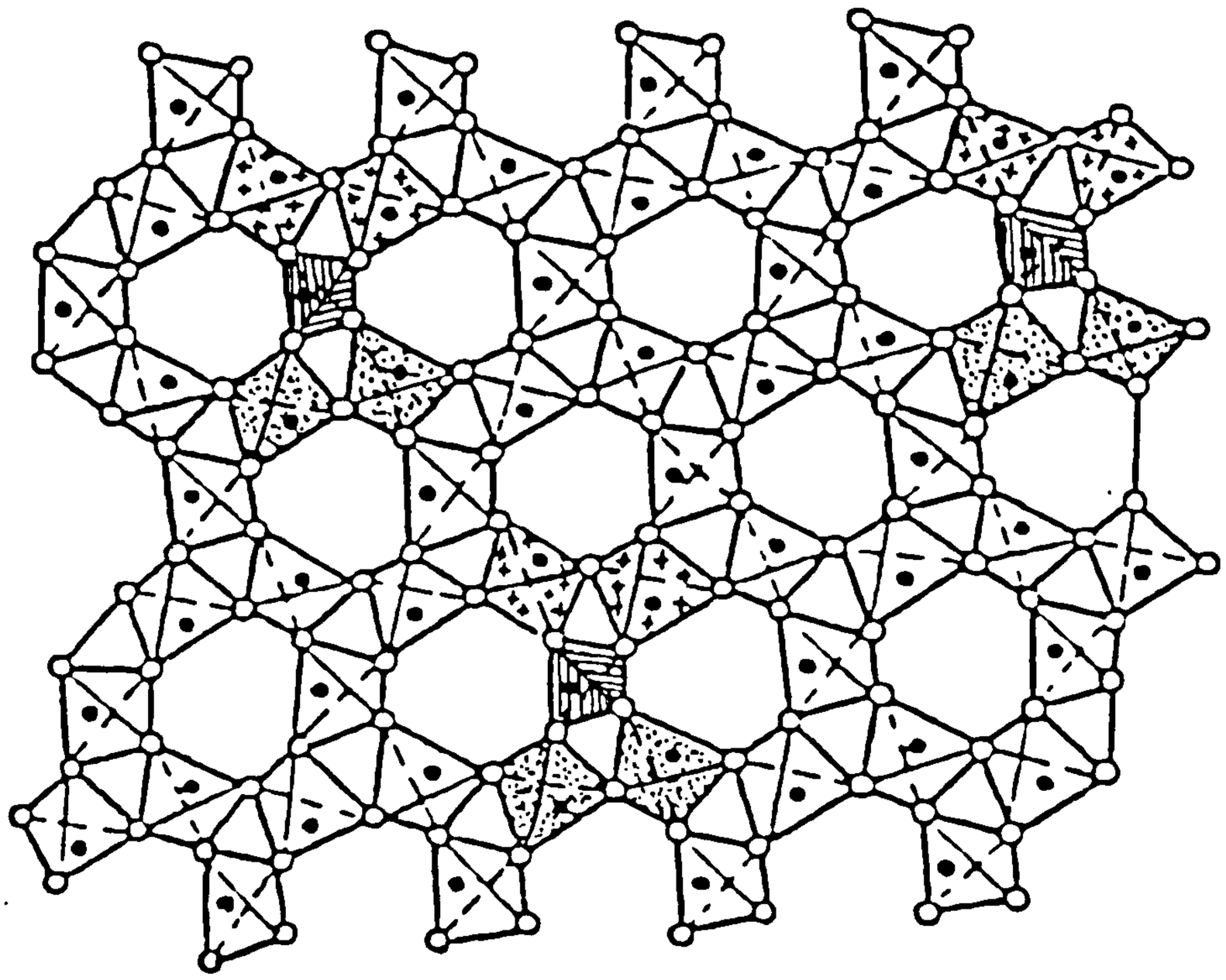

Fig. 1.24 Incorporation of Stenina's Water Defect in the Quartz crystal Lattice (From Ref. 112)

a model which incorporated molecular water between four defect tetrahedrons. These tetrahedra were consisted of two positively charged SiO_3 groups and two negatively charged substitutional Al^{3+} or Fe^{3+} groups. The former resulting from the presence of an oxygen vacancy, and the latter being a charge uncompensated aluminium centre. The electron structure of a water molecule provides two negative and two positive "terminals" with the correct tetrahedral configuration to fit into the defect cluster (see fig. 1.23). The author demonstrated that this defect unit could be repeated throughout a crystal lattice and provided a mechanism for the hydrolytic weakening of quartz without the necessity of Si-OH bond formation postulated by previous authors[57,58,106,111] (see fig. 1.24).

Chapter 2. Theory and Experimental

Chapter 2. Theory and Experimental

2.1 The Growth of High Purity Quartz Crystals

This section details the various procedures which were followed to grow the high purity quartz crystals studied during this project. All crystals were grown at the General Electric Company's Hirst Research Centre in Wembley.

2.1.1 The Hydrothermal Growth Process

Quartz crystals were grown using the hydrothermal growth process which was discussed in section 1.4. This is a technique for growing crystals from a solution which is near or above its critical temperature. In this context, the critical temperature is defined as that temperature above which spontaneous nucleation does not occur without the addition of an external stimulous, such as a seed crystal. Essentially, the hydrothermal growth process involves dissolving a quartz nutrient at a high temperature. The saturated solution so produced, moves by convection to a cooler region where it becomes supersaturated. To relieve this condition, the solution deposits quartz onto seed crystals. Temperatures in excess of 300°C are necessary to ensure adequate solubility, even when mineralisers are added to increase the solubility of quartz.

Crystal growth only occurs when the growth solution is supersaturated with respect to the seed crystals. In the case of the crystals grown during the course of this project, the

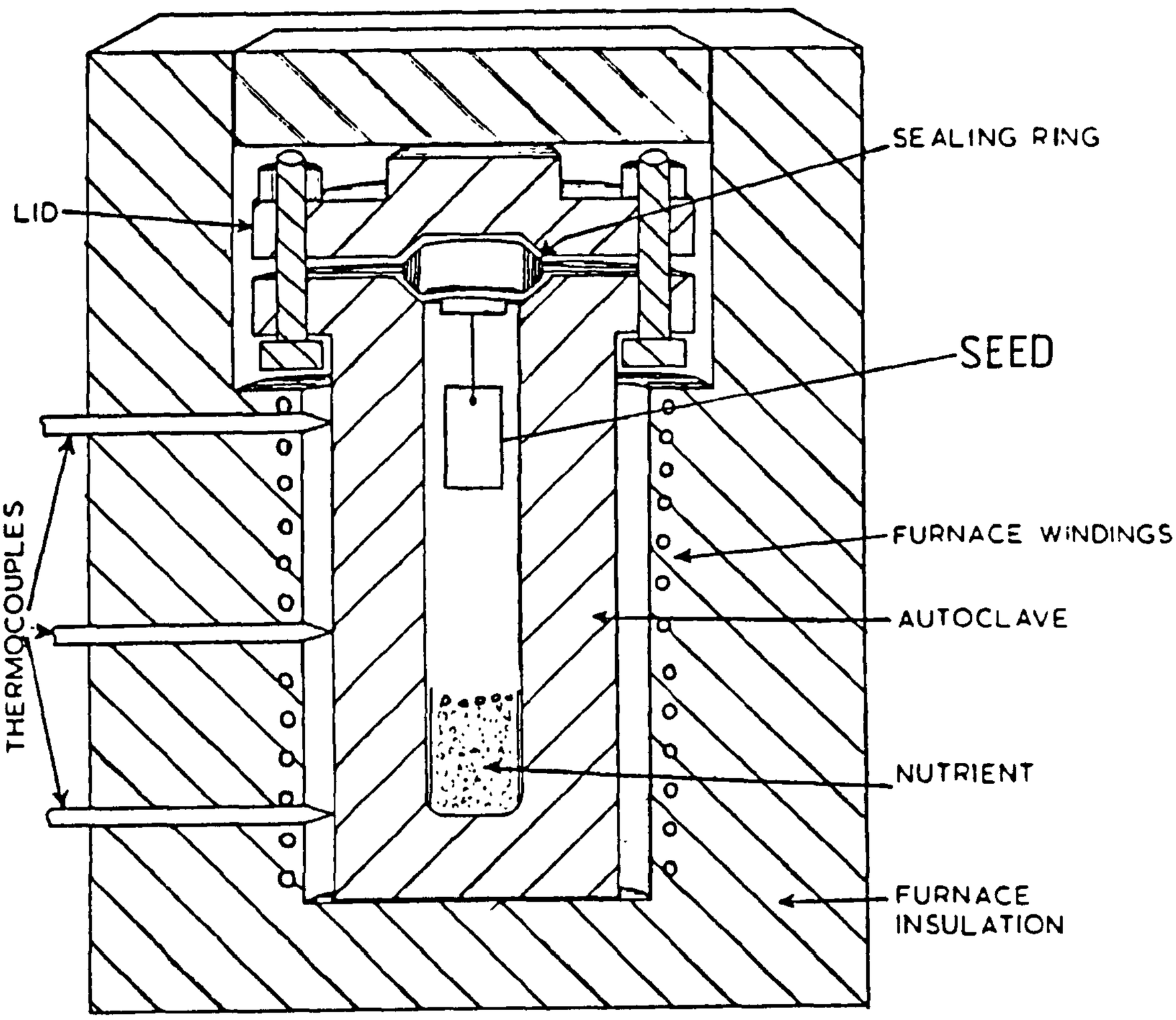

Fig. 2.1 Hydrothermal Crystal Growth Apparatus

Table 2.1 Quartz Growth Runs

Growth Run No.	Mineraliser (1Molar)	Nutrient (30g)	Autoclave Temp(°C)*	Growth Rate (mm/side/day)
1	$NaOH/D_2O$	CDS	350/375/400	0.182
2	$NaOH/D_2O$/Al	CDS	350/375/400	0.203
3	$NaOH/H_2O$	CDS	350/375/400	-**
4	$NaOH/H_2O$	CDS	350/375/400	-**
5	$NaOH/H_2O$	CDS	350/375/400	0.438***
	$NaOH/H_2O$	CDS	350/375/400	0.628****
6	Na_2CO_3/H_2O	HPQ	360/380/400	1.217
7	Na_2CO_3/H_2O/Al	CDS	360/380/400	0.480
8	$NaOH/H_2O$	CDS	350/375/400	0.141
9	Na_2CO_3/H_2O	CDS	365/380/395	0.970
10	Na_2CO_3/H_2O	CDS	360/370/380	0.910
11	Na_2CO_3/H_2O	CDS	350/360/370	0.978
12	Na_2CO_3/D_2O	HPQ	365/380/395	0.726
13	Na_2CO_3/D_2O	HPQ	330/340/350	0.251
14	$NaOH/H_2O$	HPQ	350/375/400	0.252
15	$NaOH/D_2O$	HPQ	350/375/400	0.156
16	Na_2CO_3/H_2O	HPQ	320/330/340	0.278
17	Na_2CO_3/D_2O	HPQ	330/340/350	0.268
18	$NaOH/H_2O$	HPQ	350/375/400	0.090
19	$NaOH/D_2O$/Al	HPQ	350/375/400	0.180

CDS - Converted dynasil silica HPQ - High purity quartz

* Temperatures at Top/Middle/Bottom of the autoclave
** Autoclave leak caused failure of growth run
*** Unswept seed crystal used **** Swept seed used

NB. The pressure for growth runs using NaOH and Na_2CO_3 mineralisers were 1500 and 1000atm respectively

necessary conditions were produced in a vertical steel autoclave (see fig. 2.1). A quartz nutrient was placed in the lower region of the vessel, and a suitably orientated seed crystal slice was held by a steel wire in the upper portion. The autoclave was partially filled with an aqueous solution of either sodium carbonate or sodium hydroxide, which acted as a mineraliser. The system was sealed and heated in a furnace such that a temperature gradient was maintained between the top and the base of the autoclave. The lower region of the vessel was always kept at a higher temperature than that corresponding to the upper portion. As the temperature was raised, the liquid expanded to fill the autoclave at some temperature below the critical point, which is 375°C for pure water. For a typical growth run, the average autoclave temperature was around 350°C, which produced an internal pressure of between 1500 and 1000 atm depending on which mineraliser was used. Under these conditions, quartz was soluble and a saturated solution was produced in the lower autoclave region near to the nutrient. This moved into the cooler upper region, where the seed crystal was situated, via convection currents within the autoclave. The resultant supersaturation of the solution was relieved by deposition of quartz onto the seed crystal to produce crystal growth. The exact conditions used in the growth of quartz crytals are summarised in table 2.1.

It is useful at this stage to examine the procedures which were followed for crystal growth at Hirst laboratories in detail.

2.1.2 The growth of High Purity, Low Dislocation Content Quartz

The procedure which was followed in the production of high purity quartz crystals comprised of four preparative stages, involving the seed, the nutrient, the mineraliser and the autoclave. In the following sections the reasons behind each stage will be outlined along with the experimental details.

i) Seed Preparation

Seed crystals were cut from Brazilian quartz of very high crystalline perfection. This operation was carried out by GEC Hirst technicians using a slurry saw. The dislocation content of the source crystal was evaluated using x-ray diffraction topography and seeds were generally dislocation free. Synthetic seeds were not considered because of the high concentrations of dislocations they possessed in comparison with natural crystal seeds. Surface cutting and handling damage on the seed was removed by a chemical polish which involved suspending the seed in a beaker filled with 48% hydrofluoric acid for between 30 to 60 minutes.

The dimensions of the seeds used in this project are given in table 2.2. All seeds were cut at 90° to the [001] crystallographic direction and parallel to the [010] and [2-10] directions and were composed almost entirely from (00.1) quartz growth sector material (see fig. 2.2). This

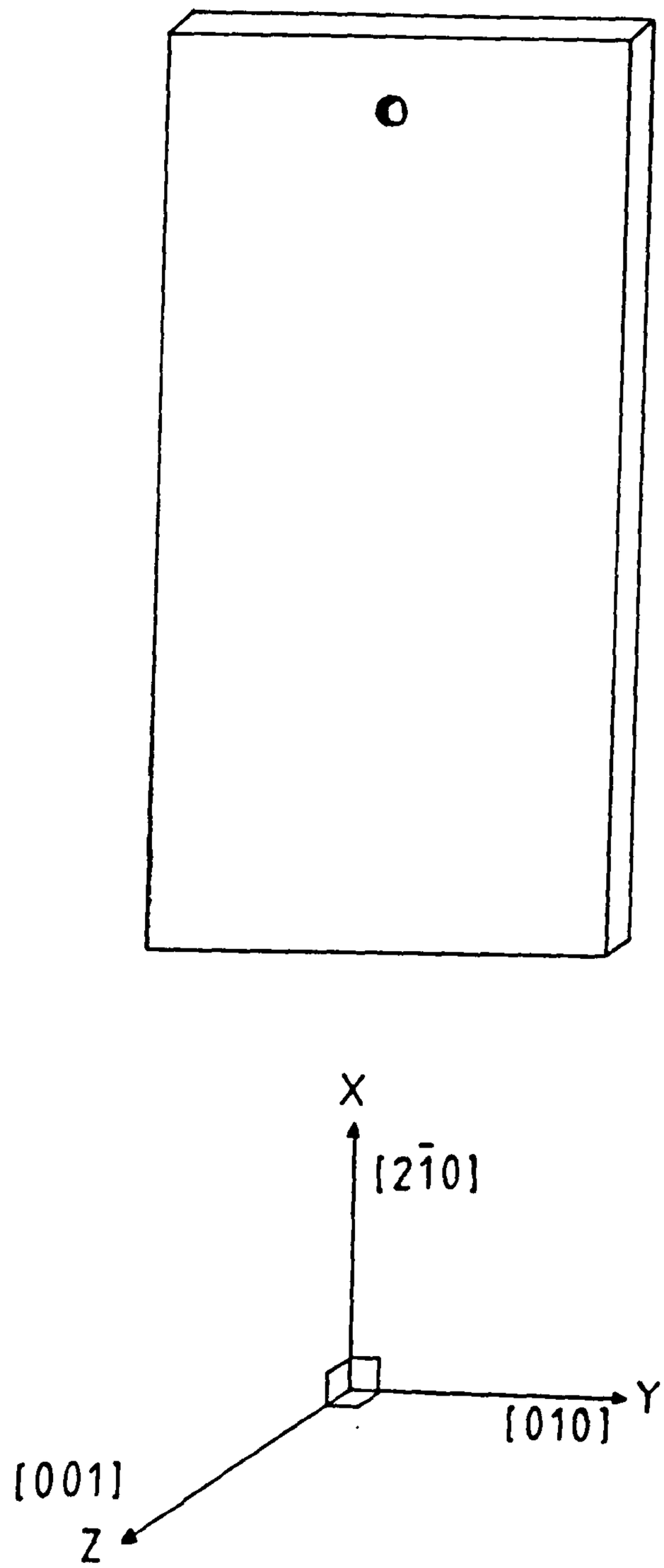

Fig. 2.2 Schematic Diagram of a Typical Seed Crystal Slice

Table 2.2 Seed Dimensions and Growth Run Durations

Growth Run No.	Seed Dimensions Before Growth (l/b/h)mm	Wt(g)	After Growth (l/b/h)mm	Wt(g)	Duration (Days)
1	33.5x14.0x1.314	1.566	35.0x14.0x6.410	8.308	14
2	36.0x15.5x1.284	1.834	36.0x15.5x6.960	10.172	14
3	-	-	-	-	-
4	-	-	-	-	-
5	24.0x12.0x1.774	1.333	28.5x14.0x12.334	NR	15*
	23.5x12.0x1.416	1.055	29.0x12.8x19.000	NR	15**
6	33.3x11.5x1.296	1.255	38.0x12.0x18.340	13.822	7
7	35.7x15.8x1.258	1.803	37.8x17.9x 7.982	7.416	7
8	31.1x30.1x1.517	4.040	NR x NR x 9.420	9.420	28
9	28.8x14.4x1.574	1.687	35.3x15.0x13.214	14.762	6
10	28.8x15.6x1.638	1.885	33.0x16.3x10.736	13.198	5
11	28.7x15.2x1.602	1.602	NR x NR x15.296	NR	7
12	31.2x19.4x1.618	1.893	NR x NR x11.784	NR	7
13	28.7x13.6x1.614	1.617	NR x NR x 5.124	NR	7
14	31.2x14.1x1.056	1.859	36.8x14.7x10.658	11.743	21
15	31.2x14.8x1.010	1.822	34.7x14.8x 7.262	8.507	20
16	28.8x13.7x1.152	1.775	34.3x14.5x11.704	12.125	19
17	33.6x15.2x1.232	1.659	39.0x15.8x 9.668	12.684	18
18	31.2x30.1x1.170	NR	NR x NR x 6.200	NR	28
19	39.2x15.1x1.056	NR	NR x NR x 8.512	NR	21

NR - Not Recorded

* - Unswept seed crystal used
** - Swept seed crystal used

choice of crystal cut resulted in the production of quartz crystals which were themselves composed of mainly (00.1) growth sector material. This type of crystal was desirable for two reasons, namely, the growth rate for synthetic quartz is fastest in the [001] direction[35] and the incorporation of aluminium and alkali metal impurities in the (00.1) growth sector is less than for any of the other of the quartz growth sectors[93]. Therefore, crystals grown on (00.1) seeds will be of a higher purity than those grown on seeds cut normal to other growth directions. This quality of the (00.1) growth sector is very important in the reduction of important impurity levels in synthetic quartz and was especially important with regard to the fabrication of high purity crystals. Seeds were drilled to allow the attachment of the steel wire which was used to suspend the crystal vertically from a support rod into an autoclave (see fig. 2.1). The support rods were custom made from stainless steel for each autoclave.

ii) Nutrient Preparation

The nutrient is the name given to the source of growth material in the autoclave. Converted silica and high purity quartz were both used for quartz growth during the course of this project. Natural quartz crystal contains high levels of impurities which are detrimental to crystal growth and so was not considered (see section 1.6 iv). Although amorphous silica was not directly applicable to quartz production (see

section 1.4), a procedure was used to convert this material into a crystalline form which could be used. Amorphous silica chips were placed into an autoclave which was partially filled with 0.1M sodium hydroxide solution and a run similar to that discussed for crystal growth was carried out. However, no seeds were added and a constant temperature was maintained along the length of the autoclave. The autoclave was sealed and heated to 360°C to produce an internal pressure of 1500 atm (see Appendix A). Under these conditions, amorphous silica was converted to a crystalline state in around twenty four hours. The converted silica was not removed from the vessel, but was washed with doubly deionised water before being used as a nutrient for quartz growth.

Crystalline quartz nutrient was also obtained by breaking up high purity crystals. This material required no conversion step but was etched in 48% hydrofluoric acid to remove surface contaminants and to dissolve quartz dust particles attached to crystal pieces. This is necesary because particulate matter can act as unwanted nucleation sites within the autoclave.

iii) Mineraliser Preparation

The solubility of quartz in pure water is extremely low, even under high temperature and pressure conditions[47,48]. However, quartz solubility increases dramatically in the presence of certain substances known as mineralisers. These substances also promote crystal growth by assisting the

Table 2.3 Impurity Analysis of Selected Samples

Sample	Impurity Levels*					Growth Rate**
	Al	Na	Fe	K	Li	
HPQ15.5[a]	0.06	0.18	0.02	<0.005	-	0.25
HPQ16.4[a]	0.04	0.15	0.01	<0.005	-	0.25
HPQP[a]	0.01	<0.005	<0.005	<0.005	-	0.20
NSW[a]	0.02	1.108	0.004	<0.005	-	0.20
COMQ[b]	1.00	0.40	0.02	<0.005	0.7	-
HPQ7[a]	0.01	-	0.02	<0.005	-	0.23
HPQ8[a]	0.50	-	-	<0.005	-	0.22
HPQ9[a]	0.07	-	<0.005	<0.005	-	0.27
NaOH[c]	1.0	1.4×10^5	2.0	50.0	1.0	-
Na_2CO_3[d]	10.0	2.8×10^5	5.0	100.0	10.0	-

* - Impurity levels were measured in microgrammes of impurity per gramme of silicon dioxide ie. ppm

** - Growth rate was measured in millimetres grown on each side of a crystal per day ie. mm/side/day

a - High purity crystal grown at Hirst research labs

b - Crystal grown by Standard Telecommunications and Cables

c - Aristar grade mineraliser used for growth runs detailed in Table 2.1

d - Analar grade mineraliser used for growth runs detailed in Table 2.1

production of a saturated growth solution. The two mineralisers used in this work were sodium hydroxide and sodium carbonate. These are thought to increase the rate of quartz dissolution via the formation of sodium silicate compounds as follows[113]

for carbonate solutions,

$$2Na^+ + 2(OH)^- + SiO_2 \rightleftharpoons Na_2SiO_3 + H_2O$$

for hydroxide solutions,

$$2Na^+ + 2(OH)^- + 3SiO_2 \rightleftharpoons Na_2Si_3O_7 + H_2O$$

In the case of a carbonate mineraliser, hydroxide ions are produced by hydrolysis. The impurity analysis of the mineralisers used is given in table 2.3. Sodium hydroxide was preferentially employed because the possibility of spontaneous nucleation was reduced in comparison to a sodium carbonate mineraliser and impurity levels were substantially lower. Doubly deionised water was used in all solution preparations.

<u>iv) Autoclave Preparation</u>

Quartz crystal growth took place in unlined steel vessels known as autoclaves. Two sizes of autoclaves were employed, these having dimensions of 200mm depth and 22mm diameter internal bore and 280mm depth and 63mm diameter internal bore respectively. One disadvantage of using an unlined autoclave was that, under the growth conditions, the internal walls of the vessel were suseptible to attack from the alkaline growth

solution. This resulted in the formation of a thin layer of a substance thought to be the mineral acmite, $Na_2O \cdot Fe_3O_4 \cdot 4SiO_2$ which covered the autoclave walls[5]. Although this layer prevents further attack, it is unfortunately a source of iron impurities. The layer is brittle and particles can be removed during growth and circulated with the growth solution to be eventually incorporated in a growing crystal. Another problem is the build up of a quartz wall deposit formed by growth nucleated on the rough acmite layer which restricted the growth on seed crystals. The way of dealing with these problems was to perform a cleaning run, which simply involved dissolving the quartz deposit using a 1M sodium hydroxide solution at a temperature of 350°C and a pressure of 1500atm (see Appendix A). Cleaning runs typically had twenty four hour durations after which time all wall deposits and loose acmite particles were removed.

Autoclaves were sealed using a steel O-ring. This was hand ground into both the lid and the autoclave to produce a good seal so that the possibility of solution leakage during growth was reduced. The bolts used to secure the ring between the autoclave body and lid were cleaned thoughly in vigourously agitated 1.1.1-trichloroethane followed by the application of a graphite loaded oil. Thorough cleaning is essential for the removal of particulate matter which can damage bolt threads, reducing their operational lifetime, and produce bolt seizure after growth. Upon heating the applied oil evaporates to leave a film of graphite on the bolt

which acts as a lubricant, reducing the possibility of bolt siezure and assisting in bolt removal. Heating was monitored using thermocouples attached to the outside of the autoclave and was maintained at the required level using a Eurotherm PID temperature controller. Specimen calculations related to the calculation of the internal autoclave pressure are detailed in Appendix A. The dimensions of the crystals produced by each growth run are given in table 2.2. A suumary of the typical impurity content in nutrients, mineralisers and selected quartz samples used during the course of this project is given in table 2.3.

2.2 Electrodiffusion of Synthetic Quartz

2.2.1 Basic Principles of Electrodiffusion

Electrodiffusion, or sweeping as it is also known, was developed to improve the radiation response of a quartz resonator[114,115]. The technique accomplishes this aim by the removal of those alkali metal ions which cause detrimental effects in resonator properties after irradiation has taken place. Impurity removal is achieved by applying an electric field across the (00.1) faces of a quartz crystal. The structure of quartz is such that fairly wide channels known as C-channels, exist at right angles to these faces (see section 1.2). Neutral particles of radii up to 0.8Å can pass freely through these channels, however any particle of greater than 0.5Å in radius has to follow a "zigzag" pathway. Charged species possessing a similar radius can also move through these channels, however co-operative movement of Si-O lattice bonds is essential as well as an external stimulus to overcome those electrostatic forces acting upon them. Sweeping is therefore carried out at high temperatures to facilitate particle movement by providing cooperative bond movement. This occurs most effectively near the α/β transition temperature at 576°C. The applied electric field provides the stimulus which removes charged impurities from their binding sites and overcomes interactions between the ions and the crystal lattice. Only interstitially incorporated monovalent metal ions can be removed using electrodiffusion, examples of which

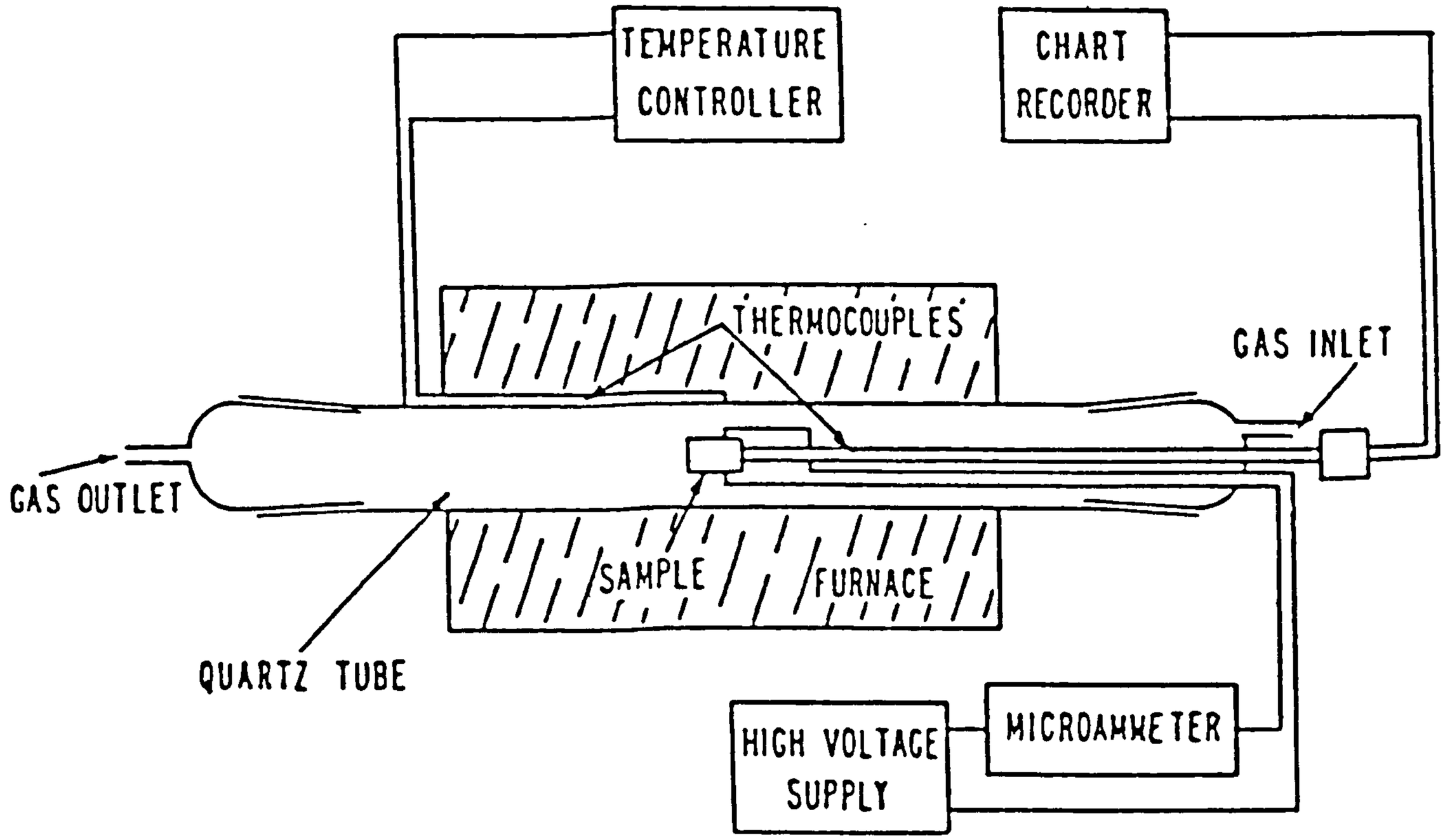

Fig. 2.3 Sweeping Apparatus
(From Ref. 116)

are given in table 1.6. Aluminium ions are substitutionally incorporated into the quartz crystal lattice and therefore cannot be removed by sweeping. The rate determining step of the process is not the migration of ions but their transport from the quartz surface to an electrode.

An additional advantage of the technique is that it greatly reduces and in many cases completely eliminates etch channel formation[116,117]. This is accomplished by the removal of those alkali metal impurities which decorate dislocation cores and which react with etchants to form the tunnel.

2.2.2 Electrodiffusion Procedure

Electrodiffusion of quartz samples was carried out at GEC Hirst Research laboratories using the sweeping apparatus shown schematically in fig. 2.3. To prevent hydrogen impurities being introduced by the process, an inert atmosphere was maintained in the apparatus by surrounding the sample arm with a fused silica tube through which dry nitrogen gas was passed. Nitrogen was used preferentially because electric arcing was less likely to occur in that medium than with other inert atmospheres such as the noble gases.

Electrodes were made from high purity platinum foil. Noble metals were used to prevent electrode oxidation resulting from air contamination of the nitrogen atmosphere. Platinum was preferred over less expensive materials such as gold and silver because of their tendency to diffuse into a crystal during sweeping[118,119]. Platinum atoms are too large for this

to occur. To ensure good electrical contact it was necessary to remove the cobbled surface of the (00.1) faces. Therefore, a crystal to be swept had its opposing (00.1) faces smoothed using a lapping machine. Starting with a coarse oil/carborundum powder suspension, the crystal was ground slowly using progressively finer powders until the (00.1) faces were flat and parallel. The direct application of platinum foil to a crystal sample provided sufficient electrical contact for successful sweeping.

The current generated across a sample by the flow of impurity ions was measured using a resistor circuit in series with the Techmation Kepco 0-2000 V range power supply which was used to generate the electric potential. The sample temperature was monitored using a chromel/nickrome thermocouple. Current and temperature against time was recorded for each sweeping run using a chart recorder. Sweeping was continued until a constant current was maintained across a sample. For the electrodiffusion studies carried out in this project, quartz samples were swept for one week at a temperature of 500 °C using a potential of 1000 V cm^{-2}.

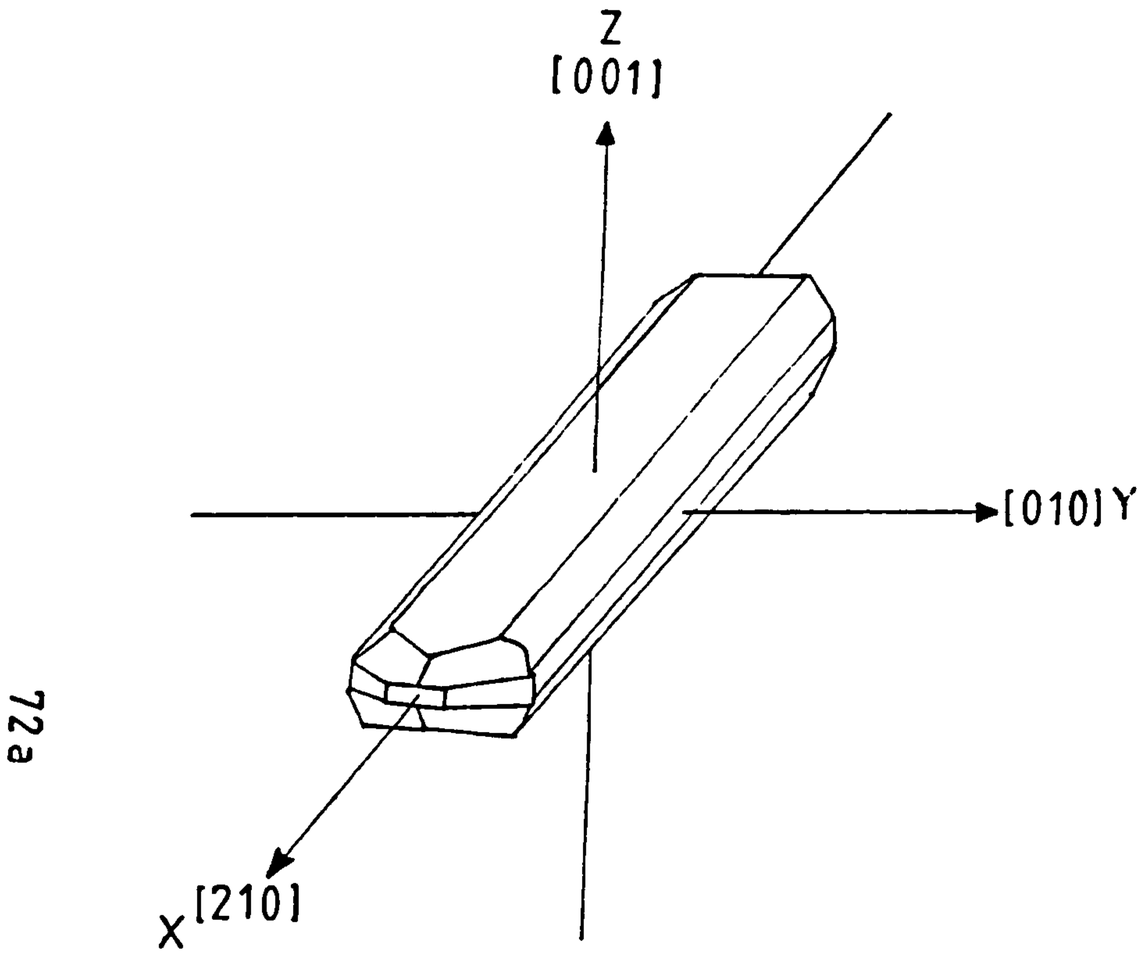

Fig. 2.4 Crystal Cuts of Quartz Sample Slices

2.3 Sample Preparation

Samples were cut from quartz crystals using a Metals Research Microslice 2 cutting machine equipped with an anular diamond blade. Crystals were held in place on an aluminium stage using a mounting wax and orientated with respect to the blade at the correct angle to produce the required crystal cut (see fig. 2.4). A lubricating oil was applied to the blade to prevent sticking as it passed through a crystal. When the blade had cut through, the stage was moved to obtain the required sample thickness. The product of this procedure was a crystal sample slice which possessed two parallel cut faces.

Cutting and handling damage was initially removed by hand grinding using a lapping machine. This procedure also ensured that cut crystal faces were flat. Failure to do this stage resulted in an uneven surface finish when a sample slice was optically polished. This was only an important consideration in the case of infrared samples. Scatter of the infrared beam results from passage through a partial optically polished sample which produces high background noise and a loss in the resolution of absorption bands. Prior to lapping, infrared samples were mounted onto a steel block and supported by pieces of glass of equivalent thickness which were placed around them. The samples were then hand ground on a lapping machine using a series of progressively finer abrasive powder suspensions in water until all signs of cutting damage were removed, by which time the surface was usually flat.

Optical polishing was carried out using a Logitech PM2

precision polishing machine. Samples were placed onto the polishing machine directly after lapping and were not removed from the steel block. The polisher was fitted with an adjustable holder and a correctly balanced sample spun as it moved resulting in an even polish. A sample arm moved the block back and forth across a rotating abrasive plate which was lubricated using a colloidal suspension of silica in sodium hydroxide known as Syton polish. This chemical produced an optically clear finish on a crystal sample. Each sample had one growth axis running through a polished face, eg. an X-slice sample face was perpendicular to the X-growth axis and similarly for Y and Z-slice samples.

Samples to be used in x-ray diffraction studies did not require optical polishing and cutting and handling damage was removed by immersion in 48% hydrofluoric acid for between 30 and 60 minutes.

2.4 Infrared Spectroscopy

2.4.1 Fourier Transform Infrared Spectroscopy

Infrared spectroscopy is based on the vibrations of the atoms in a molecule. In quantum mechanical terms these vibrations correspond to allowed transitions between vibrational levels in the same electronic state. Therefore, an infrared spectrum provides information of the vibrational structure of molecules which can be used to help understand properties such as molecular symmetry, orientation, conformation and hydrogen bonding. One of the major advantages of this technique is the group frequency concept which allows a specific functional group in a molecule to be singled out by its characteristic absorption frequency. This is a consequence of vibrational potential energy being centred around specific functional groups giving rise to normal modes of vibration.

In conventional infrared spectrometers, infrared radiation produced by a polychromatic source passes through a sample and is dispersed by a grating monochromator. The intensity of the transmitted radiation is detected directly as a function of frequency and therefore only a fraction of the spectrum collection time is utilised to collect intensity data at any particular frequency. However in a Fourier Transform Infrared, (FTIR), spectrometer the grating monochromator is replaced by a Michelson interferometer[120]. This device detects the intensity of the transmitted infrared radiation as a function of the displacement of a moving mirror, which leads to the

observation of an interferogram which is then converted into an infrared spectrum using Fourier transformation.

Fourier transformation is a complex mathematical operation which has to be performed using a computer. The observed interferogram $I(\delta)$ is related to the frequency spectrum $B(v)$ by the following expression[120],

$$I(\delta) = \int_{-\infty}^{+\infty} B(v) \exp(-2\pi.i.v.\delta)\, dv \qquad (2.1)$$

where δ is the path difference of the mirror and v is the frequency of radiation. The inverse of this Fourier transform equation yields the required infrared frequency spectrum thus,

$$B(v) = F^{-1}[\, I(\delta)\,]$$

$$= \int_{-\infty}^{+\infty} I(\delta).\exp(2\pi.i.v.\delta)\, d\delta \qquad (2.2)$$

Therefore, the interferogram in the time domain has been transformed into the infrared spectrum in the frequency domain. The signal to noise ratio of a spectrum obtained using Fourier transformation is M times greater than an identical spectrometer which uses a dispersive monochromator grating, where M is the number of resolution elements. Conversely a spectrum can be obtained M times faster than a conventional spectrometer for the same signal to noise ratio.

In addition to the elimination of an energy limiting slit, an FTIR spectrometer has several advantages over a dispersive device. The major advantages arise from two concepts known as

the Fellgett and Jacquinot advantages. The interferometer receives and therefore allows the observation of information regarding the entire frequency range of a given spectrum during each time element of a scan. This is a statement of the multiplex advantage of the technique, also known as Fellgett's advantage. Due to the elimination of dispersive elements such as the gratings and slits, the interferometer is able to collect large amounts of energy at high resolution. This statement was expressed by Jacquinot as an energy throughput advantage over conventional spectrometers. Other advantages include fast scanning times, large wavenumber range per scan and high resolving power. A standard FTIR spectrometer uses a He-Ne laser to monitor the displacement of the moving mirror and allows the frequency accuracy of data collected to be very high and usually better than ± 0.01 cm^{-1}. This increased frequency accuracy of the technique is also known as Conne's advantage. Combining this with the other mentioned advantages allows the possibility of highly accurate detection of weak signals down to millimetre wavelengths.

2.4.2 Quality Assessment Using Infrared Spectroscopy

Infrared spectroscopy is the most widely used non-destructive analytical technique for quartz quality assessment. Of particular interest is the 3100-3700 cm^{-1} frequency region of the infrared spectrum. In this portion of the quartz spectrum, absorption bands produced by the O-H stretching vibrations of hydrogen related impurity species are observed[52]. These have been shown, in natural quartz crystals, to be associated with metal impurity ions, such as Li^+ and Na^+[52,98]. The hydrogen content, C, of a crystal can be calculated using the following formula[99]

$$C = \frac{\int E dv}{d} \cdot \frac{f}{\epsilon'} = 2.11 \cdot K[\, OH / 10^6 \, Si \,] \qquad (2.3)$$

where C is the number of hydroxyl groups per million molecules of SiO_2, K is the integral absorption ($\int E dv/d$), d is the thickness of the sample in centimetres, E is the absorbance ($\log I_o/I$), ϵ' is a function of the molar absorption coefficient for integral absorption ($\epsilon' = 2/3\epsilon_m$, ϵ_m = 14000 cm/g-atom = molar absorption coefficient for integral absorption[99], 2/3 is the anisotropy factor), f is a function of the specific gravity of quartz ($f = \sigma \cdot 10^6/60, \sigma$ = 2.66g/cm^3 = the specific gravity of quartz).

This formula holds for integrated absorption values using unpolarised light and shows the concentration of O-H bonds in a quartz crystal to be directly proportional to the area under the absorption bands which they produce. This

relationship, because of the association of metal impurities with the absorption bands, allows the quality of a crystal to be assessed directly from its infrared spectrum.

Hydrogen related absorption bands in quartz infrared spectra are highly temperature dependent. At room temperature, only the strongest absorption bands are visible and then at only a fraction of their full heights. There is a general loss in peak resolution, giving rise to broad, weak absorptions. As the sample cools, O-H related peaks increase in height and sharpness enabling the observation and resolution of absorptions invisible at room temperature. This is partially a consequence of the restriction of interactions between neighbouring hydroxyl species. Essentially, the quartz crystal lattice acts as an isolation matrix at low temperature. Molecular motions are also considerably reduced at low temperatures, leading to a sharpening of the bands which are then more readily observed. The construction of a specialised cooling apparatus was therefore necessary to achieve these temperatures for spectroscopic studies of high purity crystals.

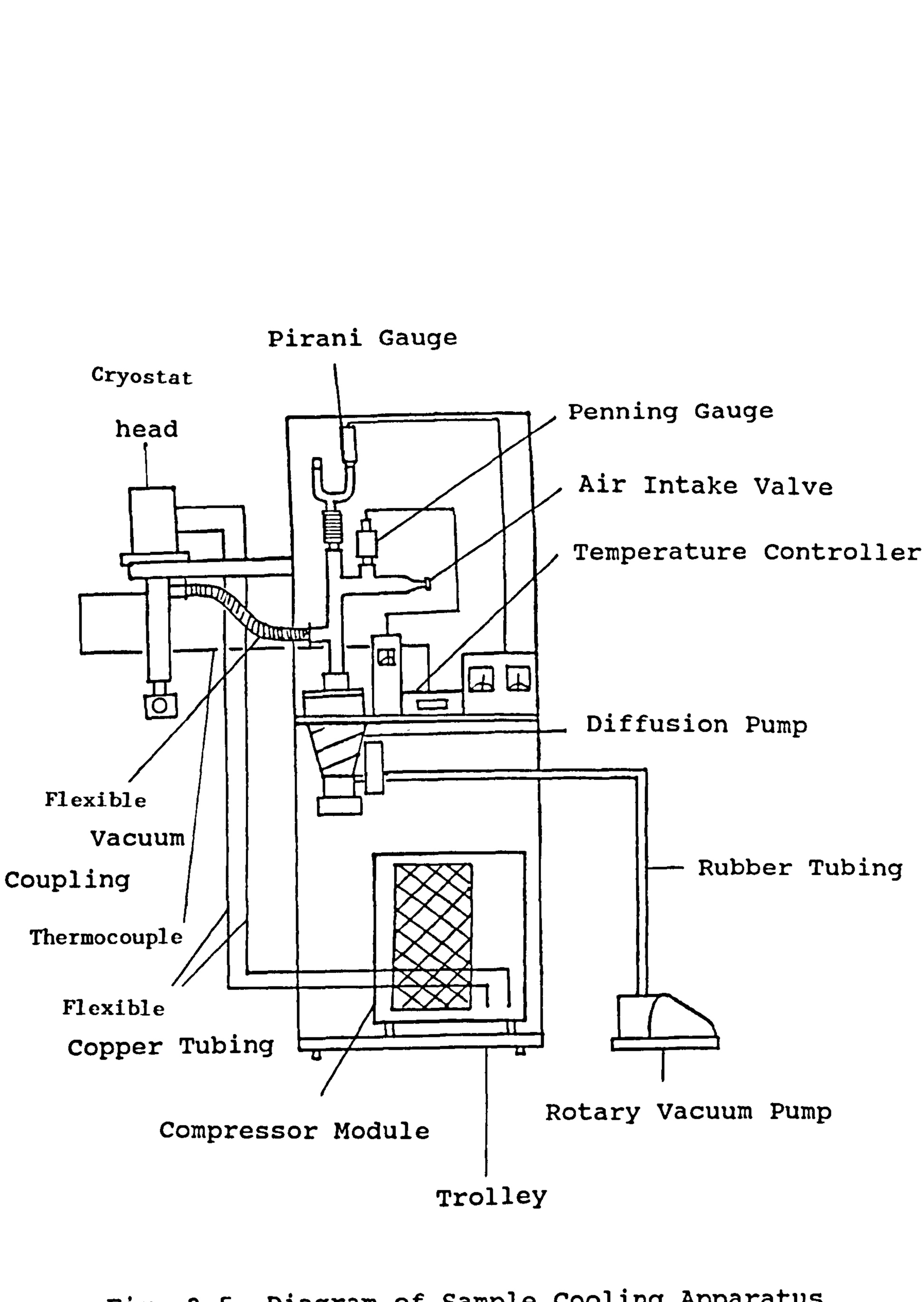

Fig. 2.5 Diagram of Sample Cooling Apparatus

2.4.3 Low temperature Equipment

The cooling apparatus which was used for low temperature FTIR studies is shown in figures 2.5 and 2.6. An Air Products CSW-202 cryostat was used to attain a base sample temperature of approximately 10°K. The cryostat was a closed cycle Helium refrigerator consisting mainly of a water cooled compressor unit and a two stage displacer module. It operated using the basic principle of adiabatic expansion, since the cooling of a sample was achieved by expansion of a gas against a constant pressure. The compressor provided the displacer module with a helium gas supply at around 20 atmospheres pressure which was expanded in a two stage process down to 6 atmospheres. The gas was then returned to the compressor for another cycle. For the gas to expand it had to work against a piston which was held at a constant pressure. As the expansion process occurred, the gas lost energy and cooled, lowering the temperature of a solid copper block situated at the base of the expansion chamber. Samples were attached to this block to acquire the temperatures necessary for low temperature spectroscopy.

The system was kept under vacuum to protect the sample from conducted external heat and condensation of atmospheric gases onto the sample. Pressure was maintained by a two stage pumping system. An NGN model PRS1 rotary pump provided a backing vacuum of $5x10^{-2}$ torr which could be further reduced to 10^{-5} torr by an Edwards Diffstak 63-150m oil diffusion pump. The vacuum system was self contained and connected to the cryostat using a flexible steel vacuum coupling. Backing

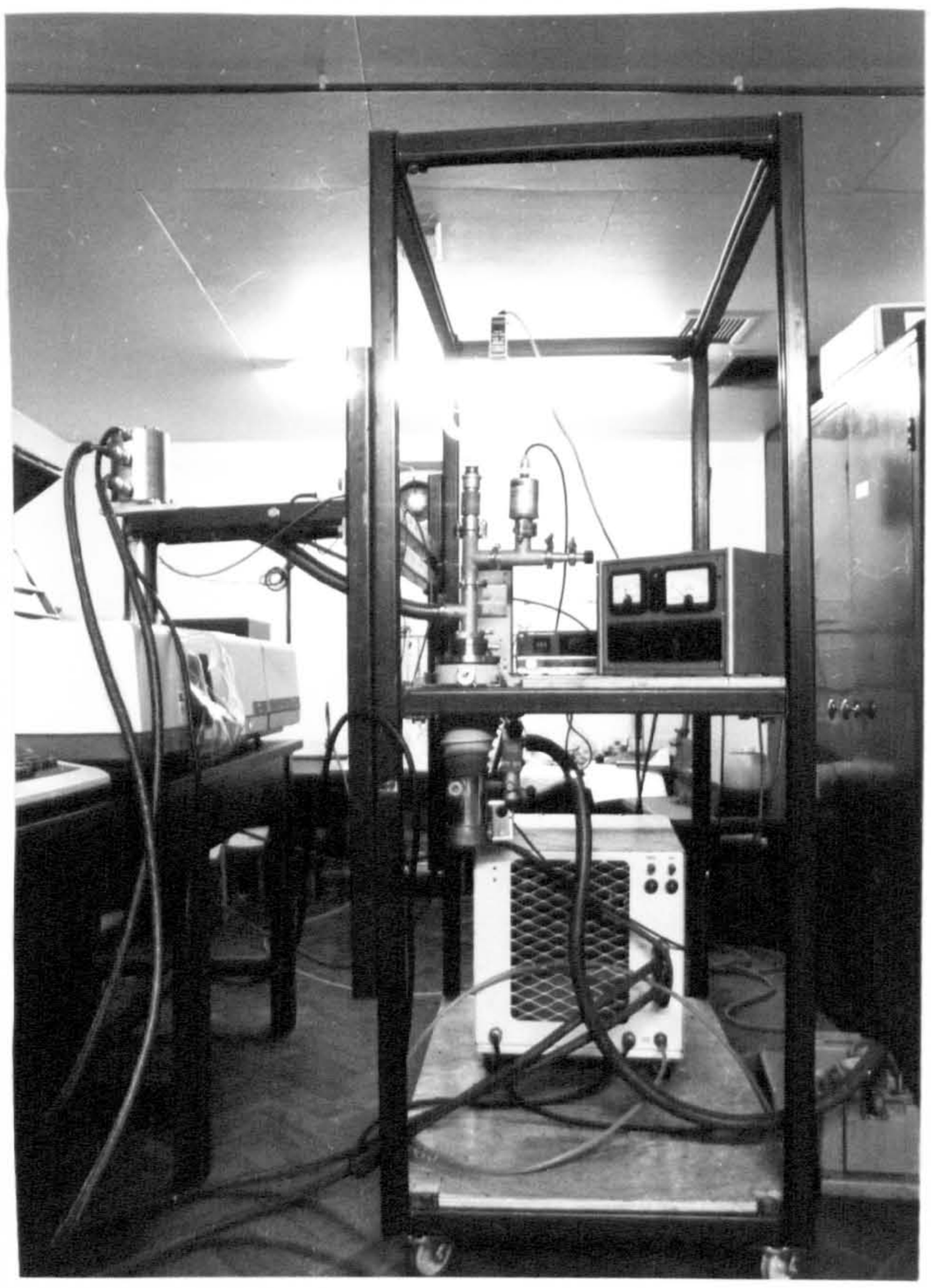

Fig. 2.6 Sample Cooling Apparatus

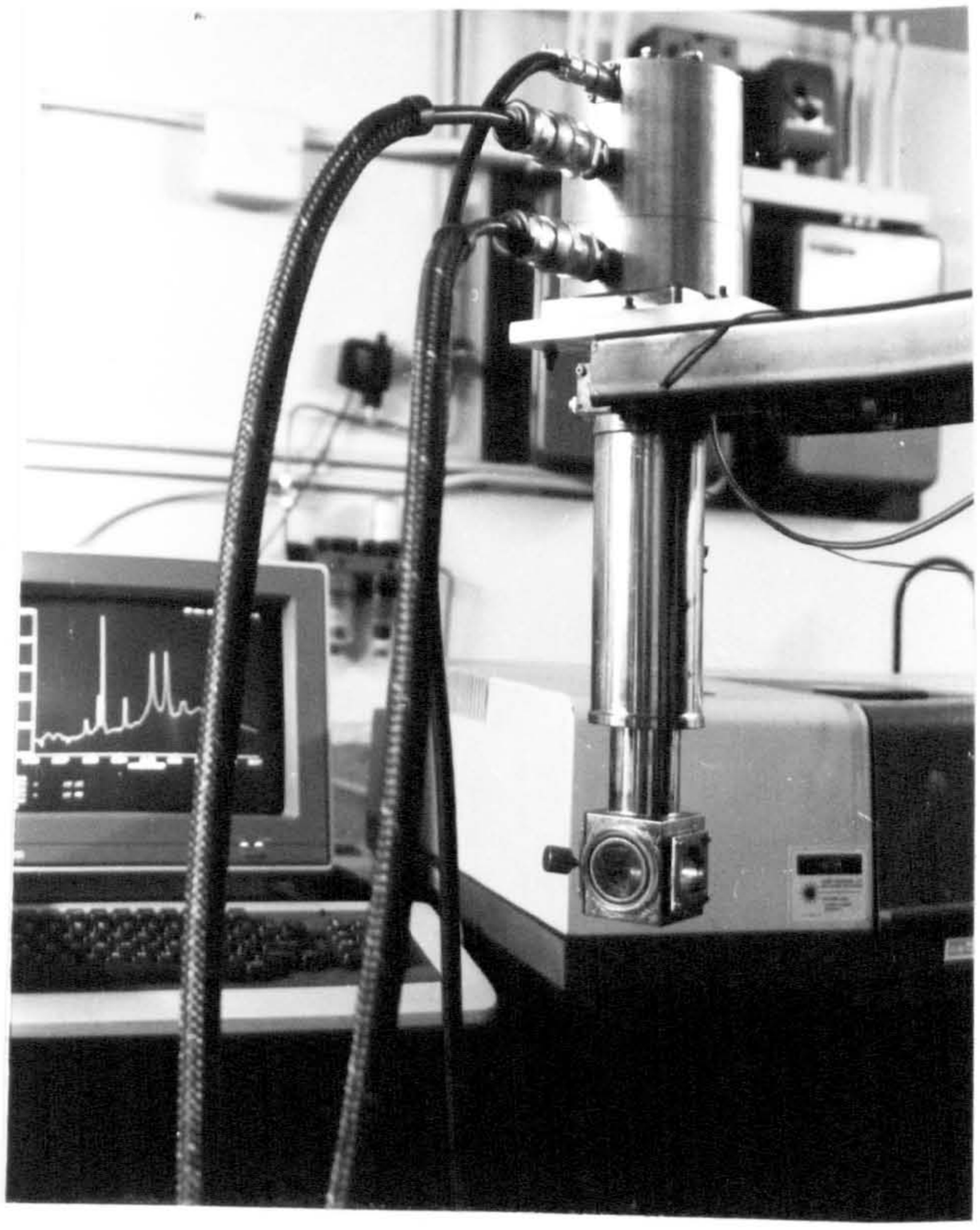

Fig. 2.7 Cryostat head and Steel Shroud

and operational vacuums were measured using a Speedivac model 2A Pirani gauge and an Edwards model 7 Penning gauge respectively. The sample and the expander module were completely enclosed in a stainless steel shroud fitted with spectroscopic windows (see fig. 2.7). These were made of sodium chloride which was transparent to infrared radiation in the frequency range under investigation. Sample temperatures were monitored and controlled using a Thor Cryogenics model S-3030 controller which was connected to a 0.07% iron in gold versus chromel thermocouple attached directly to the copper block in the expander module. The thermocouple EMF was fed to the controller via an automatic cold junction where it was converted to a temperature reading and displayed on a digital panel. Where necessary, temperature control was achieved using a 46 Ω resistance heater fitted around the copper block. This was connected to the controller which automatically heated a sample to the desired temperature.

2.4.4 Recording an Infrared Spectrum

Samples were cleaned prior to analysis using chloroform to remove grease and other surface contaminants which could produce absorption peaks in sample spectra. Air Products Crycon grease was used to attach sample crystals to a copper holder. Care was taken to ensure that the area of a sample which contained a natural seed crystal was covered by this holder. The copper loaded grease provided good thermal contact between sample and holder, ensuring that they both cooled at

Fig. 2.8 Plastic Seal for Purging of FTIR Sample Chamber

the same rate. The sample holder was screwed into the copper block at the base of the expander module and then covered by a steel shroud. The junctions between the module, spectroscopic windows and shroud were fitted with nitrile O-rings lubricated with Apiezon N grade vacuum grease to provide a vacuum seal. The steel shroud was too bulky to fit through the window in the sample chamber of the spectrometer so the cover had to be opened to permit access to the infrared beam. The FTIR spectrometer was purged with dried air to remove absorptions due to atmospheric water and carbon dioxide gas appearing in sample spectra. It was therefore necessary to re-seal the sample chamber with a polythene jacket (see fig. 2.8). Although not an ideal arrangement, this was found to eliminate atmospheric interferences after purging the sample chamber with dry air for one hour. The reference laser was used to ensure that the analysing infrared beam passed through the polished faces of a sample. The rotary pump was then started and the system allowed to reach a vacuum of 7.5×10^{-2} torr before the diffusion pump was operated. This was a precaution to prevent damage of the diffusion pump as a result of exposure to air. Once a sufficient vacuum has been reached, the backing valve and the main chamber of the diffusion pump were opened and the system allowed to reach a vacuum of 10^{-5} torr. The cryostat and temperature controller were then operated. Spectra were obtained when the sample temperature stabilised at around 10 $^{\circ}$K. All quartz spectra presented in this thesis were recorded at 1 cm^{-1} resolution using a Nicolet 20 SXB Fourier transform infrared spectrometer.

2.4.5 Polarised Infrared Spectroscopy

Infrared spectroscopy is based upon the principle that any fundamental mode of motion accompanied by an oscillating electric moment leads to the absorption of electromagnetic radiation. Polarised infrared spectroscopy utilises the fact that the oscillating electric moment is a vector quantity and can only interact with electromagnetic radiation that has an electric field component parallel to its direction[121]. For cases where the electric moment is fixed in space, such as in crystalline samples, information about its direction can be obtained using polarised radiation. If the direction of the transition moment is known it then becomes easier to correlate the absorption with a mode of motion of the species under examination. The quantity that is measured in polarisation studies of infrared spectra is the dichroic or polarisation ratio. This is defined as " the ratio of band intensity when the electric vector in the radiation falling on the orientated sample is in such a direction as to give maximum intensity to band intensity when the electric vector is perpendicular to this direction[122]". This is the ratio of the integrated areas of absorption peaks which show maximum intensity for a particular polariser orientation and the corresponding intensities of the same bands when the polariser is at 90° to this position.

A series of polarised infrared studies were carried out in an attempt to uncover information regarding the spatial orientations of hydrogen related impurity species in

Fig. 2.9 Polarised Infrared Spectroscopy Sample Set-Up

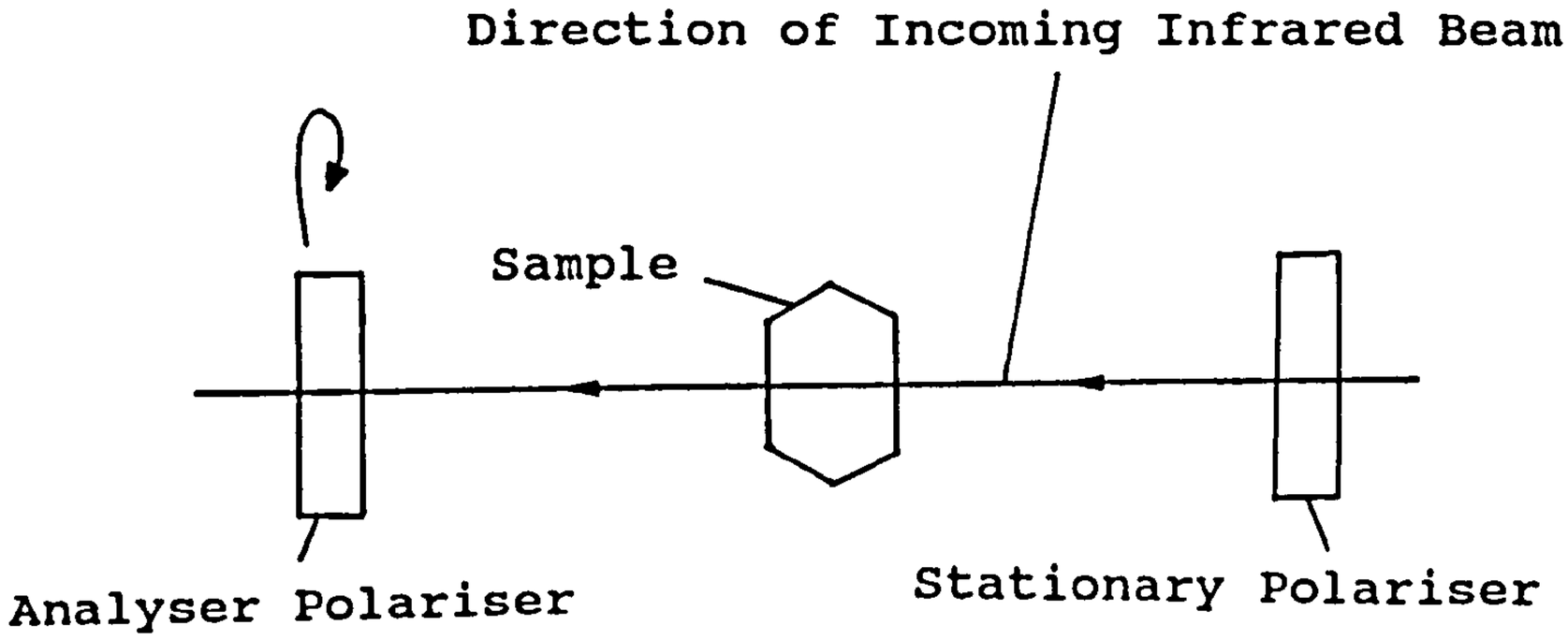

a) Two Polariser Configuration

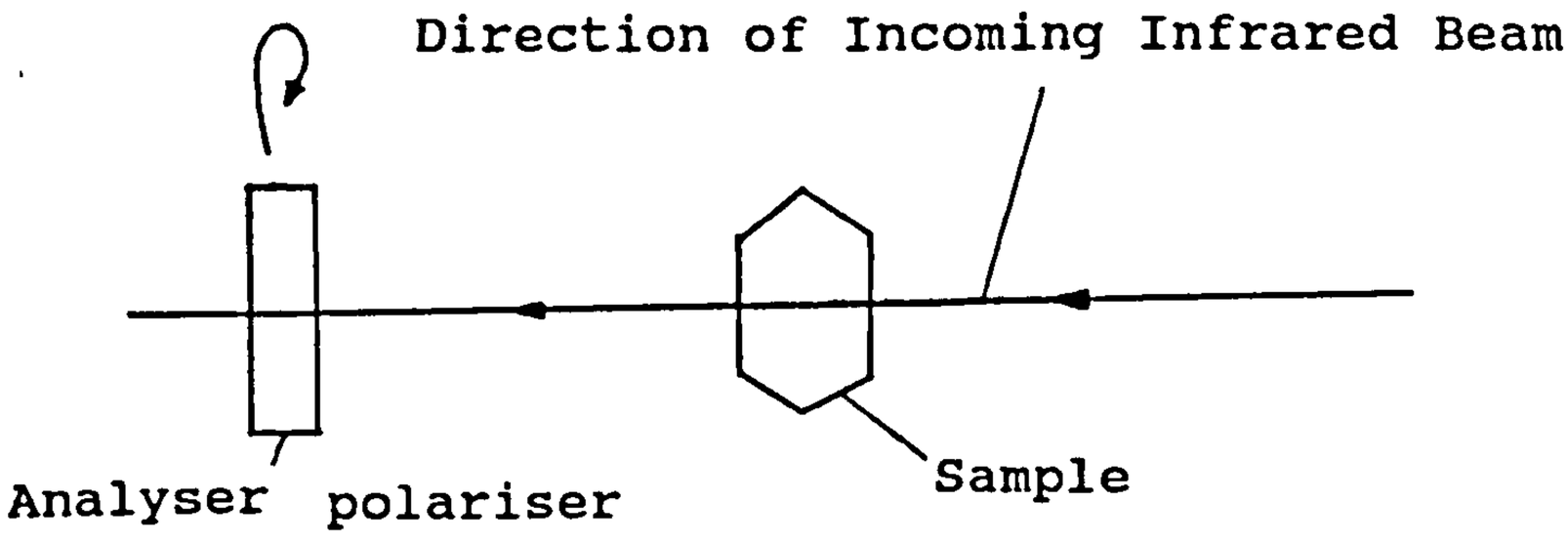

b) One Polariser Configuration

quartz crystals. Samples were cut normal to the three growth directions X, Y and Z for each crystal studied. Sample spectra obtained at low temperatures following the procedures outlined in the previous section with the additional step of the placement of a polariser between the sample and the detector. The incident infrared beam was effectively unpolarised. An ideal experimental set-up would consist of two polarisers positioned one before and one after the sample and set at right angles to each other (see fig. 2.9a). Unfortunately only one polariser was available and an alternative set-up was used. The polariser/sample arrangement chosen was that used by Walarafen and Luongo[102]. A single polariser was positioned after the sample so that information on the direction of absorbing species could be measured directly (see fig. 2.9b). As a check, several spectra were taken with the polariser before the sample. When compared with the spectra of the same samples recorded with the polariser in the forward position, polarisation features were found to be identical in both cases.

2.5 X-Ray Diffraction Topography

2.5.1 Lang Transmission X-Ray Diffraction Topography

In 1912, Max Von Laue[123] pointed out that if radiation was passed through a crystalline material such that the wavelength of the radiation used was as small as the distance between the planes of a crystal lattice, then a diffraction pattern would result. X-rays proved to be of a suitable wavelength and have been used in numerous diffraction techniques to investigate crystal structures[71,124]. One such technique that is commonly used in defect characterisation is Lang transmission x-ray topography[125,126]. The technique utilises the fact that diffraction of x-rays by crystals is sensitive to lattice strain. As a consequence, there is a difference in the intensities of X-rays diffracted by perfect and imperfect regions of a crystal. The general procedure developed by Lang[70,71,126], was to orientate a chosen set of crystal planes with respect to an x-ray beam such that diffraction of x-rays from these planes would occur. Diffraction will only result if Bragg's Law is satisfied, as follows

$$n\lambda = 2d.\sin\theta \qquad (2.4)$$

n - non zero integer d - interplanar spacing

λ - wavelength of radiation θ - Bragg angle

Diffraction from a reflection plane which has its lowest possible integral set of Miller indices is called a first order reflection and corresponds to values of n equal to

unity, eg. (10.0), (02.3), (12.1). All other integral values of n correspond to diffraction from integral multiples of first order reflection planes, eg. (30.0), (04.6) and (48.4), which are called high order reflections. The order of the reflection equals that of the value for n , eg. (04.6) is a multiple of (02.3) and corresponds to a second order reflection, n=2.

When devising an x-ray diffraction experiment, some way of satisfying the Bragg condition must be found. Conventional laboratory x-ray sources produce effectively monochromatic radiation and so in a typical experimental set-up, the radiation wavelength is fixed and the sample, which is usually a single crystal slice, is orientated by the Bragg angle to produce diffraction from a set of chosen planes. Calculations for quartz reflection planes were based on a hexagonal crystal system and the corresponding equation for lattice spacing is as follows[127] (see Appendix A),

$$d^2_{hkl} = \frac{1}{(h^2 + k^2 + hk)\, a^{*2} + l^2 c^{*2}} \qquad (2.5)$$

where, $a^* = \frac{2}{a\sqrt{3}}$ $\qquad$ $c^* = \frac{1}{c}$

d - interplanar spacing a,c - lattice parameters

h,k,l - Miller indices of chosen diffraction plane

When diffraction occurs, the diffracted rays leave a crystal at an angle equal to twice that of the Bragg angle

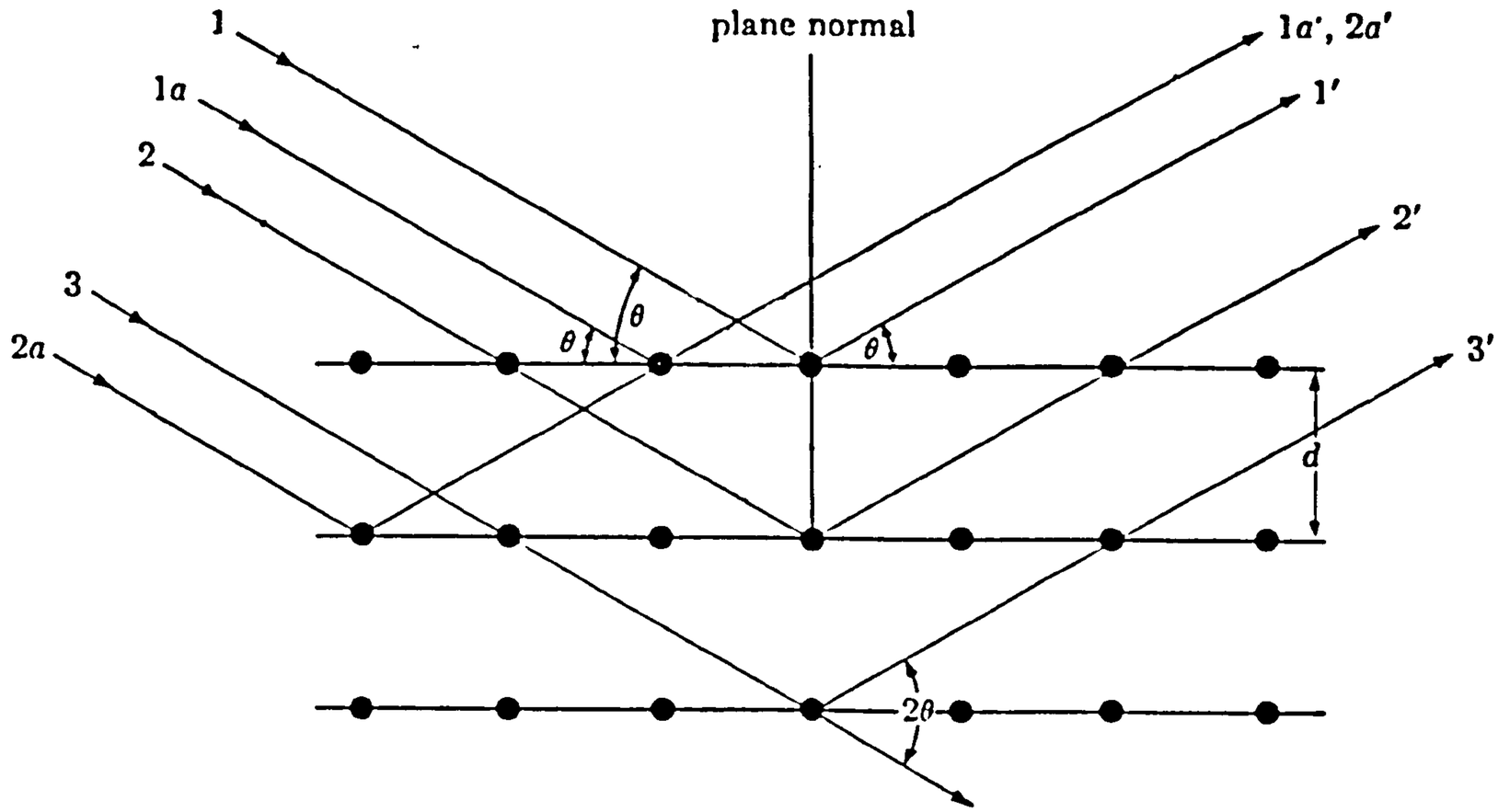

Fig. 2.10 Diffraction of X-Rays by a crystal.

with respect to the incident x-ray beam (see fig. 2.10). These diffracted rays are normally recorded using photographic methods and the images they produce are known as x-ray diffraction topographs.

2.5.2 Elements of Dynamical Theory

Two theories have been developed to describe the diffraction of x-rays by crystals namely, the kinematic and the dynamic theories. In the case of the kinematic theory, the assumption is made that the amplitude of diffracted waves is small in comparison with that of the incident waves and no interaction between the two occurs. This is valid only for very thin or highly defective crystals. In the case of thick, highly perfect crystals all the interactions between the incident and diffracted x-rays must be taken into account. This is achieved by the dynamical theory of diffraction. This theory has been described in numerous reviews, notably Tanner[125], Hart[128] and Authier[129]. Certain important features of the theory relevant to this thesis will now be discussed.

i) Rocking Curve Width , $\Delta\theta_{\frac{1}{2}}$

One of the most important parameters in x-ray diffraction topography is the rocking curve width, $\Delta\theta_{\frac{1}{2}}$[125]. If a crystal is rotated through the Bragg condition, the intensity of diffracted x-rays will vary according to the position of the reflection planes. A plot of diffracted

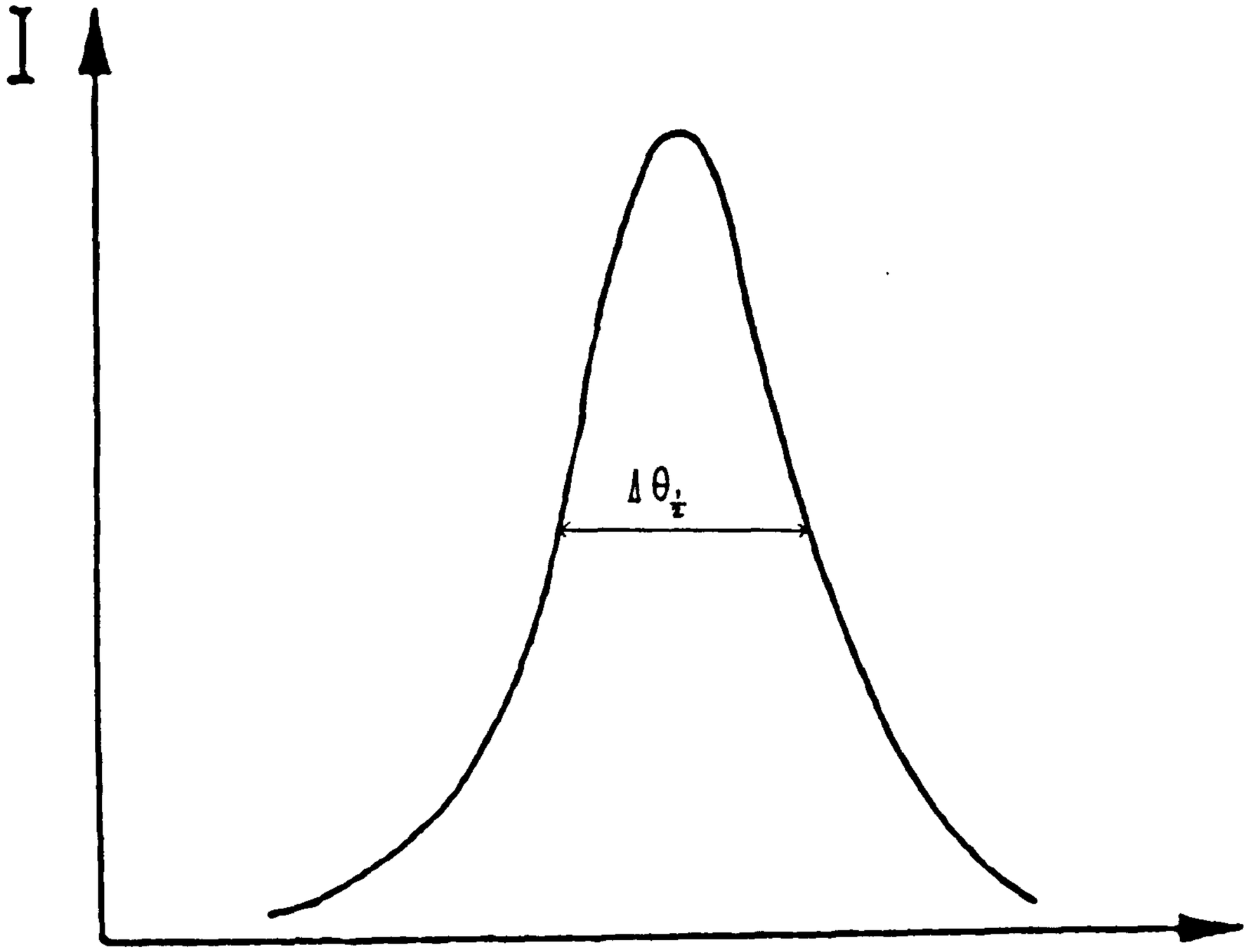

Fig. 2.11 Schematic Diagram of Width at Half Height

on a Rocking Curve

intensity against rotated angle shows the maximum angular limits within which a crystal can be moved from the Bragg condition and still produce diffraction. This plot produces a diffraction peak for the chosen reflection planes known as a rocking curve (see fig. 2.11). The width of this curve is measured at a position half way up the height of the peak and represents the effective angular range which can be accepted for diffraction by a perfect crystal. This parameter can be calculated using the following formulae[125],

for a symmetric reflection,

$$\blacktriangle\theta_{\frac{1}{2}}(\text{sym}) = \frac{2d.C.\delta.|F|}{\pi.V.\cos\theta_B} \qquad (2.6)$$

for an asymmetric reflection,

$$\blacktriangle\theta_{\frac{1}{2}}(\text{asym}) = \blacktriangle\theta_{\frac{1}{2}}(\text{sym}) \sqrt{\frac{\tau_h}{\tau_o}} \qquad (2.7)$$

where,

d - interplanar spacing

C - polarisation factor, C = 1 or $|\cos 2\theta_B|$

δ - wavelength of x-rays

F - structure factor in absolute units

V - unit cell volume

θ_B - Bragg angle

τ_h - Cos $(\theta_B + \alpha)$

τ_o - Cos $(\theta_B - \alpha)$

α - angle between the diffraction plane and the normal to the crystal surface

The rocking curve is important in defining both the strain sensitivity and the spatial resolution of an x-ray reflection. These two parameters are dependent on one another and consequently one can only be improved at the expense of the other. A reflection which has a large $\Delta\theta_{\frac{1}{2}}$ value, that is a low order reflection and a high structure factor, will have high spatial resolution but poor strain sensitivity. Conversely, a weak high order reflection which possesses a low $\Delta\theta_{\frac{1}{2}}$ will have high strain sensitivity but poor spatial resolution.

ii) Contrast on X-Ray diffraction Topographs

The contrast on x-ray topographs depends on both the absorption and diffraction of x-rays by a sample crystal. There are three main types of diffraction images, namely direct, dynamic and intermediate[128-130].

1. Direct Images

The angular range or rocking curve width of a perfect crystal is generally in the order of between 1 to 10 seconds of arc. In comparison, the divergence of a standard x-ray beam is in the region of several minutes. Therefore, in the case of a perfect crystal only a very small fraction of the incident beam will satisfy the Bragg condition and be diffracted. However, the distortion of lattice planes around a crystal defect allows a much larger proportion of the incident beam to meet this condition. The increased diffraction intensity

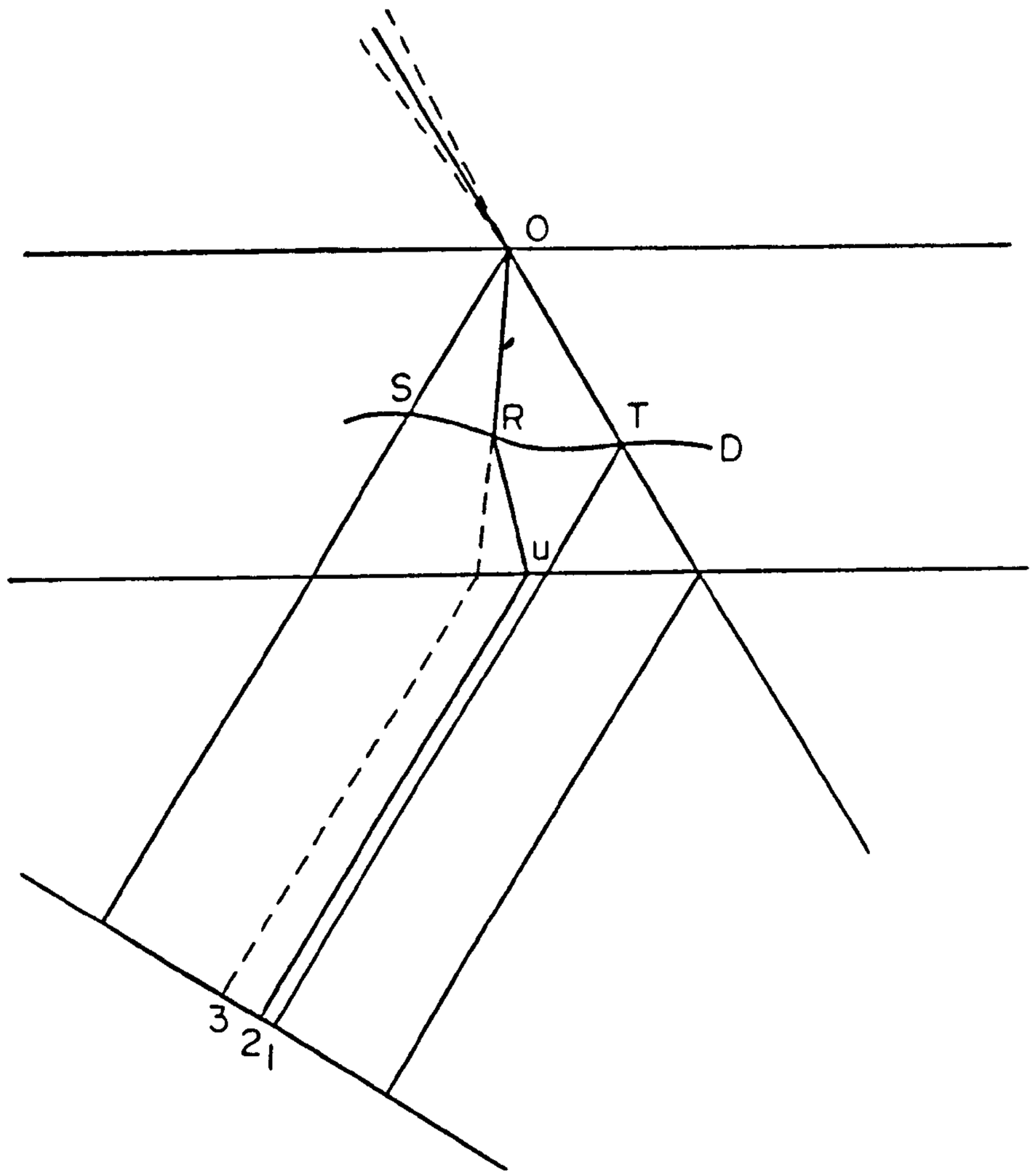

Fig. 2.12 Formation of the three types of image in section and projection topographs: 1, Direct image, 2, Intermediary image, 3, Dynamical image (after A. Authier).

(From Ref. 125)

arising from the region of a defect will result in increased contrast on an x-ray topograph in the area associated with the imperfection and produce an image of the strain field around the defect. This type of image is known as the direct or kinematical image[129] (see fig. 2.12).

2. Dynamical Images and Pendellösung Fringes

When the incident x-ray beam enters a crystal, it propagates a spherical wave which can be considered as a series of plane waves (see fig. 2.13). For those waves orientated by the Bragg condition, diffraction will occur whereas those not meeting this condition will leave the crystal in a parallel direction to that of the incident beam. This produces a Bragg diffracted and a forward diffracted wave respectively which interact to produce two standing wavefields, one whose nodes correspond to atomic positions and one with nodes located between these positions. These are known as type 1 and type 2 wavefields respectively. Both of the wavefields have diffracted and forward diffracted components which form the exit and diffracted x-ray beams respectively. The wavefields also form a fan between these two beams known as the Borrmann fan. The strain field of a defect causes a change in the ratio of the diffracted to forward diffracted component of a wavefield passing through the imperfection. This effect is also known as wavepoint migration and causes a change in the intensity of the diffracted beam[128]. This change produces a dynamical image which is

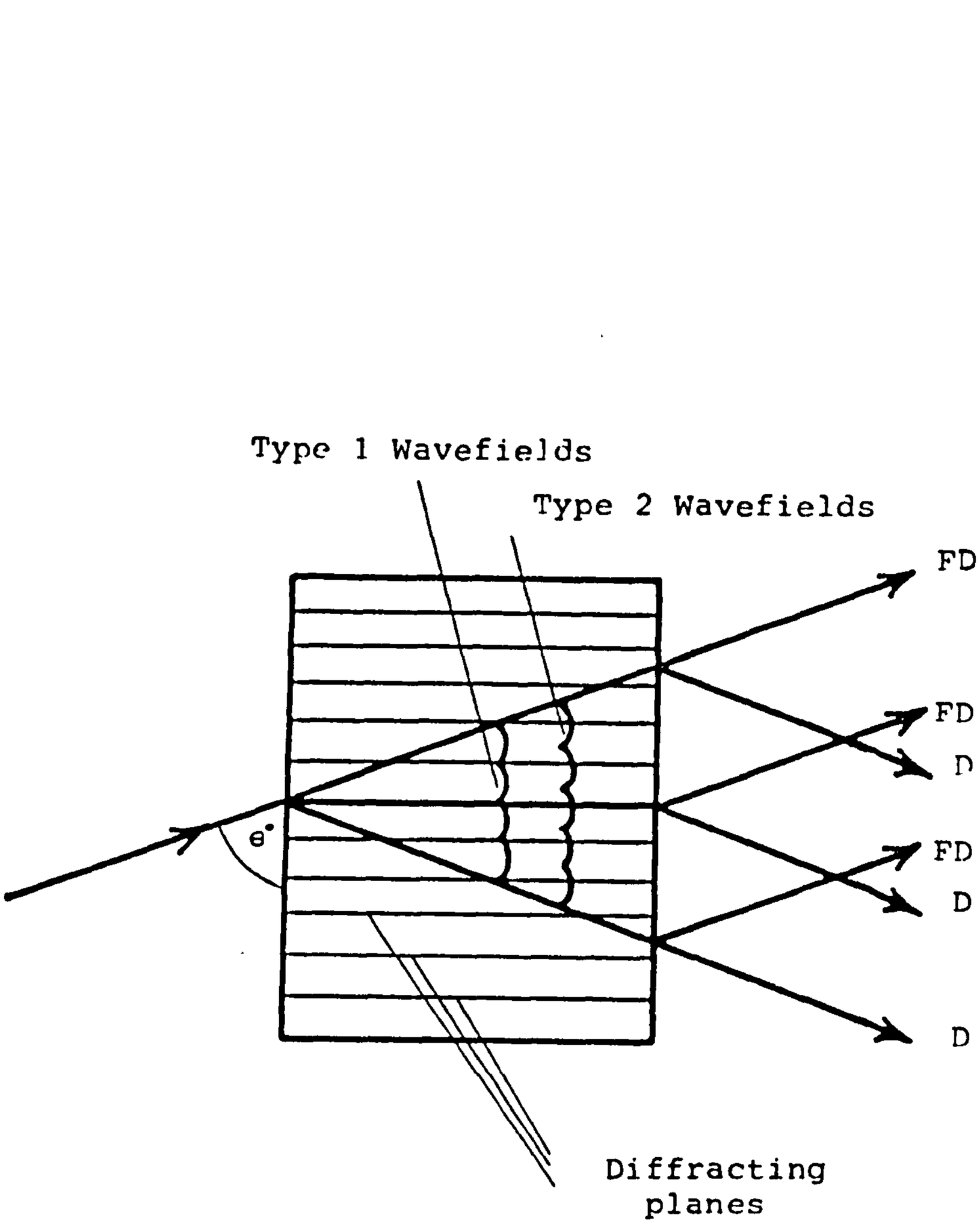

Fig. 2.13 Formation of the Dynamic Image

normally observed as an area of black/white contrast corresponding to the strain field around the defect.

Pendellösung fringes are produced by the interference of the two wavefield types as they pass through a perfect wedge shaped crystal. They are usually observed as a series of equally spaced parallel lines.

3. Intermediary Images

This third type of image arises when the strain around a defect is strong enough to decouple wavefields which encounter the imperfection into their diffracted and forward diffracted components. These recombine when leaving the defect to produce two new wavefields which then interfere to produce Pendellösung fringes. This effect is also known as interbranch scattering[129,130].

4. Absorption Effects

The type of image which is produced on x-ray topographs is strongly influenced by the absorption properties of a crystal. Absorption of x-rays is related to the thickness, t, of the crystal through which they pass and governed by the parameter μt, where μ is the linear absorption coefficient which can be calculated as follows[125],

$$\mu = \frac{n \Sigma_i (\mu_i)}{V_c} \qquad (2.8)$$

where,

n - number of molecules per unit cell

V_c - volume of unit cell

μ_i - atomic absorption coefficient of the atomic species i

In the case of a thin crystal, where $\mu t < 1$, absorption of x-rays is low. Direct images are strongly contrasted and, because both type 1 and 2 wavefields are transmitted with little attenuation, Pendellösung fringes can be imaged when interference occurs. Intermediary images can also form because neither of the wavefields which produce these images are absorbed to any extent. However a consequence of the lack of absorption is that the ratio of the two wavefields does not change significantly thereby cancelling the effects of wavepoint migration and preventing the formation of dynamical images.

For a significantly thicker crystal, where, $1 < \mu t < 10$, absorption effects are much stronger and the direct image is a much weaker feature in comparison to the thin crystal case. Similarly, both Pendellösung and interbranch scattering effects are still visible but are much less pronounced. However, there is now significant absorption of both wavefields which give rise to dynamic image formation. This absorption is not equal for each wavefield type and the corresponding changes in ratio between the forward diffracted and the diffracted components no longer cancel each other. As a consequence, wavepoint migration effects can produce

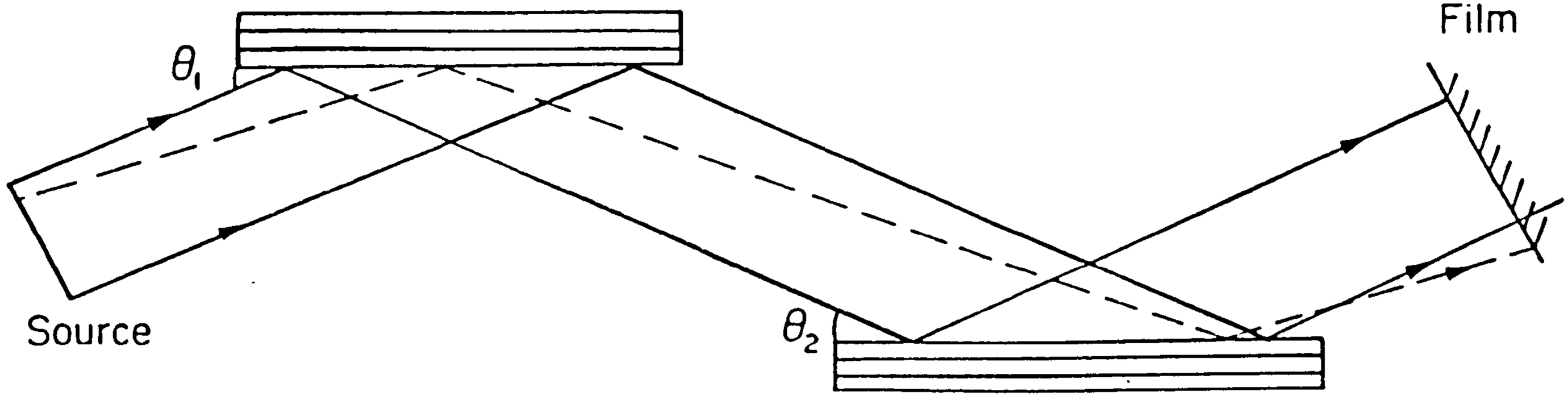

Fig. 2.14 (+ -) Parallel Crystal Configuration

(From Ref. 125)

dynamical images of a crystal imperfection.

For very thick crystal, where $\mu t > 10$, both the direct beam and type two wavefields are completely absorbed and no direct images or Pendellösung fringes will be observed. The only images possible will arise from defects lying close to the crystal exit surface and will be a product of wavepoint migration or interbranch scattering effects and anomalous transmittion.

The x-ray diffraction samples which were studied during the course of this project satisfied the condition $\mu t < 1$ and hence only direct images were important.

2.5.3 Double Crystal X-Ray Diffraction Topography

The double crystal technique utilises two successive Bragg diffractions to enhance the strain sensitivity in x-ray diffraction topography[84,131]. The standard double crystal orientation is known as the (+ -) parallel setting with the Bragg planes of both crystals being parallel and of equal lattice spacing[125] (see fig. 2.14). In this geometry the rocking curve is very narrow and the technique is very sensitive to lattice distortions and misorientations. To understand this more fully, it is necessary to examine the Du Mond diagram of the system (see fig. 2.15a). This is essentially a graphical representation of Bragg's law which shows the angles at which Bragg reflection will occur at various wavelengths of radiation for a chosen set of crystal planes. The point at which the two curves intersect indicates

Fig. 2.15 Du Mond Diagram Corresponding to the (+ -)

Parallel Crystal Configuration of Two Crystals

(From Ref. 125)

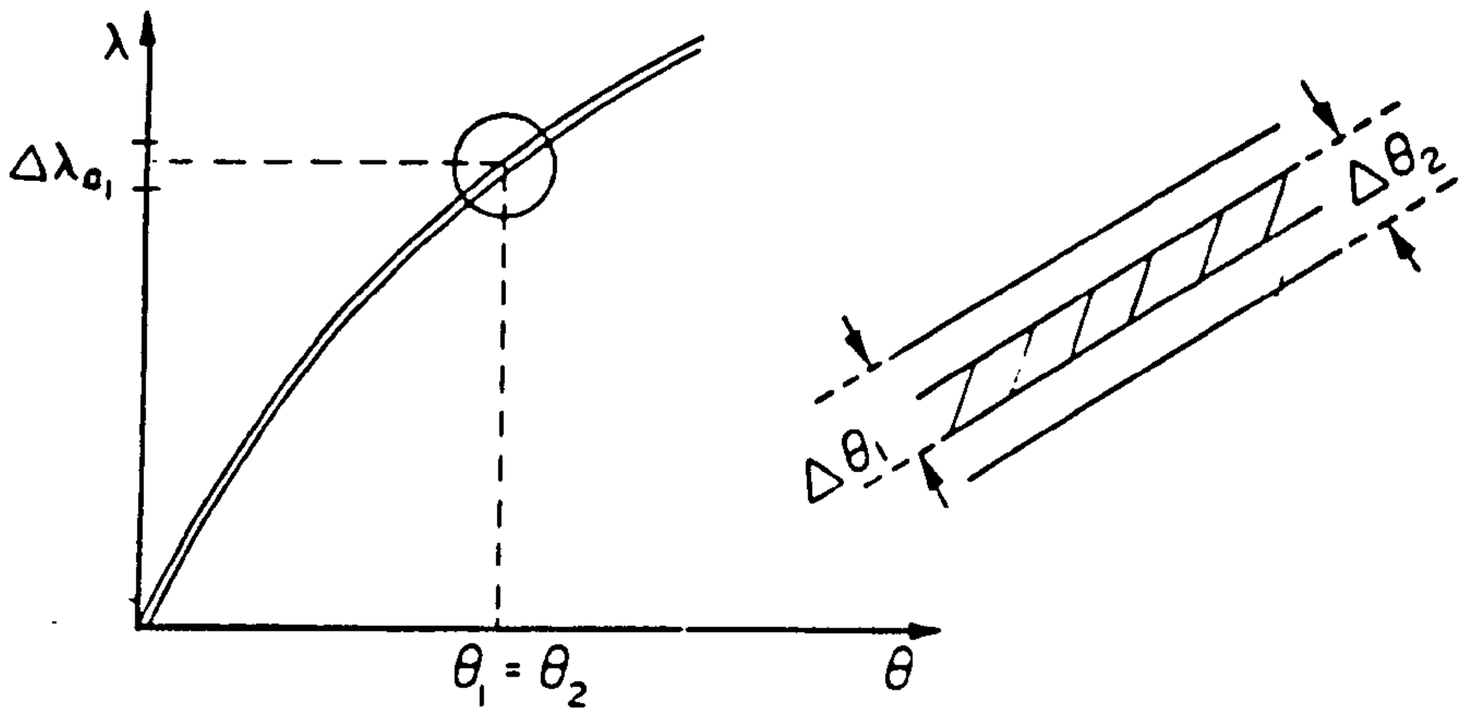

a) Two Perfect Crystals

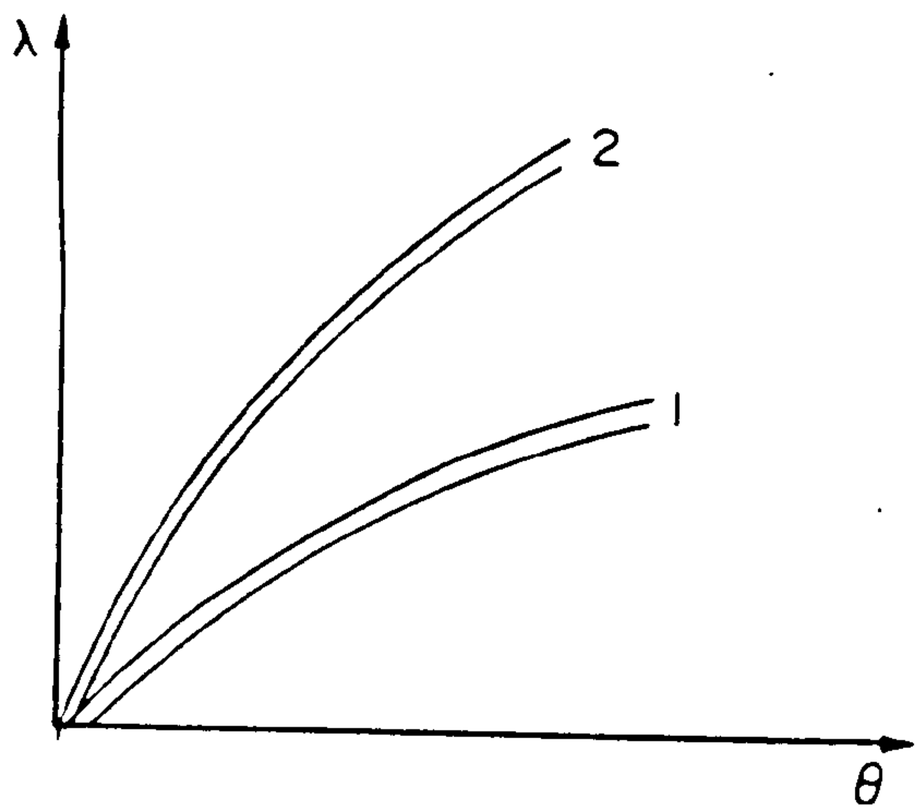

b) Local Rotation of the Lattice

in the Sample Crystal

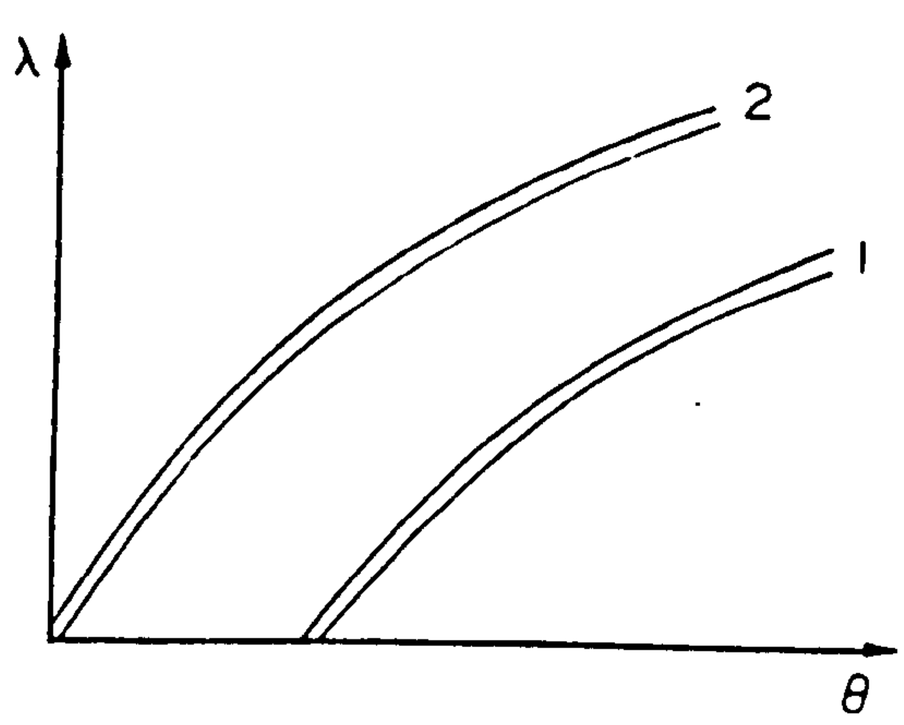

c) Local Dilation in the Sample Crystal

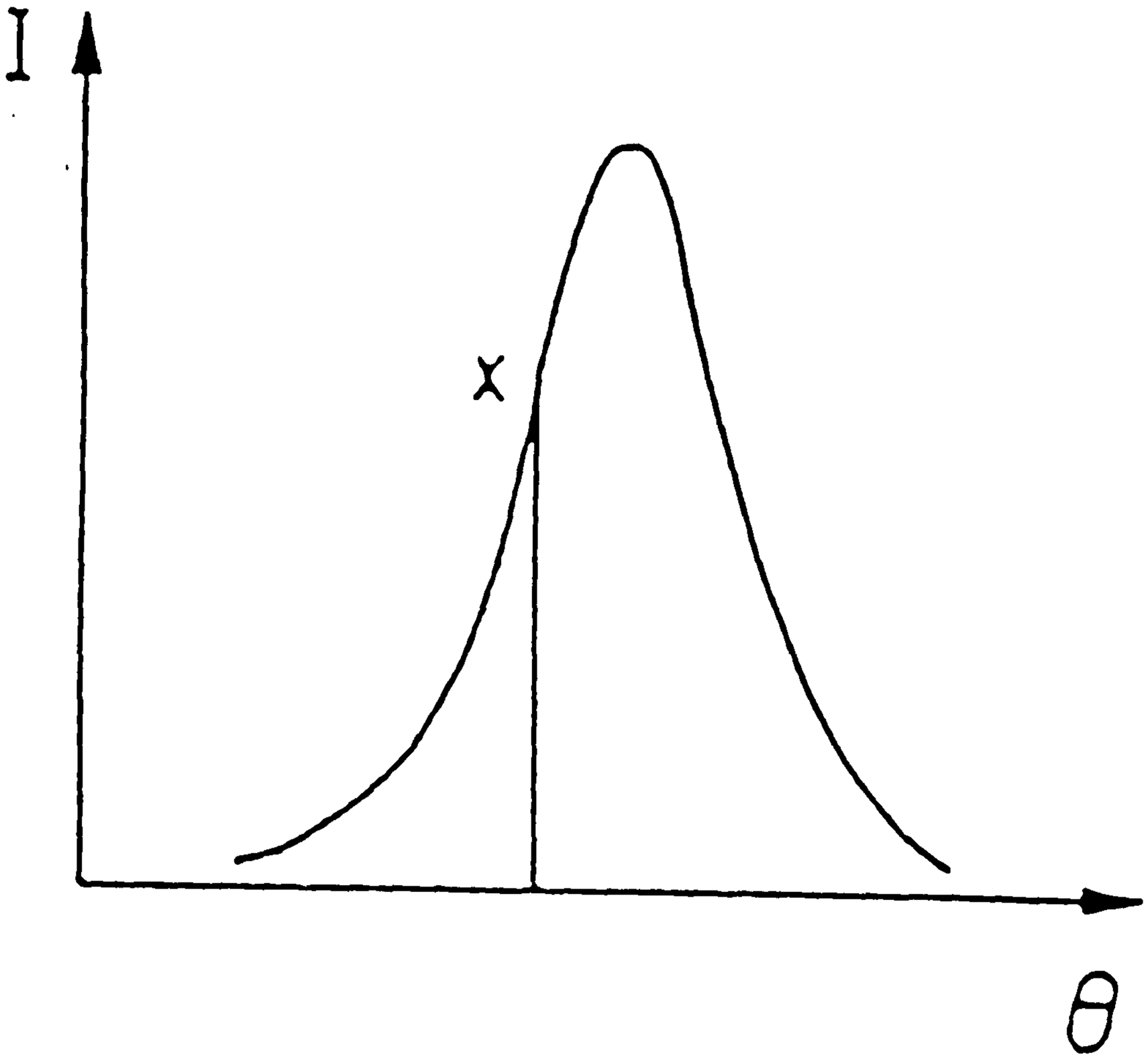

Fig. 2.16 Position of Maximum Strain Sensitivity on a Rocking Curve

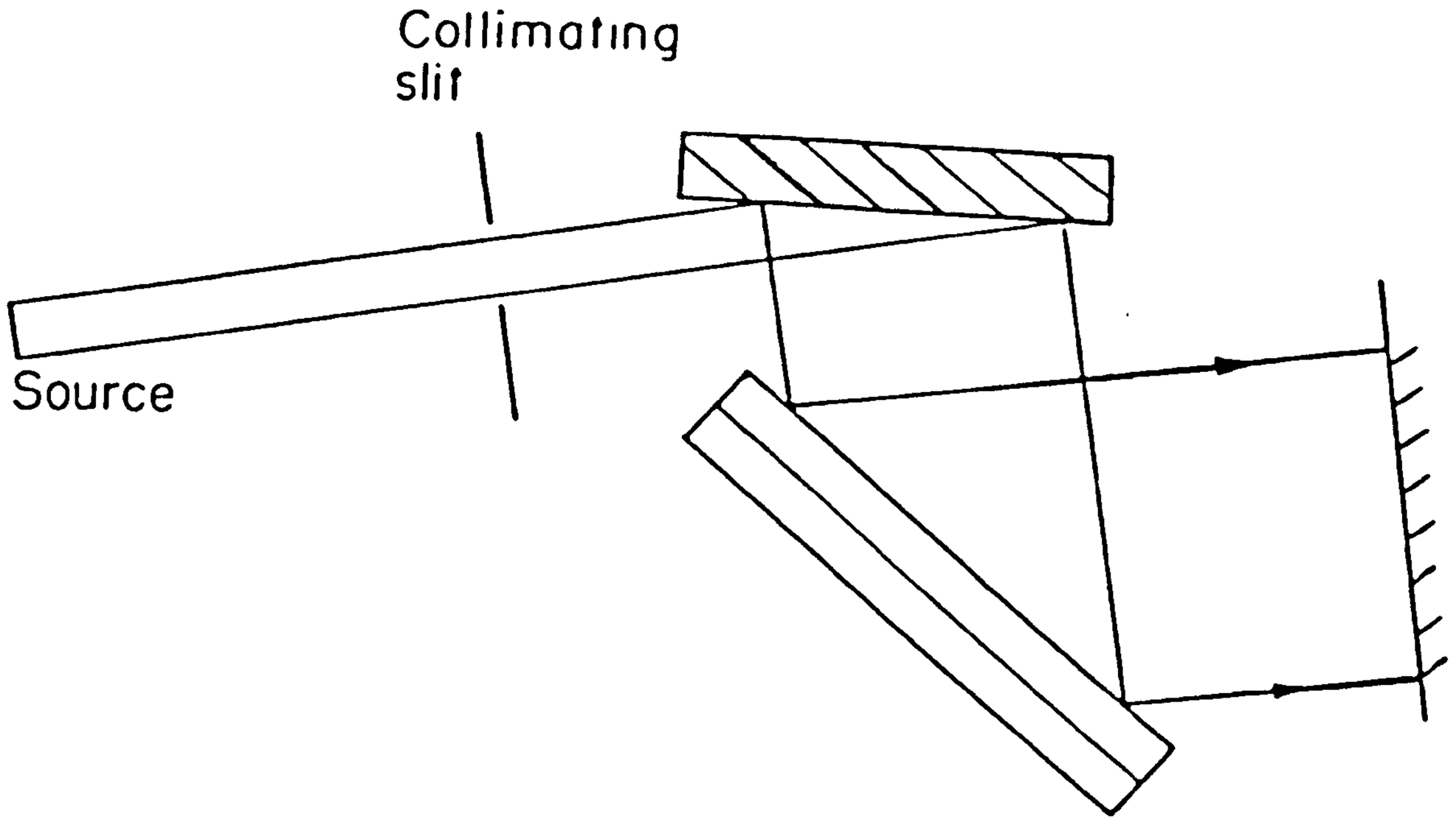

Fig. 2.17 (+ -) Parallel Setting with Asymmetric Reflection Planes (From Ref. 125)

the position at which simultaneous diffraction will occur. The angular range over which this occurs is very narrow in the (+ -) configuration and can be in the order of tenths of seconds of arc. This is in comparison with the 1-10 seconds angular range typical of a conventional Lang diffraction set-up. If there is local misorientation or distortion of the sample crystal lattice, misplacement of the two diffraction curves occurs which prevents curve overlap. This results in loss of simultaneous diffraction conditions which in turn produces a local loss of diffracted beam intensity (see figs. 2.15 b-c). The very narrow angular range of double crystal diffraction means that much smaller lattice variations will produce curve misplacement, and can therefore be detected, compared with single crystal methods.

Strain sensitivity also varies with the position on a rocking curve. The relative change in intensity, $\blacktriangle I/I$, is related to the lattice distortion, $\blacktriangle d/d$, by the following formula[125],

$$\frac{\blacktriangle I}{I} = k \left(\tan \theta . \frac{\blacktriangle d}{d} \pm n_g . n_t . \blacktriangle \theta \right) \qquad (2.9)$$

k - slope of rocking curve

θ - angular position on rocking curve

I - intensity of diffracted x-rays

d - interplanar spacing

n_g - unit vector normal to incident plane

n_t - unit vector parallel to tilt axis

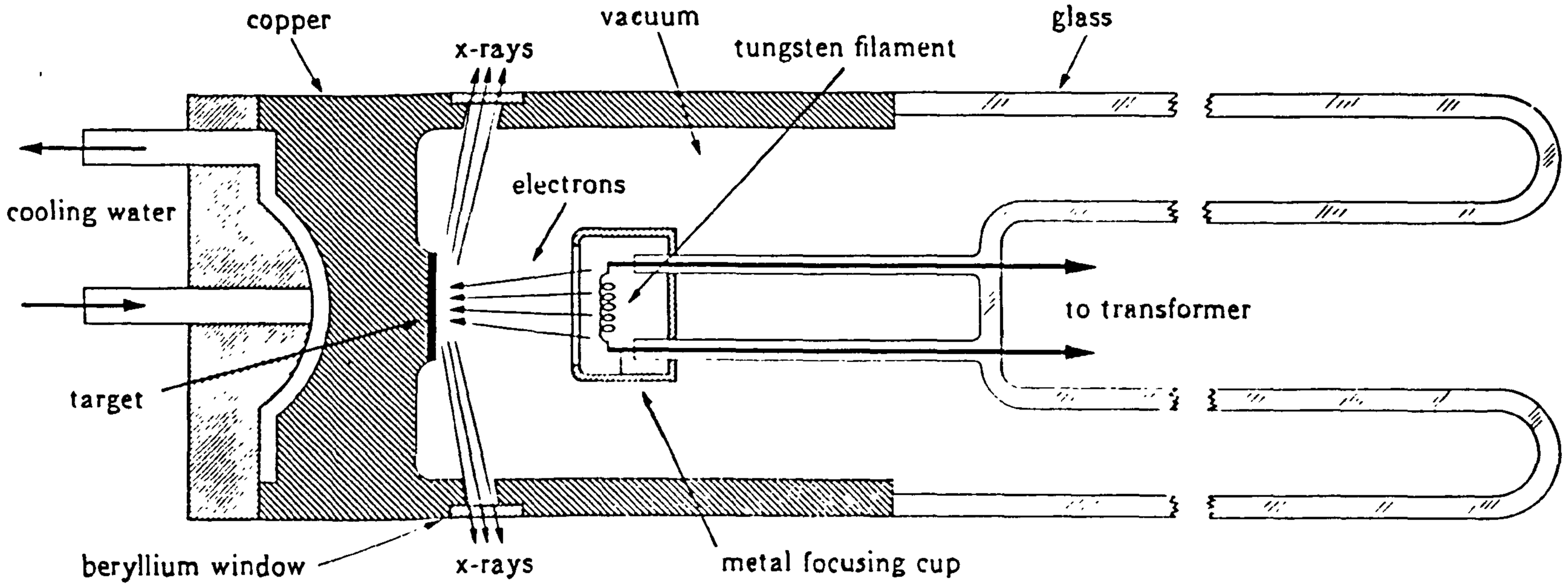

Fig. 2.18 Cross Section of a Sealed Source X-Ray Tube

(Schematic)

(From Ref.10)

Therefore the position of maximum strain sensitivity will correspond to the region of greatest slope on the rocking curve (see fig. 2.16). Another important feature of this procedure concerns the use of asymmetric reflections (see fig. 2.17). When these are utilised, the result is a widening of the beam diffracted from the sample crystal. In the case of a symmetric reflection, the dimensions of the incident x-ray will define the area of the crystal which is imaged. The widening in the asymmetric case results in a much larger area of the crystal being imaged than that corresponding to the dimensions of the x-ray beam.

2.5.4 The Production of X-Rays

X-rays are produced whenever any electrically charged particle of sufficient kinetic energy is rapidly decelerated[10]. Electrons are normally used for this purpose, the radiation being produced in an x-ray tube (see fig. 2.18). This device is essentially an evacuated glass tube which contains a source of electrons and two electrodes. A high electric potential is maintained across the electrodes which rapidly draws electrons to the anode, or target, which they strike at very high velocity. X-rays are produced at the point of impact and radiate in all directions. Most of the kinetic energy of the electrons is converted into heat, however approximately 1% is transformed into x-rays. The rays coming from the anode are composed of a mixture of different wavelengths. The variation of radiation intensity with

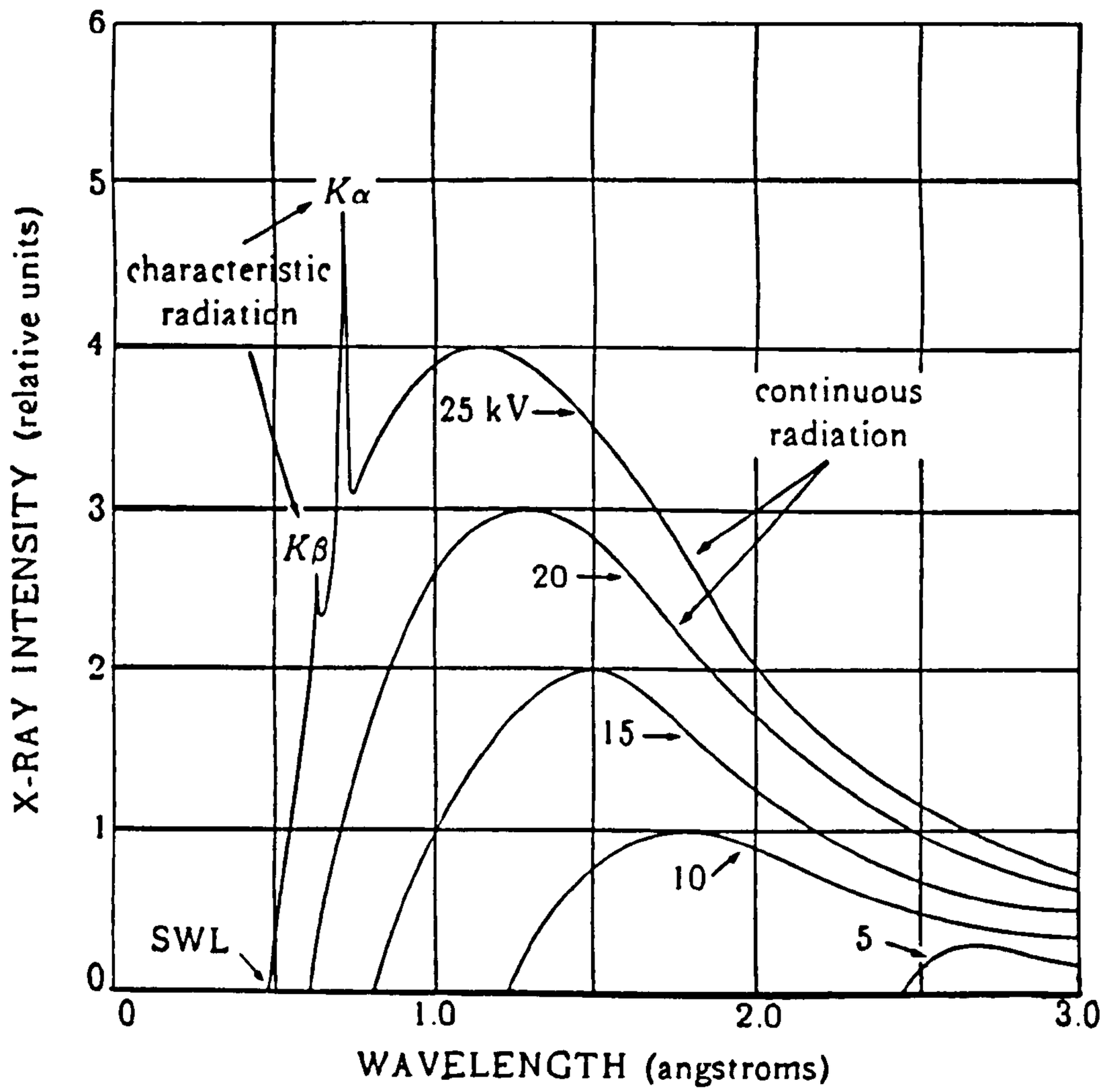

Fig. 2.19 X-Ray Spectrum Produced by a Molybdenum Sealed Source X-Ray Tube as a Function of Applied Voltage (From Ref.10)

wavelength is dependent on the voltage applied across the x-ray tube (see fig. 2.19). The intensity is zero up to a certain wavelength, known as the short wavelength limit λ_{SWL}, after which it increases rapidly to a maximum before decreasing to an unspecified minimum value. There is no sharp limit on the long wavelength side. The smooth curves on figure 2.19, correspond to the applied voltages of 20 kV or less in the case of a molybdenum target. The radiation represented by such curves is known as hetrochromatic, continuous or white radiation since, like white light, it is composed of many wavelengths of radiation. White radiation is also called bremsstrahlung after the German word for "braking radiation", because it is produced by the deceleration of electrons.

The production of a continuous spectrum is a consequence of the fact that not every electron is decelerated in the same way. Some electrons are stopped in one impact and give up all their energy at once, whereas others undergo a series of glancing collisions, successively losing fractions of their total kinetic energy until all is spent. Electrons which are stopped in a single impact will produce photons of the greatest energy, or shortest wavelength. All other types of collision will produce photons which possess only a fraction of the energy of the single impact electrons. The sum of all the different wavelengths of radiation constitutes the continuous spectrum. The short wavelength limit, λ_{SWL}, therefore corresponds to the highest energy of photon which can be produced at a given applied tube voltage.

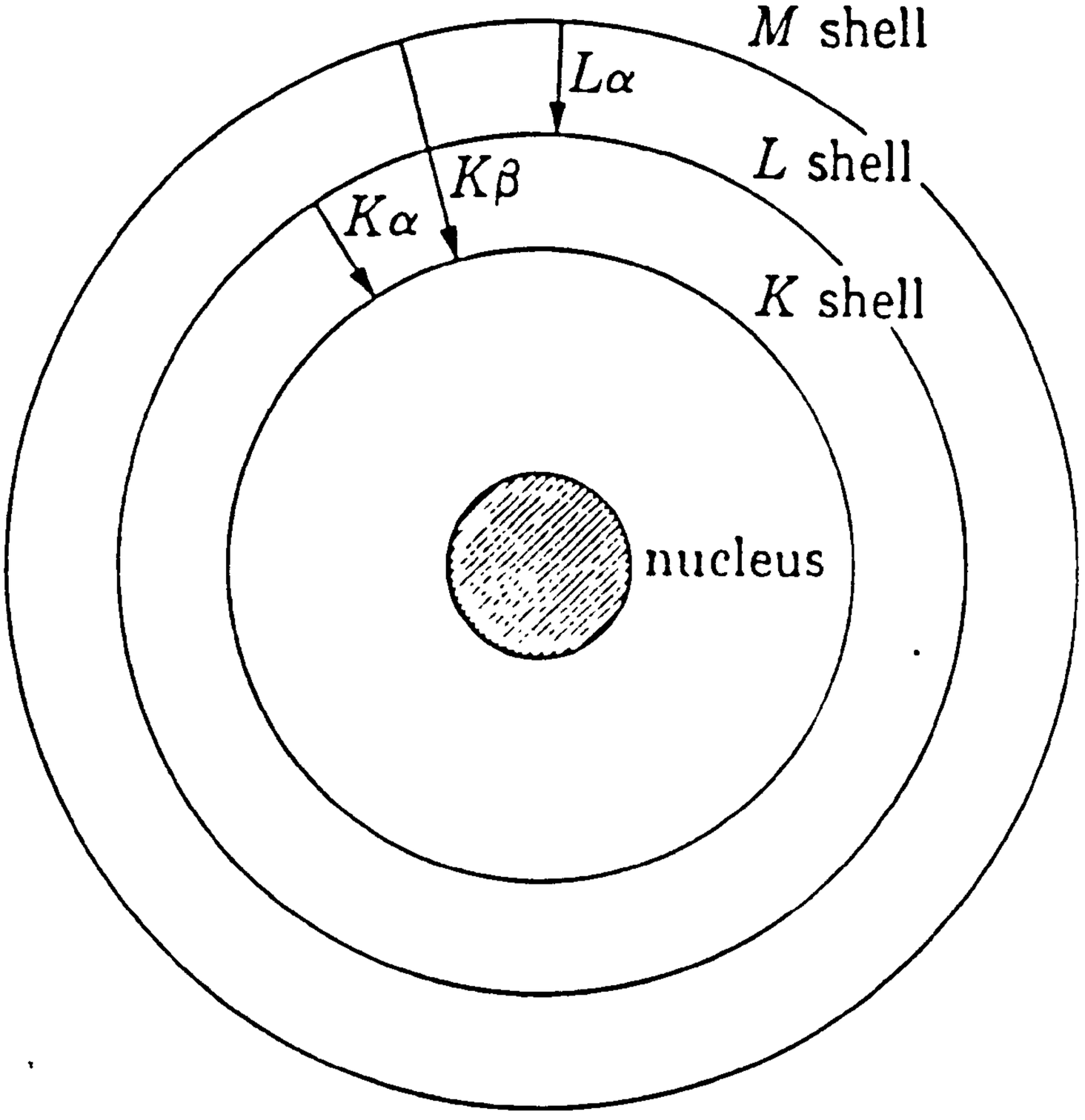

Fig. 2.20 Electronic Transitions in an Atom (Schematic)

(From Ref.10)

When the voltage on an x-ray tube is increased above a certain critical value, sharp intensity maxima appear at certain wavelengths, characteristic of the target metal, superimposed on the continuous spectrum (see fig. 2.19). These features are known as characteristic lines and fall into several sets, referred to as K, L, M and so on in order of increasing wavelength. Usually only the K lines are useful in x-ray diffraction methods because the longer wavelength lines are too easily absorbed. Characteristic radiation is produced not by the deceleration of electrons but by relaxation of electrons in excited energy levels within the atoms of the target material. To understand the process, it is necessary to consider an atom as consisting of a central nucleus surrounded by electrons lying in various defined orbitals or shells. The principal quantum numbers 1, 2, 3 ... etc. are denoted by the designation K, L and M etc. (see fig. 2.20). When an electron colliding with a target atom has sufficient energy, it can knock an electron out of one of these quantised shells to leave the atom in an excited state. Characteristic radiation is produced by the relaxation of the excited state by the movement of an outer electron into the vacancy, which emits radiation of a wavelength specific to both the element which composes the target and to the difference between the original and the final energy levels.

However an x-ray tube is not an ideal x-ray source for Lang diffraction topography. As there are a limited number of elements which are suitable target materials, the wavelength

range of radiation which can be produced using an x-ray tube is limited.

An additional disadvantage concerns the intensity of x-rays which can be produced by x-ray tubes. Diffraction images are recorded on photographic emulsions which darken on exposure to x-rays. The darkening is proportional to the intensity of the radiation which passes through the emulsion. In the case of an x-ray tube, this process is slow and high quality images can require exposure times in the order of several days. These lengthy exposures are undesirable when considering the fact that typical diffraction experiments can require dozens of topographs in order to obtain the necessary information. The reduction of exposure times requires the use of more intense x-rays which can be produced by increasing the tube voltage. However, as most of the energy of the colliding electrons is converted to heat, the energy of electrons which can be used is limited to the melting point of the target. Elaborate cooling methods, such as the use of a rotating anode to limit the time any part of the target is subjected to electron bombardment, can increase the current that can be applied across an x-ray tube and so produce a corresponding increase in radiation intensity. However, the melting point of the target is always a physical limitation to the intensity of the x-rays which can be produced.

An x-ray source which is not limited in terms of radiation wavelength range or of target melting point is a synchrotron radiation source or SRS[132,133]. Synchrotron

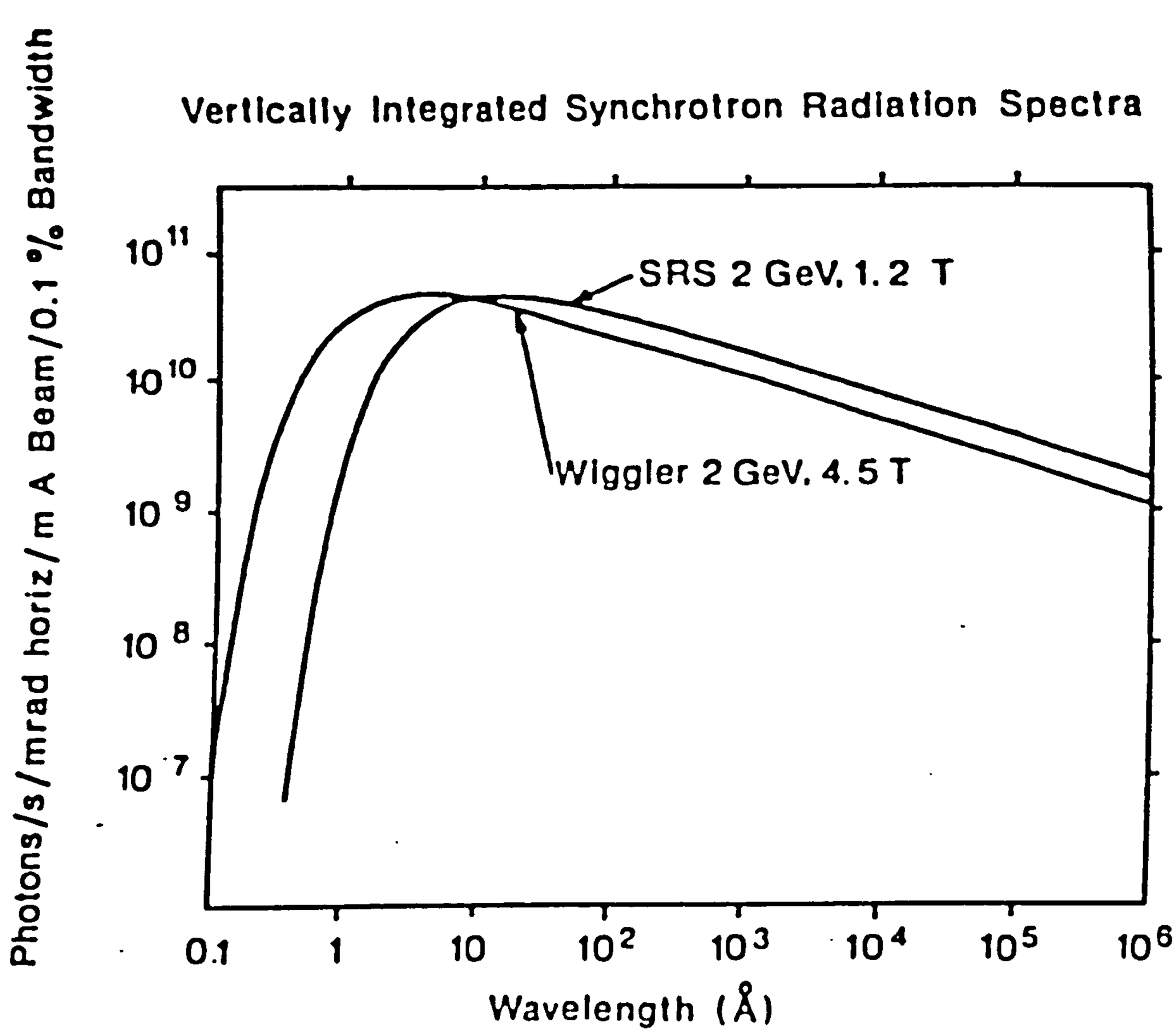

Fig. 2.21 Electromagnetic Spectrum of the Synchrotron Radiation Source at Daresbury (From Ref. 134)

radiation is generated by the radial acceleration of electrons using powerful magnets to confine their orbit to a circular arc[134]. According to classical physics, any charged particle which is accelerated will emit radiation and as acceleration is a vector quantity, the constrainment of the electron path to a circular orbit will result in the emission of radiation. The wavelength of this emitted radiation will depend upon the kinetic energy, K, of accelerated electrons and the strength, B, of the magnetic field through which they pass. The intensity of this radiation is proportional to the current produced for a given set of E and B values[132,134]. The electromagnetic spectrum of the SRS used in this project is shown in figure 2.21. This spectrum shows the SRS to produce radiation which is both several orders of magnitude more intense than an x-ray tube[133,134] and is of a wavelength range which covers a large proportion of the x-ray region of the electromagnetic spectrum[134]. One of the many applications for this powerful source is that of x-ray diffraction topography. Since no target is used in the generation of x-rays, no characteristic radiation is produced and so the SRS is effectively a white radiation source of tremendous intensity. Exposure times required to obtain diffraction images the SRS are reduced by several orders of magnitude with respect to a conventional x-ray source.

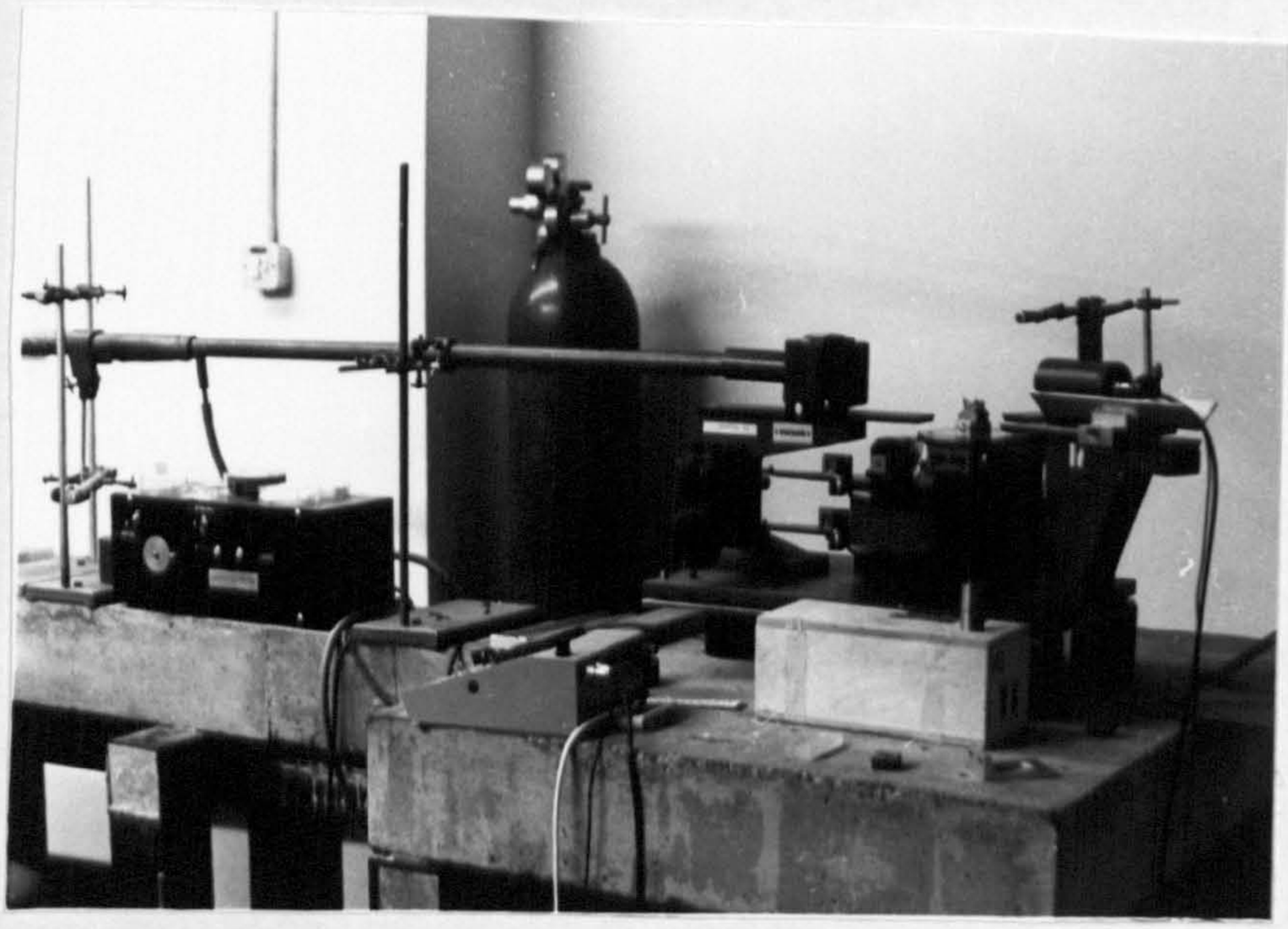

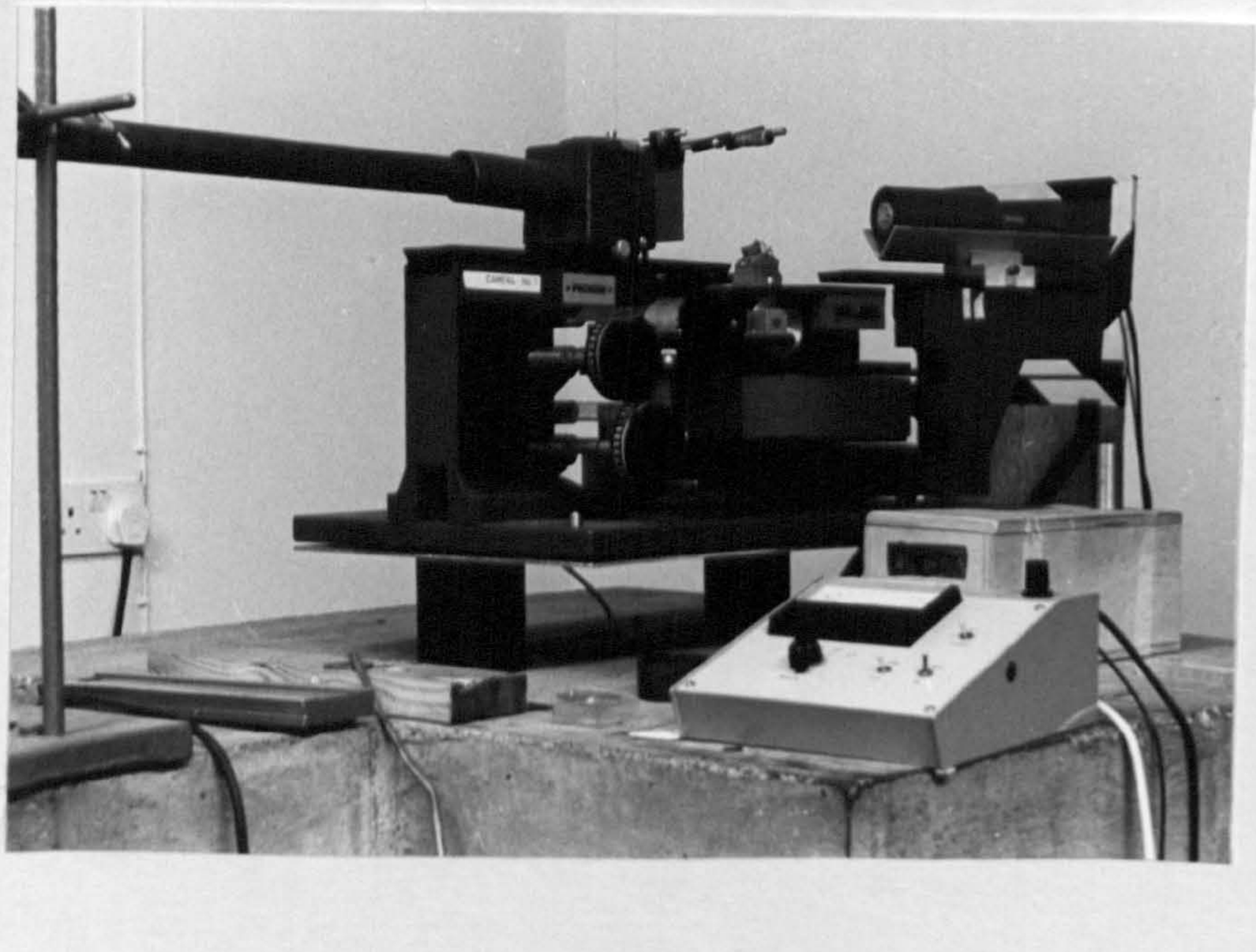

Fig. 2.22 Lang Camera Commercially Built by Picker

2.5.5 Recording X-Ray Diffraction Topographs

i) Conventional Lang Topography Procedure

Transmission Lang topographs were obtained at Strathclyde University using a Lang camera commercially built by Picker with a molybdenum target sealed beam x-ray tube as the x-ray source (see fig. 2.22). The main components of the camera were a collimator, two sets of vertical slits, two rotary stages and a traverse mechanism (see fig. 2.23). The x-ray tube was essentially a point source and as such, the x-rays produced by it were not parallel and diverged with distance form the source. Near parallel x-rays are required for Lang topography, otherwise resolution of the diffraction image is reduced. To collimate means, literally, to render parallel, and so a collimator is a used to produce a parallel x-ray beam. The effectiveness of this approach is limited by the length of the collimator, which is restricted by the dimensions of the room in which the camera occupies. The collimator used with the Picker camera was 1.4 m long and lead shielded. The collimator exit slits had dimensions of 3 cm in the vertical and 0.05 cm in the horizontal. As the reflection planes of sample crystals were always aligned vertically, the divergence of x-rays in the horizontal plane was less important. A consequence of the narrow x-ray beam was that to image a complete crystal required it to be continually moved through the x-ray beam. This was accomplished using a reciprocating stage which moved the crystal back and forth through the x-ray beam (see fig. 2.23b).

Fig. 2.23 Schematic Diagram of the Picker Lang Camera

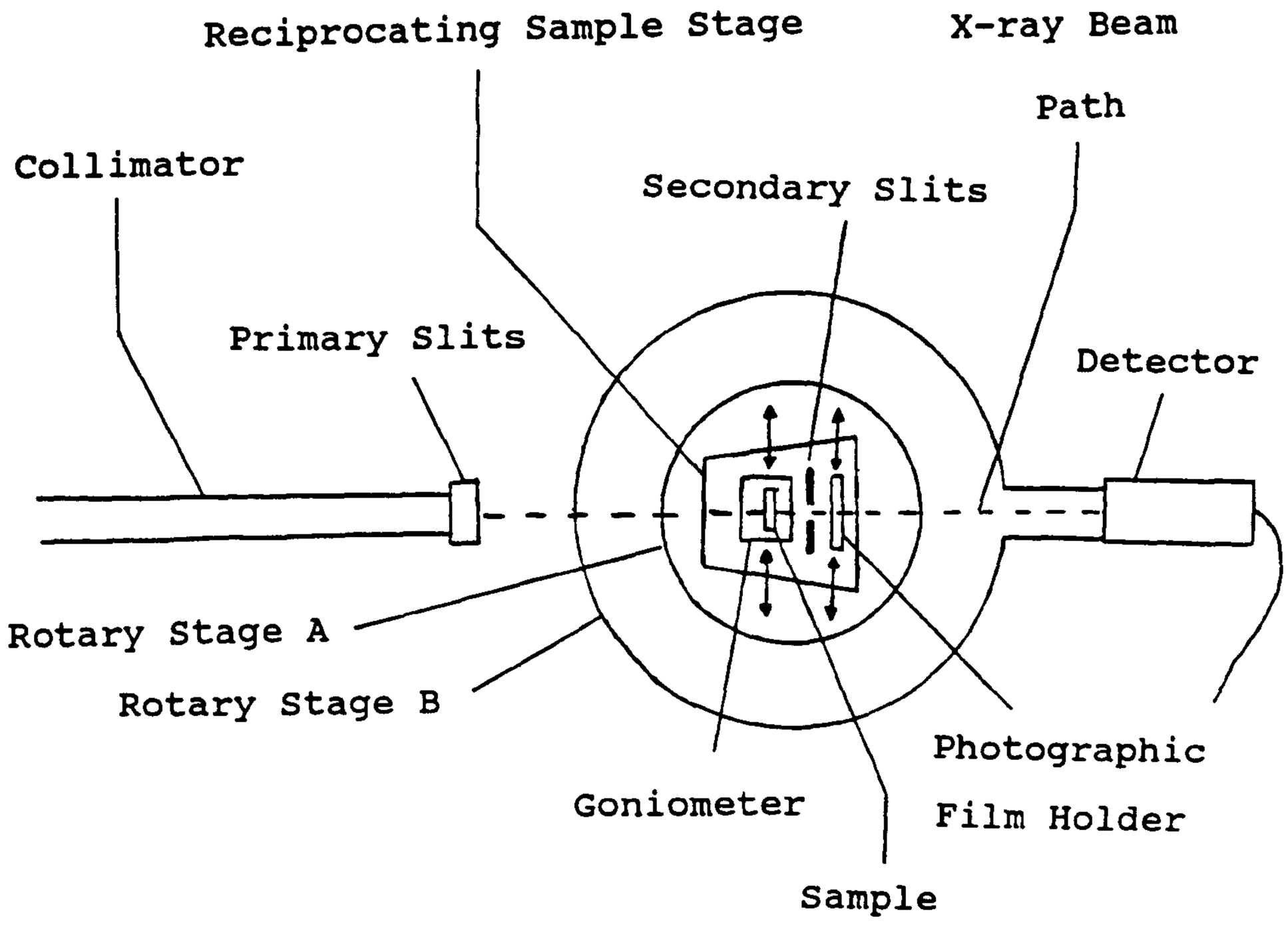

a) Initial Set-Up Position

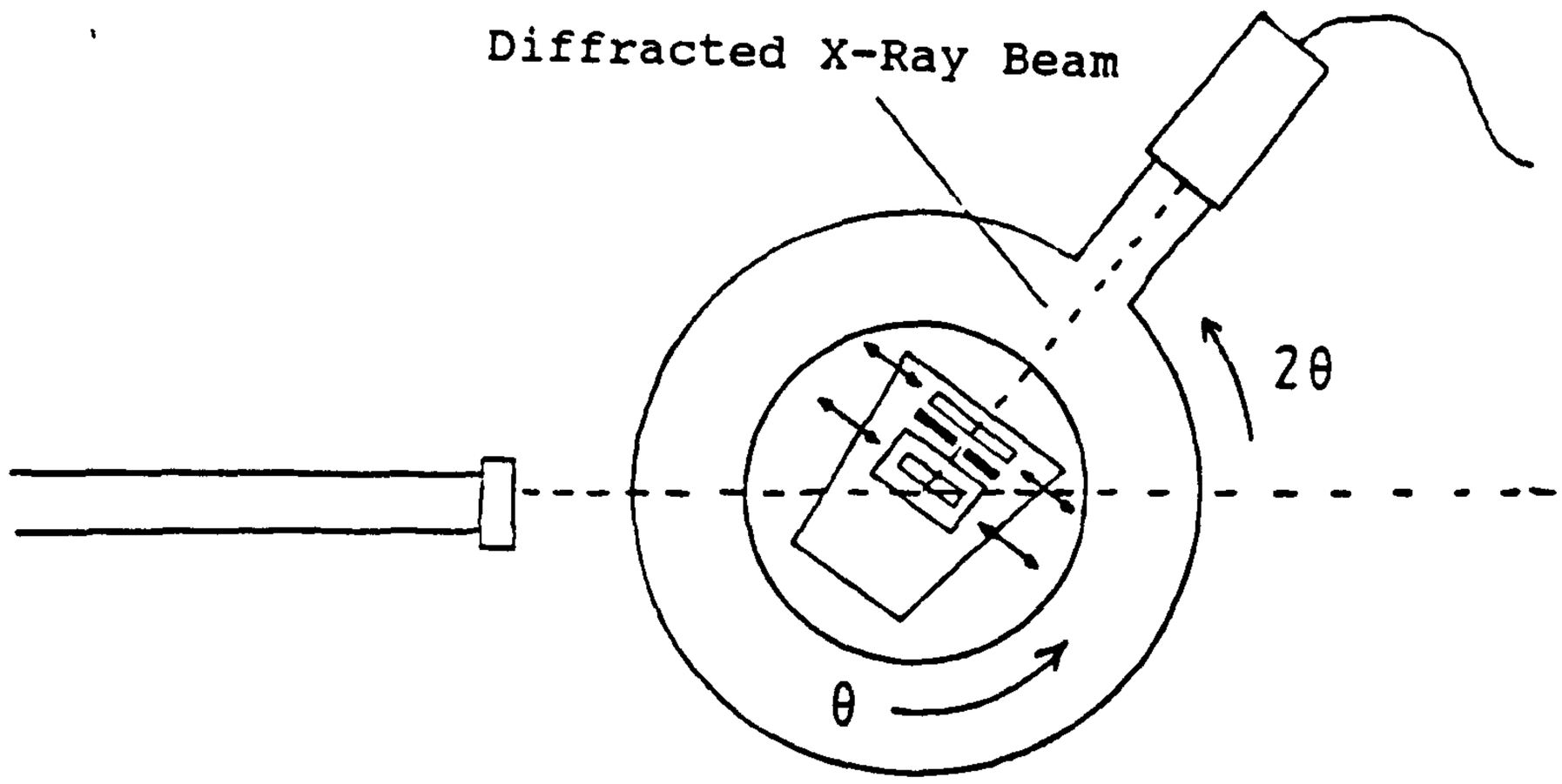

b) Diffraction Set-Up Position

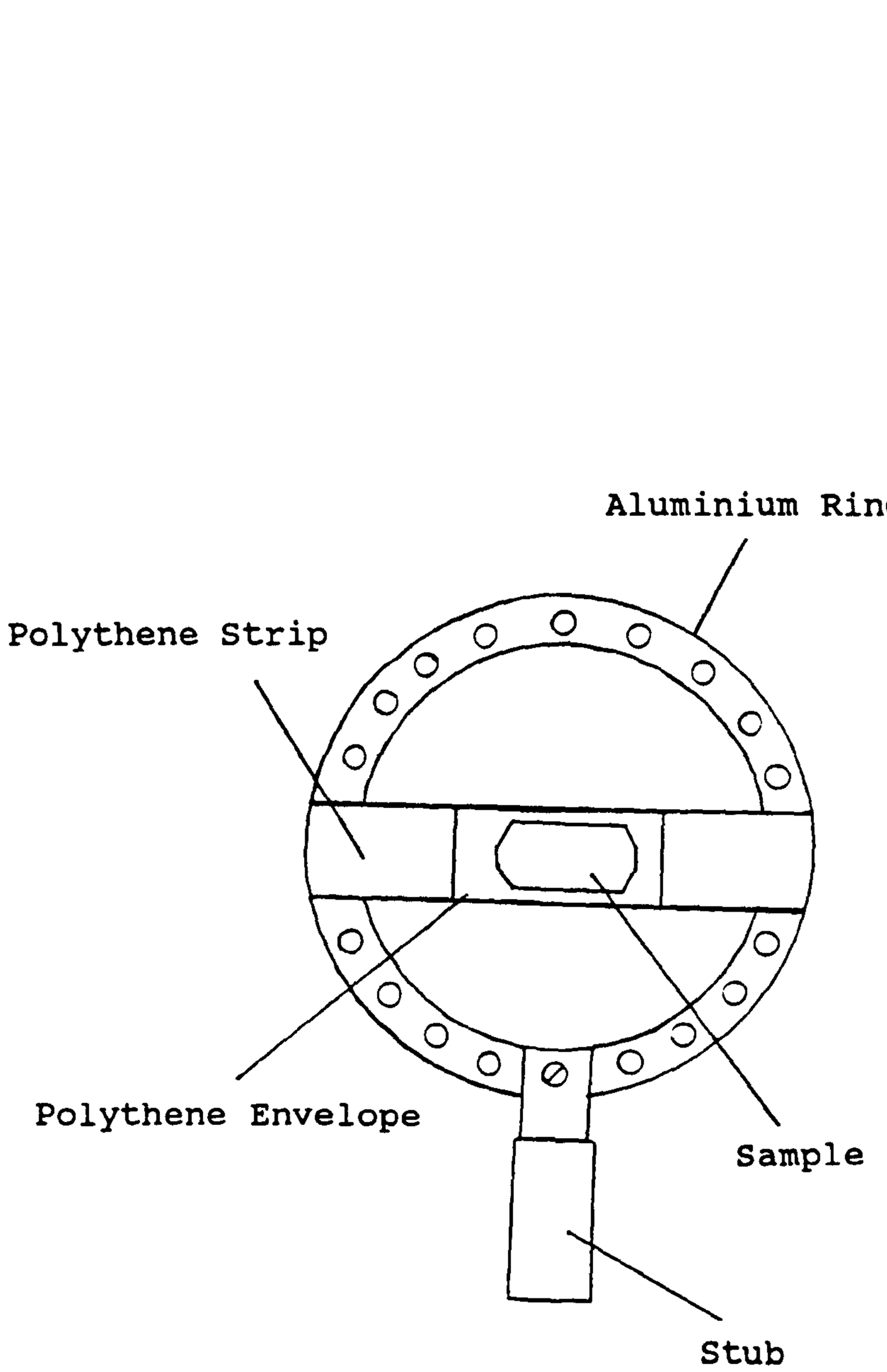

Fig. 2.24 Sample Mounting

The procedure for the obtaining Lang topographs was as follows,

1. A sample crystal was placed in a polythene envelope which was then stretched across an circular aluminium ring and attached securely with adhesive tape. The ring was then bolted to an aluminium stub (see fig. 2.24).

2. The mounted sample was then clamped onto the goniometer such that the desired reflection planes were vertical and parallel to the main x-ray beam. Orientation to approximately $\pm 1^{\circ}$ was achieved using an adjustable set square and adjusting the goniometer using a known cut crystal face as a reference. The slice plane as adjusted to be normal or perpendicular to the x-ray beam.

3. The position of the x-ray beam with respect to the sample slice was found using a fluorescent screen. The sample was then moved using the reciprocating stage until the beam passed through the centre of the crystal.

4. The scintillation counter detector was covered with a 5mm thick aluminium filter and moved, using rotary stage B, through the x-ray beam until a maximum reading was obtained. This indicated the zero position of the detector and ensured that the beam, sample and detector were in line (see fig. 2.23a). The filter was necessary to protect the detector form damage caused by exposure to the full strength of the x-ray beam.

5. The aluminium filter was then removed and the detector moved to an angle of 2θ with respect to the x-ray beam (see fig. 2.23b).

6. The sample crystal was then rotated about its vertical axis by the Bragg Angle, θ, using rotary stage A (see fig.2.23b).

7. The crystal was rotated slowly through the Bragg angle, using the fine adjustment controls on rotary stage A, until a peak was observed on the ratemeter.

8. The traverse limits of the reciprocating stage were set by scanning the crystal through the x-ray beam and noting where the diffracted intensity dropped to background level.

9. The sample slits were then positioned perpendicular to the diffracted beam and closed down to allow only the diffracted beam to pass. This was a precaution to prevent unwanted darkening of the photographic film by scattered radiation and exposure to the incident x-ray beam.

10. The film holder was then loaded with the required type of photographic film and positioned parallel with the sample slit. The sample, sample slit and film holder were positioned as close as possible to each other to minimise the effects of the divergence of the diffracted x-ray beam.

11. The traverse motor was then activated and a topograph was recorded.

ii) Processing and Enlargement of Topographs

The recording medium used for all topographs in this study was Agfa x-ray photographic film. Exposure times for quartz topographs were in the order of 1-7 days depending on the type of photographic film which was used (see table 2.4). The higher the resolution of film which was used, the longer was the exposure time necessary to obtain a topograph. The procedure used to process the photographic films is given in table 2.5.

The diffraction image obtained from a crystal was an unmagnified projection and so enlargement had to be achieved photographically. By convention, x-ray topographs are presented as they appear on the x-ray film. Therefore to obtain an enlarged image required an internegative to be made, followed by enlargement to a positive print. Negatives of diffraction images were recorded on fine grain 35 mm Kodak Panatomic-X photographic film using an Olympus PMT-35 photomacrography system fitted with an Olympus OM-2 automatic camera. The topographs were photographed using transmitted light at a magnification such that the 35mm frame was almost filled. The resulting negatives were processed following the procedures listed in table 2.6. The enlarged positive prints of the topographs were obtained using a Leitz Valoy 35 mm enlarger.

Table 2.4 Exposure Times of X-Ray Photographic Films

Film Type	Exposure Time[a] (hrs.)	Relative Exposure[b]
Agfa Osray M3	24	1
Agfa Structurix D7	48	2
Agfa Structurix D4	96	4
Agfa Structurix D2	192	8

a - Minimum time necessary to obtain a topograph using an Mo x-ray tube source

b - Minimum exposure time relative to M3 photographic film

Table 2.5 Processing of X-Ray Photographic Films

Process	Time (mins)
Develop (Undiluted D19 developer)	5 to 10
Fix (Kodafix diluted 1+3 of distilled water)	10 to 20
Wash (Running tap water)	60
Dry (Air)	Overnight

Table 2.6 Processing of Kodak Panatomic-X

Process (at 21°C)	Time (Mins)
Develop (D76 developer diluted 1+1 distilled water)	7
Stop (1% solution of glacial acetic acid)	1
Fix (Kodafix diluted 1+3 of distilled water)	4
Wash (Running tap water)	30

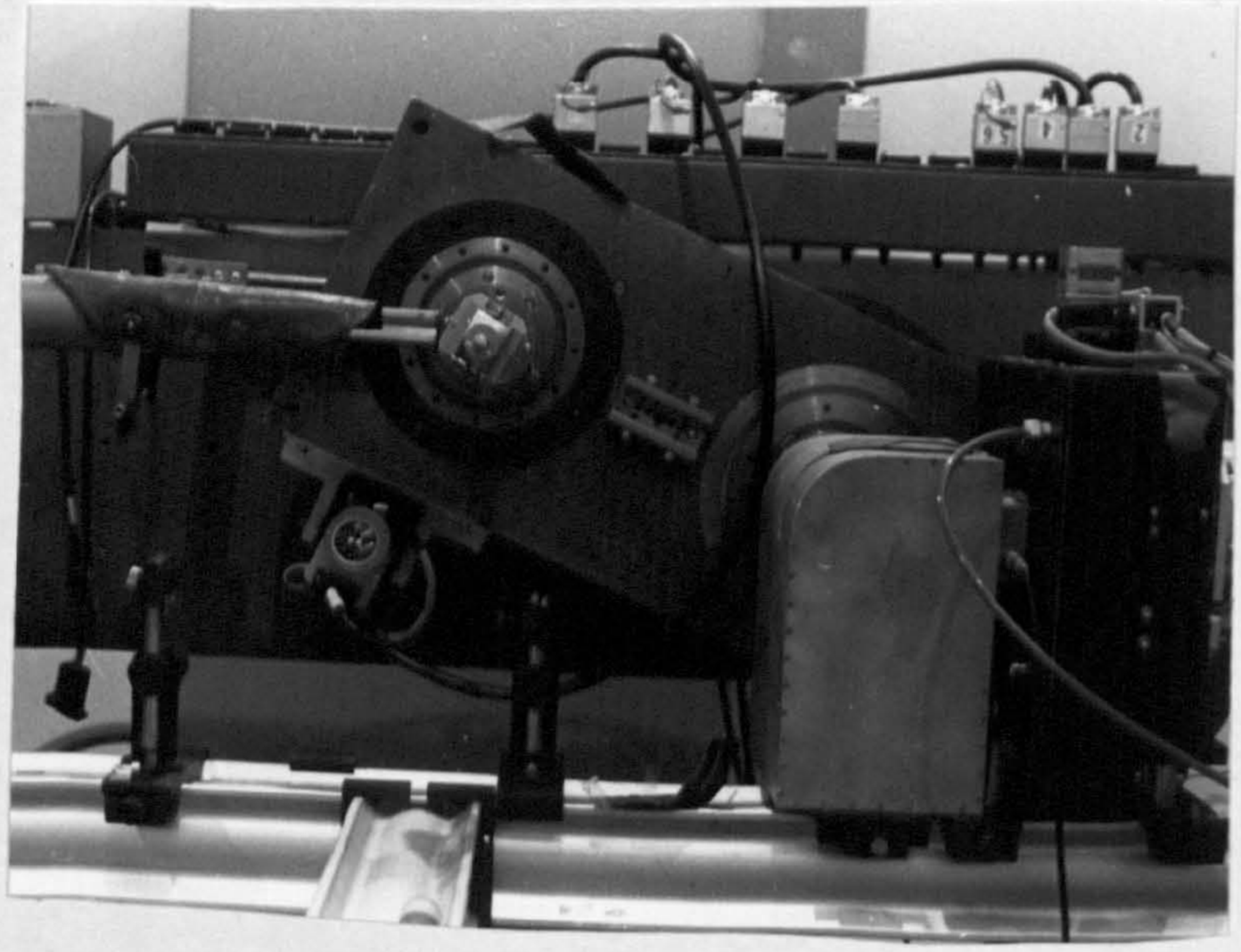

Fig. 2.25 Double Crystal Camera at Daresbury

iii) Double Crystal Diffraction Topography Procedure

Double crystal topographic studies were carried out using the synchrotron radiation source, SRS, at Daresbury Laboratory. The effective collimator length at Daresbury is 80 m and so the divergence of the x-ray beam was insignificant and did not affect the resolution of diffraction images. The camera which was used is shown in figures 2.25, 2.26 and 2.28. This experimental set-up corresponded to most strain sensitive (+ -) parallel crystal configuration. For maximum strain sensitivity, the reflection planes of the sample and the monochromator crystals must be both parallel and have equivalent interplanar spacings. This is normally accomplished by the use of a monochromator crystal fashioned from the same material as the sample to be analysed and being of an identical crystal cut. However, because no quartz monochromator was available, a silicon crystal was used in its place. It was therefore necessary to choose a set of diffraction planes which would provide the match between the two crystals with the least error. Differences in the interplanar spacings of reflection planes increase the rocking curve width of the reflection and reduce the strain sensitivity of the technique. These losses were compensated for by the use of high order reflections and diffraction planes with low structure factors[125] (see section 2.5bi and table 2.7).

The mounting procedure detailed in the previous section was found to allow movement of the sample as it was rotated

Fig. 2.26 Schematic Diagram of the Double Crystal Camera

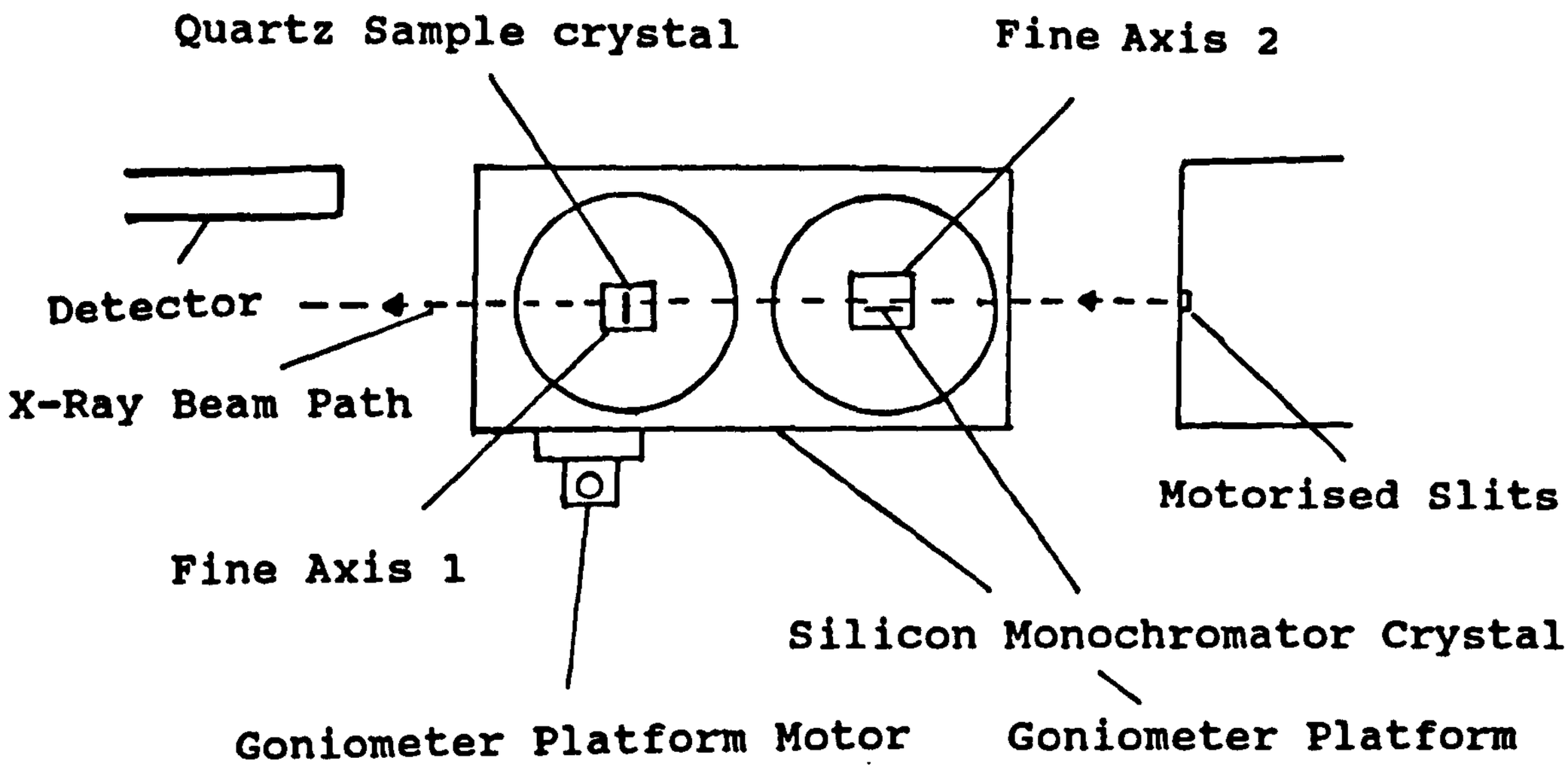

a) Initial Set-Up Position

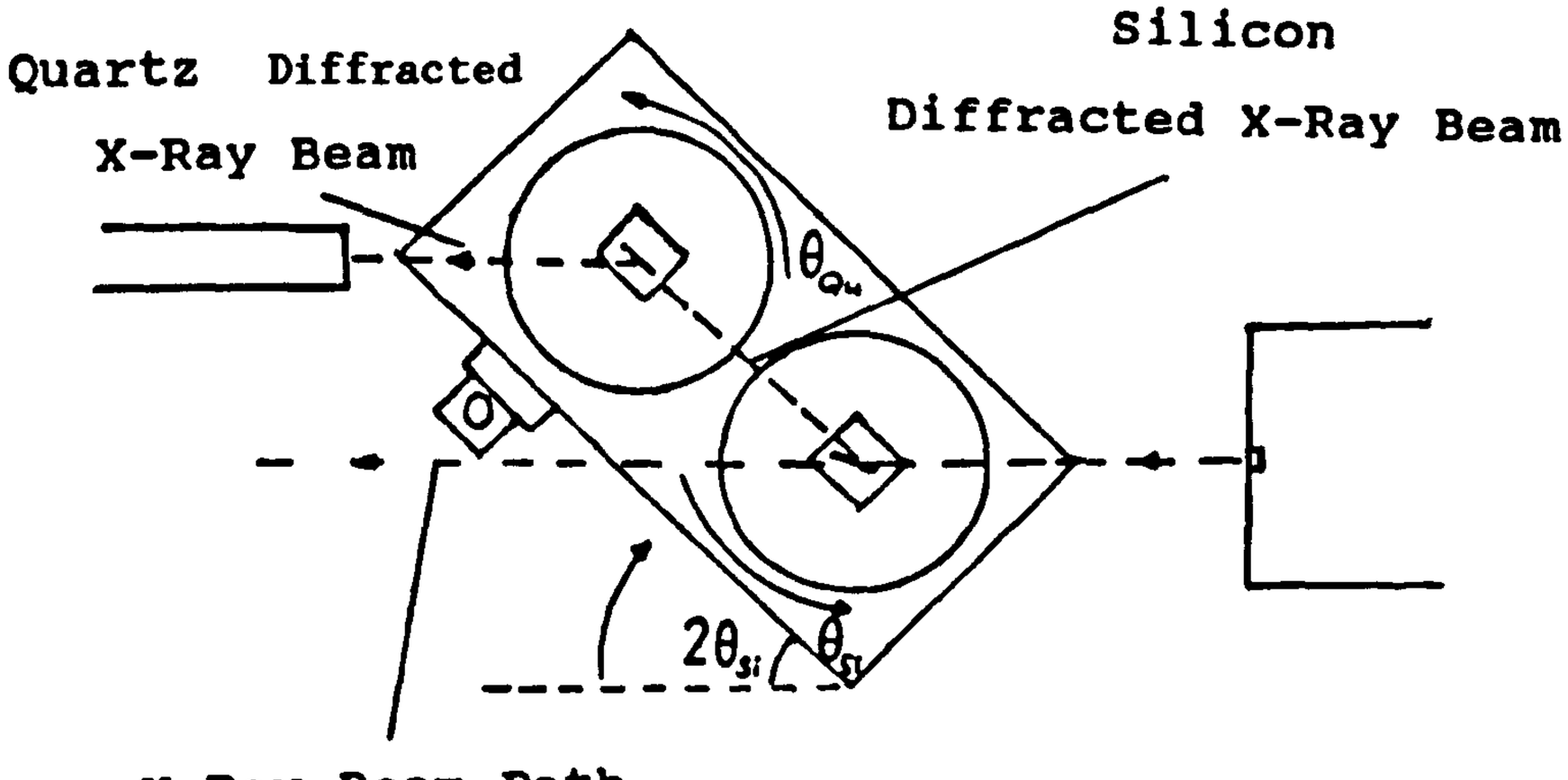

b) Diffraction Set-Up Position

Table 2.7 Errors Associated with Double Crystal Reflection Planes

Quartz Reflection Plane	Silicon Reflection Plane	d_{Qu} (Å)	d_{Si} (Å)	% Error
(02.-3)	(400)	1.375	1.358	1.24
(2-1.3)	(400)	1.453	1.358	6.99
(03.0)	(400)	1.418	1.358	4.42

Fig. 2.27 Theoretica Laue Diffraction Patterns

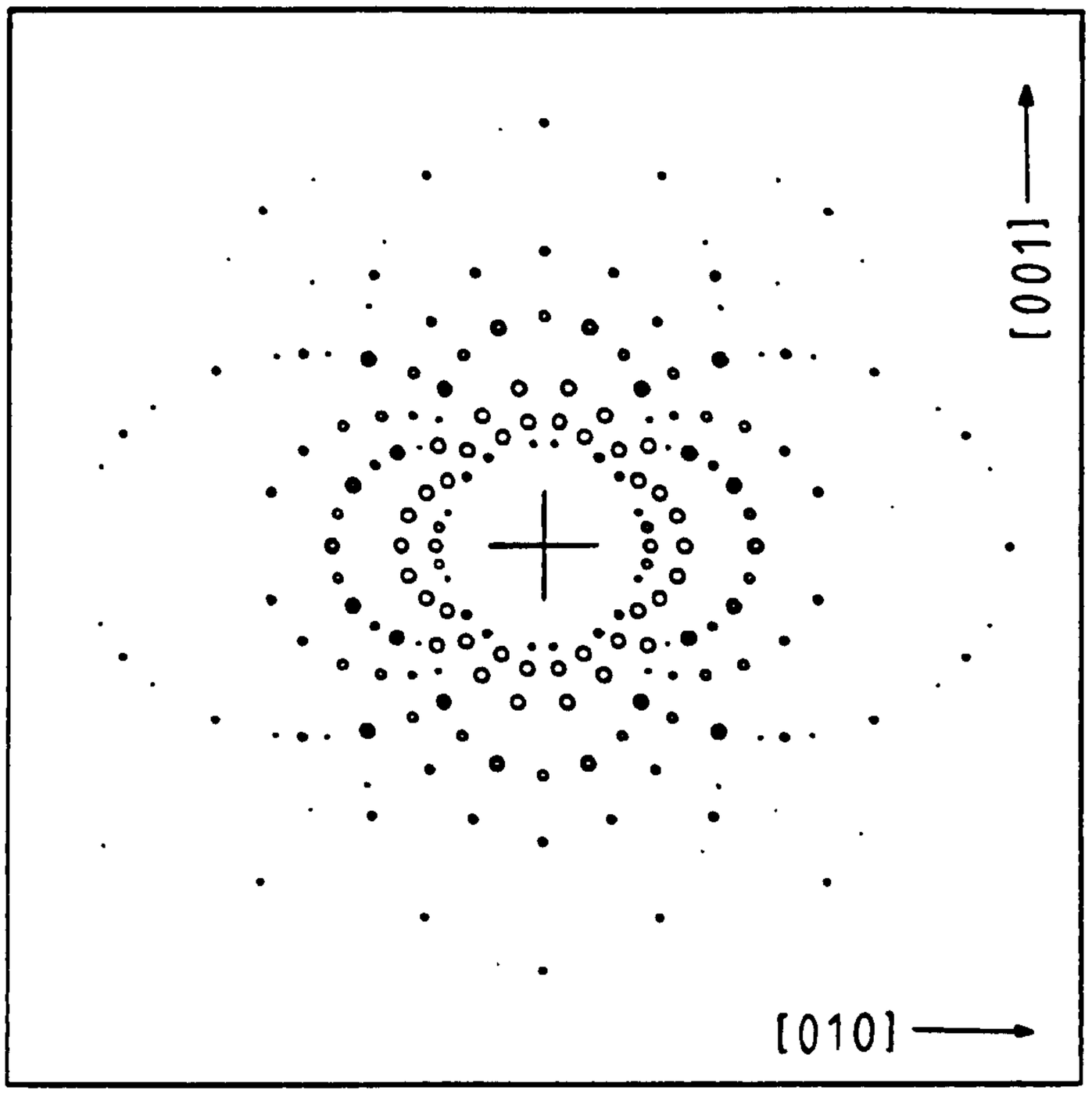

a) X-Slice Quartz Sample

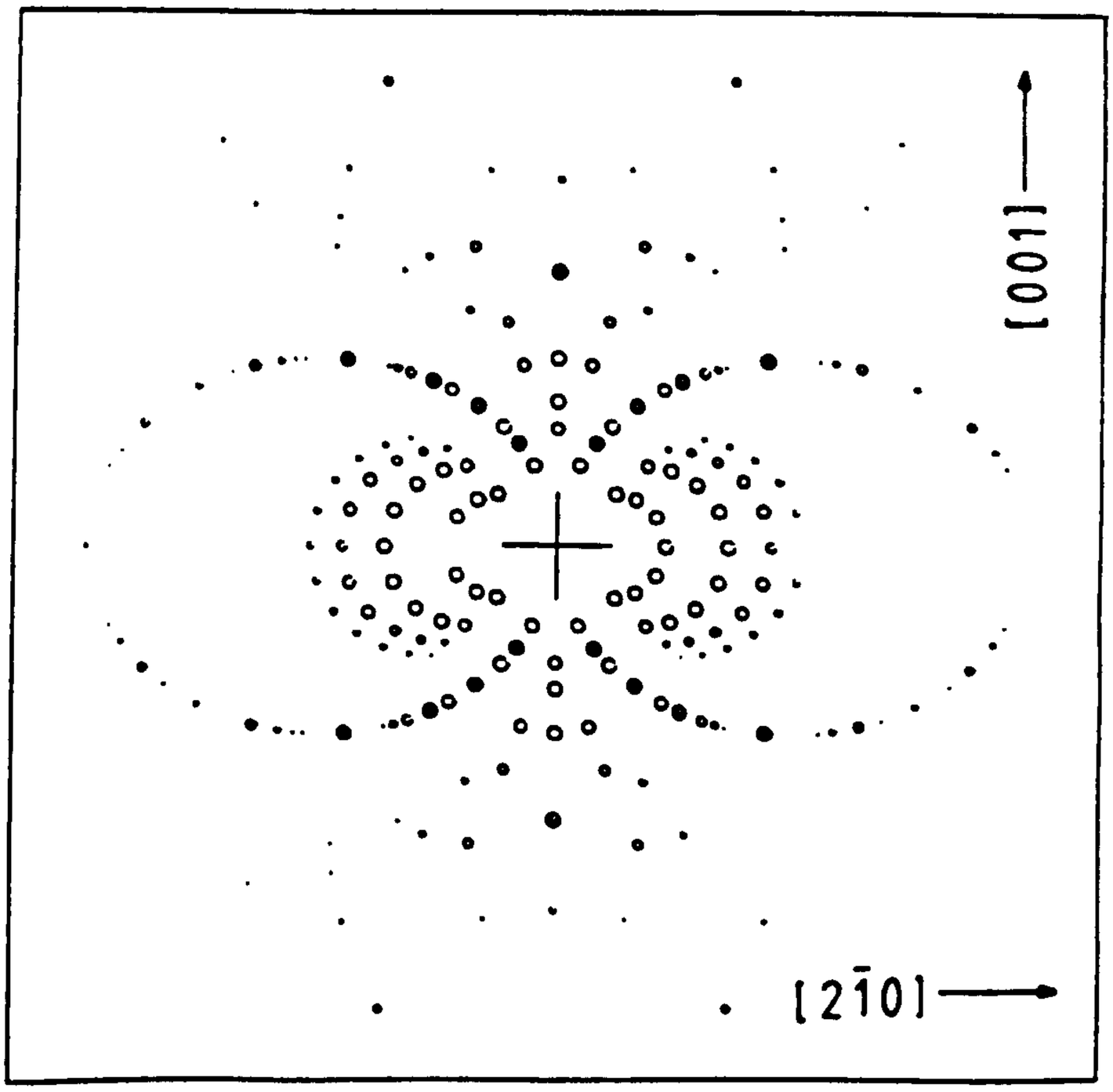

b) Y-Slice Quartz Sample

through the Bragg condition which lead to a loss of the diffracted x-ray beam. Sample crystals were therefore attached directly onto an aluminium stub using a hard mounting wax which was then was secured onto a goniometer as before.

The Procedure for the obtaining double crystal topographs was as follows,

1. A mounted sample crystal was clamped onto the goniometer, which was attached to the FINEAXIS1 motor, such that the slice plane was normal to the x-ray beam. A He/Ne reference laser was used to position the crystal with respect to the x-ray beam path. The laser was aligned along the centre of the x-ray beam path (see fig. 2.26a). The sample slice plane was orientated normal to the x-ray beam by adjusting the goniometer. A known cut crystal face was used as a reference.

2. The silicon monochromator was clamped onto the goniometer which was attached to the FINEAXIS2 motor such that the x-ray beam would pass over (see fig. 2.26a).

3. The motorised entrance beam slits were closed down to allow only a 1mm x 1mm cross sectional x-ray beam to pass and a Laue pattern of the quartz crystal was obtained. The crystal position was adjusted using the goniometer until the experimental Laue pattern matched the theoretical pattern associated with the chosen crystal slice. The theoretical Laue pattern was simulated by the computer program LAUE, which was modified at Strathclyde University [135] (see fig. 2.27).

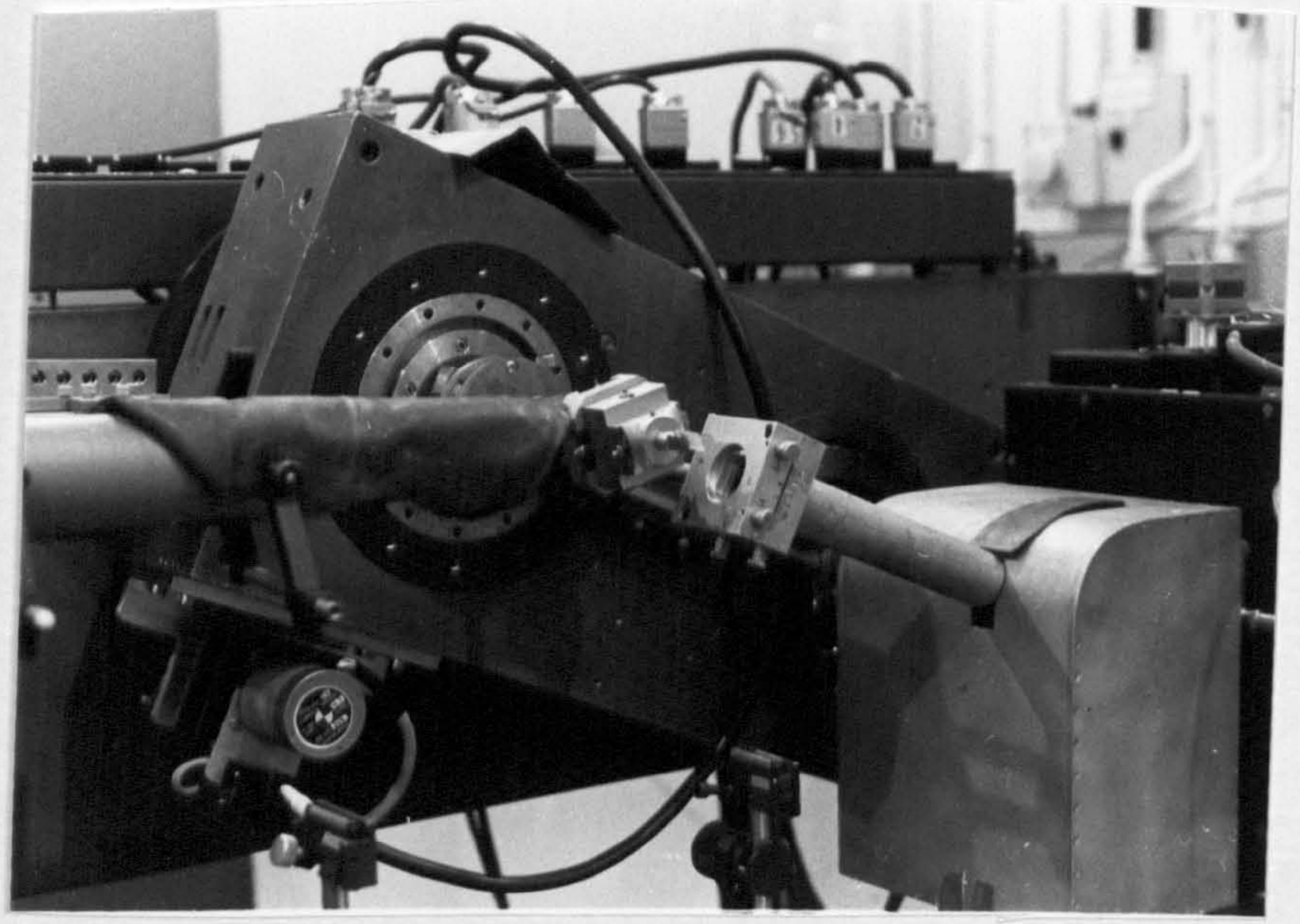

Fig.2.28 Shielding for the Prevention of Scattered Radiation

4. The silicon monochromator was then positioned normal to the x-ray beam and was aligned using the back reflection Laue method. Once the correct pattern had been obtained, the silicon crystal was moved through 90° using FINEAXIS2.

5. The goniometer stage was moved clockwise through $2\theta_{Si}$ using the goniometer motor (see fig. 2.26b).

6. The silicon crystal was moved anticlockwise through θ_{Si} using FINEAXIS2 (see fig. 2.26b).

7. The quartz crystal was moved through the angle necessary to align the chosen reflection planes to be parallel to the diffracted x-ray beam, using FINEAXIS1, and then moved anticlockwise through θ_{Qu} to meet diffraction conditions (see fig. 2.26b).

8. The Scintillation counter detector was positioned to receive the quartz diffracted x-ray beam (see fig. 2.26b).

9. The silicon monochromator was then covered in a lead shield and a set of hand adjustable slits placed between the two crystals. The slits were connected to the lead shield by an aluminium tube (see fig. 2.28). The high intensity of the SRS made unwanted film darkening by radiation scattered off camera fittings a major problem. The extra shielding was therefore essential to reduce the amount of scattered radiation which reached the recording photographic film.

10. The motorised entrance beam slits were then opened to

allow the passage of a 10mm x 10mm cross-sectional x-ray beam.

11. The hand adjustable slits were closed down to allow only the passage of the silicon diffracted x-ray beam. A Kodak fast exposure polaroid film was placed behind the slits and examined to ensure that passage of the diffracted beam was not blocked.

12. A polaroid film was placed behind the sample crystal to verify that the diffracted beam passed through the sample crystal.

13. The motorised entrance beam slits were then closed down again to a 1mm x 1mm size. The intensity of the x-ray beam when the slits were opened further overloaded the detector.

14. The sample was then rotated ± 0.5° about the Bragg angle until the diffraction peak was found. This movement was carried out automatically by a computer program which controlled the FINEAXIS1 motor.

15. A loaded film cartridge was then positioned normal to the quartz diffracted beam.

16. The quartz crystal was automatically rotated until the position of maximum strain sensitivity on the rocking curve was reached, at which point the motion was stopped.

17. The motorised entrance beam slits were then opened up again to 10mm x 10mm and a topograph was recorded.

18. After the appropriate exposure time, the photographic film was removed, processed and enlarged following the procedures discussed in the previous section. The average exposure time necessary for different types of film are given in table 2.4.

Chapters 3. and 4. Results and Discussion

Chapter 3. Infrared Spectroscopic Studies

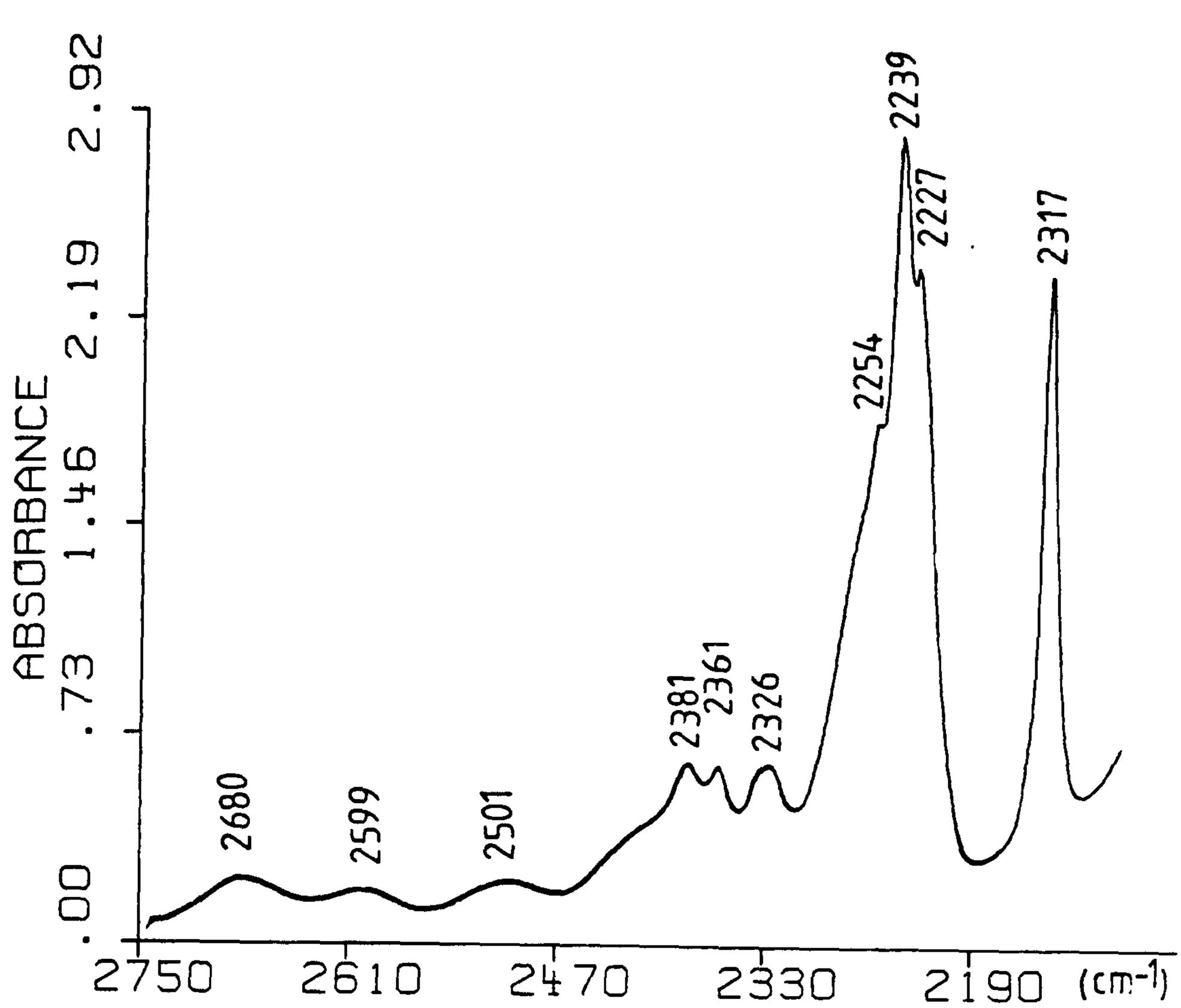

Fig. Fundamental Si-O overtone and combination absorption

3.1 bands of quartz in the 2750-2000 cm-1 infrared region

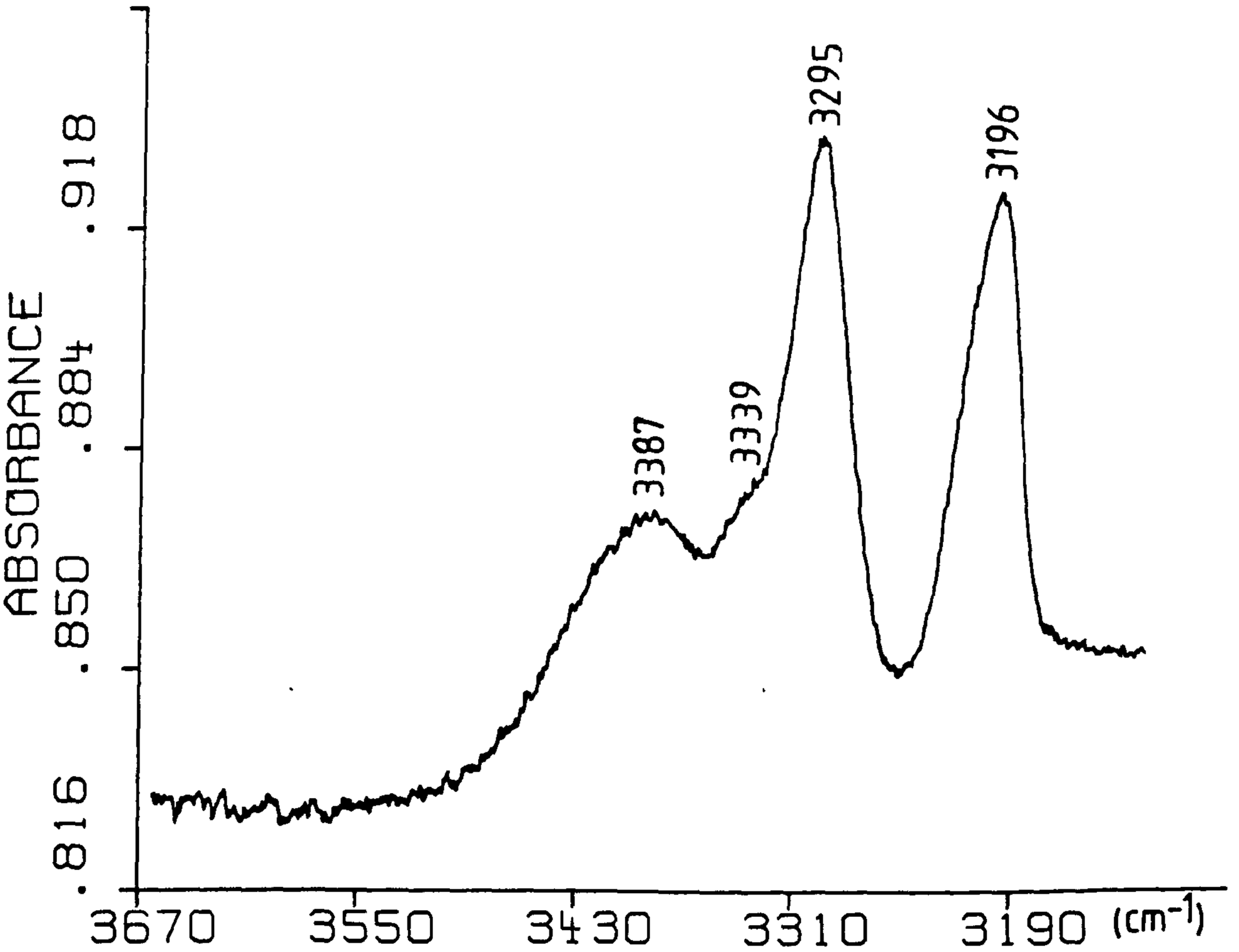

Fig. Fundametal Si-O overtone and combination absorption

3.2 bands of quartz in the 3700-3000 cm-1 infrared region

Chapter 3. Infrared Spectroscopic Studies

3.1 Interpretation of High Purity Quartz Infrared Spectra

3.1.1 The Infrared Spectrum of High Purity Quartz

The primary objective of the spectroscopic investigations carried out in this project was the assignment of impurity related absorption bands in the 3700-3000 cm^{-1} region of high purity quartz infrared spectra to specific defect models. Preliminary investigations in the near and far infrared regions of the electromagnetic spectrum failed to detect any useful features and were not continued. The exceptional purity of the samples was thought to be the probable cause for the lack of information in these regions. Reflection spectroscopic techniques were incompatible with the apparatus used to cool a sample and were therefore not considered. Consequently, quartz samples were examined exclusively using transmission infrared spectroscopy in the 4000-400 cm^{-1} mid infrared region.

The first stage in interpretation of quartz infrared spectra was that of distinguishing between impurity absorption bands and those absorptions produced by the quartz crystal lattice vibrations. The frequencies of infrared absorption bands associated with quartz lattice vibrations are shown on figures 3.1 and 3.2. These features were present in spectra obtained from all varieties of quartz and were roughly constant with respect to both band intensity and frequency. The portion of the spectrum shown in figure 3.2 was obtained

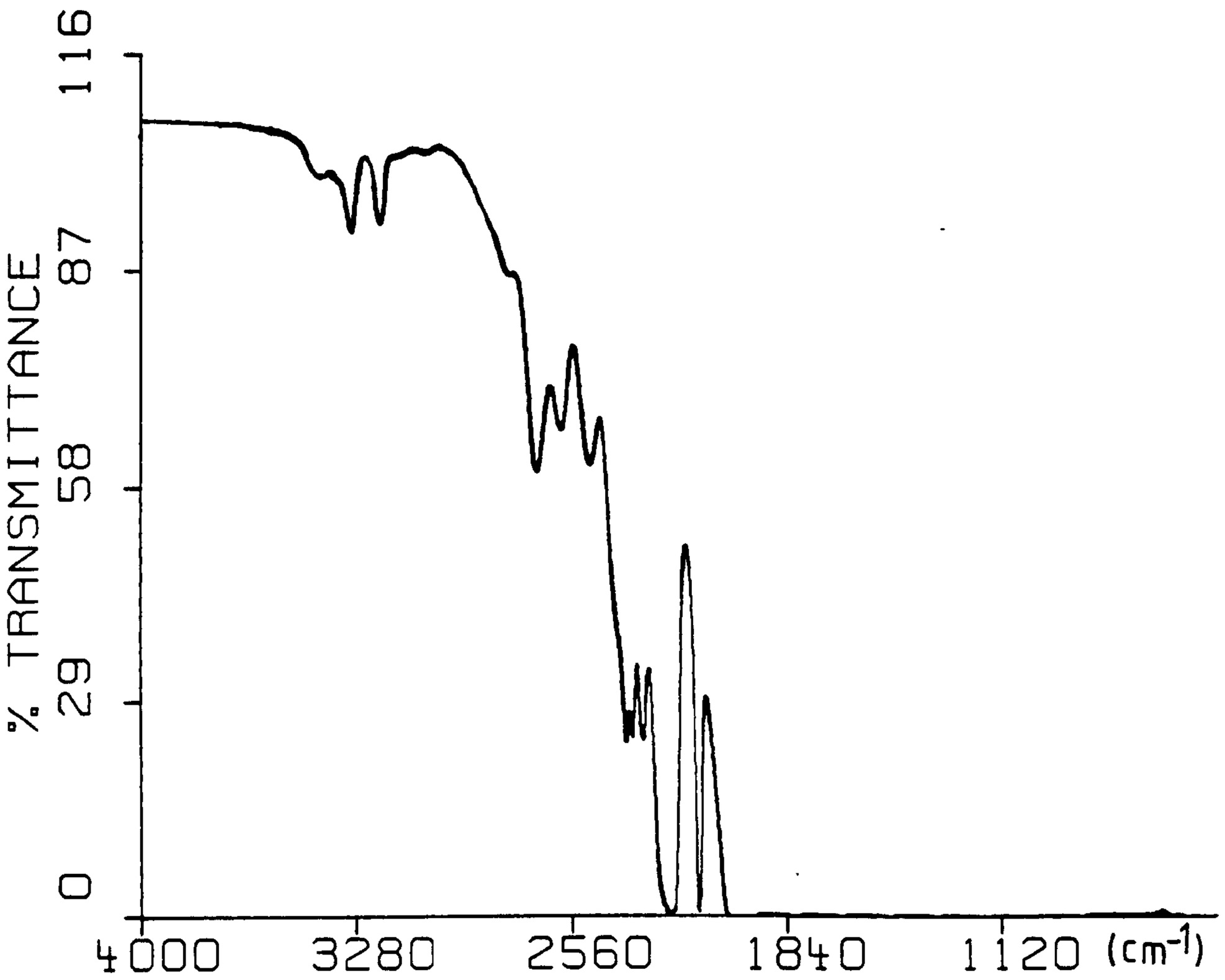

Fig. 3.3 Transmission IR spectrum of a hydrogen free quartz crystal

Table 3.1 Fundamental Overtone and Combination Absorption Bands in Quartz Infrared Spectra

This Thesis (cm^{-1})
3387
3339
3295
3196
-
2680
2599
2501
2381
2361
2326
2254
2239
2227
2137

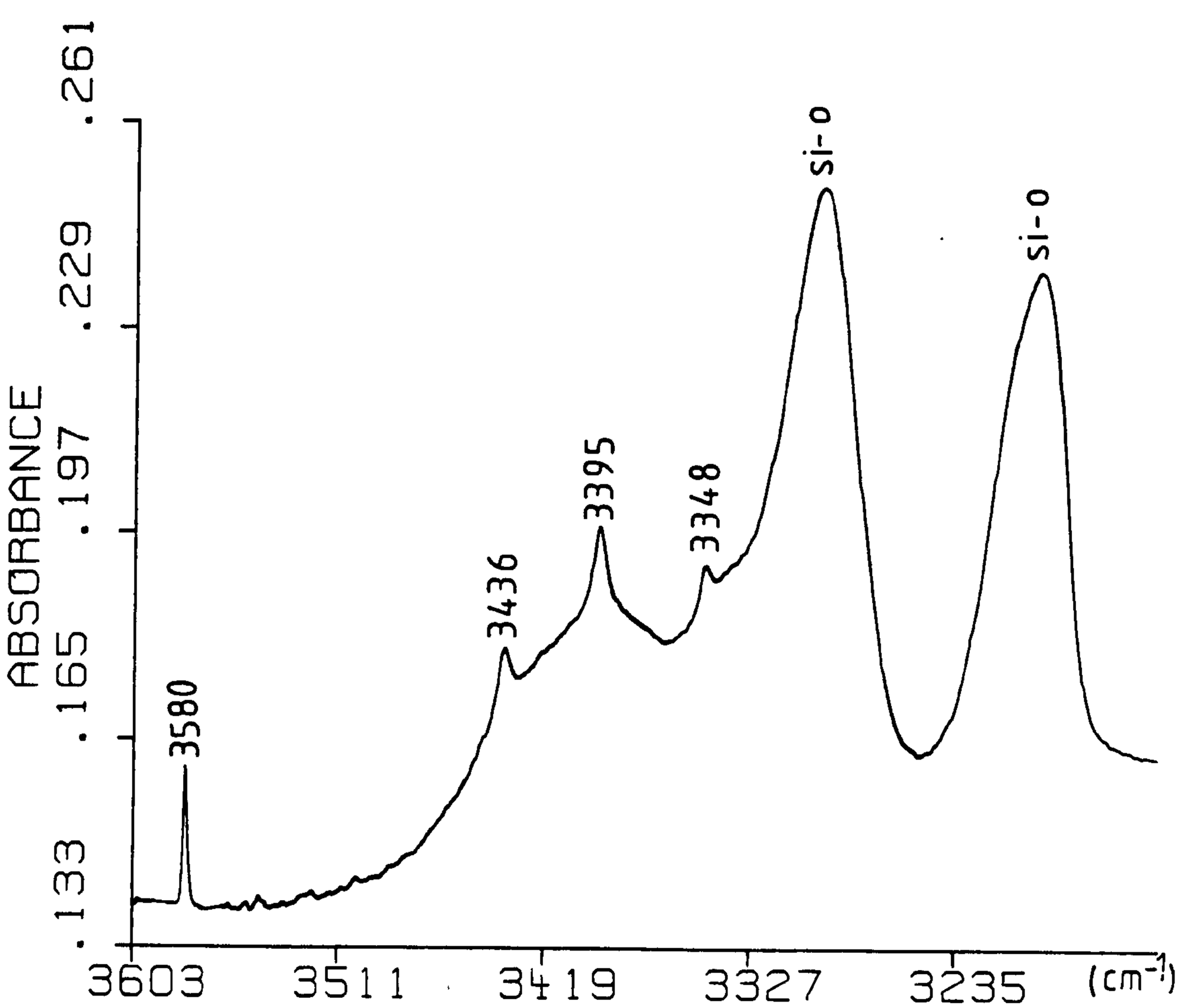

Fig. 3.4 Infrared spectrum of high purity quartz crystal HPQP.1

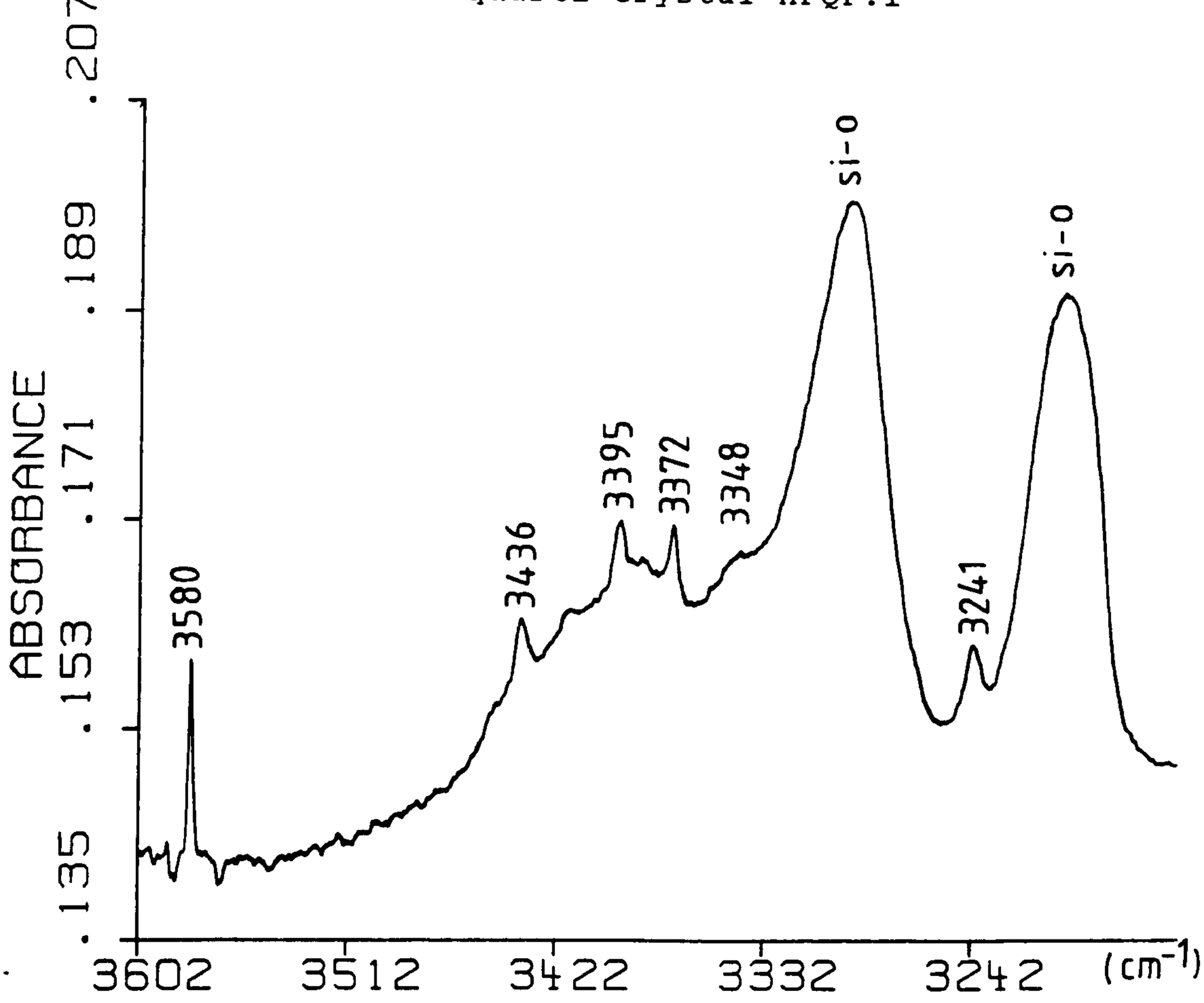

Fig. 3.5 Infrared Spectrum of high purity quartz crystal HPQ7.1

from a deuterated crystal to remove hydrogen impurity associated absorption bands. This was combined with the spectrum of a high purity undeuterated crystal to produce a quartz spectrum completely free of impurity related peaks (see fig. 3.3). Absorption bands present on this spectra were produced solely by combinations and overtones of fundamental Si-O lattice vibrations (see table 3.1). No information could be obtained at wavenumber values of 2000 cm^{-1} and below because quartz absorbs infrared radiation very strongly in this region.

The features with which this project was concerned were the impurity related absorption bands which are superimposed upon intrinsic lattice vibrations. Figure 3.4 is a spectrum obtained from HPQP.1, a typical high purity quartz crystal, which shows four sharp absorption peaks at 3580, 3436, 3395 and 3348 cm^{-1} respectively. These absorptions are produced by O-H stretching vibrations associated with impurities in a quartz crystal[52,92,93]. Usually these were the only non-lattice vibrational peaks present in high purity spectra. These bands are also characteristic of synthetic quartz infrared spectra and were not observed in spectra obtained from natural crystals[98]. In addition, there were two other absorption bands which were characteristic of material grown at GEC Hirst (see fig. 3.5). These peaks, which occurred at 3372 cm^{-1} and 3241 cm^{-1}, were only present in spectra of crystals grown in an autoclave thought to have been contaminated by an unidentified impurity. These anomalous

Table 3.2 Hydrogen Concentration in High Purity Quartz

	Hydrogen Concentration (ppm)*						
ν_{O-H}**	3580	3436	3395	3365	3348	3304	Total
Sample							
HPQP.1							
Untreated	0.221	0.227	0.396	-	0.097	-	0.941
Swept in N2	0.144	0.146	0.410	0.005	0.120	-	0.825
Swept in Air	0.146	0.140	0.352	0.025	0.122	-	0.785
Na swept in Air	0.167	0.157	0.346	0.017	0.103	-	0.790
HPQ15.5	0.347	0.348	0.530	-	0.186	-	1.411
HPQ16.4	0.375	0.376	0.628	-	0.283	-	1.662
HPQ7.1							
Untreated	0.243	0.201	0.233	0.010	0.043	-	0.730
Irradiated	No Change						
HPQ8.1							
Untreated	0.307	0.371	0.264	0.043	0.039	-	1.024
Irradiated	0.031	0.011	-	1.276	-	0.087	1.405
HPQ9.1							
Untreated	0.249	0.237	0.205	0.008	0.033	-	0.734
Irradiated	0.088	0.068	0.144	0.239	-	0.010	0.549

* - Number of O-H groups per 10^6 SiO_2 molecules (see section 2.4.2)

** - Frequencies of O-H stretching vibrations associated with hydrogen impurities in quartz (units = cm^{-1})

peaks had not been reported in the literature and were not present in spectra of crystals grown using other autoclaves. For these reasons these peaks have not been included as absorptions characteristic of high purity quartz despite their being present in several sample spectra.

The effect of various treatments and growth conditions common to synthetic quartz will now be discussed with respect to high purity samples.

3.1.2 Effect of Growth Rate on Hydrogen Content

The rate at which a crystal is grown can greatly affect the concentration of hydrogen related impurities which are incorporated in the quartz lattice. This is reflected in the spectra shown in figure 3.6 which compares a high purity crystal HPQP.1 with HNAQ.1, a crystal grown at a much faster rate. The spectrum of the later crystal displays a very intense broad band centred around 3200 cm^{-1}, thought to be produced by hydrogen bonded polymeric hydroxyl groups[102], which is a characteristic feature observed on spectra of rapidly grown crystals. The intensity of bands in spectrum HNACQ.1 are more intense than the corresponding absorptions in the high purity spectrum, even after the underlying broad absorption has been taken into account (see tables 3.2 and 3.3). In general, the faster a crystal is grown, the higher the hydrogen content will be. As a consequence, a greater variety of hydrogen associated species will be incorporated into the crystal lattice. This is indicated by the appearance

Table 3.3 Hydrogen Content of Crystals HNACQ.1 (R6) and R8

	Hydrogen Concentration (ppm)*			
Sample	HNACQ.1	R8		
ν_{O-H}**		HGS	HGB	IHGB
3590	4.180	-	-	-
3580	21.646	0.048	0.040	0.035
3515	4.131	-	-	-
3436	23.991	0.050	0.047	-
3395	44.669	0.049	0.030	0.041
3348	14.188	-	-	-
Total	7.5×10^3a	0.147	0.117	0.076

* - Number of O-D groups per 10^6 SiO_2 molecules (see section 2.4.2)

** - Frequencies of O-D stretching vibrations associated with hydrogen impurities in quartz (units = cm^{-1})

a - Approximate value which includes the broad absorption band centred at 3400 cm^{-1}.

HGS - Obtained from dislocation free section of crystal

HGB - Obtained from high dislocation content crystal section

IHGB - As for HGB except crystal was also irradiated

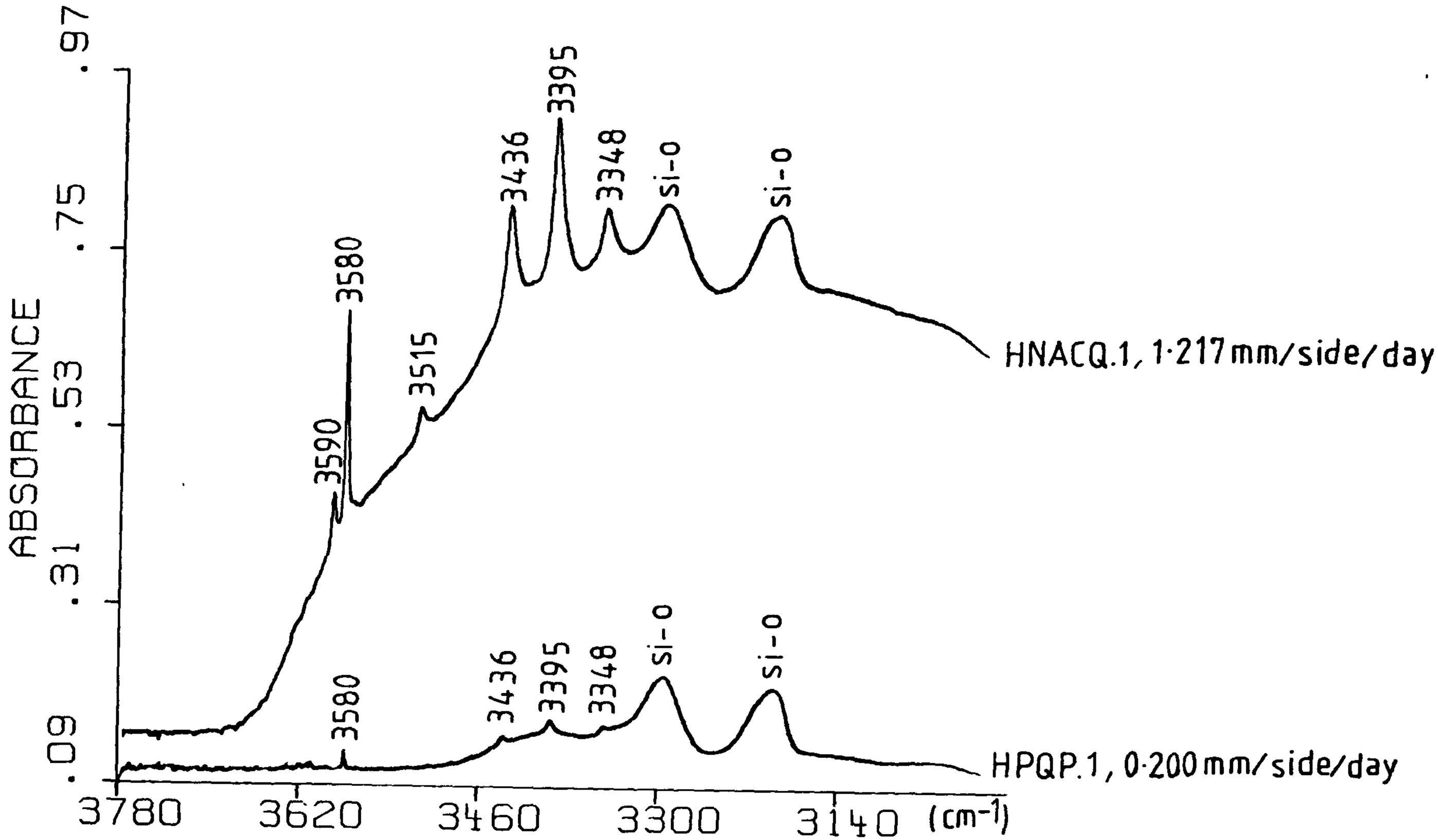

Fig. 3.6 Effect of growth rate on hydrogen content of quartz

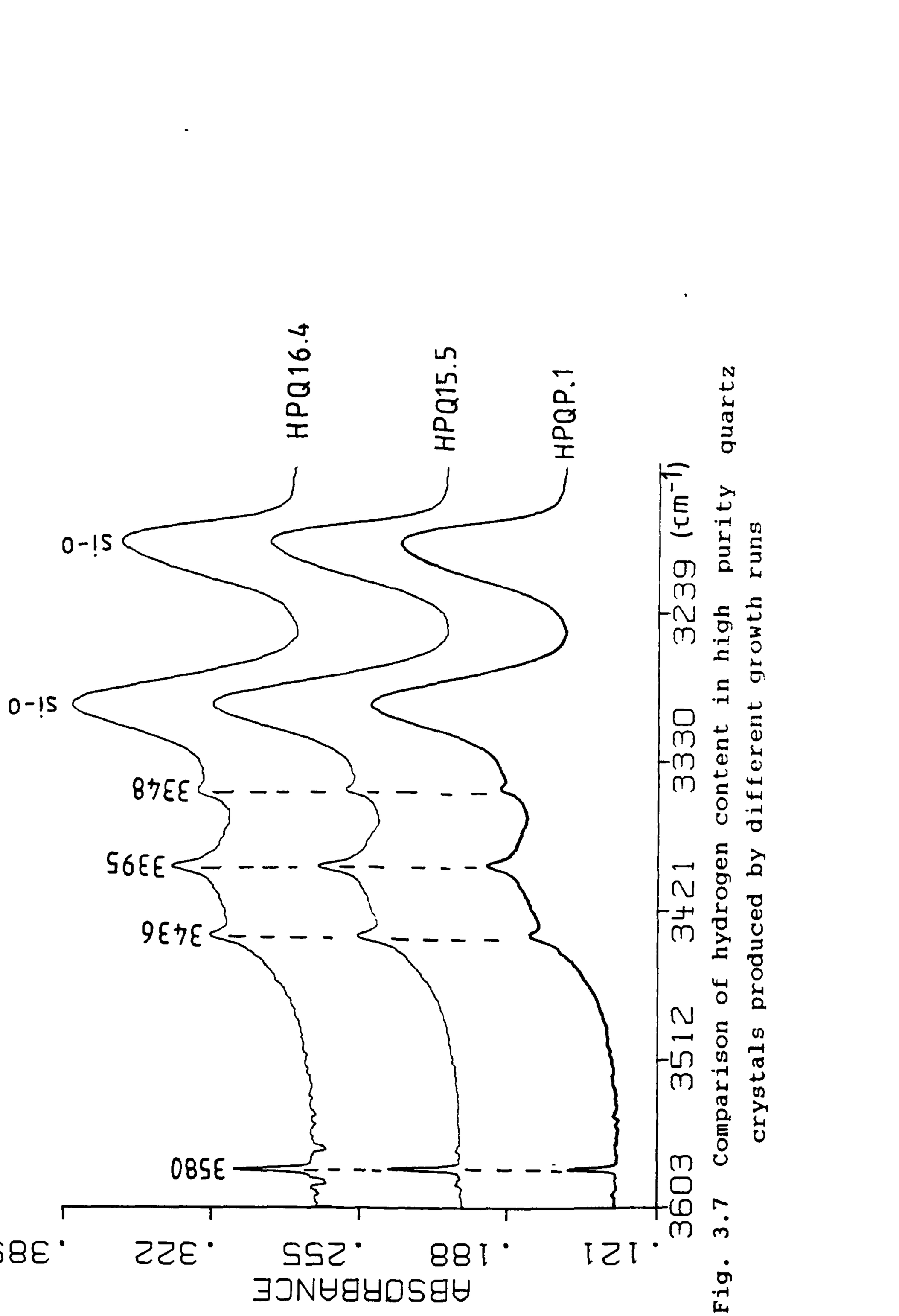

Fig. 3.7 Comparison of hydrogen content in high purity quartz crystals produced by different growth runs

of additional absorption bands at 3590, 3572 and 3515 cm^{-1} in the fast growth sample spectrum.

The conditions employed in high purity growth resulted in consistent and repeatable O-H concentrations being present in crystals (see fig. 3.7 and table 3.2). There were no significant differences between these spectra even although each sample was taken from a different high purity run. Therefore, although there have been reports of widely varying hydroxyl content throughout a crystal[99], this has generally not been the case for the high purity crystals studied during the course of this project.

3.1.3 Radiation Effects

Only two radiation produced absorptions in the synthetic quartz infrared spectrum have been conclusively identified. The absorptions, which occur at 3365 and 3304 cm^{-1} respectively, arise from the O-H stretching frequency of a hydroxyl ion associated with an interstitial aluminium impurity[104] (see section 1.8). Irradiation causes charge compensating alkali metal ions to be released from aluminium substitutional sites and these migrate through the crystal to be replaced by mobile hydrogen ions to form Al-OH defect centres. This radiation damage mechanism can be observed using infrared spectroscopy. The spectra shown in figure 3.8a were obtained from three samples analysed prior to irradiation for aluminium content (see table 2.3). Crystal HPQ7.1 had an impurity content typical of a high purity crystal. The other

Fig. Effect of aluminium concentration on the response of

3.8 quartz to x-irradiation

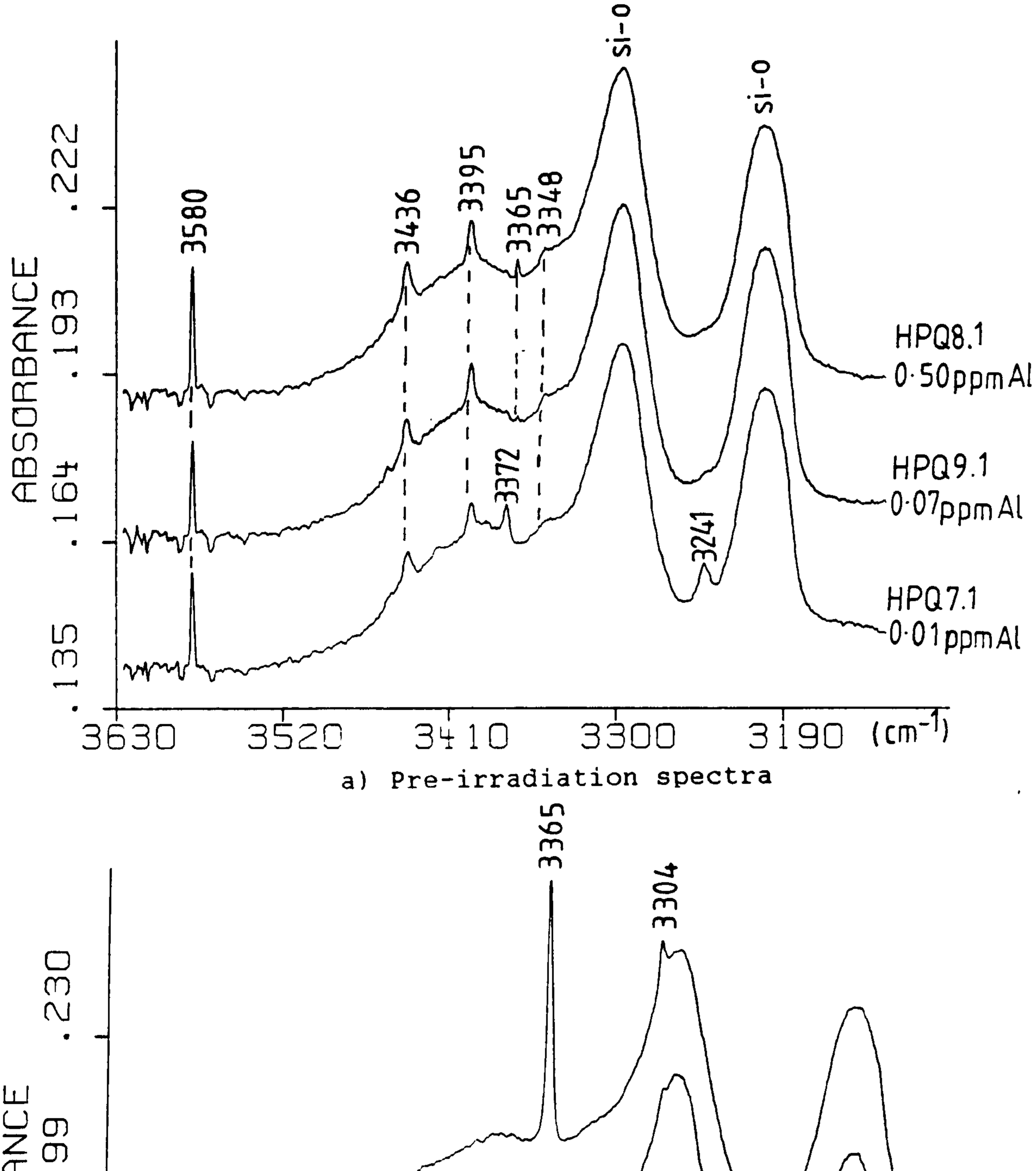

a) Pre-irradiation spectra

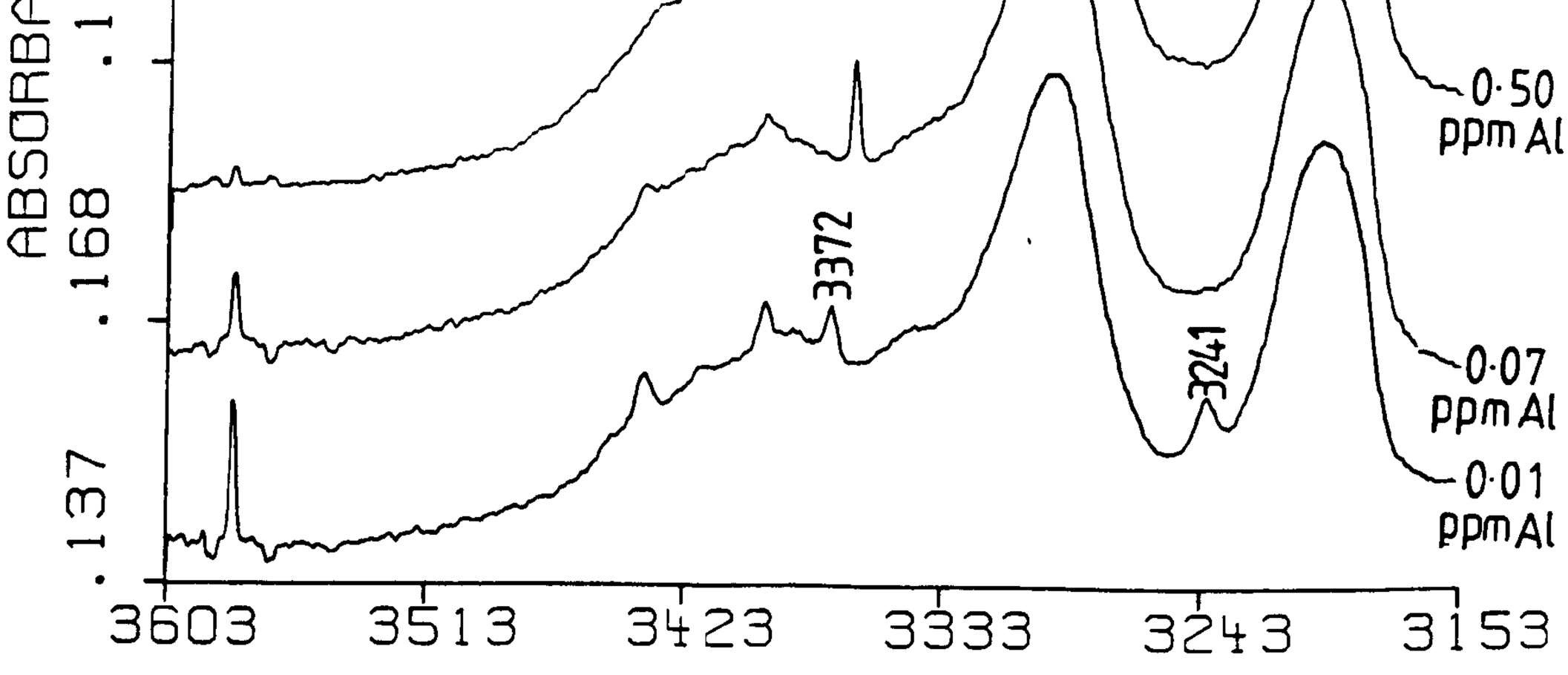

b) Post-irradiation spectra

two crystals had higher aluminium levels as a result of being deliberately doped with that impurity. In all other respects the three samples could be considered as high purity crystals. Pre-irradiation spectra obtained from the three samples were very similar, with the only major difference being two contamination peaks on the spectrum of HPQ7.1. All three sample spectra displayed the four absorptions characteristic of synthetic quartz spectra, with equivalent intensities indicating similar amounts of hydrogen related impurities. Apart from a very weak absorption at 3365 cm^{-1} on the spectra of HPQ8.1 and HPQ9.1 there was little evidence to suggest that increased aluminium concentration had any significant effect. Aluminium content only played an important role when the samples were irradiated (see fig. 3.8b and table 3.2). The intensity of all hydrogen related absorption bands was greatly reduced upon irradiation in the spectra of samples HPQ8.1 and HPQ9.1. This was accompanied by the appearance of two absorptions at 3365 cm^{-1} and 3304 cm^{-1}, which indicated the formation of Al-OH centres in the crystals. The appearance of a very weak absorption at 3365 cm^{-1}, in the spectrum of the irradiated sample HPQ7.1 was the only indication that irradiation had taken place as the intensities of the other O-H related absorptions were unaffected by the treatment.

The reduction of O-H band intensities is shown on table 3.2 to be proportional to aluminium content of a crystal. It is also apparent that the primary sources of charge compensating hydrogen ions are the infrared active species

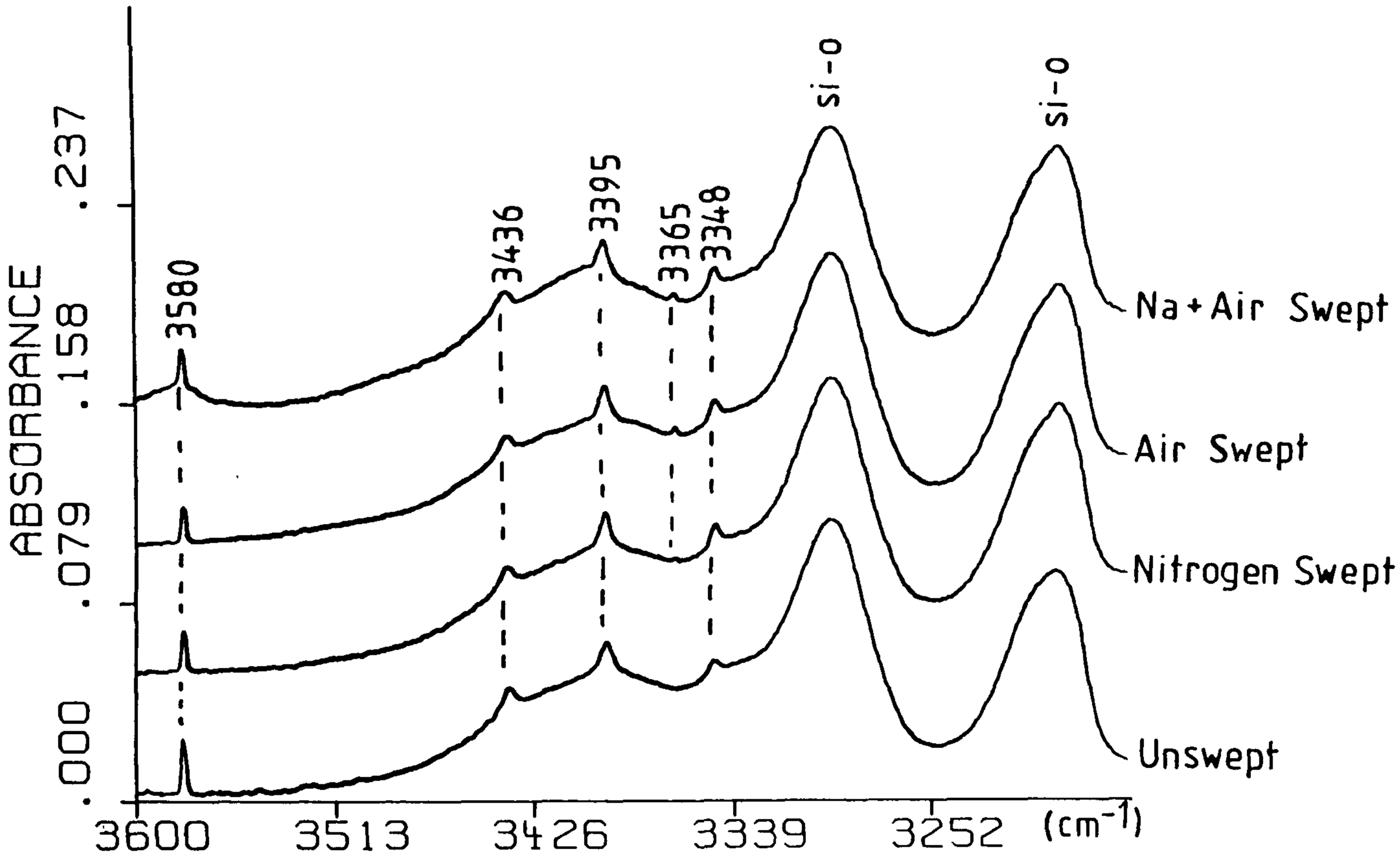

Fig. 3.9 Electrodiffusion study of high purity quartz

associated with the production of the O-H absorption bands. Crystal HPQ7.1 exhibited the radiation response typical of a high purity crystal.

3.1.4 The Effects of Electrodiffusion

Lipson et al.[103] reported that hydrogen could be incorporated into a quartz crystal which had been subjected to electrodiffusion in an air atmosphere. The effects of this treatment were observed by a dramatic increase in the intensities of O-H associated bands present in the infrared spectra of swept samples in comparison with the pre-treatment sample spectra. To study this behaviour in high purity quartz, samples taken from the high purity crystal HPQP.1 were swept in air and nitrogen atmospheres. In addition, sodium ions were swept into a crystal in an air atmosphere to induce an intensity change in any band associated with these ions.

The spectra obtained from the various treatments showed a slight decrease in O-H absorption band intensities (see table 3.2). The most apparent changes were a reduction of the intensities of the 3580 cm^{-1} and 3436 cm^{-1} absorption bands and the appearance of a weak aluminium associated band at 3365 cm^{-1} (see fig. 3.9). The intensities of the 3395 cm^{-1} absorption bands were unchanged in each of the sample spectra, however the 3348 cm-1 bands were shown to increase significantly. The use of an air atmosphere during sweeping did not produce any increase in hydrogen content in the crystal and no absorptions were effected by the sweeping of

sodium ions through the crystal.

The production of an aluminium band to the detriment of the 3580 cm^{-1} and 3436 cm^{-1} band intensities suggests that electrodiffusion produces effects similar to those associated with irradiation. The process removes monovalent metal ions from the crystal thereby depriving any aluminium centres present of charge compensators. The preferential reduction of the 3580 cm^{-1} and 3436 cm^{-1} bands indicates that, when a quartz crystal is swept, the hydrogen ions associated with those absorption species are used to replace alkali metal ions in the charge compensation process. The absence of any overall increase in band intensities for air swept samples indicates that hydrogen is not incorporated directly from the atmosphere by the sweeping process in the case of high purity quartz. Similarly, the absence of changes in the sodium swept sample spectra confirms that electrodiffusion cannot be used to produce impurity absorption bands in synthetic quartz spectra. The lack of any significant change in the overall hydrogen content of high purity crystals, combined with the increase in 3348 cm^{-1} band intensity strongly suggests that sweeping does not remove H^+ ions from quartz but merely rearranges them in the crystal lattice.

3.1.5 Dislocations and Hydrogen Content

Growth run 8 was designed to produce a crystal which possessed a high dislocation density on one side and a perfect crystalline region on the other (see section 2.1 and table

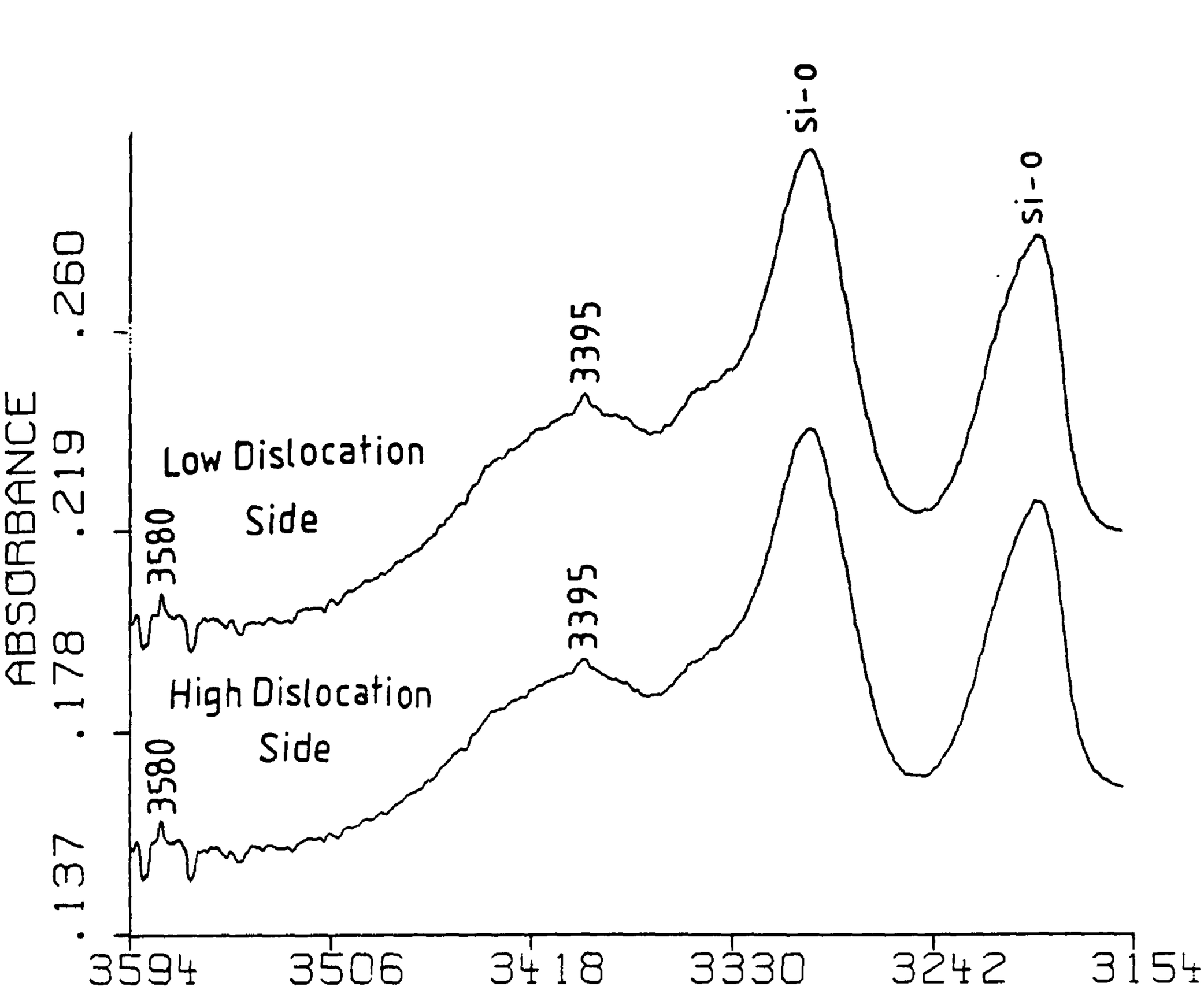

Fig. 3.10 Comparison of hydrogen content in dislocation free and high dislocation content synthetic quartz

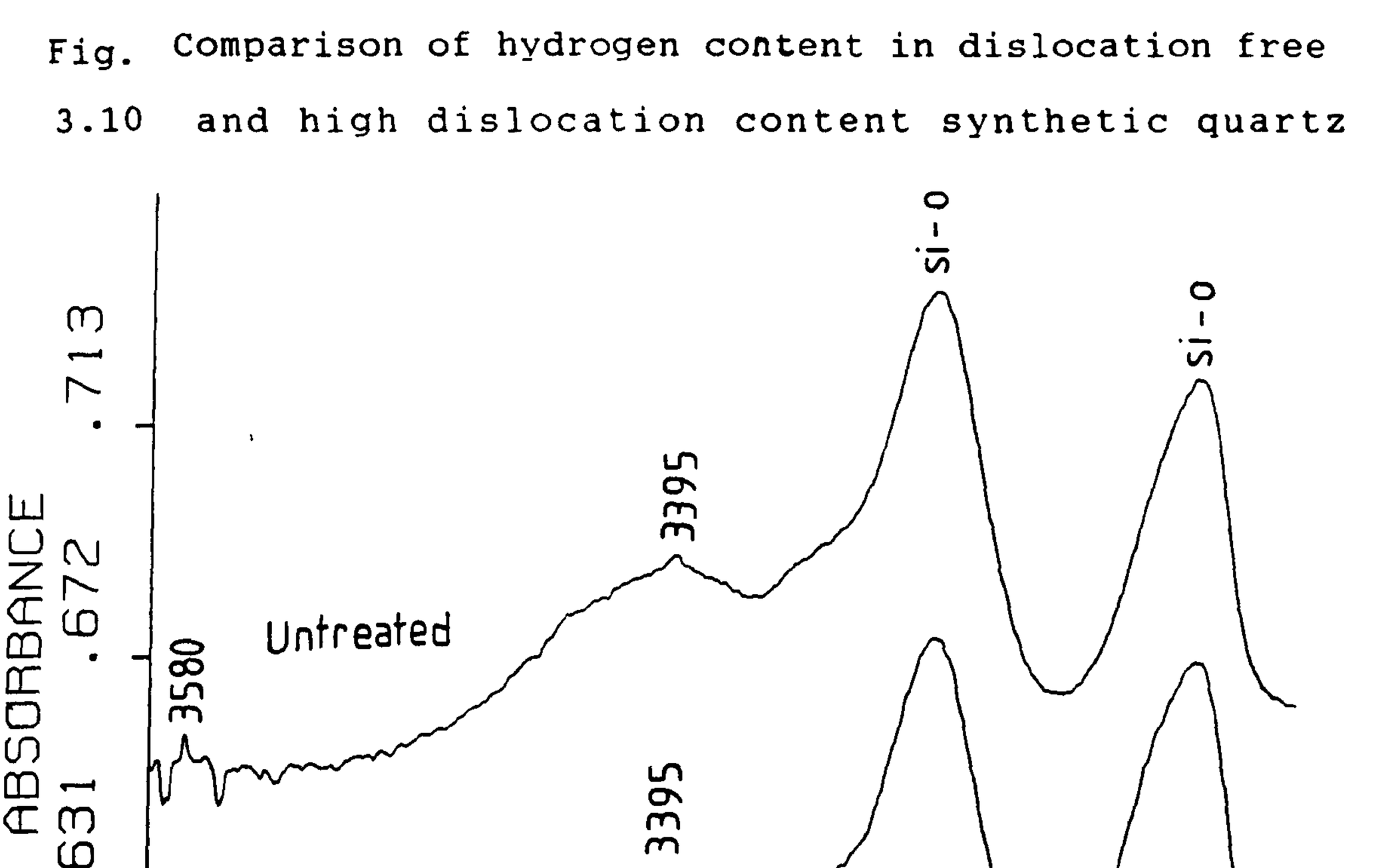

Fig. 3.11 Effects of x-irradiation on the infrared spectrum of high dislocation content quartz

3.3). This was accomplished by mounting the seed horizontally thereby sacrificially protecting the lower crystal surface from dislocation formation[136]. One use of crystal R.8 was in the study of the relationship between dislocation density and hydrogen content. Dislocations are known to concentrate impurities along their lengths[113,114] and so an increase in the levels of dislocations should produce a corresponding increase in both impurities and hydrogen content which could be detected by use of infrared spectroscopy.

Run 8 produced a crystal with both a perfect side and one which showed a very high concentration of dislocations , $\approx$ 1-2000 per cm^2, (see fig. 4.12). Infrared spectra were recorded from both sides of the crystal before and after x-ray irradiation (see figs. 3.10 and 3.11). The absence of the characteristic 3348 cm^{-1} absorption combined with the weakness of the 3580 cm^{-1}, 3436 cm^{-1} and 3395 cm^{-1} bands showed the crystal to be exceptionally free from hydrogen impurities even in comparison with high purity quartz samples (see tables 3.2 and 3.3). The purity of the sample was substantiated by the absence of any absorption intensity change after irradiation on both sides of the crystal which indicated that levels of aluminium in crystal R.8 were less than 0.01 ppm/SiO_2.

As the spectra from the two crystalline regions of the crystal R.8 were virtually identical, both before and after irradiation, it can be concluded that dislocation density has no effect on the hydrogen concentration of high purity

Table 3.4 Characteristic Infrared Absorption Bands

Quartz Type	Characteristic Absorption Bands (cm^{-1})
Natural Quartz	3594
	3515
	3503
	3473
	3434
	3425
	-
	-
	-
Natural and Swept	3365
Electronic Grade*	3304
Swept Electronic,	3580
Premium** grade and	3436
High Purity Quartz***	3395
	3348

* - Standard commercial quality quartz crystals (STC)

** - Highest quality commercial quartz crystals (STC)

*** - High purity quartz (GEC)

crystals that can be detected by infrared spectroscopy.

A summary of the frequencies at which absorption bands occur in the infrared spectra of different types of quartz is given in table 3.4.

3.2 Impurity Doped Quartz Infrared Spectra

3.2.1 Nature of Absorption Peaks

Impurity doped synthetic quartz crystals were grown in an attempt to identify individual infrared absorption peaks with specific impurities. The basis of this procedure was work carried out by Kats[52] and later workers, notably Dodd and Fraser[97] and Brown and Kahan[98], who suggested that impurities were directly associated with the hydrogen species giving rise to hydroxyl peaks in the 3100-3700cm^{-1} region of quartz infrared spectra (see table 1.6). This was certainly the case for impurities present in natural quartz but had not been conclusively established for those peaks present in synthetic quartz infrared spectra. Indeed, these workers all failed to find any correlation between hydrogen and impurity content in synthetic crystals. They concluded that the three major synthetic quartz absorption peaks at 3580, 3436 and 3395 cm^{-1} were independent of any impurity but tentatively suggested that the 3348 cm^{-1} band was associated with Li^+ or K^+ ions. However, these workers were hampered by a lack of good quality synthetic material. Each of the crystals which they examined displayed an intense broad absorption centred around 3200 cm^{-1} which obscured and broadened absorption bands and produced measurement errors in the frequency at which they occurred. They also did not have access to either the high resolution and data manipulation facilities afforded by the FTIR spectrometer used in this study or the high purity growth techniques detailed in section 2.1. As the spectrum of a

Table 3.5 Doped Quartz Growth Runs

Sample Title	Mineraliser (Molar)	Dopant (g)	Autoclave Temperature* (°C)	Growth Rate (mm/side/day)	Colour
CRDHPQ.1	1.25 NaOH	Cr_2O_3	300/350/400	0.390	None
CODHPQ.1	1.25 NaOH	Co(m)	300/350/400	0.330	Blue
TIDHPQ.3	1.25 NaOH	1g TiO_2	300/350/400	0.388	None
FEDHPQ.1	5% K_2CO_3**	2g Fe(m)	300/350/400	0.404	Rusty Brown
FEDHPQ.6	5% K_2CO_3**	1g Fe(m)	330/355/380	0.660	None
AlKDHPQ.2	1.25 NaOH	K_2AlO_3	300/350/400	0.140	Green
AlKDHPQ.4	1.25 NaOH	K_3AlO_3 +Fe(m)	330/355/380	0.394	None
PDHPQ.1	1.25 NaOH	Na_3PO_4 (4g)	300/350/400	0.460	None
CUDHPQ1	1.25 NaOH	Cu_2O	330/355/380	0.410	None

m - metal
* - Temperatures at Top/Middle/Bottom of autoclave
** - Solution of 5% w/w K_2CO_3/H_2O

NB. The operating pressure for all doped runs was 1500 atm. Converted silica gel was used as the nutrient in all cases except for CRDHPQ.1 where converted dynasil silica was used.

non-doped high purity quartz sample does not display the broad polymeric O-H absorption band at 3200 cm^{-1}, the frequencies and intensities of absorption bands can be recorded accurately and the data manipulation routines of the FTIR spectrometer can be used to detect weak absorptions and distinguish them from background noise. The lack of strong O-H associated absorption features in the high purity quartz infrared spectra allows any difference between the spectra of doped and undoped high purity samples to be easily identified and attributed to the dopant added.

A series of crystal growth runs were carried out by Hirst personnel using high purity quartz growth procedures but with the addition of a dopant (see table 3.5). Analysis of samples produced by these growth runs was carried out using FTIR spectroscopic studies exclusively. Conventional impurity analysis using atomic absorption spectroscopy was rendered impractical because of the limited quantities of doped material available. Incorporation of a dopant was confirmed in several cases by the colouration of the grown crystal and by the examination of low temperature infrared spectra in all other cases (see table 3.5).

The spectra of each doped sample was very different to that of a high purity crystal (see figs. 3.12-14). In general, each spectrum displayed almost identical absorption features and could only be distinguished from each other by the relative intensities of individual absorption bands and in those cases where iron was present in the growth solution

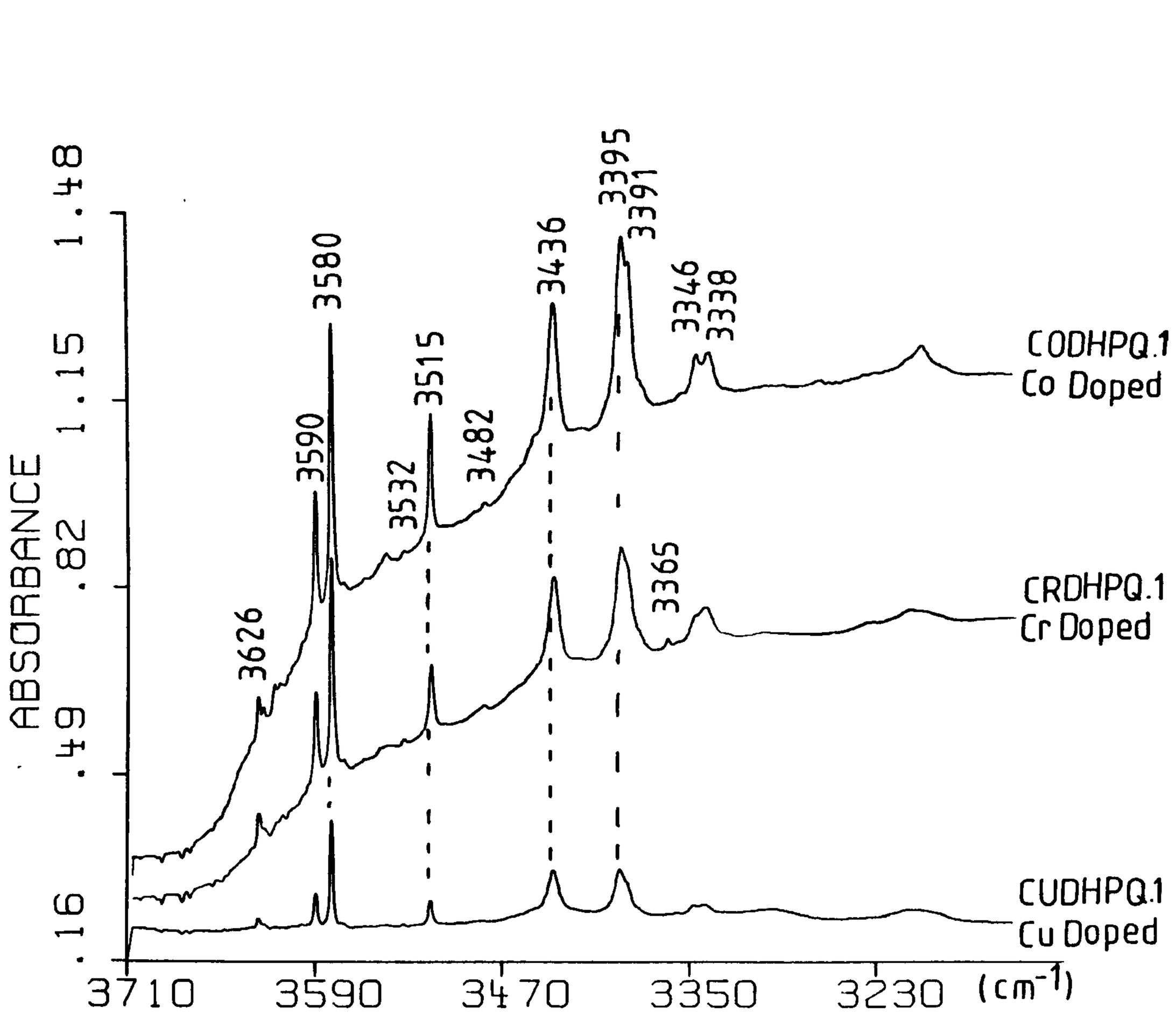

Fig. 3.12 Cobalt, chromium and copper doped high purity quartz spectra

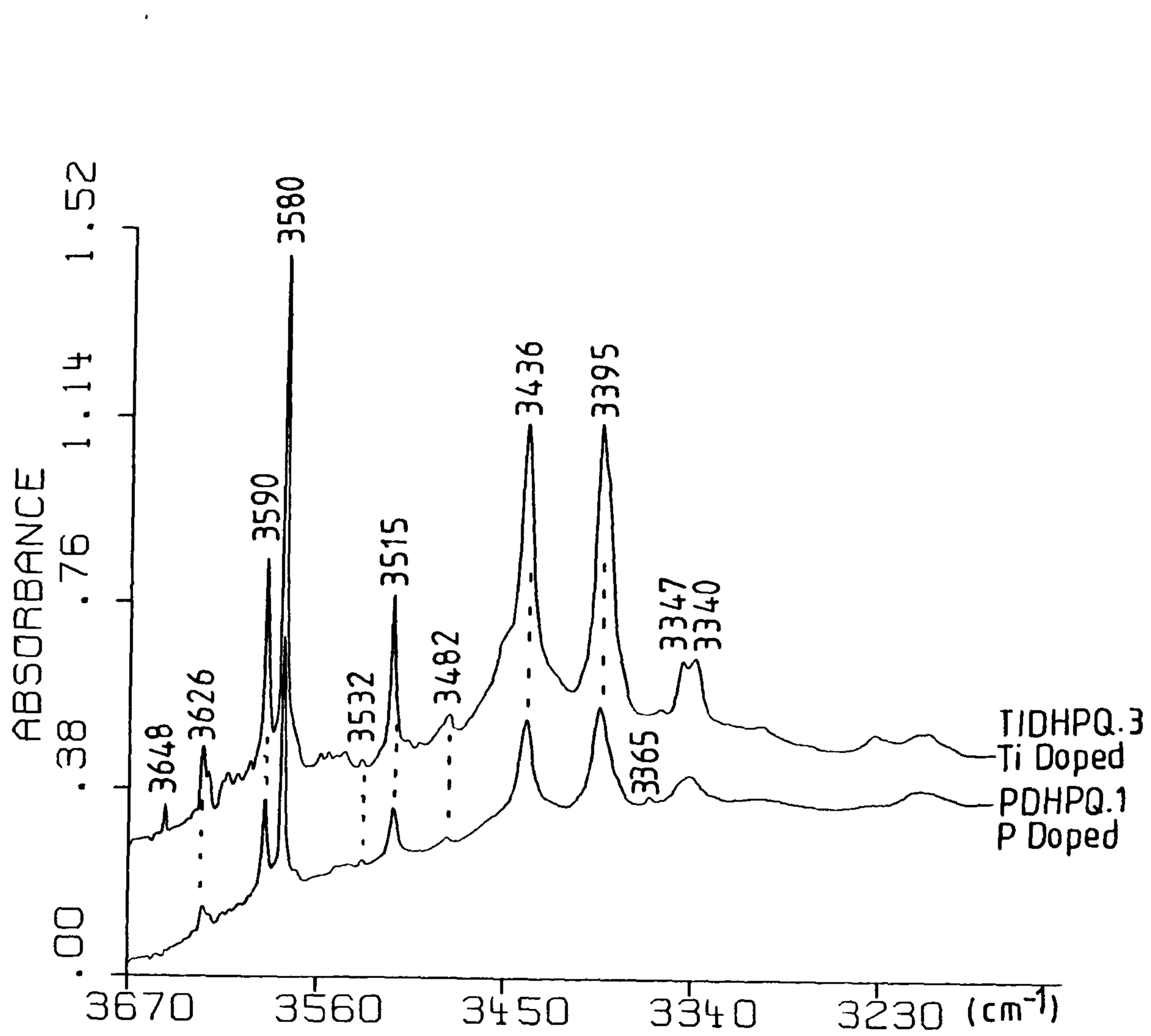

Fig. 3.13 Titanium and phosphorous doped high purity quartz spectra

Table 3.6 Hydrogen Content in Doped Quartz Crystals

	Hydrogen Concentration (ppm)*				
Sample	CRDHPQ.1	CODHPQ.1	TIDHPQ.3	PDHPQ.1	CUDHPQ.1
ν_{O-H}**					
3648	-	-	2.338	-	-
3626	4.855	4.501	12.434	4.813	1.561
3615	0.481	1.916	-	-	-
3611	0.815	0.618	-	-	-
3590	12.875	15.719	31.851	16.226	4.764
3580	30.196	36.053	81.948	39.478	11.945
3571	0.479	0.344	-	-	0.129
3532	0.451	0.289	0.879	0.611	0.193
3515	9.647	14.726	24.413	9.600	3.161
3482	0.433	0.695	2.521	0.690	-
3436	31.460	34.794	69.398	29.983	10.763
3395	49.585	81.762[a]	132.846	49.057	17.697
3364	0.667	-	-	0.861	-
3340	13.831	18.631[b]	34.351[c]	12.225	4.311b
Total[d]	7.3×10^3	1.6×10^4	3.1×10^3	7.7×10^2	3.9×10^2

* - Number of O-H groups per 10^6 SiO_2 molecules (see section 2.4.2)

** - Frequencies of O-H stretching vibrations associated with hydrogen impurities in quartz (units = cm^{-1})

a - Value includes 3391 cm^{-1} absorption band

b - Absorption band split into two absorptions at 3346 cm^{-1} and 3338 cm^{-1}

c - As for b) except bands at 3347 cm^{-1} and 3340 cm^{-1}

d - Approximate value which includes the broad absorption band centred at 3400 cm^{-1}.

(see tables 3.6 and 3.7). The most characteristic feature of doped sample spectra was the appearance of the broad polymeric O-H absorption around 3200 cm^{-1}. The presence of the broad absorption made the accurate determination of the O-H content of doped crystals difficult and consequently the values given on tables 3.6 and 3.7 are approximations.

When compared to high purity samples, it is clear that the addition of a dopant has increased the hydrogen content of the crystals by a significant amount in every case. The principle absorption bands occurred at 3580, 3436 and 3395 cm^{-1} respectively and corresponded to the three major O-H bands observed in synthetic crystal spectra. However in the case of a doped crystal, the intensities of the absorptions and therefore the concentrations of the associated hydrogen related species were greatly increased in comparison with typical high purity samples (see tables 3.2, 3.6 and 3.7). The fourth peak characteristic of high purity sample spectra at 3348 cm^{-1} was very weak in doped spectra, most of which were obtained from Z-slice samples. As explained later in section 3.3, the species associated with this peak was aligned along the Z-axis which was an unfavourable position to absorb infrared radiation in the case of Z-cut crystal samples. However, an absorption in the near vicinity of the fourth absorption band frequency was present at values which varied between 3340 cm^{-1} and 3346 cm^{-1}. This band was weak in comparison with the other absorptions and was frequently split into two peaks (see fig. 3.13). This band could be associated

with a similar hydrogen species to that which produced the 3348 cm^{-1}, aligned approximately along the Z-axis but present at much higher concentrations to allow its observation even in Z-slice sample spectra. The 3580 and 3395 cm^{-1} absorptions were split into multiple peaks in several spectra, the extra peaks occurring at 3590, 3571 and 3391 cm^{-1} respectively (see figs. 3.12 and 3.13). These were probably caused by interactions between identical absorption species being present in similar chemical environments. The 3436 cm^{-1} absorption was not observed to split into multiple peaks on any of the doped sample spectra but a shoulder was observed on the spectra of titanium and cobalt doped samples (see fig. 3.13). The other major absorption band on doped sample spectra occurred at 3515 cm^{-1}, which also has been observed on several high purity quartz spectra.

The exception to the identical features observed in doped sample spectra was a set of three peaks at 3576, 3542 and 3467 cm^{-1} (see fig. 3.14). Absorptions at these positions had not been observed on any previous spectrum or reported in literature. The intensities of these absorptions were strongest on the spectrum of the iron doped sample FEDHPQ1, which was a rust coloured crystal (see table 3.5). The other three spectra which exhibited the peaks were obtained from samples FEDHPQ6, ALKDHPQ4 and ALKDHPQ2, of which only the latter was coloured. ALKDHPQ2 was a green coloured sample which contained several large inclusions of acmite particles. These particles were responsible for the poor quality of the

Table 3.7 Hydrogen Content in Iron Doped Quartz

Sample	Hydrogen Concentration (ppm)*			
ν_{O-H}**	FEDHPQ.1	FEDHPQ.6	ALKDHPQ.2	ALKDHPQ.4
3619	1.362	-	-	-
3590	-	0.263	-	-
3580[a]	67.731	9.598	67.182	12.622
3576[a]				
3555	-	-	7.083	-
3542	18.393	1.946	3.247	3.040
3467	22.725	2.077	5.425	5.421
3436	43.972	6.640	10.978	12.021
3395	53.362	7.524	9.552	17.618
3348	6.494	0.984	-	1.632
Total[b]	2.1×10^4	3.1×10^3	2.9×10^4	1.2×10^4

* - Number of O-H groups per 10^6 SiO_2 molecules (see section 2.4.2)

** - Frequencies of O-H stretching vibrations associated with hydrogen impurities in quartz (units = cm^{-1})

a - Values given for these absorption bands have been combined because of peak overlap

b - Approximate value which includes the broad absorption band centred at 3400 cm^{-1}.

Note - Underlined absorption bands were only present in iron doped quartz spectra

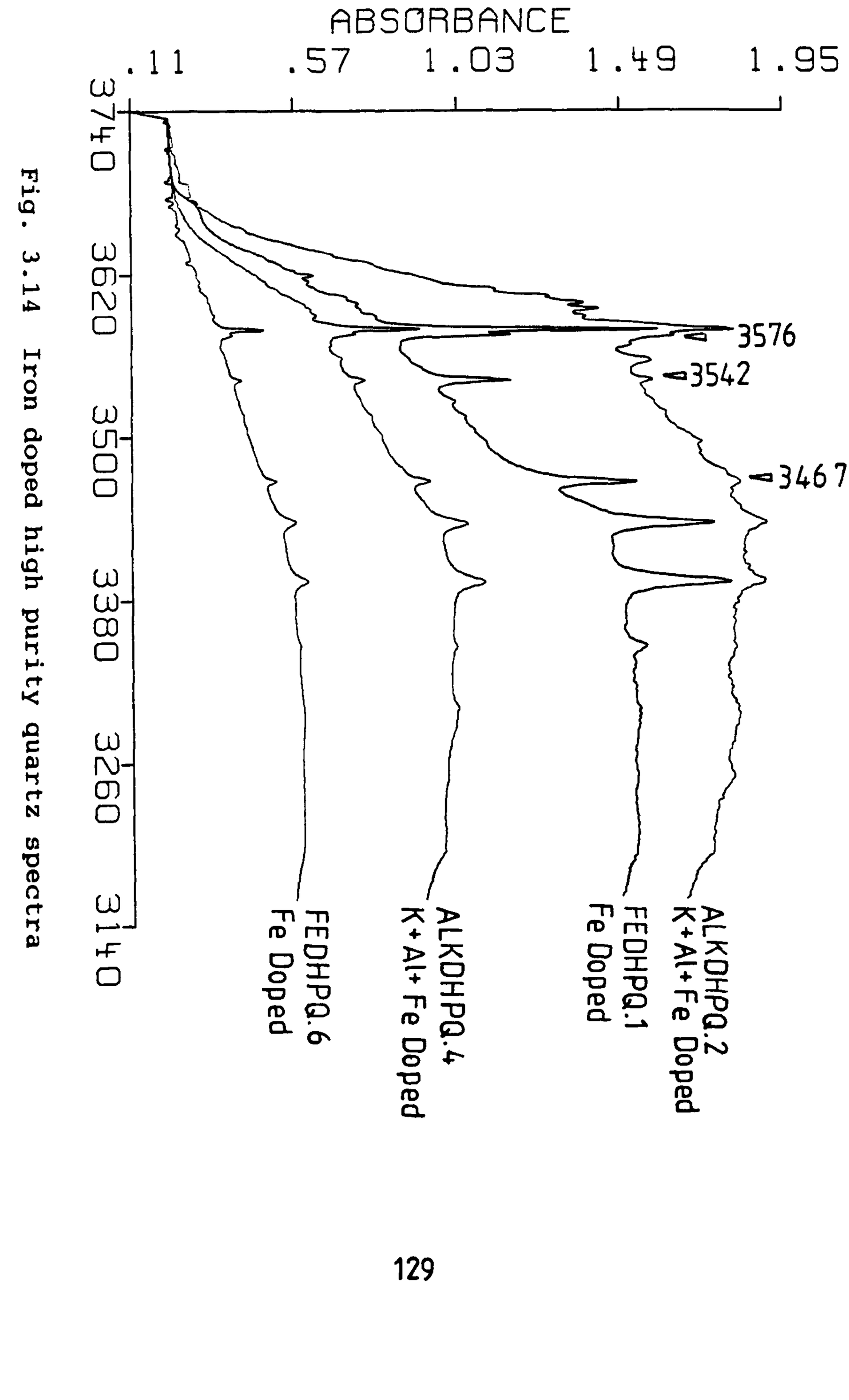

Fig. 3.14 Iron doped high purity quartz spectra

spectrum and provided the factor common to each of the samples. The growth conditions in the case of ALKDHPQ2 were sufficient to cause increased attack of the autoclave walls and induce high levels of iron impurities to contaminate the growth solution. In each of the other three crystal growth runs, iron was deliberately added and in each case the three new absorption bands were observed. The absorptions were not observed in the spectra of those samples whose dopant did not include iron, thereby suggesting that the absorption bands were associated with iron impurities.

The only reported case of an absorption peak being associated with a specific impurity was that of substitutional aluminium impurities (see section 1.7). The absorptions at 3576, 3542 and 3467 cm^{-1} respectively, were therefore thought to be possibly associated with substitutional iron impurity sites in the crystal. The existence of such sites was postulated by Chakraborty and Lehmann[99,100], but they were unable to find any spectroscopic evidence to substantiate their claim. The observation of the iron associated absorption bands discussed in this section was probably a consequence of deliberately doping crystals with iron to produce a much higher concentration of these defect sites than would normally be expected for synthetic crystals.

The other absorptions observed in doped sample spectra were mostly very weak and therefore produced by minor hydrogen species (see tables 3.6 and 3.7). Therefore, the major absorptions were produced by those impurities which were also

the strongest features in the high purity spectra. These were increased in intensity solely by the addition of a dopant regardless of which impurity was added. This confirmed the lack of association between absorption peaks to a particular impurity but suggested a link between overall hydrogen content and the presence of impurities. This behaviour can be accounted for by two explanations. The dopants themselves could have been contaminated by identical quantities of similar impurities and therefore would produce similar infrared spectra. However even if this was the case, it could be expected that those peaks which were associated with the main dopant impurity would be of much greater intensities than those of any unwanted contaminant. However for each doped spectrum, the absorption bands possessed similar relative intensities and no new absorptions were produced. A more credible explanation would be that most impurities were incorporated interstitially and not substitutionally into a quartz crystal lattice. In the previously discussed cases of Al and Fe impurities, specific peaks associated with these impurities were observed. The lack of similar specific absorptions for the other impurity dopants combined with the evidence for the incorporation of impurities shown by both the increased hydrogen content in each case and the blue colouration of the cobalt doped crystal, indicates that although impurities were present in doped crystals they did not influence the frequencies of hydrogen associated absorptions directly. This can be explained if the impurities

were incorporated interstitially into the crystal. If this were the case then the hydrogen species would only act as charge compensators and would not be associated with the crystal lattice as is the case for those examples postulated by Kats (see section 1.8). The mode of hydrogen uptake could be either directly as a hydration sphere surrounding an impurity ion or indirectly as migrating hydrogen ions trapped by incorporated impurities requiring charge compensation. The species which would result from these operations would essentially give the same absorptions irrespective of the nature of the incorporated impurity ion. This is a consequence of the impurity-oxygen bond being infrared inactive resulting in all absorptions being produced by the O-H vibrations of the original hydrogenated species. Therefore, the observations discussed in this section suggest that the hydrogen content of a crystal is directly related with the overall impurity content and that in most cases impurities are interstitially incorporated and are not associated with any specific absorption band. They also suggest that the specific impurity that is incorporated is relatively unimportant and any impurities that are not incorporated substitutionally will produce very similar infrared spectra.

Table 3.8 Hydrogen Content in Doped Quartz after Sweeping

ν_{O-H}**	Sample	Hydrogen Concentration (ppm)* FEDHPQ.1 Unswept	FEDHPQ.1 Swept	CRDHPQ.1 Unswept	CRDHPQ.1 Swept
3626		-	-	4.855	-
3619		1.362	-	-	-
3615		-	-	0.481	-
3611		-	-	0.815	-
3590		-	-	12.875	0.523
3580		67.731[a]	14.352[a]	30.196	4.051
3576				-	-
3532		-	-	0.451	-
3542		18.393	0.453	-	-
3515		-	-	9.647	0.690
3481		-	-	0.433	-
3467		22.725	0.881	-	-
3436		43.972	6.602	31.460	3.887
3395		53.362	5.722	49.585	3.737
3364		-	-	0.667	-
3348		6.494	-	-	-
3340		-	-	13.831	-
Total[b]		2.1×10^4	1.5×10^4	7.3×10^3	7.8×10^3

* - Number of O-H groups per 10^6 SiO_2 molecules (see section 2.4.2)

** - Frequencies of O-H stretching vibrations associated with hydrogen impurities in quartz (units = cm^{-1})

a - Value given for these absorption bands have been combined because of peak overlap

b - Approximate value which includes the broad absorption band centred at 3400 cm^{-1}.

3.2.2 Nature of the 3200 cm^{-1} Absorption Band

A feature common to all doped sample spectra was that of the broad absorption band centred around 3200 cm^{-1} (see figs. 3.12 and 3.14). This was also a characteristic of rapidly grown crystals, such as with the growth run 6 crystal sample, HNACQ.1 (see fig. 3.6). The 3200 cm^{-1} band has the correct frequency in the infrared spectrum to be assigned to polymeric hydrogen bonded O-H vibrations common to spectra of alcohols and water. However the absence of a characteristic ice peak upon cooling has always been the obstacle to assign the band to water absorptions even although incorporation of water is a likely occurrence for hydrothermally produced quartz (see sections 1.7b and 1.8).

Figure 3.15 shows the effects of sweeping on two doped samples , FEDHPQ1 and CRDHPQ1 respectively. The drastic changes in the swept crystal spectra were thought to be largely due to the effect of heating the crystals and not as a consequence of the applied electric field. Only the strongest absorptions survived the electrodiffusion treatment but even they had been considerably reduced in intensity (see table 3.8). On cooling the treated samples, a broad ice absorption band appeared at 3216cm^{-1}. Both of the treated samples had a milky appearance where previously they had been optically clear. The combination of the appearance of ice bands as well as the milky appearance suggested that upon heating the doped samples, the hydrogen species present in the lattice came together to form fluid bubbles which persisted after the

Fig. 3.15 Electrodiffusion of doped quartz crystals

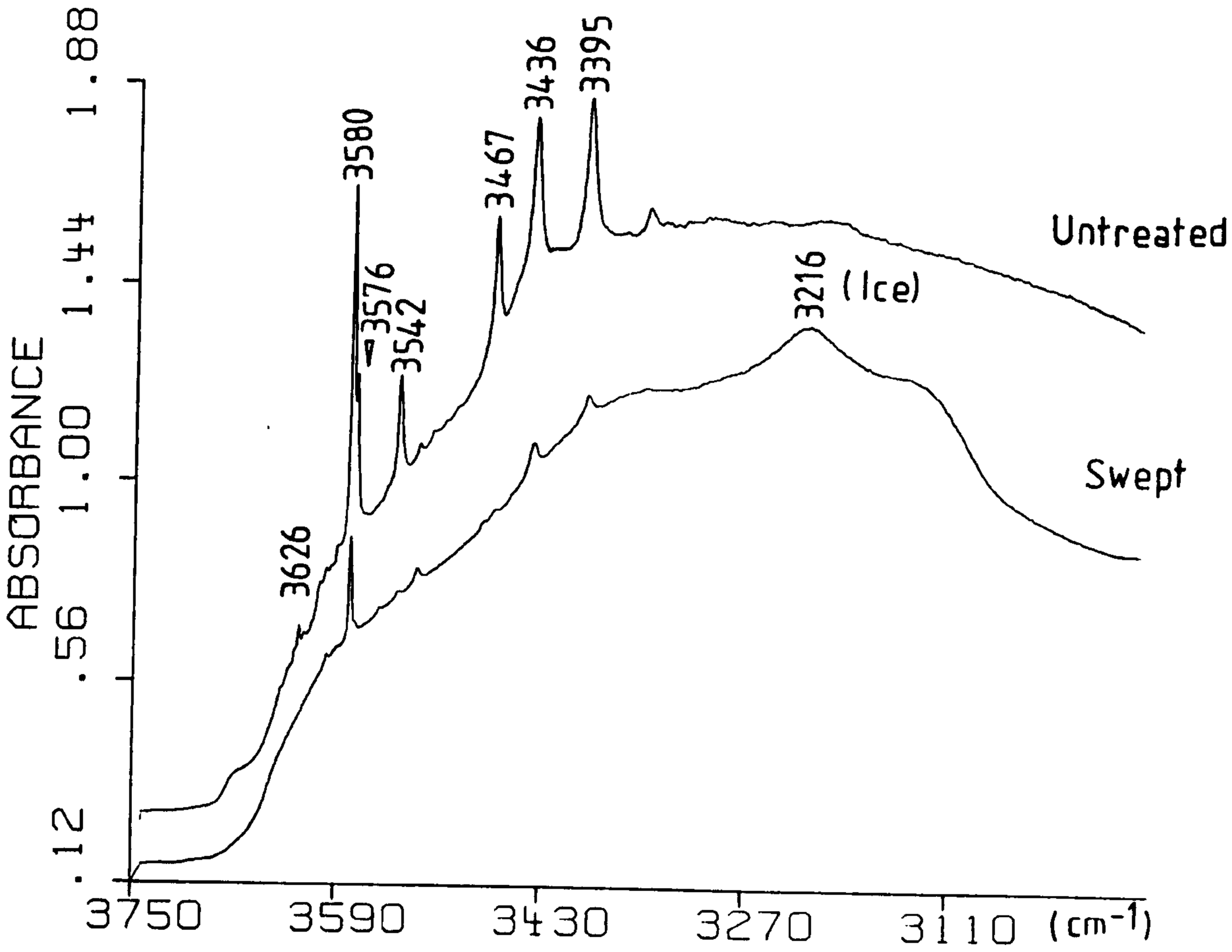

a) FEDHPQ.1

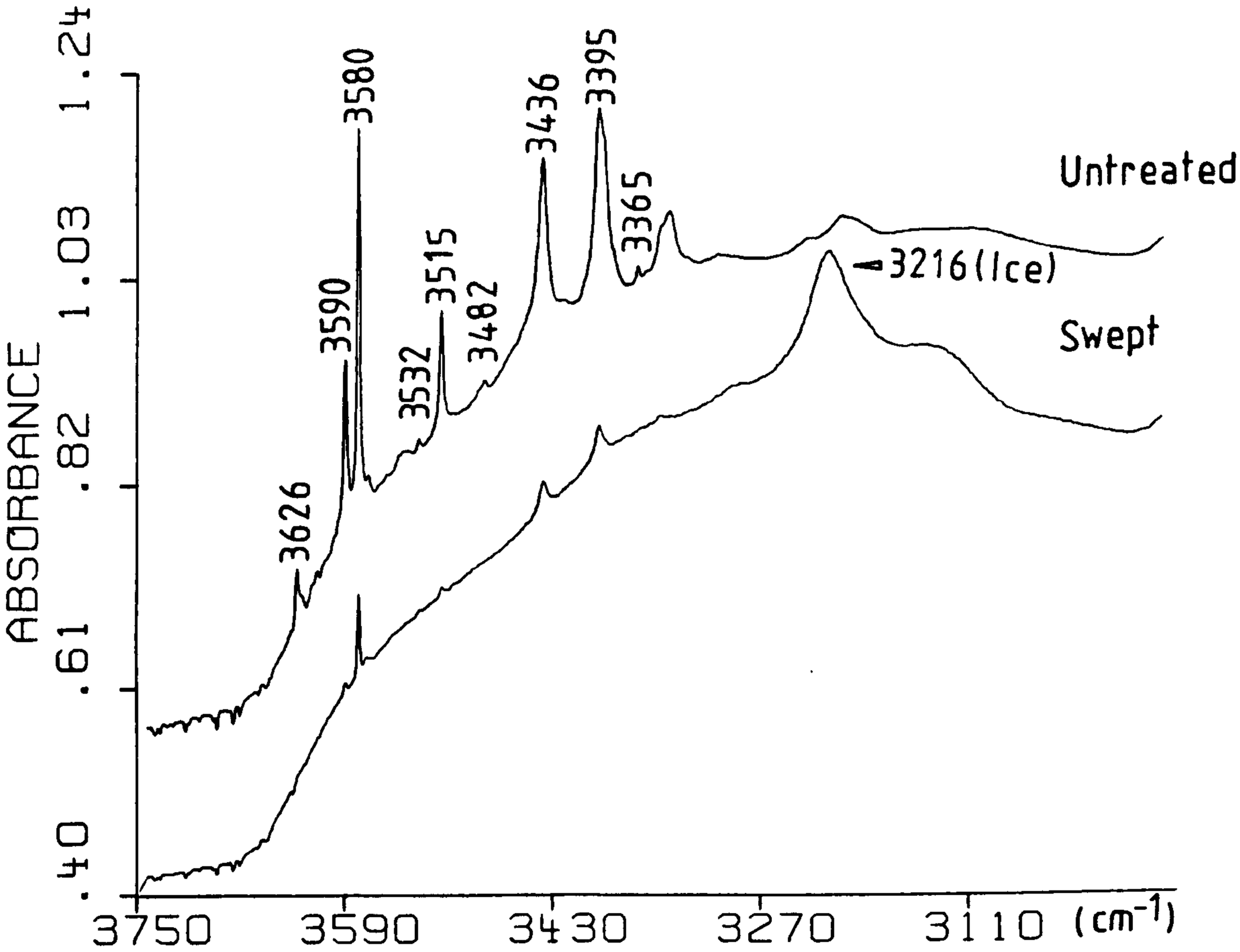

b) CRDHPQ.1

sample had returned to room temperature. The formation of bubbles was discussed by McLaren et al.[76] and Kekulawala et al.[137] who cited this as a mechanism for plastic deformation and hydrolytic weakening of synthetic quartz crystals. A possibility they did not explore was that the broad absorption band in untreated samples was produced by water molecules. The absence of the ice bands upon cooling quartz samples only suggests that the water is not present in fluid inclusions. The appearance of ice bands upon cooling of water is a consequence of the formation of a defined solid water structure[138]. If this structure was disrupted by a host crystal lattice then it could not form and no ice peaks would result from cooling.

This could explain the situation for water in quartz. The appearance of an increased hydrogen content in both rapidly grown and impurity rich materials suggests an uptake of fluid by the growing crystal. If this liquid did not form inclusions but was incorporated in the open quartz structure, the crystal lattice would disrupt and prevent the formation of a regular water structure, and the associated ice peaks, after the crystal was cooled. However, when a water rich sample is heated, these fluid molecules would expand and force their way out of the crystal lattice to congregate together producing fluid bubbles. These were observed in doped samples as an opaque, milky feature in the crystal bulk. The water in the bubbles would not be disrupted by the crystal lattice and would produce a solid ice structure on cooling of the sample

resulting in the appearance of ice peaks in sample spectra. The similarities between the spectra obtained from fast grown and doped crystals combined with the fact that after heating to 500°C, fast growth rate crystal HNACQ.1 became milky in appearance, indicates that water could be incorporated in the same way in both cases.

The results from the doped crystal study therefore suggest that the broad absorption peak present on rapidly grown and doped crystal spectra are caused by the presence of a high concentration of water interstitially incorporated into the quartz crystal structure.

3.3 Orientation of Hydrogen Species in Quartz

Information regarding the orientation of hydrogen associated impurities was obtained using polarised transmittance infrared spectroscopy. Previous research carried out by Walarafen and Luongo[102], studying commercial quartz, had indicated that hydrogen species were orientated along specific directions in a crystal. Unfortunately their studies were carried out at room temperature and the quality of quartz examined was poor. A spectrum of typical commercially grown quartz exhibits a very broad absorption band centred around 3200 cm^{-1}, which obscures any fine detail of hydrogen peaks at room temperature. However this work gave enough indication that impurities were aligned along preferential directions to justify an in-depth study and a preliminary case polarisation study at low temperature was carried out to confirm the accuracy of their conclusions and to expand upon them.

The polariser which was used for the polarisation studies would only pass radiation which possessed an associated electric vector which was perpendicular to the polariser grid line direction. Therefore, when the bond direction of an infrared absorbing species, and also therefore the electric vector associated with it, was perpendicular to the direction of the polariser grid lines, the intensity of the associated absorption peak on an infrared spectrum would be altered with respect to the unpolarised case. For the purposes of this thesis, radiation which was passed was said to be polarised

Fig. 3.16 Relationship Between the Polariser Grid Line Direction and the Growth Directions of X, Y and Z-Slice Quartz Samples

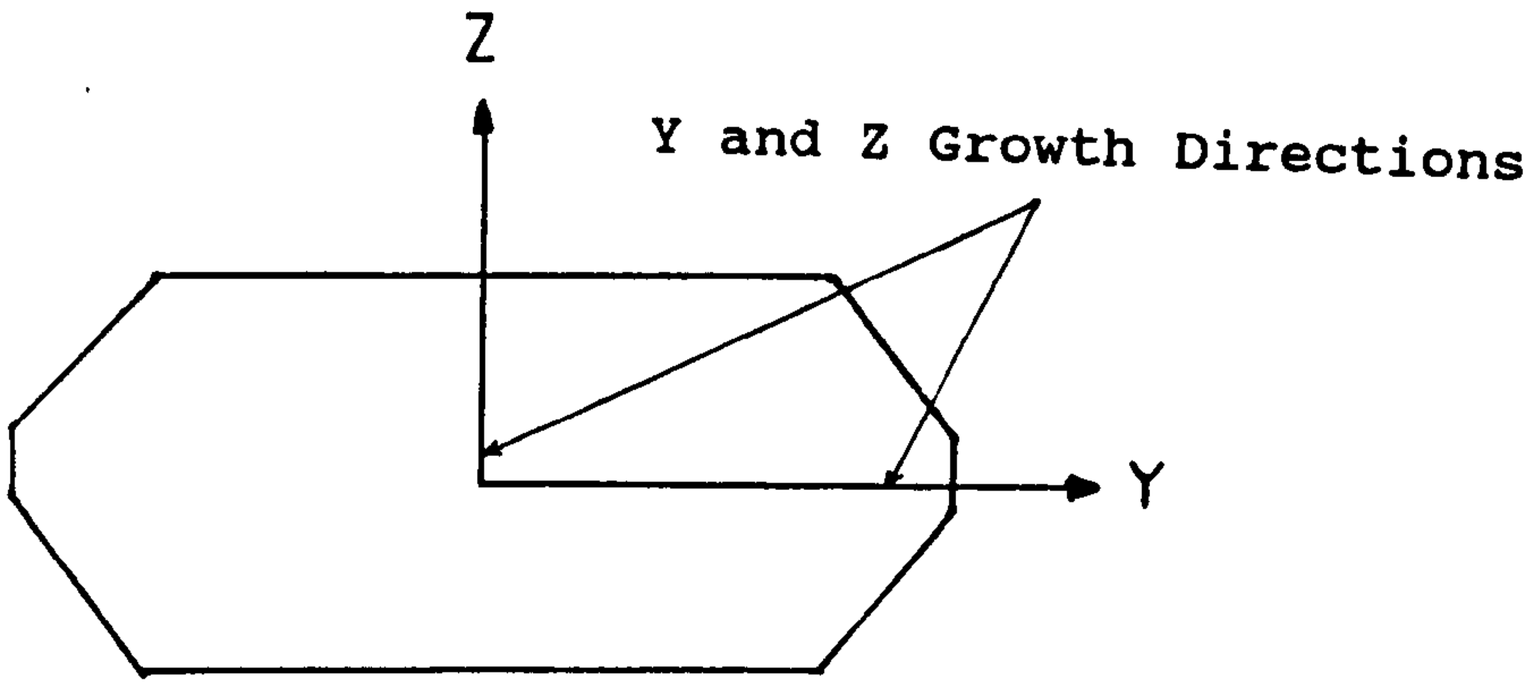

X-Slice

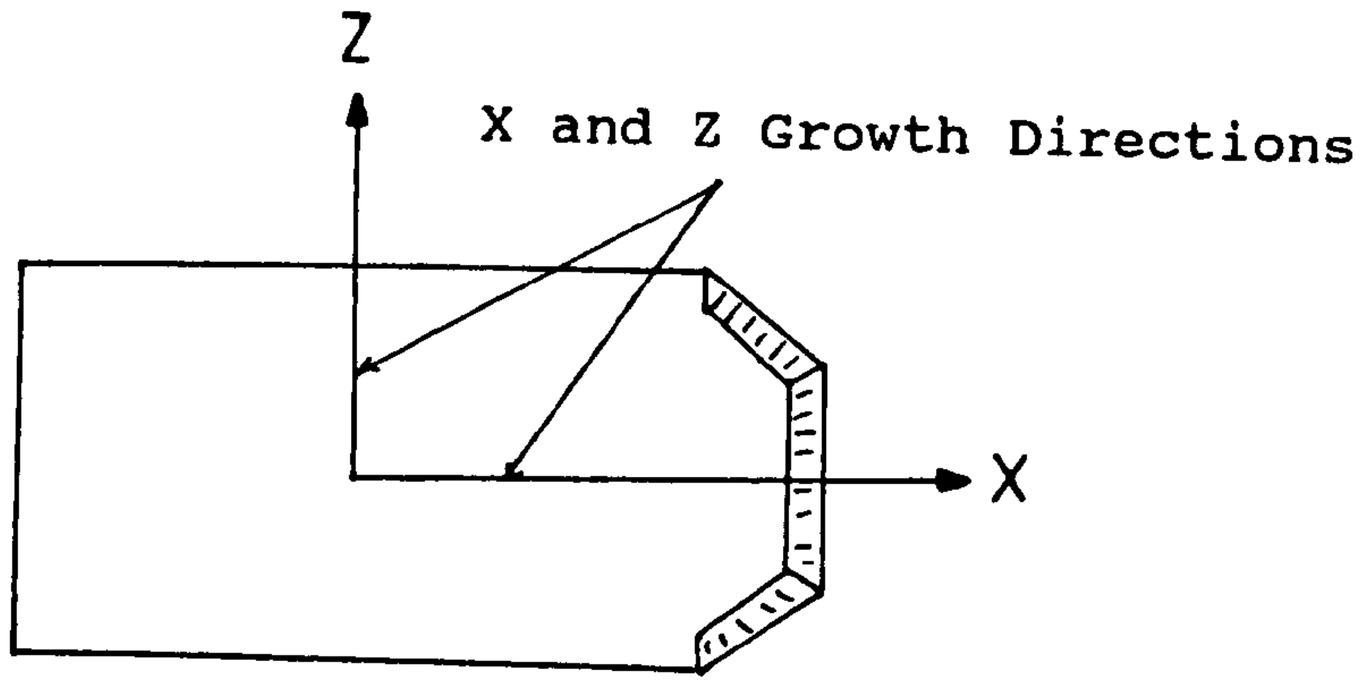

Y-Slice

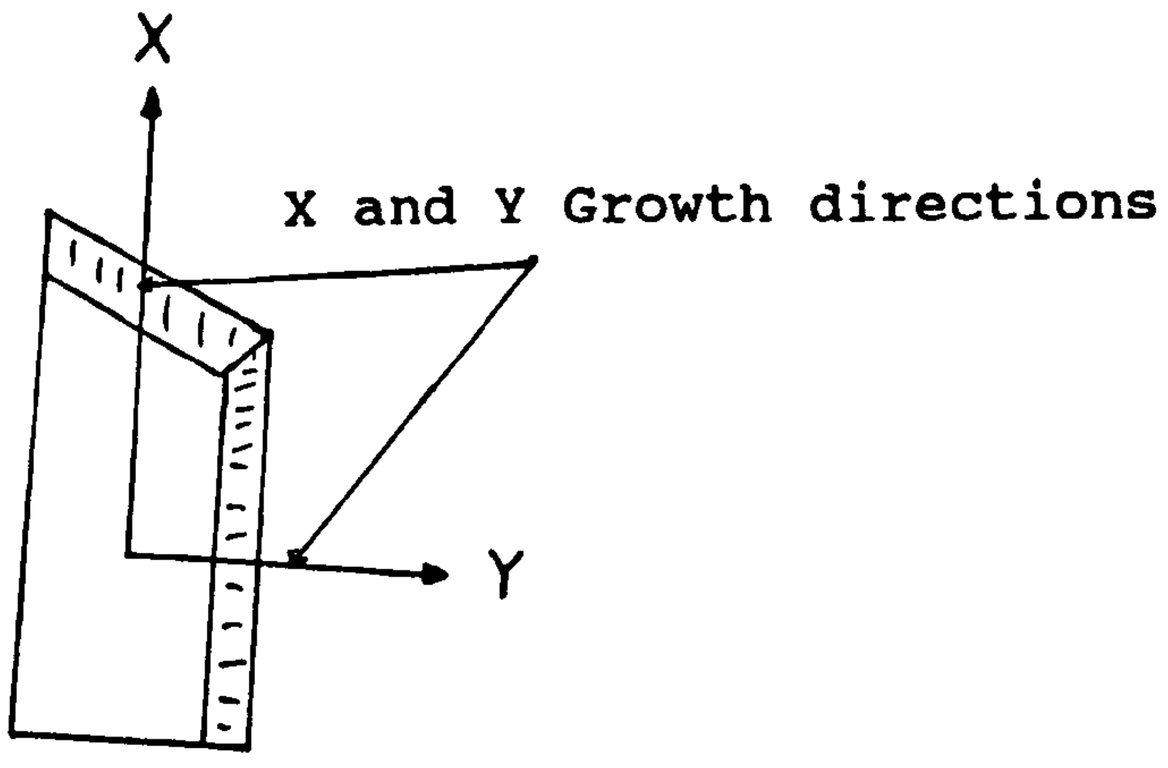

Z-Slice

Polariser grid Lines in the horizontal position 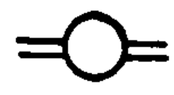

Polariser grid lines in the vertical position 

No Polariser 

in the direction of the electric vector eg. if the polariser grid lines were parallel to the X or Y growth direction then any radiation which was passed through the polariser would have an electric vector which was parallel to the Z-direction and the corresponding peak on the infrared spectrum would be denoted as being Z-polarised. The relationship between grid direction and polarised radiation for each crystal slice is summarised in figure 3.16. Normally the addition of a polariser can only decrease the intensity of absorption bands. However in the studies discussed in the following sections, several bands in polarised sample spectra were observed to increase intensity with respect to the unpolarised case. This was a direct consequence of the use of only one polariser. The addition of the polariser after an unpolarised spectrum has been obtained, changes the conditions under which the spectrum is recorded and complicates the direct comparison with the unpolarised sample spectrum. The analysing infrared beam of the FTIR spectrometer was tested to ensure that the radiation was randomly polarised. The polariser was found to transmit proportionally more radiation when the grid lines were in the vertical position. However this was not sufficient to account for the significant increases observed on several polarised sample spectra. The only acceptable explanation was that the combination of polariser addition and the alignment of O-H bonds focused the infrared radiation to produce the observed absorption band intensity increases. Consequently, to ensure that polarisation

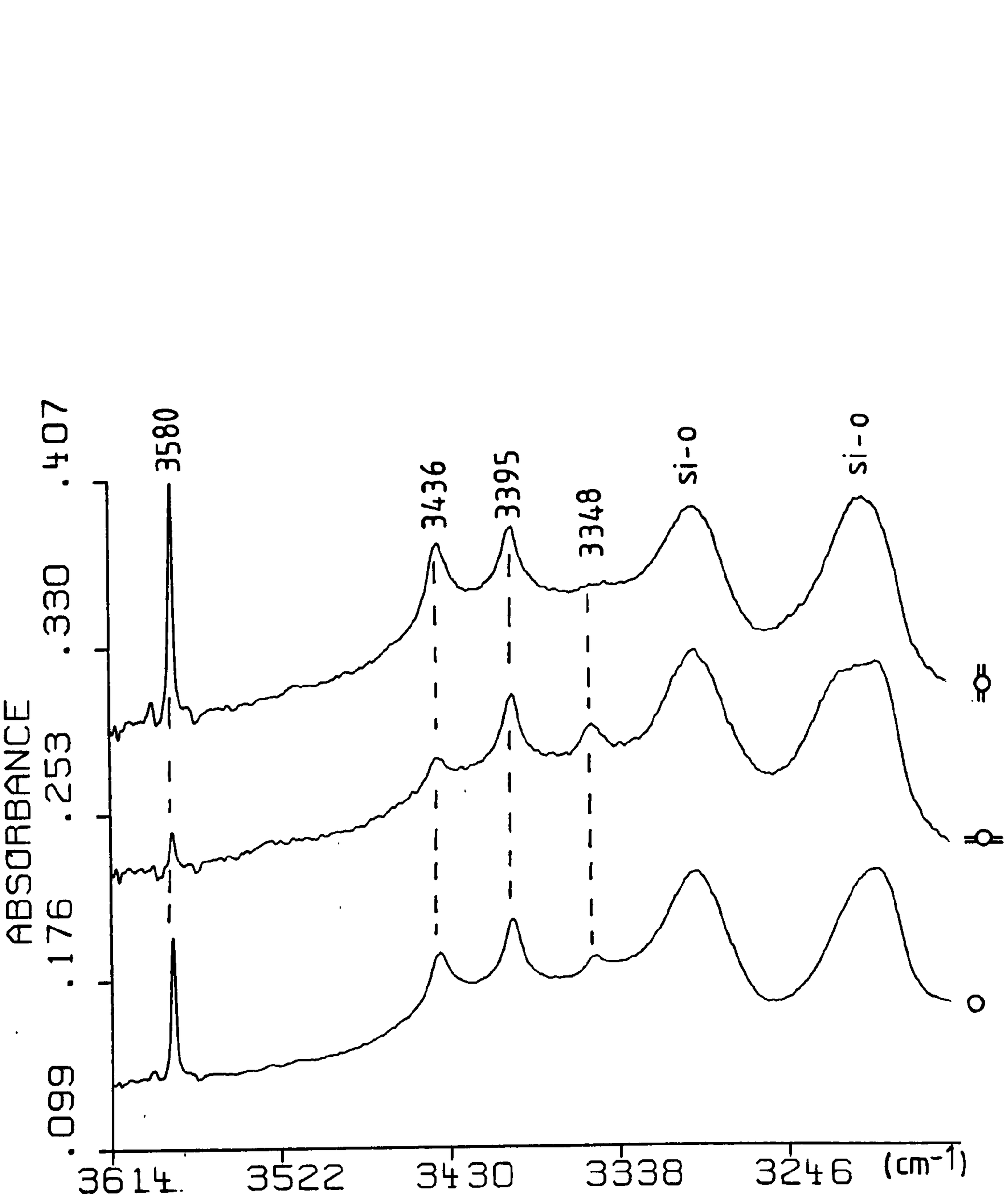

Fig. 3.17 Polarised IR spectra of X-slice crystal KVHPQ12

ratios were an accurate indication of O-H bond alignments, all polarisation calculations were normalized with respect to the relative intensities of absorptions compared with the band at 3395 cm^{-1} which had been reported by Walarafen and Luongo as being unaffected by polarisation.

3.3.1 High Purity Quartz Case Polarisation Study

This study involved examining a high purity quartz sample, KVHPQ12, supplied by Hirst laboratories. Infrared samples were cut normal to the three growth directions X, Y, and Z to enable the spatial orientation of the absorbing species to be studied. The preparation of these samples and the procedures used to collect the polarised spectra were outlined in sections 2.3 and 2.4 respectively.

The combined sample spectra obtained from the X-slice crystal are shown in figure 3.17. The unpolarised spectrum was virtually identical with that previously obtained from high purity quartz crystals. The characteristic absorptions of synthetic quartz at 3580, 3436, 3395 and 3348 cm^{-1} respectively were present as well as intrinsic Si-O lattice overtone and combination bands and a a weak absorption at 3590 cm^{-1} was also formed. The intensities of absorption bands at 3590 cm^{-1}, 3580 cm^{-1} and 3436cm^{-1} were reduced significantly when the polariser grid lines were parallel to the Y-direction (see tables 3.9 and 3.10). Therefore, since the radiation associated with the absorbing species did not pass through the polariser, the electric vector was not

Table 3.9 Polarisation Study of Crystal KVHPO12

Sample	ν_{O-H}**	Hydrogen Concentration (ppm)* 3580	3436	3395	3348	Total
X-Slice						
Unpolarised		0.943	0.904	1.354	0.253	3.454
PolH[a]		0.245	0.364	1.363	0.535	
PolV[c]		1.508	1.458	1.348	-	
Y-Slice						
Unpolarised		0.878	1.061	2.004	0.627	4.570
PolH[a]		0.117	0.543	1.929	1.048	
PolV[b]		1.393	1.540	1.929	0.126	
Z-Slice						
Unpolarised		1.121	1.085	1.040	-	3.161
PolH[a]		1.262	1.369	1.291	-	
PolV[b]		1.306	1.304	1.172	-	

* - Number of O-H groups per 10^6 SiO_2 molecules (see section 2.4.2)

** - Frequencies of O-H stretching vibrations associated with hydrogen impurities in quartz (units = cm^{-1})

a - Polariser grid lines parallel to the Z-Axis

b - Polariser grid lines parallel to the X-Axis

c - Polariser grid lines parallel to the Y-Axis

perpendicular to the grid line direction. This indicated that the alignment of these absorbing species was not parallel to the Z-axis of the crystal. The presence of weak absorption bands on the polarised spectrum suggests either inefficiencies associated with the polariser or a partial alignment along the Z-direction. The degree of polarisation given by the KRS-5 polariser which was used was quoted to be 95% in the manufacturers specification. The observed intensities were larger than could be accounted for by the error expected for this type of polariser. Therefore, there is probably a partial alignment of a component of the O-H bonds which produced the 3590 cm^{-1}, 3580 cm^{-1} and 3436 cm^{-1} absorption bands along the Z-direction. The intensity of the three absorptions increased, with respect to the unpolarised values, when the polariser grid lines were positioned parallel to the Z-direction. In this case, the radiation had passed through the polariser and so the electric vector was aligned at right angles to the polariser grid direction. This shows that the major component of both the electric vector and the associated bond direction of the absorbing species was aligned along the Y-axis of the crystal.

The absorption band at 3348 cm^{-1} showed the opposite polarisation behaviour to that of the three peaks already discussed (see tables 3.9 and 3.10). This absorption virtually disappeared when the polariser grid lines were parallel to the Z-direction. It follows from this that the electric vector of this O-H bond could not lie along the Y-direction and there

Table 3.10 Polarisation Ratios for Crystal KVHPO12

	X-Slice		Y-Slice		Z-Slice	
ν_{O-H}*	Pol H[a]	Pol V[b]	Pol H[c]	Pol V[b]	Pol H[a]	Pol V[b]
3580	-74	+60	-86	+65	-8	+3
3436	-60	+62	-47	+51	+2	+7
3395	± 0	± 0	± 0	± 0	± 0	± 0
3348	+110	-100	+73	-79	-	-

* - Frequencies of O-H stretching vibrations associated with hydrogen impurities in quartz (units = cm^{-1})

a - Polariser grid lines parallel to the Y-Axis

b - Polariser grid lines parallel to the Z-Axis

c - Polariser grid lines parallel to the X-Axis

Note - Polarisation ratios were calculated with respect to the intensity of the 3395 cm-1 absorption band. The values given in the above table are the percentile change between the polarised and the unpolarised ratios for each absorption band.

was no alignment of the bonds themselves along this direction. The absorption reappears in the spectrum taken when the polariser grid lines were running parallel to the Y-direction. The electric vector must be perpendicular to the polariser grid lines for this to occur. Therefore the O-H bonds associated with this absorption are aligned along the Z-axis of the crystal.

The intensity of the remaining absorption at 3395 cm^{-1} was virtually unaffected by the position of the polariser (see tables 3.9 and 3.10). However, since the polariser will only pass radiation which has an electric vector perpendicular the grid line direction, the direction of the O-H bonds must have components which lie equally along both the Y and Z directions. There is also the possibility that the bonds are aligned along an intermediate position such as 45° between the two axes. To establish the bond positions with greater accuracy requires the examination of samples taken from different crystal cuts.

The Y-slice sample showed very similar polarisation behaviour to the X-slice sample (see fig 3.18). In this case the intensities of the unpolarised absorption bands were greater than those recorded for the X-slice and there were additional weak absorptions at 3515 cm^{-1} and 3366 cm^{-1} (see table 3.10). This can be explained either by better thermal contact between the Y-slice crystal and the cold finger of the cryostat or by a higher concentration of hydrogen related impurities in this crystal slice. Of these explanations,

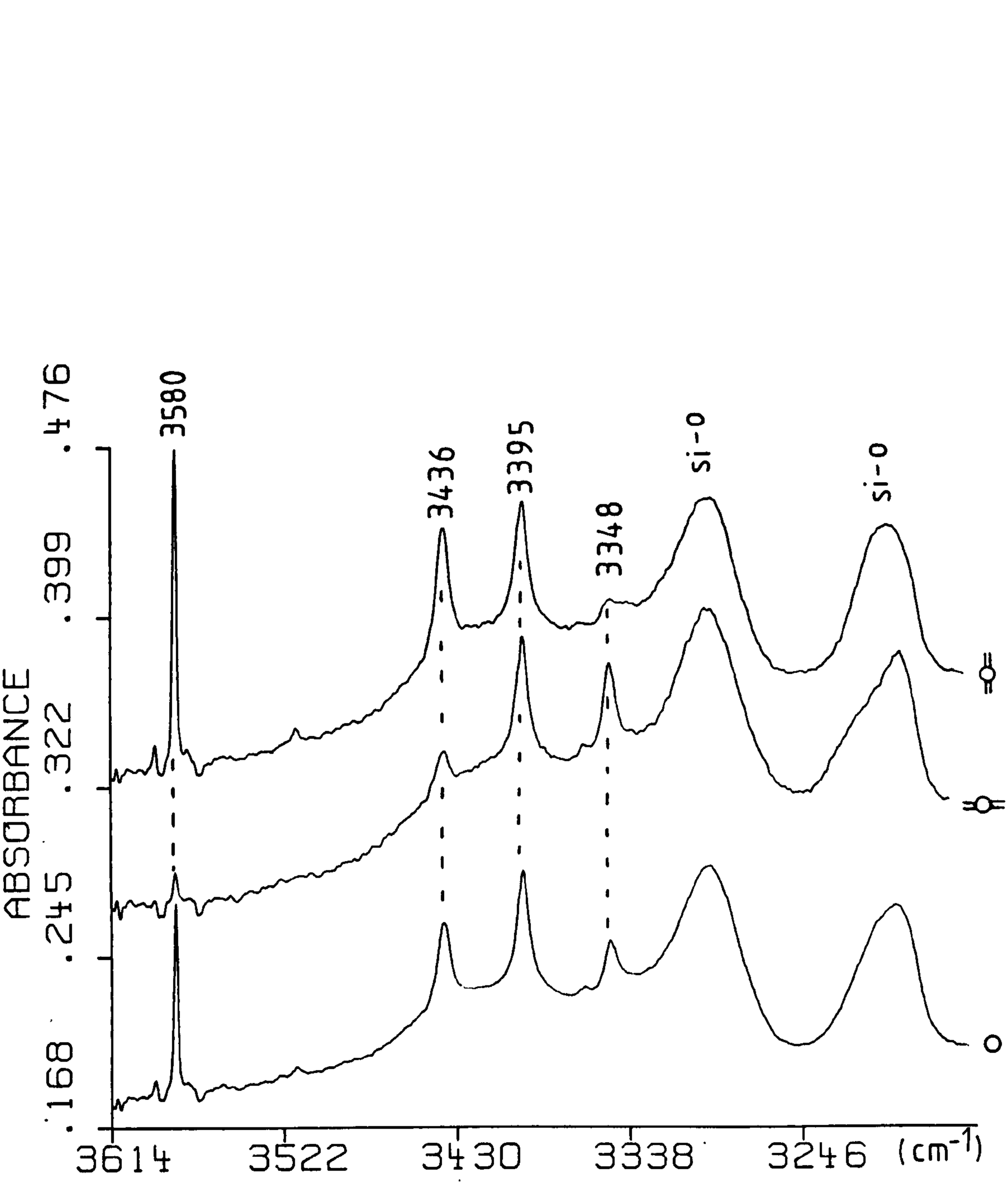

Fig. 3.18 Polarised IR spectra of Y-slice crystal KVHPQ12

thermal contact is the most likely solution because the content and distribution of infrared active hydrogen species has been found to vary very little for high purity samples studied in this project (see section 3.1). The absorptions at 3590, 3580, 3515 and 3436 cm-1 respectively were greatly reduced in intensity when the polariser grid lines were parallel to the X-axis (see tables 3.9 and 3.10). The weaker 3590 and 3515 cm^{-1} absorptions disappeared completely and the other bands were reduced by a degree similar to that observed for the same absorptions in X-slice spectra. Therefore, although the bond directions associated with these absorptions were not aligned along the Z-direction, the presence of the weak bands in the spectrum indicates a component along that axis. When the polariser was moved through ninety degrees, the four absorptions reappeared on the spectrum. Their intensities had increased in comparison with the 3395 cm^{-1} absorption band, thereby indicating an alignment of the O-H bonds for this configuration of the polariser (see tables 3.9 and 3.10). In this case the polariser grid lines were parallel to the Z-direction and for the radiation to pass required the electric vector to be perpendicular to this direction. Therefore, the corresponding bond directions of the absorbing species were aligned along the X-axis. The absorptions at 3395 cm^{-1} and 3347 cm^{-1} were polarised in exactly the same way as was observed for the X-slice crystal (see tables 3.9 and 3.10). The 3347 cm^{-1} absorption was only present in the spectrum taken when the polariser grid line direction was

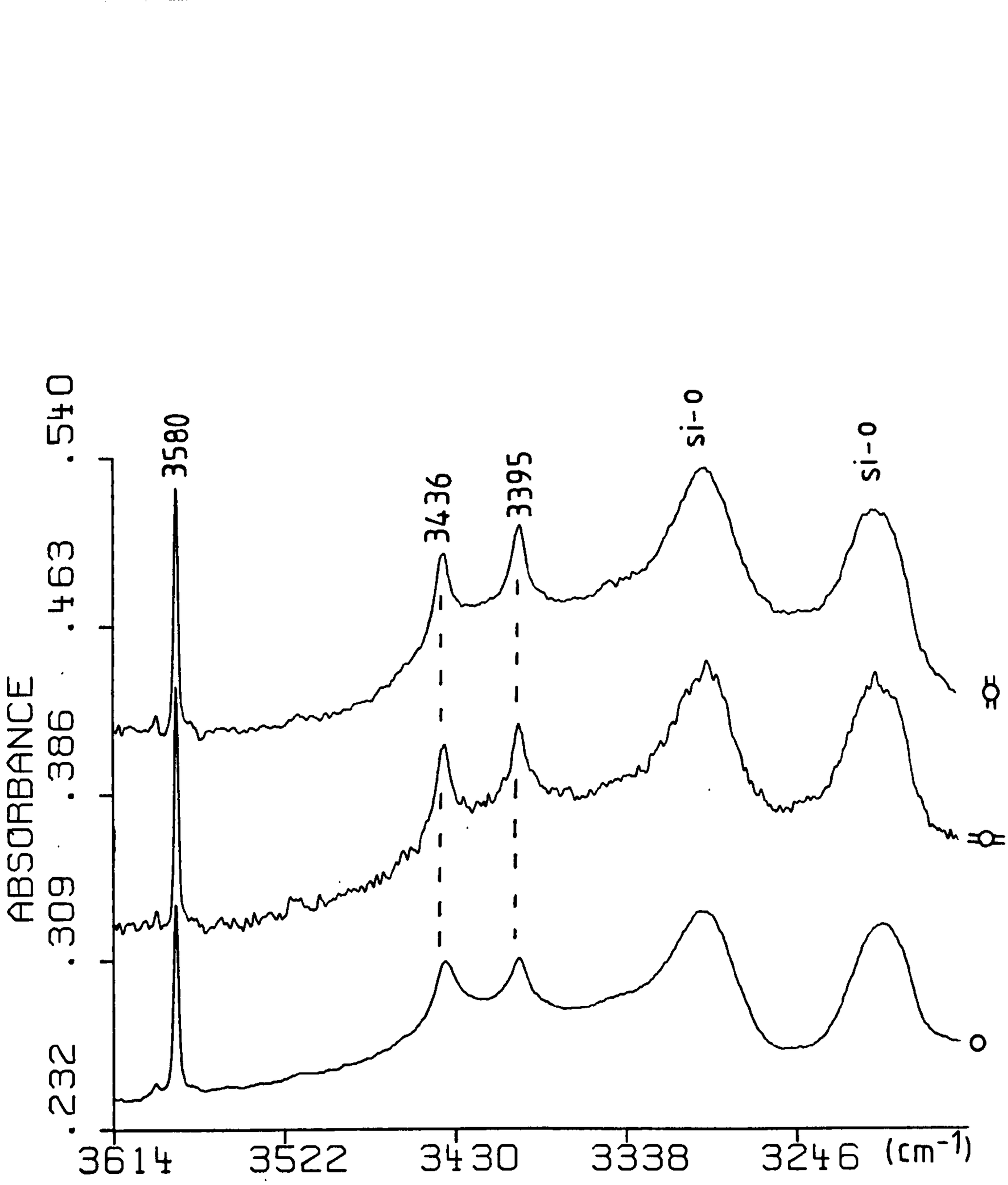

Fig. 3.19 Polarised IR spectra of Z-slice crystal KVHPQ12

parallel to the X-axis. This shows the O-H bonds associated with this absorption to be aligned parallel to the Z-direction. The 3395 cm^{-1} absorption as well as the new 3366 cm^{-1} peak were unaffected by the position of the polariser and were therefore not aligned preferentially along either the X or Z axis.

The final crystal cut that was examined was the Z-slice (see fig. 3.19). The only hydrogen related absorptions in the unpolarised spectrum were those at 3590, 3580, 3515 and 3395 cm^{-1} respectively (see table 3.9). There was no absorption at 3348 cm^{-1} and none of the absorption bands present were significantly affected by the position of the polariser (see tables 3.9-10).This was not altogether unexpected considering that the polariser grid lines were parallel to either the X or the Y axis in both the vertical and horizontal polariser positions and, with the exception of the 3395 cm^{-1}, 3366cm^{-1} and the 3347cm^{-1} bands, all previously discussed absorbing species have been aligned along these axes. For infrared radiation to pass through the polariser, in the case of the Z-slice, requires the electric vector of the radiation associated with the absorbing species to be perpendicular to either the X or the Y axes. Since the absorptions at 3590 cm^{-1}, 3580 cm^{-1} and 3436 cm^{-1} were present in approximately equal relative intensities for both polariser orientations, alignment of O-H bonds associated with these peaks must be aligned either equally along each axis or be aligned at 45° to both. The missing band at 3348 cm^{-1} can be

explained by considering the crystal cut. The absorption is polarised along the Z-axis in each of the previously discussed crystal slice cases and so the electric vector will be parallel to this axis. The O-H bonds of the 3348 cm^{-1} absorbing species will be aligned along the Z-axis of the crystal and will not be in the correct position to absorb infrared radiation. Therefore , the absorbing species associated with the 3348 cm^{-1} absorption band will not produce a band on the infrared spectrum of a Z-crystal slice. The band at 3395 cm^{-1} was again unpolarised in either polariser position. This indicated that the O-H bonds associated with this absorbing species were aligned equally along both the X and Y axes. However, in all the polarised sample spectra discussed so far, this absorption band was unaffected by polarisation. Therefore the bond directions were either equally aligned along all three growth directions or were randomly distributed throughout the crystal. The total lack of polarisation tends to suggest the latter as the more likely option.

The interpretation of this polarisation study shows a definite orientation of three of the four characteristic infrared peaks present in spectra of synthetic quartz. The O-H bonds producing the peaks at 3580 and 3436 cm^{-1} are aligned along both the X and Y axes. Differences in relative intensities of hydrogen species observed in the unpolarised spectra of the three samples were assumed to be caused by differences in thermal contact with the cold finger and not

due to differences in hydrogen concentrations. The increase in intensity of the two peaks when the polariser grid was parallel to the Z-axis shows that the O-H bonds are not perfectly aligned along the X and Y axes but possess some Z component also. However the absence of polarisation on Z-slice samples indicates that the hydrogen species either have no specific orientations on the X-Y plane with respect to the Z-axis or were equally aligned along both the X and the Y directions. In either case, polarisation data suggests that the O-H bonds lie in the X-Y plane slightly tilted towards the Z-direction. The absence of the 3348 cm^{-1} on Z-slice spectra indicates that the O-H bond of the species associated with this peak is aligned directly along the Z-axis. The bond is never in any position to absorb infrared radiation when viewed using a Z-slice sample. The polarisation studies on X and Y slices confirm this orientation as the 3348 cm^{-1} peak always disappeared when the polariser grid was parallel to the Z-axis. The species associated with the 3395 cm^{-1} peak showed no polarisation in any polariser position for any crystal slice. The relative intensities of the peak in all three sample spectra was approximately constant. This indicates a completely random distribution of this species throughout the sample.

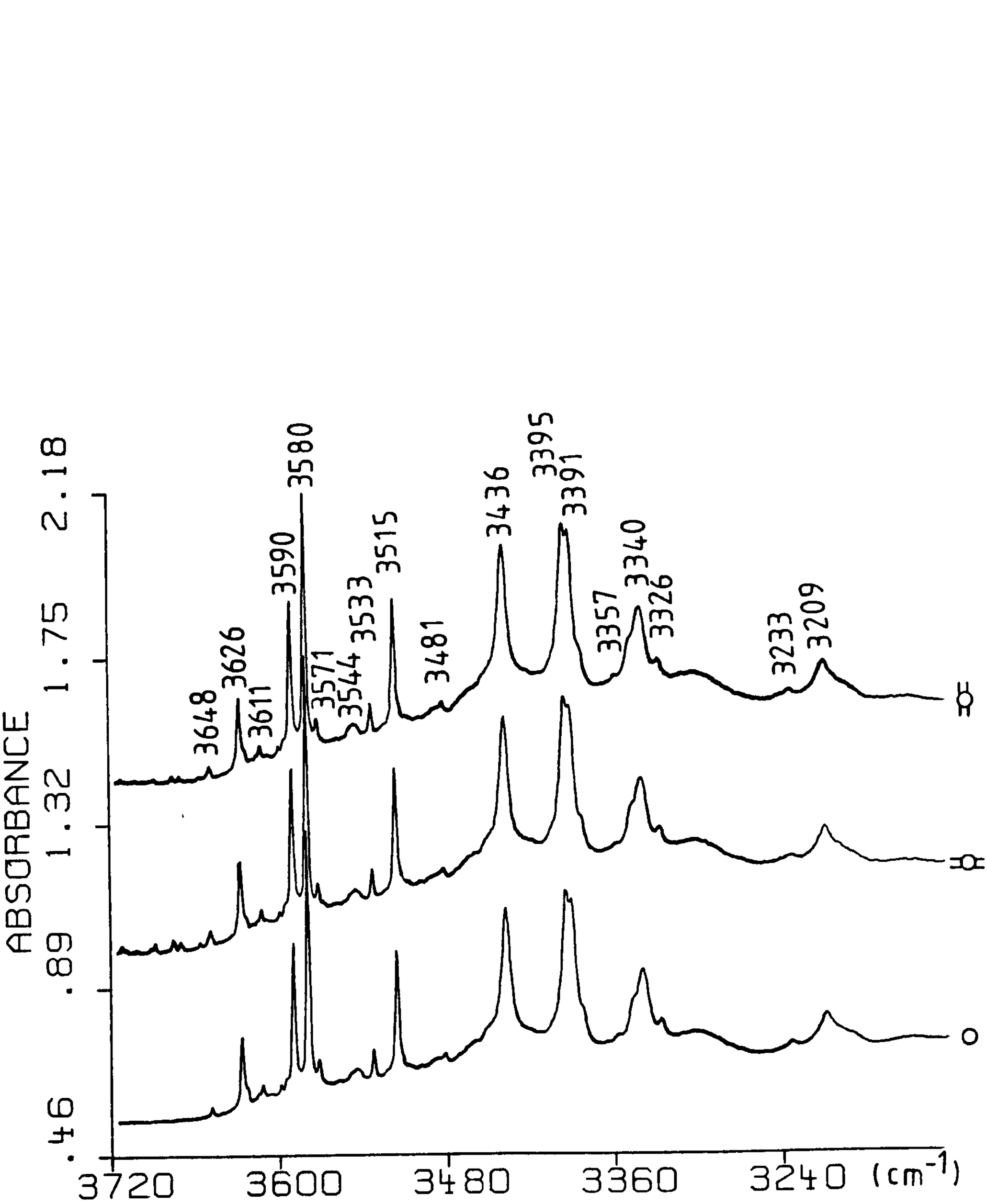

Fig. 3.20 Polarised IR spectra of Z-slice crystal R6

3.3.2 Impure Quartz Polarisation Study

This study was carried out in the same fashion as discussed in the previous section with the exception that the three crystal cuts were taken from a sample produced by growth run 16. This crystal showed a considerably increased hydrogen content in comparison with high purity samples which was attributed to a higher impurity concentration (see section 3.2). This was thought to be a consequence of using a sodium carbonate mineraliser which has significantly higher levels of impurity than the sodium hydroxide which was normally used for high purity growth (see table 2.3). This resulted in many more absorptions being present in sample spectra in comparison to the four bands seen in the high purity case (see table 3.11).

However, although the sample spectra were considerably more complex than those discussed earlier, the same polarisation behaviour was observed. The absorptions present in the Z-slice sample spectra were unaffected by the polariser position (see fig. 3.19 and table 3.11). The absorption at 3348 cm^{-1} was present in sample spectra but only as a broad shoulder on a peak at 3340 cm^{-1}. Absorptions in X and Y slice sample spectra again showed identical polarisation behaviour (see figs. 3.21 and 3.22). The polarisation behaviour of the absorption bands is summarised in tables 3.12 and 3.13. For the purposes of this summary, only a decrease in the relative band intensity upon polarisation of an absorption was considered important.

Group 1 absorptions were greatly reduced in intensity when

Table 3.11 Polarisation Study of Crystal R16

	Hydrogen Concentration (ppm)*						
	X-Slice			Y-Slice			Z-Slice
ν_{O-H}**	NoP[a]	PolH[b]	PolV[c]	NoP[a]	PolH[b]	PolV[d]	All[e]
3648	0.670	0.387	0.275	0.239	0.277	0.209	0.152
3626	2.997	1.318	4.262	0.852	0.513	1.136	2.238
3611	0.125	0.000	0.350	-	-	-	0.090
3590	3.062	0.304	8.331	2.379	0.075	5.556	5.107
3580	7.553	1.176	13.262	4.490	0.395	10.463	8.887
3571	0.310	0.039	0.862	0.178	0.086	0.336	0.350
3544	0.730	0.000	1.180	-	-	-	0.620
3533	0.837	0.481	1.213	0.470	0.266	0.765	0.716
3515	3.664	0.906	6.634	2.370	0.262	4.640	4.262
3481	0.208	0.123	0.291	-	-	-	0.152
3436	11.816	6.903	21.632	7.621	3.593	14.905	11.840
3395	22.184	21.237	23.612	12.983	11.907	14.847	19.631
3365	0.140	0.336	0.000	0.057	0.142	0.000	-
3348	10.373	16.015	-[f]	6.617	9.457	-[f]	-[f]
3326	0.362	0.000	0.518	0.159	0.000	0.270	-
3233			See Notes				
3209			See Notes				
Total	65.031			38.415			54.045

* - Number of O-D groups per 10^6 SiO_2 molecules (see section 2.4.2)

** - Frequencies of O-D stretching vibrations associated with hydrogen impurities in quartz (units = cm^{-1})

a - No polariser

b - Polariser grid lines parallel to the Y-Axis

c - Polariser grid lines parallel to the Z-Axis

d - Polariser grid lines parallel to the X-Axis

e - Values are identical for all polariser positions

f - Band appears as a shoulder on the 3340 cm^{-1} band

Notes - The absorption bands at 3233 and 3209 cm^{-1} were too broad to be accurately distinguished from the background of the spectrum. However the bands were observed to completely disappear when the polariser grid line direction was parallel to the X and Y axes and increase when this was parallel to the Z-axis.

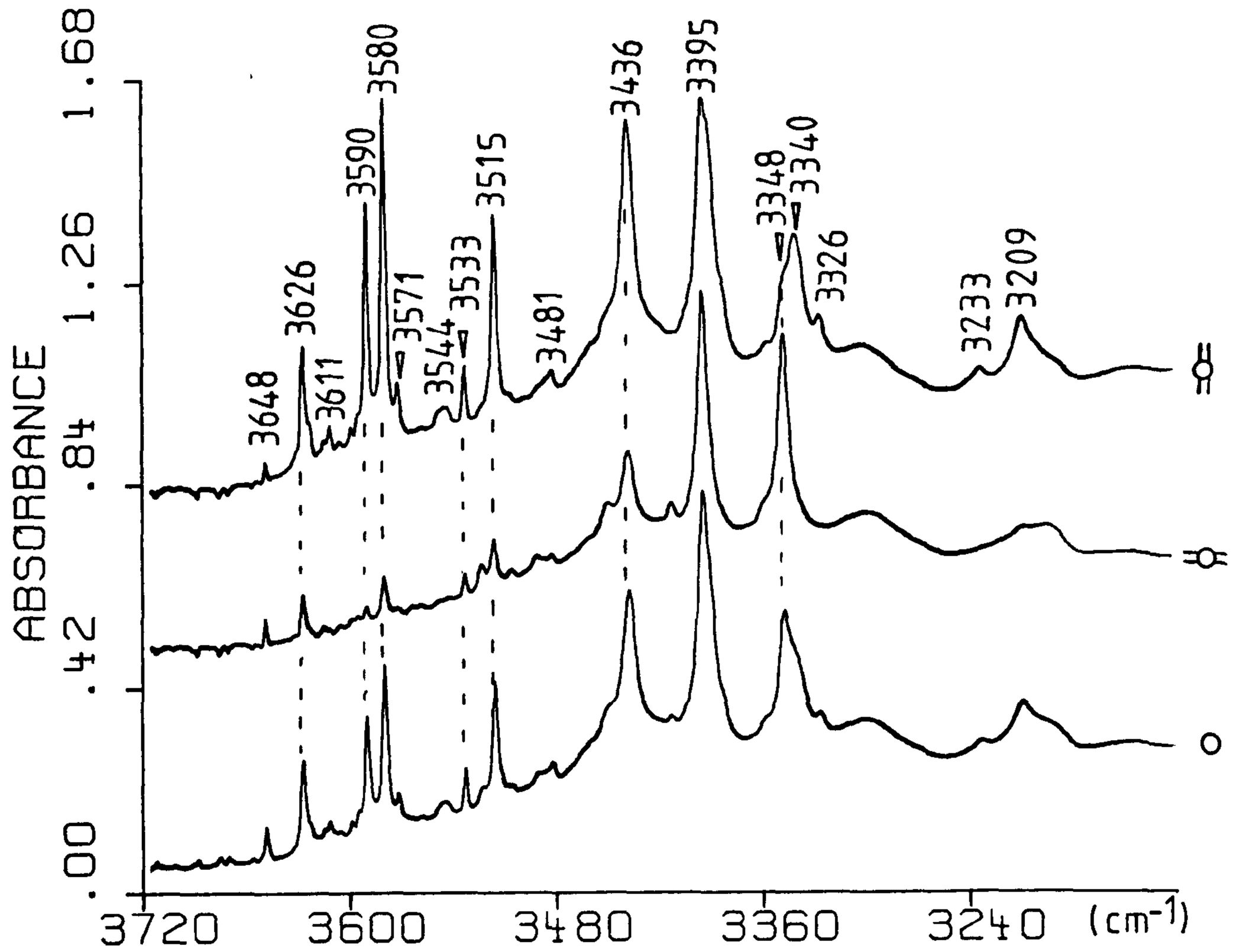

Fig. 3.21 Polarised IR spectra of X-slice crystal R6

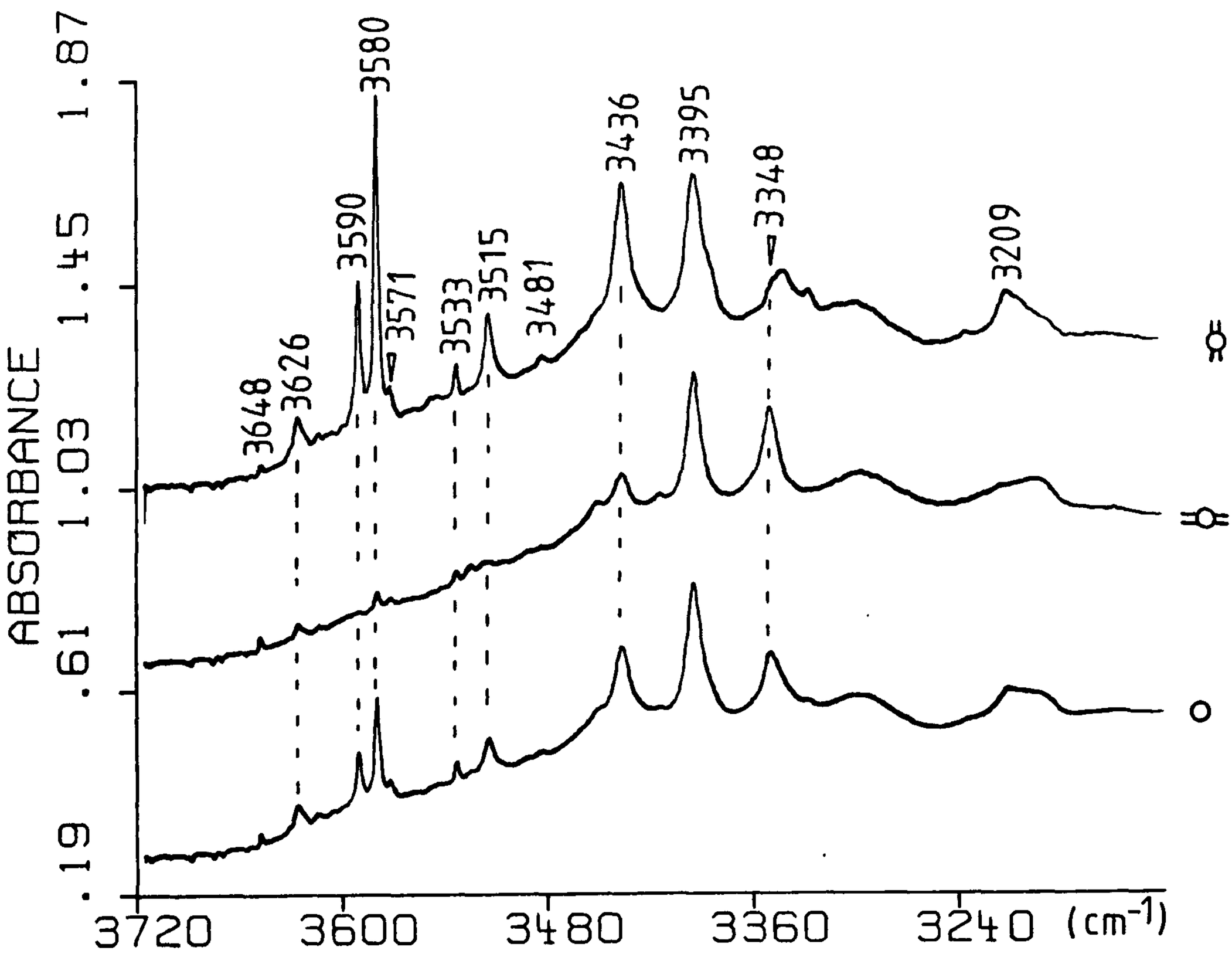

Fig. 3.22 Polarised IR spectra of Y-slice crystal R6

the polariser grid lines were aligned along either the X or the Y axis. This indicated that the electric vector, and therefore the O-H bond direction of the absorbing species, did not lie along the Z-axis. The increase in intensity of group 1 absorptions, in relation to the 3395 cm^{-1} band intensity, when the polariser grid lines were parallel to the Z-axis showed that there was an alignment of O-H bonds equally along the X and the Y-directions. Polarisation ratios shows that there was only a partial alignment of approximately 10% alignment of O-H bond directions along the Z-direction. This alignment was not as significant when compared to the alignment along the X and Y axes. Therefore the O-H bonds of the species which were associated with group 1 frequencies were preferentially aligned approximately parallel with the X-Y plane but with a partial orientation towards the Z-axis.

The O-H bonds of the impurity species which produced group 2 absorption bands were identical to those of group 1 but were not as highly aligned. A much greater Z-component was evident for group two absorptions.

Group 3 absorptions were virtually eliminated when the polariser grid lines were parallel to the Z-axis, but were greatly increased when the lines were aligned along either the X or the Y axis. This showed that the O-H bonds of the species producing the absorption bands were preferentially aligned parallel to the Z-axis.

Group 4 absorption bands showed no significant intensity change for any polariser position. The O-H bonds of these

Table 3.12 Polarisation Ratios for Crystal R16

	X-Slice		Y-Slice	
ν_{O-H}*	Pol H[a] (%)	Pol V[b]	Pol H[c] (%)	Pol V[b]
3648	-40	-60	+28	-22
3626	-54	+33	-35	+15
3611	-100	+150	-	-
3590	-91	+56	-97	+104
3580	-84	+65	-90	+104
3571	-87	+57	-94	+64
3544	-100	+51	-	-
3533	-40	+34	-39	+42
3515	-74	+71	-86	+71
3481	-33	+33	-	-
3436	-39	+87	-49	+71
3395	± 0	± 0	± 0	± 0
3365	+160	-100	+200	-100
3348	+60	-100	+56	-100
3326	-100	-37	-100	+50

* - Frequencies of O-H stretching vibrations associated with hydrogen impurities in quartz (units = cm^{-1})

a - Polariser grid lines parallel to the Y-Axis

b - Polariser grid lines parallel to the Z-Axis

c - Polariser grid lines parallel to the X-Axis

Note - Polarisation ratios were calculated with respect to the intensity of the 3395 cm-1 absorption band. The values given in the above table are the percentile change between the polarised and the unpolarised ratios for each absorption band.

Table 3.13 Summary of Polarisation Studies

	Frequency of Infrared Absorption Band (cm-1)
Group 1 (> 70% change)	3611, 3590, 3580, 3571, 3544, 3515, 3326, 3233, 3209
Group 2 (40-70% change)	3626, 3533, 3436,
Group 3 (100% change)	3365, 3348
Group 4 (< 40% change)	3648, 3481, 3395

Group 1 - O-H bonds preferentially aligned along both the X and Y growth axes

Group 2 - O-H bonds preferentially aligned along both the X and Y growth axes

Group 3 - O-H bonds preferentially aligned along the Z growth axis

Group 4 - Absorption bands show no significant preferential alignment

species were therefore either aligned equally along all three axes or more probably were randomly orientated throughout a crystal. Confirmation of which of these was the correct solution could not be established from the polarisation studies carried out in this thesis.

3.3.3 Band Intensity Variations in Unpolarised Spectra

A feature which was more pronounced in the impure, as opposed to the high purity, quartz study was the variation in absorption band intensities in unpolarised spectra obtained from different crystal cuts. In the high purity study, these variations were slight and most obvious on the Y-slice spectra (see fig. 3.23 and table 3.9) with the only major difference being an increase in the intensities of the 3395 cm^{-1} and 3348 cm^{-1} bands. The band intensities for the X and Z-slice sample spectra were very similar. This observation could easily be accounted for by better thermal contact for the Y-slice sample in comparison with these samples. Previous spectra of high purity quartz samples show that the hydrogen concentrations do not vary to any great extent for this type of crystal (see section 3.1b). The validity of the thermal contact hypothesis was confirmed by securing the X-slice sample to the cryostat cooling block and recorded the spectrum again. The second spectrum compared favourably with the Y-slice sample spectrum, thereby confirming the differences in unpolarised band intensities were due to differences in sample cooling in the case of the high purity samples.

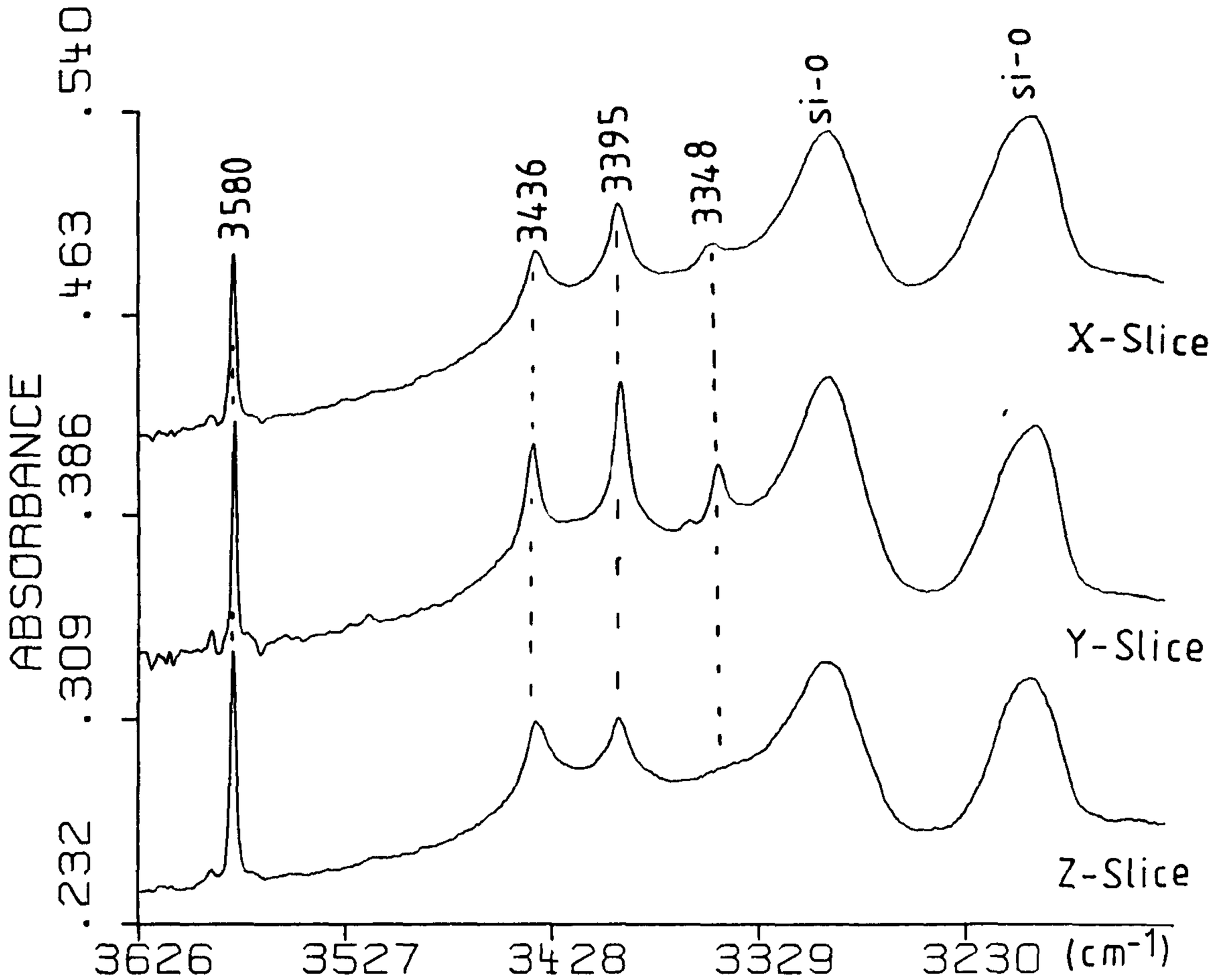

Fig. 3.23 Unpolarised IR spectra of crystal KVHPQ12

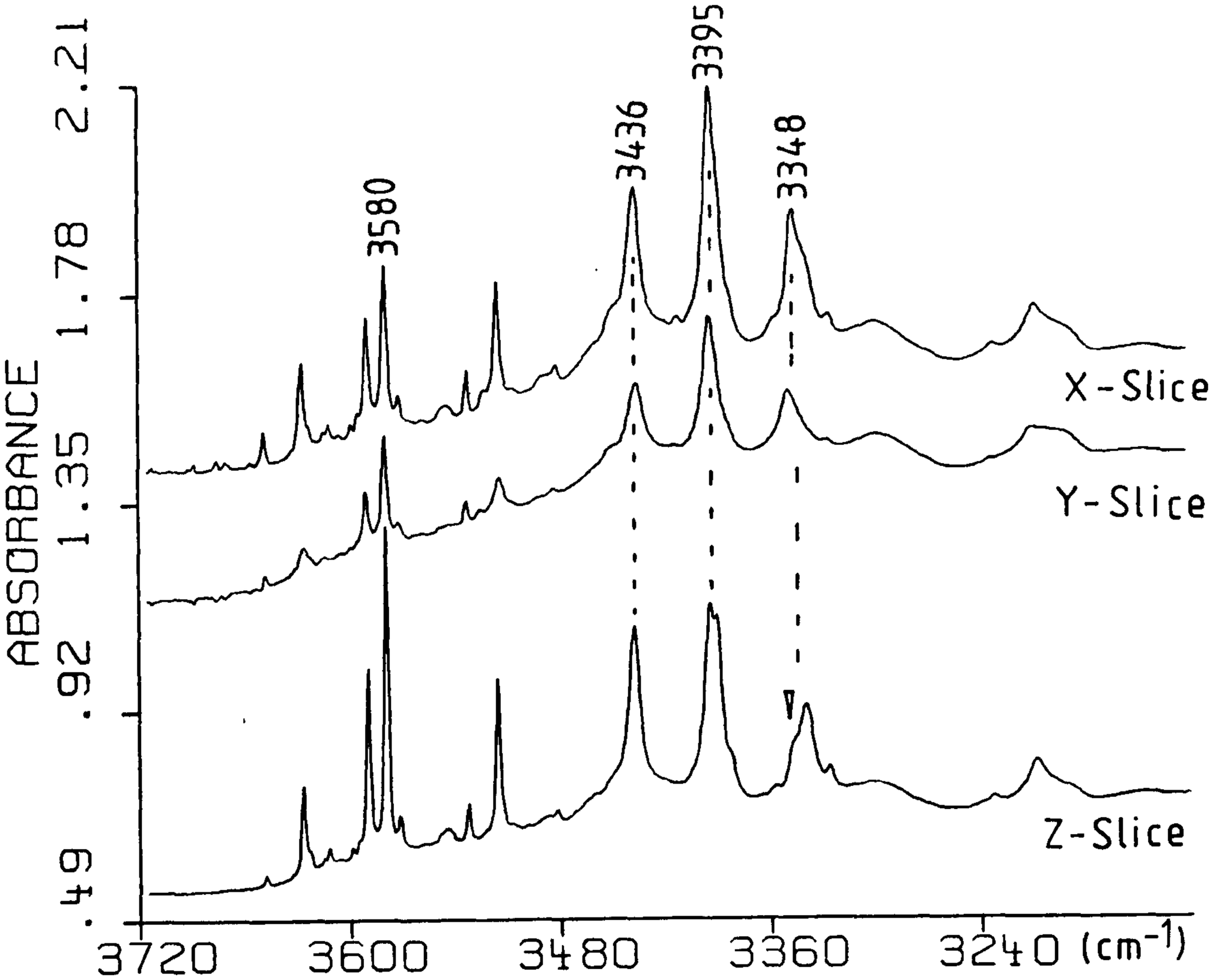

Fig. 3.24 Unpolarised IR spectra of crystal R16

However this argument does not sufficiently explain the significant variations observed in the impure sample polarisation study (see fig.3.24 and table 3.11). In this case the thermal contact was not to blame for the band intensity differences because samples were firmly secured to the cooling block. Lipson et al.[91] reported intensity variations in their unpolarised infrared study of X, Y and Z-slice samples. These authors accounted for the intensity variations by attributing them to polarisation effects. However the studies carried out in this thesis and those by Walafaren and Luongo[102] conclusively show that the absorption band at 3395 cm^{-1} was not polarised in any sample configuration or polariser position. The intensities of that band do change depending on what crystal cut is examined thereby ruling out that the intensity variation is a polarisation effect. The most plausible explanation is that the distribution of hydrogen associated species is random throughout the lattice and will vary depending on what crystal cut is examined. There seems to be no preferred crystal cut which shows the highest overall hydrogen content. This was evident from the Y-slice exhibiting the highest hydrogen content in the case of the high purity study but showing the lowest content in the impure crystal study (see figs. 3.23 and 3.24 respectively). Hydrogen content has been shown to vary dramatically between individual impure samples (see table 3.6). Therefore, it would not be unreasonable to suggest that any hydrogen variations which are present within an individual crystal would be more pronounced

in the case of an impure sample. Therefore, the observed intensity variations of absorption bands in impure sample spectra obtained from different crystal cuts taken from the same sample were probably a consequence of an uneven distribution of hydrogen species throughout the crystal.

3.4 Studies of Deuterated Synthetic Quartz

Deuteration of Quartz can be accomplished directly by crystal growth from heavy water solutions[48,52] or indirectly by electrodiffusion in a deuterium rich atmosphere[139]. The procedure can be used to assign hydrogen species to absorption peaks in infrared spectra of sample crystals. This is possible because the vibrational frequency of an infrared absorbing hydrogen related species is shifted to longer wavelength values when a hydrogen atom is replaced by a deuterium atom. This frequency shift is a result of the greater mass of deuterium with respect to hydrogen and does not indicate a change in the chemical nature of the absorbing species. The amount by which the frequency changes can be calculated if the absorbing species is known. As the sharp absorption bands present on quartz infrared spectra occur in a region associated with O-H stretching vibrations, the O-H species is chosen for frequency shift calculations[52]. Kats showed that, upon deuteration, hydrogen associated absorption bands in quartz spectra shifted to frequencies predicted by the following formula[52,139]

$$V_D^+ = V_H^+ \left(\mu_{OD} / \mu_{OH} \right)^{1/2} \qquad (3.1)$$

where μ_{OD} and μ_{OH} are the reduced masses and V_D^+ and V_H^+ are the vibrational frequencies of OD^- and OH^-.

This prediction proved conclusively that the absorption bands were associated with the O-H stretching vibrations of

hydrogen impurity species in quartz.

Studies prior to this project regarding deuterated quartz did not investigate either the mode of incorporation or the spatial orientation of the deuterium species, both of which could provide information useful to assign hydrogen impurity absorption peaks. Therefore more extensive studies on deuterated Quartz were carried out specifically to gain information for hydrogen defect models. Electodiffusion was ruled out for this purpose because the incorporation of deuterium at sites other than those originally present in pre-treatment samples had been reported[139]. Sample crystals were therefore grown hydrothermally from heavy water solutions. Crystal growth was carried out using procedures described in section 2.1 with the exact growth conditions being given in table 2.1.

Growth run 1 produced the first deuterium grown crystal, R1. The mineraliser used to promote crystal growth was sodium hydroxide. In this way the incorporation of hydroxyl impurities from the mineraliser as well as deuterium related species from the heavy water solvent could be studied. Previous workers had used non-hydrogen containing mineralisers such as sodium deuteroxide[52] and sodium carbonate[48] and did not report the presence of any hydrogen related absorption peaks on the infrared spectra of samples. Deuterated crystals produced by growth runs 1, 2, 15 and 19 were specifically grown in sodium hydroxide heavy water solutions to determine whether or not hydrogen species originating from

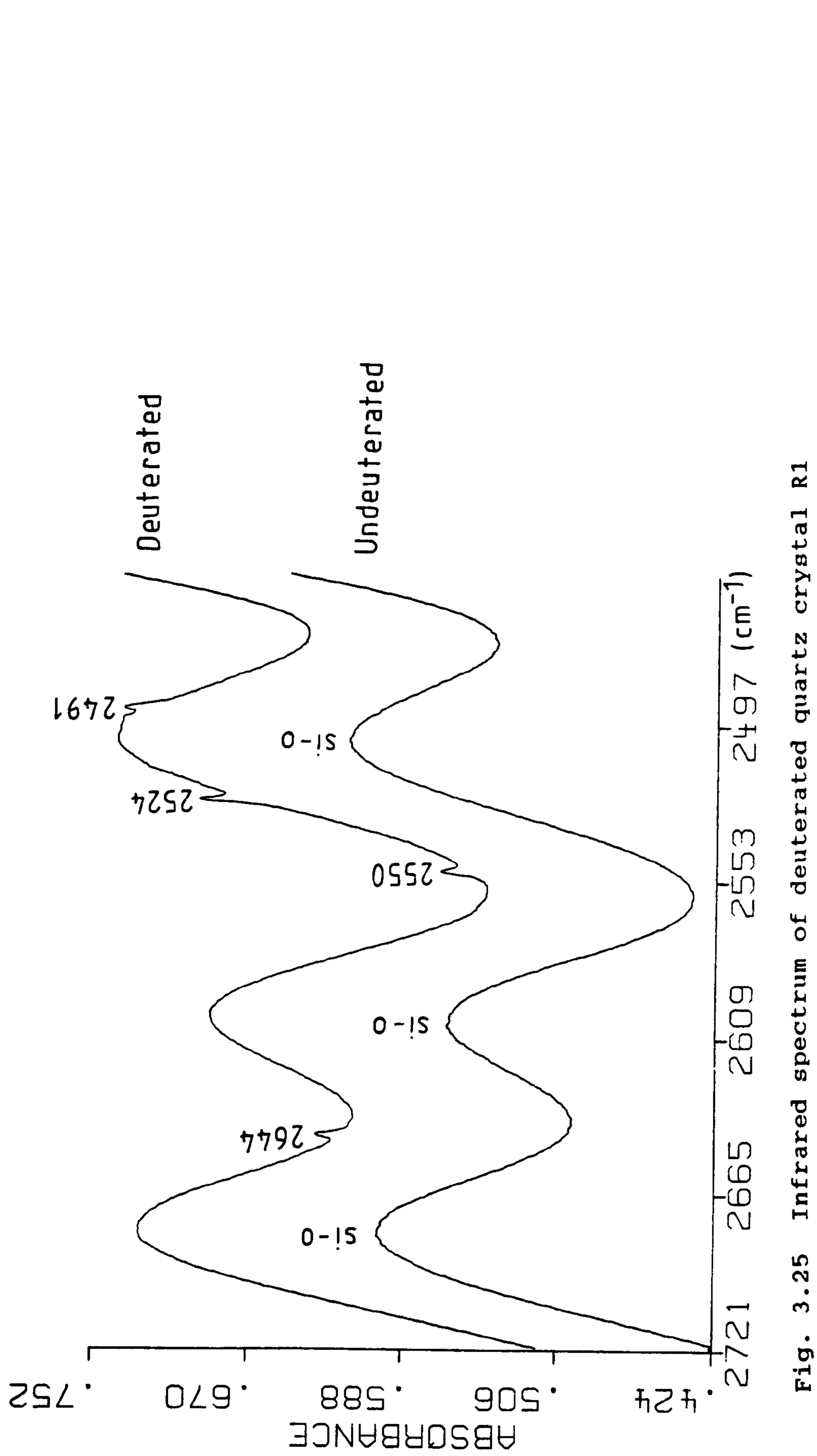
Deuterated
Undeuterated
2491
Si-O
2524
2550
Si-O
2644
Si-O
ABSORBANCE
.752
.670
.588
.506
.424
2721
2665
2609
2553
2497 (cm-1)
Infrared spectrum of deuterated quartz crystal R1

Fig. 3.25

the mineraliser could be incorporated into a quartz crystal lattice. This would be indicated by the appearance of hydrogen related absorption peaks in infrared spectra of sample crystals in addition to their deuterium analogue peaks. Growth conditions followed those used in high purity quartz production as no published data for deuterated growth from sodium hydroxide solutions was available. The resultant crystal was therefore an accurate deuterium analogue of high purity quartz, enabling direct comparison of deuterated and non-deuterated high purity crystals.

The low temperature spectrum of a sample taken from the deuterated crystal R1 is shown in fig. 3.25 with a spectrum of a non-deuterated high purity quartz sample, HPQP.1, shown underneath for comparison. The figure shows the region of the infrared spectrum where O-D stretching vibrations predicted by formula (3.1) occur. The absorption bands at 2678, 2602, and 2502 cm^{-1} respectively were intrinsic to all types of quartz, being secondary overtones produced by Si-O lattice vibrational absorptions. The predicted and experimental values for O-D stretching vibrational frequencies are given in table 3.14. Although the average difference between theoretical and experimental wavenumber values was around 47 cm^{-1}, the observed absorption peak values agreed well with published O-D stretching frequency values[52,139]. The experimental frequency V_{OH}/V_{OD} ratios were comparable to the theoretical values and confirmed the report by Kats[52] of reduction in ratio values with decrease in the wavenumber value of an

Table 3.14 Frequencies of O-D Stretching Vibrations from the Infrared Spectra of Crystal R1

Experimental			Theoretical		
ν_{OH}	ν_{OD}	ν_{OH}/ν_{OD}	ν_{OD}	ν_{OH}/ν_{OD}	$\delta\nu_{OD}$*
3580	2644	1.3540	2603	1.375	41
3436	2550	1.3474	2499	1.375	51
3395	2524	1.3451	2484	1.375	40
3364**	2494	1.3483	2455	1.375	40
3348	2491	1.3440	2436	1.375	55
3304**	2456	1.3453	2402	1.375	52

* - Difference between experimental and theoretical wavenumber values

** - Only appear after irradiation or sweeping

Table 3.15 Deuterium Content of Crystal R1

	Deuterium Concentration (ppm)*						
Sample ν_{O-H}**	2644	2550	2524	2494	2491	2456	Total
Untreated	0.097	0.126	0.108	0.010	0.114	-	0.455
Irradiated	0.027	0.006	0.007	0.614	-	0.098	0.752
Swept	0.129	0.190	0.247	0.207	0.092	0.016	0.881
Irradiated then Swept	0.131	0.107	0.319	0.416	0.112	0.037	1.186

* - Number of O-H groups per 10^6 SiO_2 molecules (see section 2.4.2)

** - Frequencies of O-H stretching vibrations associated with hydrogen impurities in quartz (units = cm^{-1})

absorption band. The wavenumber discrepancy can be explained as a result of interactions between deuterated species and the quartz crystal. The theoretical calculations did not take into consideration that the deuterium species were incorporated into a crystal lattice and may have been influenced by their surrounding environment.

To prove that the observed peaks were deuterium analogues of hydrogen related peaks and were not produced by some different deuterium species, it was necessary to examine the 3100-3600 cm^{-1} region of the infrared spectrum (see fig. 3.2). Comparison of the deuterated and non-deuterated crystals shows the complete absence of hydrogen related peaks on the spectrum of the deuterated sample with only intrinsic Si-O lattice vibrational bands being present. Comparison of figures 3.4 and 3.25 shows the occurrence of four sharp absorption bands for both types of quartz. When the agreement with both published results and theoretical frequency ratios were taken into consideration, the appearance of equal numbers of impurity related peaks on deuterated and undeuterated sample spectra could not be considered as a coincidence. Therefore the peaks at 2644, 2550, 2524 and 2491 cm^{-1} respectively were assigned to O-D stretching vibrations and the absorbing species as deuterium analogues of the 3580, 3436, 3395 and 3348 cm^{-1} hydrogen related impurity peaks present in high purity Quartz.

The absence of hydrogen related absorption bands in the infrared spectrum was an indication that hydrogen impurities were not directly incorporated into the crystal as hydroxyl

ions from the mineraliser. It could be argued that there were insufficient numbers of hydroxyl ions in the growth solution and that incorporation did occur, but at levels below detection limits. Indeed, even although the concentration of the sodium hydroxide solution was 1 molar, only 80 ml was used in the growth run. If the numbers of molecules present are compared, the ratio of D_2O molecules to hydroxide ions was over 50:1. The deuterium absorptions were weak features on the infrared spectrum indicating that levels of deuterium species in the crystal were very low (see table 3.15). Since the numbers of hydroxyl ions were only a small fraction of total deuterium species present, it would not be unreasonable to assume that any incorporation that takes place will be undetectable. However , as stated previously, growth conditions were selected to be identical to those used for high purity quartz production, with the replacement of H_2O with D_2O being the only difference. Therefore, if the hydrogen related peaks shown in fig. 3.4 were produced solely by hydroxyl ions from the mineraliser, they would still have appeared on the spectrum of the deuterated sample. The O-H absorption bands were present in spectra of quartz crystals grown using a sodium carbonate mineraliser, where the source of hydrogen impurities was the water present. The spectrum of crystal R1 has shown that hydrogen impurities from the mineraliser are insignificant in comparison to those from the water present and are not incorporated into a crystal in any quantities which can be detected by infrared spectroscopy when

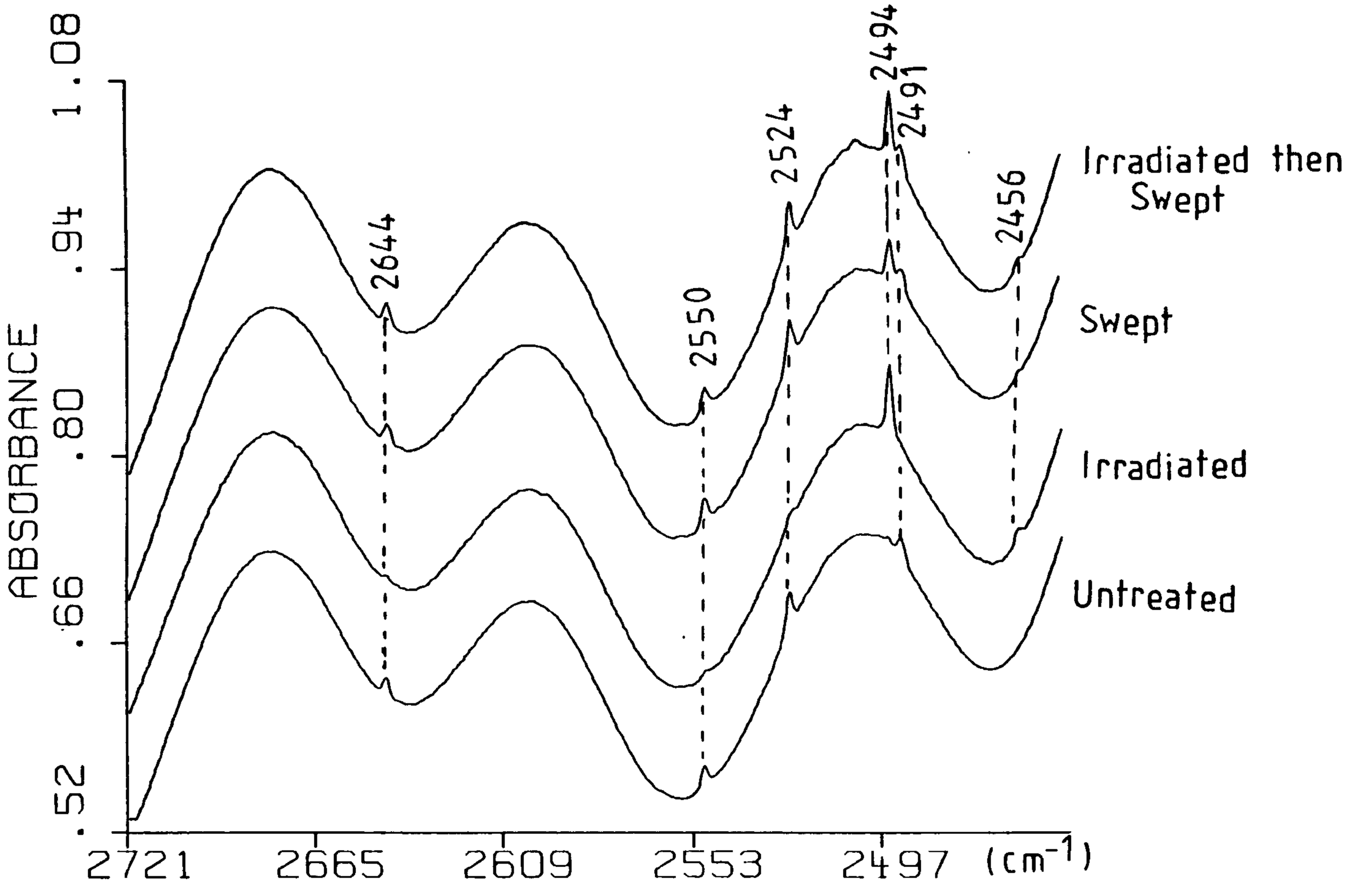

Fig. 3.26 IR spectra of irradiated and swept deuterated quartz

high purity Quartz growth procedures are followed.

Growth run 1 also provided enough material for the effects of several treatments commonly experienced by synthetic quartz crystals to be studied. The combined infrared spectra of treated samples are shown in figure 3.26. Radiation response was examined by subjecting a sample to high energy x-rays produced by an x-ray fluorescence spectrometer. Irradiation continued until the natural quartz seed crystal present in the sample slice turned black. Quartz discolours in the presence of radiation due to the formation of aluminium colour centres[93]. The deuterated growth did not discolour, indicating that levels of aluminium were substantially lower than in the natural material. The infrared spectrum of the irradiated sample showed the virtual disappearance of the four deuterium absorption bands, which were replaced by two new absorption peaks at 2495 and 2456 cm^{-1} respectively. The frequency of the most intense absorption band at 2494 cm^{-1} was in agreement with the value reported by Koumvakalis and Markes for their postulated Al-OD stretching vibration[139]. The comparison of the theoretical and experimental values of Al-OD vibrational frequencies given in table 3.14 shows the disagreement between the two values to be in the region of 40-50 cm^{-1}. This discrepancy is similar to that discussed earlier for the high purity analogue O-D absorption peaks. The two peaks are probably the deuterium analogues of the 3365 and 3304 cm^{-1} Al-OH absorption bands present in irradiated undeuterated quartz spectra. The

presence of these peaks showed that aluminium contamination of the deuterated sample had taken place. By comparison with the values given in table 3.2, the level of aluminium in crystal R.1 was approximately 0.25 ppm. Fortunately , as shown in table 2.3, this level of aluminium content was much lower than that found in commercially grown quartz and so crystal R1 was still a good analogue of the high purity material. The appearance of Al-OD peaks was confirmation that internal rearrangements of deuterium impurities had taken place. In a deuterated crystal, deuterium ions fulfil the task of charge compensation of substitutional aluminium defect sites. Since irradiation took place in the absence of a deuterium atmosphere, the only source for these ions was from those impurities already present in the crystal. The reduction of the intensities of O-D as-grown absorption bands was therefore a consequence of the migration of deuterium ions to form Al-OD centres.

The final treatment carried out on crystal R1 was electrodiffusion in a dry nitrogen atmosphere. Two samples were swept under identical conditions, although one of these was irradiated with x-rays prior to the treatment. Irradiation was carried out so that electrodiffusion efficiency could be studied. The effectiveness of electrodiffusion, with regard to the completeness of impurity ion removal from a crystal, is variable[61]. The cause of sweeping inefficiency could be that, in certain instances, the process lacks the strength to overcome the attractive

forces which hold an impurity ion in the lattice. Irradiation of a sample prior to sweeping has been reported by several workers[115,117] to facilitate alkali metal ions removal however, no such work had been carried out on deuterated quartz. Sweeping is also useful in the comparison of the relative strengths of the deuterium and hydrogen impurity species with respect to the sites they are bound into.

The combined infrared spectra of the two swept R1 samples are shown in figure 3.26. A noticeable feature in both spectra was the appearance of the 2494 cm^{-1} absorption peak associated with Al-OD defect sites. In addition, the four peaks at 2644, 2550, 2524 and 2491 cm^{-1} respectively associated with as-grown O-D stretching vibrations were also present. The only other significant feature was a new peak at 2505 cm^{-1} not observed in the untreated sample spectrum. The relative areas of the Al-OD peak could be used as a rough estimate of the efficiency of the sweeping process. Al-OD peaks were only formed upon the removal of an alkali metal impurity and so the area under the Al-OD absorption bands indicated the amounts of ions which had been removed. The sample which was irradiated prior to sweeping contained the largest numbers of Al-OD centres (see table 3.15). Assuming that aluminium centres were evenly spread throughout the crystal, then the pre-irradiation treatment did improve the efficiency of electrodiffusion by a noticeable degree. Comparison of the pre-irradiated swept and irradiated sample spectra shows that although Al-OD centres

were formed in both crystals, the as-grown O-D stretching vibrations were unaffected by irradiation. These peaks should have been reduced in intensity after irradiation. The persistence of the O-D peaks suggests that sweeping regenerated the deuterium species which were depleted in charge compensating aluminium defect sites. As shown in the spectrum of the solely irradiated sample, most of the deuterium atoms from as-grown O-D related impurity sites were needed in the charge compensation process. The regeneration of the O-D peaks suggests that more deuterium was present in the crystal than could be detected by infrared spectroscopy. This alternative source of deuterium could be infrared inactive species such as deuterium molecules and atoms randomly dispersed at interstitial and vacancy sites throughout the crystal. Several workers have reported the detection of atomic hydrogen species in quartz[107,108] therefore, this observation was supported by published work.

Growth run 2 was carried out under the same growth conditions as the first deuterated run with the exception that the crystal, R2, was doped by the addition of aluminium foil to the growth solution. The run was originally designed to produce an aluminium doped deuterium analogue of high purity quartz so that Al-OD centres could be assigned to absorption peaks on the infrared spectrum of a sample. The contamination of crystal R1 produced by growth run one was not discovered until after the doped crystal had been grown. The spectrum of

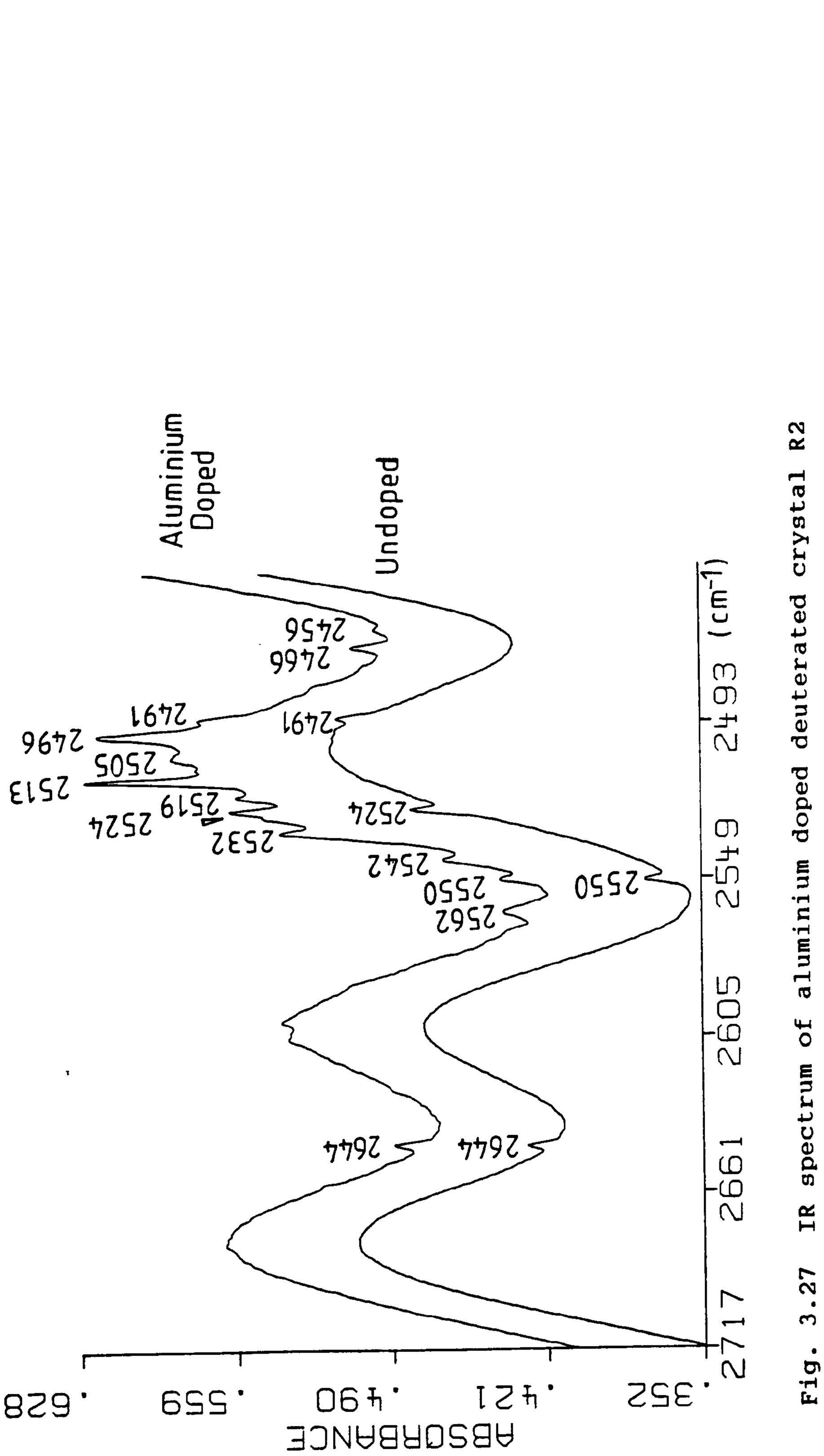

Fig. 3.27 IR spectrum of aluminium doped deuterated crystal R2

Table 3.16 Frequencies of O-D Stretching Vibrations from the Infrared Spectra of Crystal R2

ν_{OD} (cm-1)	ν_{OH}* (cm-1)	ν_{OH}/ν_{OD}
2644	3580	1.3547
2562	3458	1.3497
2550	3436	1.3474
2542	3426	1.3478
2532	3410	1.3468
2524	3395	1.3451
2519	3390	1.3458
2513	3380	1.3450
2505	3366	1.3442
2496	3353	1.3433
2491	3348	1.3440
2466	3304	1.3404

* - frequencies obtained from graph of experimental values (see fig. 5.10).

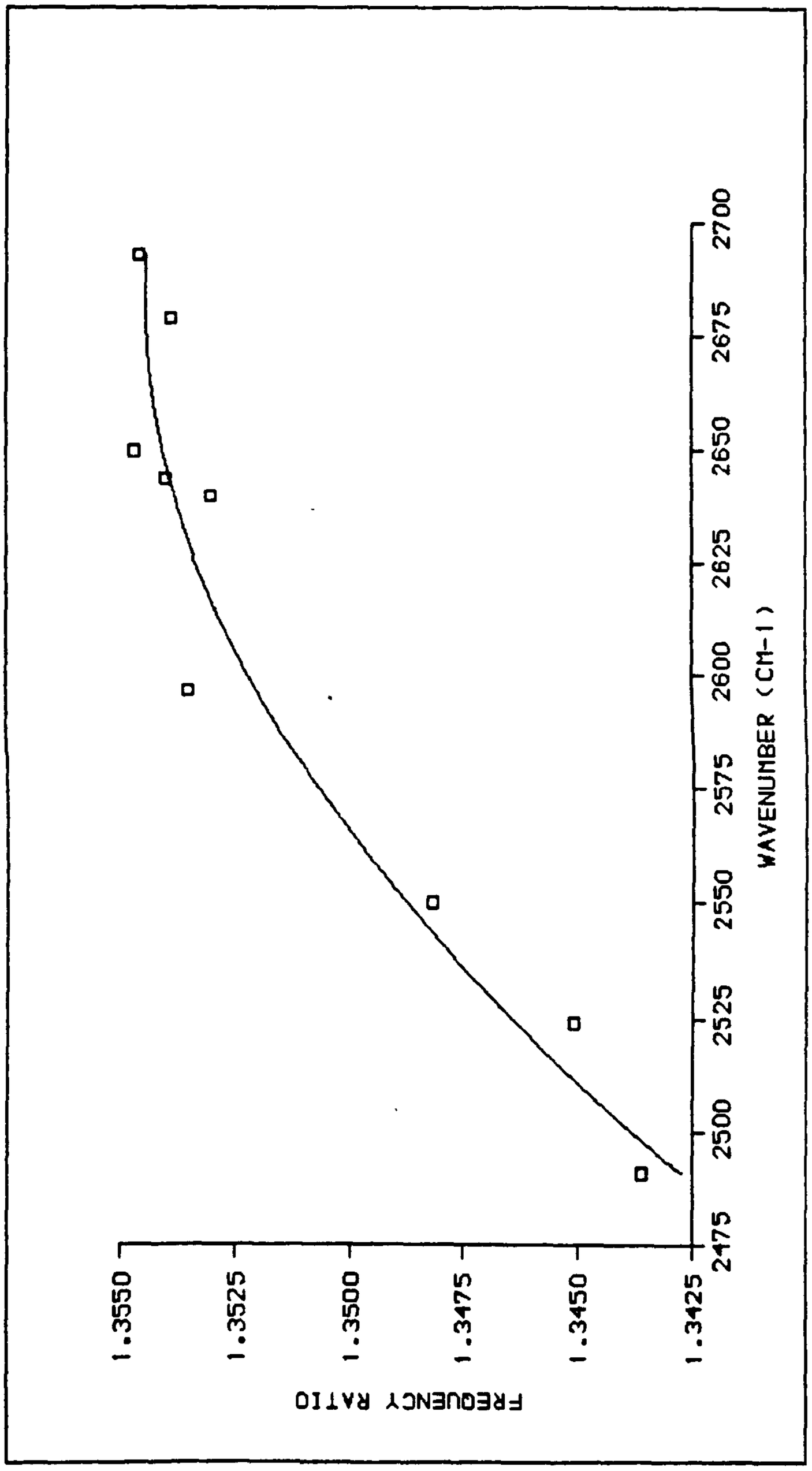

Fig. 3.28 O-D/O-H stretching fr

a sample taken from doped crystal R2 is shown in figure 3.27. with the spectrum of a growth run 1 sample shown for comparison. The most obvious difference between the two spectra are the numbers and intensities of the absorption bands. The doped sample spectrum exhibited many peaks in addition to those seen in the undoped sample spectrum. The vibrational frequencies of these absorption peaks together with theoretical estimates of the corresponding hydrogen species are given in table 3.16. The position of the hydrogen absorption bands was calculated using ν_{OH}/ν_{OD} ratios obtained from a graph derived from experimental values (see fig. 3.28). The use of experimental values increased the accuracy of the peak predictions compared with those calculated using formula (3.1). Unfortunately the predicted vibrational frequencies did not agree with any absorption bands common to synthetic quartz infrared spectra. Absorption bands attributed to Al-OD defect sites were not present on the sample spectrum. Since runs 1 and 2 had produced crystals at very similar growth rates and under identical growth conditions, the new peaks were a consequence of the addition of the aluminium foil. The most likely cause of the bands was the purity of the aluminium. If high levels of impurities other than aluminium were present in the foil, additional peaks associated with these foreign species could appear on the sample spectrum.

The remaining portion of crystal R2 was divided into sections which were treated using the irradiation and

Table 3.17 Deuterium Content of Crystals R2 and R19

	Deuterium Concentration (ppm)*				
ν_{O-D}**	R2 Untreated	R2 Irradiated	R2 Swept	R2 Irradiated Then Swept	R19 Untreated
2679	-	0.075	0.040	0.031	-
2651	-	-	0.050	0.055	-
2644	0.106	0.270	0.517	0.518	0.030
2640	-	-	0.038	0.048	-
2562	0.275	0.223	0.343	0.420	-
2557	-	-	0.048	0.041	-
2550	0.108	0.250	0.932	0.902	0.025
2542	0.121	-	0.205	0.235	-
2532	0.143	0.395	0.063	0.089	-
2524	0.197	0.374	1.939	1.836	0.028
2519	0.079	0.087	0.091	0.096	-
2513	0.443	0.657	0.551	0.654	-
2505	0.102	0.622	0.315	0.365	-
2496	0.637	0.116	0.997	1.250	-
2494	-	0.857	-	-	-
2491	0.077	0.134	1.393	1.307	-
2466	0.130	0.158	0.456	-	-
2456	-	0.106	-	-	-
Total	2.418	4.324	7.978	7.847	0.083

* - Number of O-D groups per 10^6 SiO_2 molecules (see section 2.4.2)

** - Frequencies of O-D stretching vibrations associated with hydrogen impurities in quartz (units = cm^{-1})

N.B. Underlined values denote high purity quartz analogue bands

sweeping procedures described earlier in this section for the crystal R1. The combined sample spectra are shown in figure 3.29. The absorption bands associated with Al-OD impurity sites were only present in the spectrum of the irradiated sample. The absence of these bands on the spectra of the swept samples, which included a pre-irradiated crystal, showed that levels of aluminium were very low in the swept sample slices, probably in the order of 0.01 ppm (see section 3.1c and table 3.2). This was unusual since the growth solution had been doped with 100 ppm aluminium which should have produced an impurity content of around 10 ppm Aluminium in the grown crystal. The appearance of Al-OD related absorption peaks on the irradiated spectrum indicated that some incorporation of aluminium into the crystal had taken place. Therefore, it can be concluded that the addition of aluminium foil produced a partially doped sample with aluminium content being dependent on the area of the crystal under investigation.

The spectra of swept samples showed a marked increase in the intensity of absorption bands at 2624, 2550, 2524 and 2491 cm^{-1} with respect to the untreated R2 sample spectrum (see table 3.17). The other deuterium related peaks on the swept sample spectra also exhibited an increased intensity but not to such a noticeable extent. As no external supply of deuterium was used during the sweeping process, the changes in the intensity of O-D associated absorption peaks must have been be caused by the rearrangement of internal sources of deuterium atoms. If all the absorption band intensities had

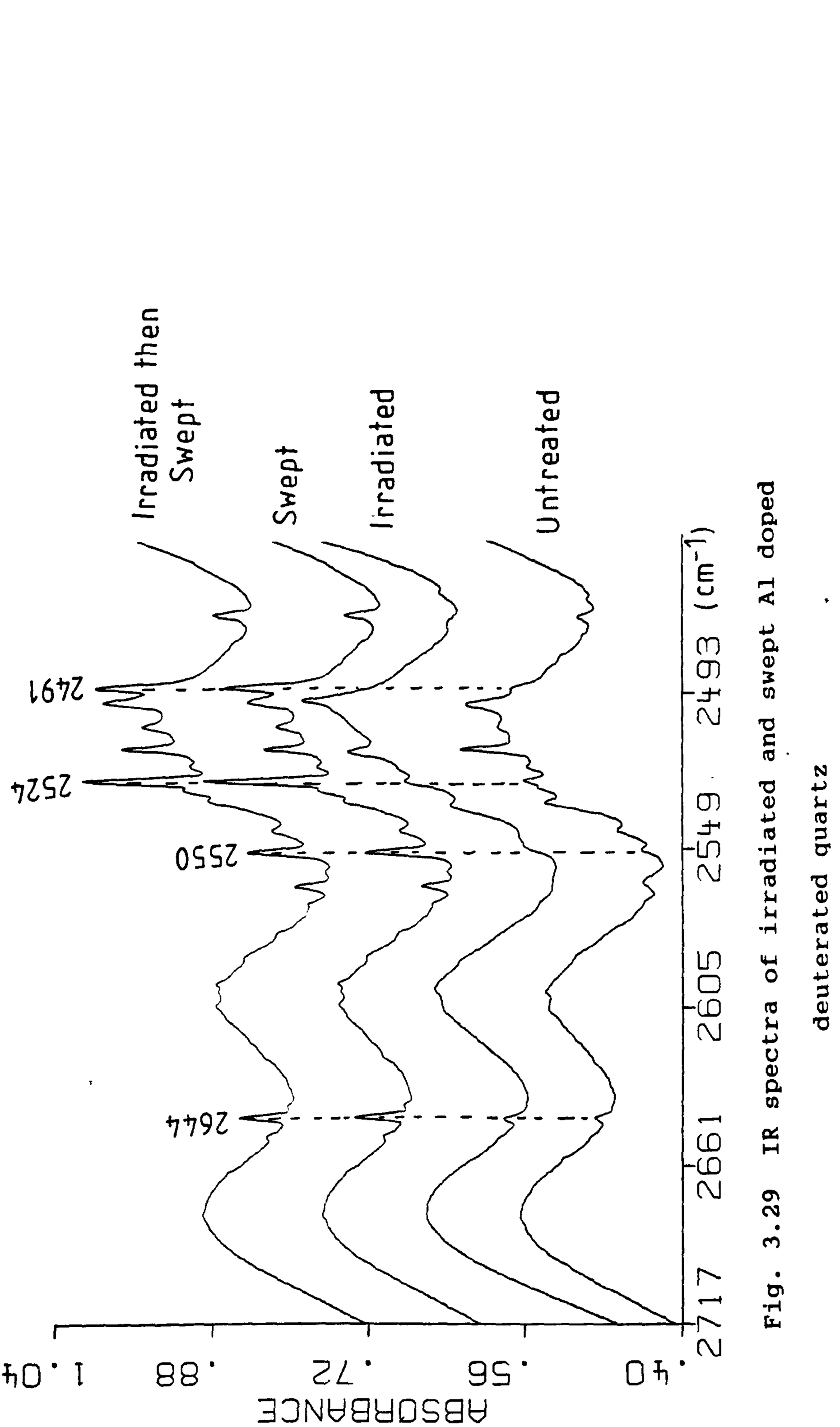

Fig. 3.29 IR spectra of irradiated and swept Al doped deuterated quartz

increased by the same relative amount, it could be argued that the cause of the differences may have been cooling conditions caused by differences in thermal contact with the cold finger. However, the preferential band intensity increase rules out this suggestion. The four peaks corresponding to the deuterium analogues of high purity quartz O-H absorptions increased in intensity by a much higher degree than the other absorptions (see table 3.17). To explain the observed differences requires a more detailed examination of the spectrum. As discussed previously in this section, deuterium atoms from O-D sites are used in charge compensation processes resulting in a decrease in intensity of absorption peaks associated with these species. Sweeping draws deuterium atoms from infrared inactive sites which become trapped at these vacant O-D sites thereby regenerating the absorption peaks. However, for this to take place there must be aluminium impurities in the crystal or else there are no species to charge compensate. As indicated by the absence of Al-OD associated absorption peaks, there were no infrared detectable amounts of aluminium in either of the swept sample crystals. Therefore, since there was no reason as to why the electrodiffusion process should not still cause deuterium atoms to be drawn from the crystal lattice, the intensity enhancement was probably a result of these excess atoms forming infrared active sites. The preferential intensity increase of the high purity quartz analogue absorption peaks shows that the formation of the new sites is not random and that certain O-D configurations are

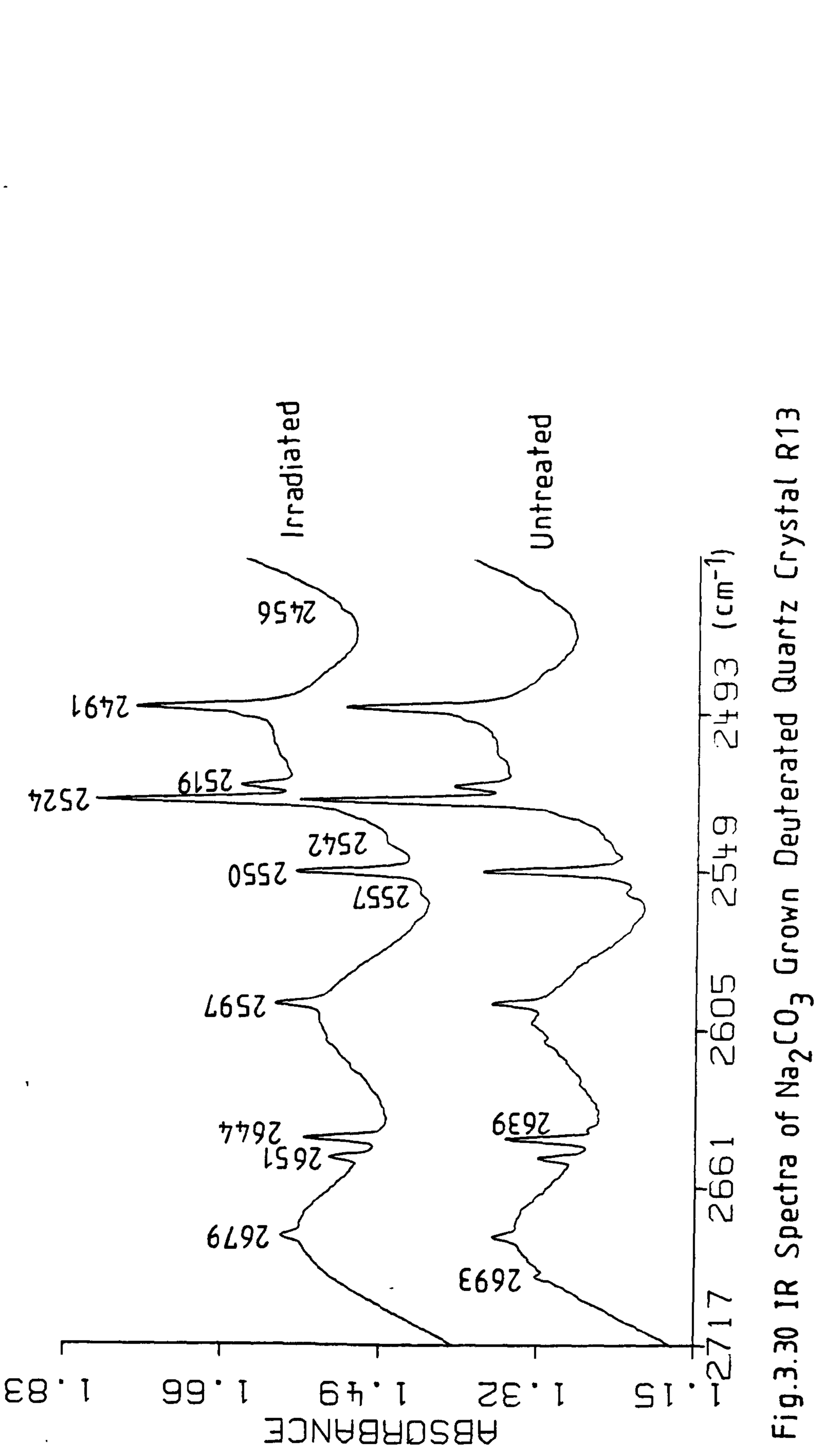

Fig.3.30 IR Spectra of Na_2CO_3 Grown

Table 3.18 Frequencies of O-D Stretching Vibrations from the Infrared Spectra of Crystal R13

ν_{OD} (cm-1)	ν_{OH}* (cm-1)	ν_{OH}/ν_{OD}
2693	3648	1.3546
2679	3627	1.3539
2651	3590	1.3547
2644	3580	1.3540
2640	3572	1.3530
2597	3515	1.3535
2550	3436	1.3474
2524	3395	1.3451
2519	-**	-**
2491	3348	1.3440

* - Frequencies obtained from infrared spectrum NAC03.1

** - No hydrogen analogue for this absorption band

more favourable.

Growth run 13 provided a deuterium analogue, R13, of a crystal grown from a sodium carbonate solution. Results obtained from the spectra of samples from growth runs 1 and 2 made the original purpose of providing a hydrogen free deuterated sample obsolete. In the case of both crystals R1 and R2, no hydrogen related peaks were present on the infrared spectra of untreated samples thus disproving the assumption that significant amounts of hydrogen was incorporated into the crystal from the mineraliser. Growth run 13 was carried out before this information was known however, crystal R13 allowed a direct comparison between deuterated samples grown using the two most important commercial mineralisers to be made. The spectra of samples taken from the crystal and the vibrational frequency values of absorption bands are given in figure 3.30 and table 3.18 respectively. Comparison between growth run 1 and 13 sample spectra shows the latter to exhibit a greater number of more intense absorption bands (see tables 3.15 and 3.19). All bands present in the spectrum of the hydroxide grown crystal are also present in that of the carbonate grown sample with the addition of absorptions at 2693, 2679, 2651, 2639, 2597 and 2519 cm^{-1} respectively. In addition, there was a shoulder on the 2491 cm^{-1} absorption peak in the region where an Al-OD associated peak is observed. To assign the absorptions required the examination of an undeuterated crystal grown under identical conditions. Such a crystal was produced by growth run 17. By assigning the major

Table 3.19 Deuterium Content of Crystal R13

	Deuterium Concentration (ppm)*	
	Untreated	Irradiated
ν_{O-D}**		
2693	0.070	-
2679	0.259	0.278
2651	0.259	0.414
2644	0.816	0.966
2639	0.030	-
2597	0.565	0.788
2557	0.137	0.020
2550	2.012	2.012
2542	-	0.102
2524	2.481	2.964
2519	0.421	0.553
2496	-	-[a]
2491	2.794	3.053
2456	-	0.020
Total	9.844	11.170

* - Number of O-D groups per 10^6 SiO_2 molecules (see section 2.4.2)

** - Frequencies of O-D stretching vibrations associated with hydrogen impurities in quartz (units = cm^{-1})

a - The shoulder on the 2491 cm^{-1} absorption band was probably produced by a 2494 cm^{-1} Al-OD absorption

absorption bands present in the spectrum of a sample taken from crystal R16, which was the hydrogen analogue of R13, with those from the deuterated crystal R13, a list of frequency ratios was obtained which were in good agreement with those obtained for growth run 1 and 2 samples (see table 3.18). Published data concerning peak assignments was unavailable for the confirmation of the peak assignments however, the frequency ratios showed the relationship of declining values of ratio with reduction in wavenumber reported by Kats[52]. This is illustrated on a graph of frequency ratio against wavenumber (see fig. 3.28). With the exception of the peak at 2519 cm^{-1}, all the absorptions on the deuterated sample spectra could be assigned satisfactorily with an hydrogen analogue on the spectrum of the undeuterated crystal. The increased intensities of the absorption peaks in comparison with those of growth run 1 samples may have been a consequence of the higher growth rate of the carbonate grown crystal. However, the intensity increase was much greater than would be expected for such a small growth rate difference. A more probable explanation was the presence of considerably higher levels of impurities than those present in the hydroxide grown crystal. This is in agreement with observations discussed for the undeuterated carbonate grown crystal presented in section 5.1.

The irradiated sample spectrum showed only minor changes when compared to the untreated sample spectrum (see table 3.19). A slight shoulder in the region of 2456 cm^{-1} and the

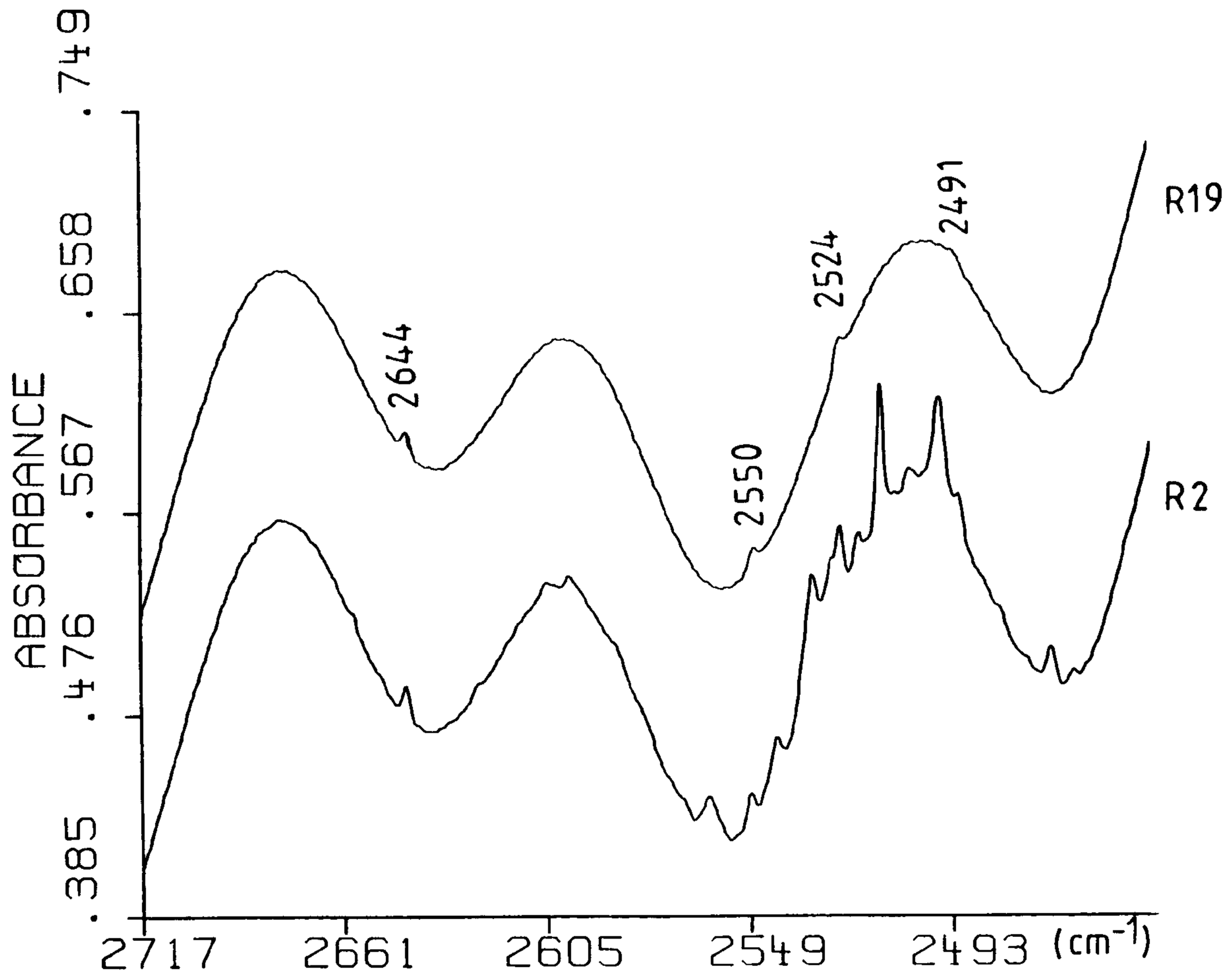

Fig. 3.31 Comparison of aluminium doped crystals R2 and R19

disappearance of two minor absorption peaks at 2693 and 2639 cm^{-1} were the major differences. The slight decrease in intensity of the absorption peaks on the irradiated sample was not unexpected, however the absence of aluminium associated absorption bands was. This can be explained by the levels of aluminium in the crystal being sufficiently high to affect the absorption band intensities upon irradiation but not high enough to produce any Al-OD absorptions which were strong enough to be distinguished from the 2491 cm^{-1} band. Comparison of the area of the shoulders present in the region of the Al-OD absorptions with those from spectra of samples with known aluminium levels, indicates that levels of the impurity may be in the region of 0.05 ppm.

The other growth runs to produce deuterated crystals were runs 15, 17 and 19. Their purpose was to provide comparisons with the growth runs already discussed in this section to verify the repeatability of the growth process. The combined sample spectra showed no significant changes for runs 15 and 17, the repeats of runs 1 and 13 respectively. Absorption bands occurred in the same intensity and numbers and at the same frequencies as those observed in the original sample spectra. However growth run 19, the repeat of the aluminium doped run, produced a crystal sample whose spectrum was very different to that of the original sample R2 (see table 3.17). The comparison of spectra from both runs is shown in figure. 3.31. The absence of all absorptions except the four bands present on the undoped spectra was a strong indication that

the doping procedure had completely failed in this case. The bands that were present in the spectrum were very weak, showing that incorporation of deuterium had been reduced significantly. The difference between the spectra obtained from crystals R2 and R19 can be explained by the absence of impurities in the latter crystal. The repeat run crystal was simply much purer than the original doped sample and consequently the numbers of impurity related hydrogen impurities were significantly reduced.

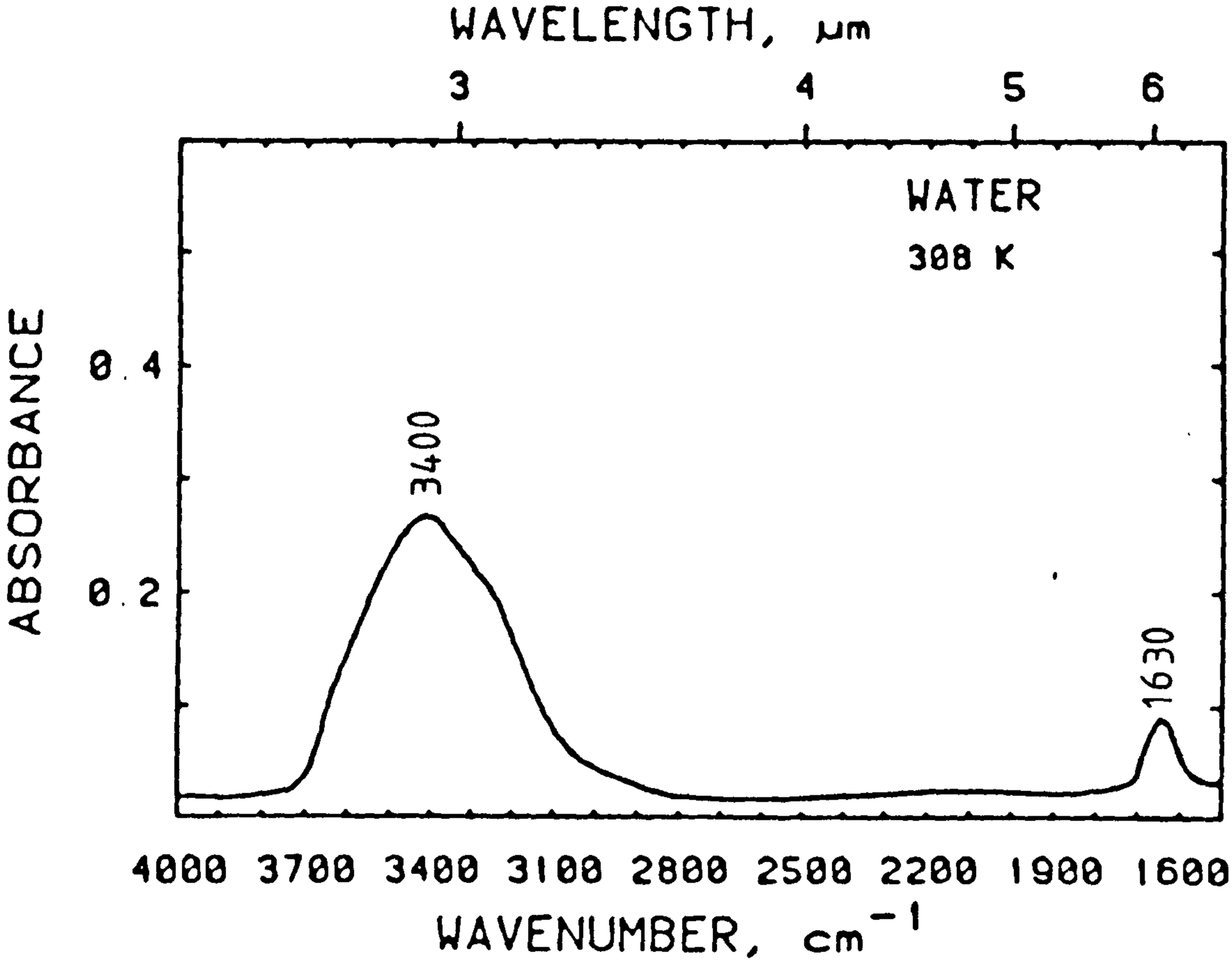

Fig. 3.32 Infrared Spectrum of a Film of Liquid Water (From Ref. 111)

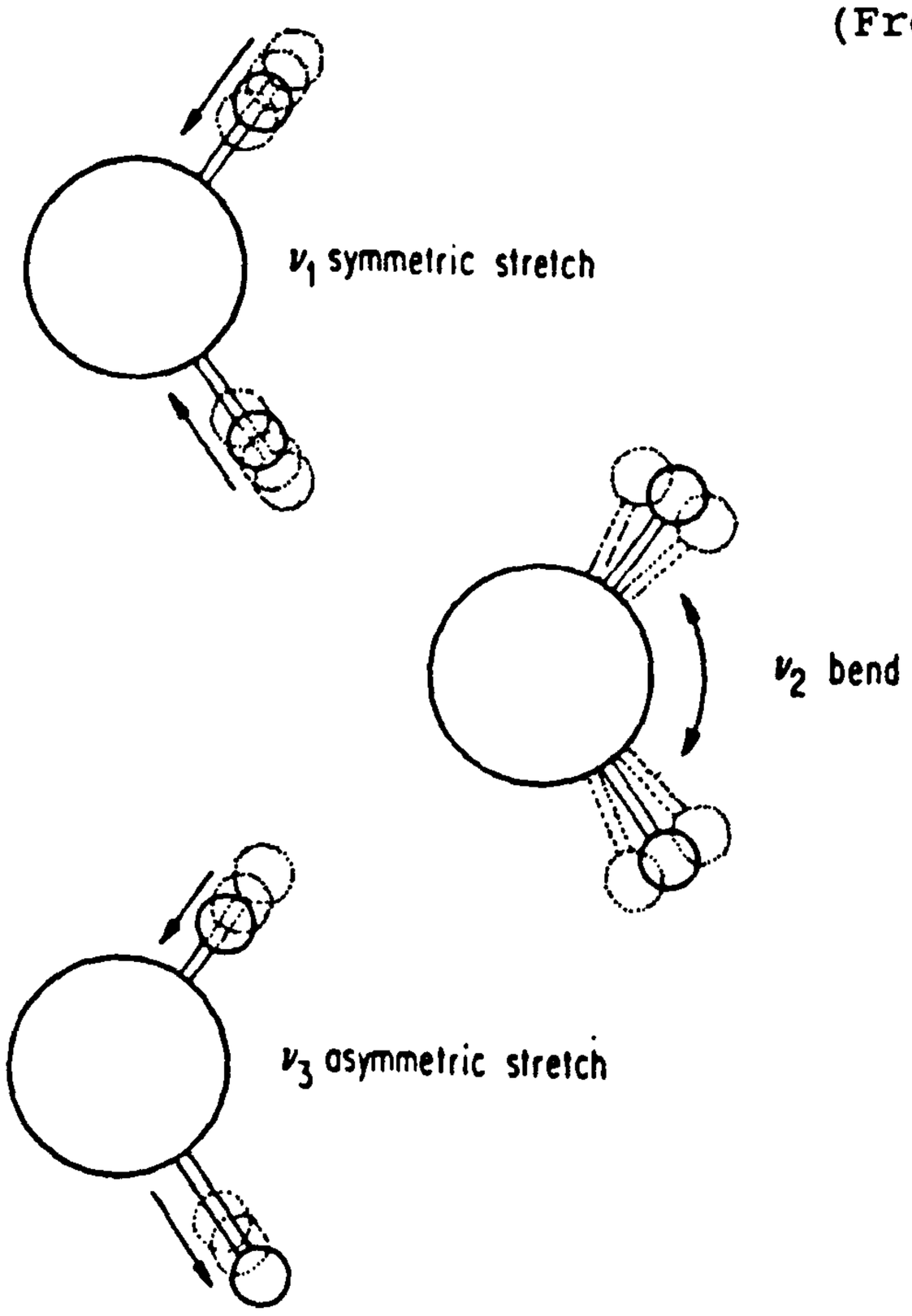

Fig. 3.33 Modes of Vibration of the H_2O Molecule (From Ref. 111)

3.5 The Nature of Hydrogen Impurities

The nature of the hydrogen species responsible for the sharp absorption bands in low temperature infrared quartz spectra was investigated by comparison with case studies of hydrogen impurities in several different crystalline materials. The following sections concentrate on the two species which are of particular relevance to hydrogen in quartz namely, water molecules and hydroxyl ions.

3.5.1 Molecular Water in Crystals

The most common species containing hydrogen is water. The infrared spectrum of liquid water is shown in figure 3.32[111]. The major features in the spectrum are two broad bands centred around 3400 and 1630 cm^{-1} respectively produced by different modes of vibration of a water molecule[111] (see figs. 3.32 and 3.33). The more intense 3400 cm^{-1} band consists of a symmetric O-H stretching absorption at 3220 cm^{-1} and an asymmetric O-H stretching vibration at 3445 cm^{-1}. The 1630 cm^{-1} absorption band is attributed to the bending mode of the water molecule. The broadening of the absorption bands is a consequence of the extended hydrogen bonded networks present in liquid water[138]. When frozen, water forms a regular crystalline structure which can be detected by the formation of a broad absorption band at 3200 cm^{-1} [111] (see fig. 3.34).

When water is in a crystalline environment, and free from an extended hydrogen bonded network, sharp absorptions can be

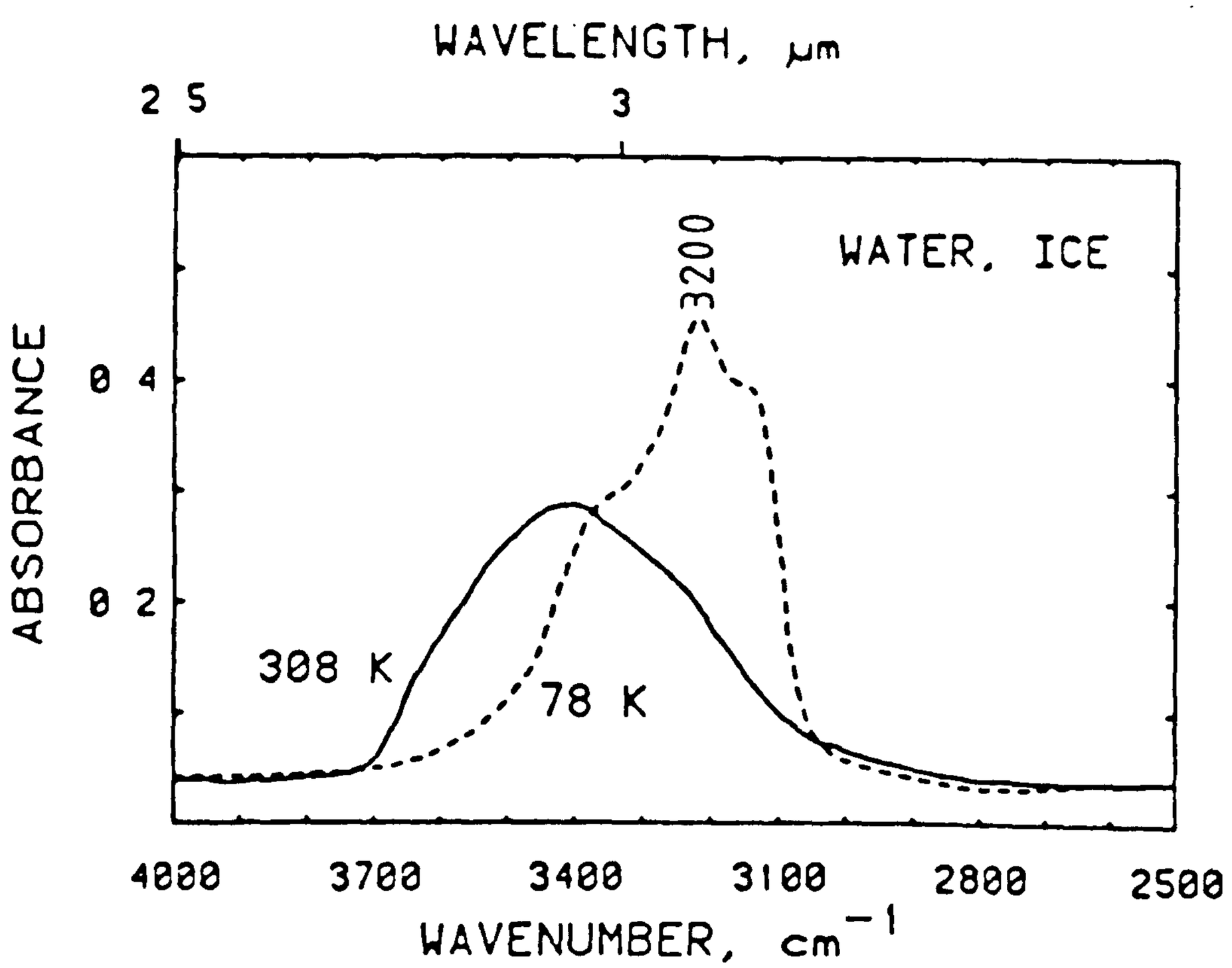

Fig. 3.34 Infrared Spectrum of Ice

(From Ref.111)

produced. Figures 3.35 and 3.36 show the spectra which were obtained from crystals in which water molecules were present in stoichiometric proportions and which were therefore a part of the compound structure as opposed to a random orientated impurity. In crystals of calcium dihydrogen phosphate, $Ca(H_2PO_4)_2.H_2O$, one molecule of water was associated in the crystal structure for every molecule of the compound. The spectrum showed the two O-H stretching modes to be well resolved from each other, but displaced to 3465 and 3225 cm^{-1} respectively from their frequency values in liquid water spectra (see fig. 3.35 and table 3.21). The absorption band at 1652 cm^{-1} corresponded to the displaced 1630 cm^{-1} bending mode and was proof that molecular water was present. However, the broad underlying absorption from 2500-3700 cm^{-1} showed that although individual water molecules were separated from each other, interactions still occurred between them. The most significant difference to that of the liquid water spectrum was the sharpness of the asymmetric stretching absorption at 3465 cm^{-1}. This gave the spectrum an appearance similar to that observed for room temperature doped synthetic quartz. Figure 3.36 shows the spectrum obtained from a sample of Brushite, $CaHPO_4.2H_2O$, in which two molecules of water were present for every molecule of the compound. Differences in the chemical environments of the two molecules produced two sets of stretching vibrations, one set at 3543 cm^{-1} and 3289 cm^{-1} and the other at 3489 cm^{-1} and 3161 cm^{-1} (see table 3.21). Two bending mode absorptions at 1728 cm^{-1} and 1649 cm^{-1} were also

Table 3.20 Infrared Bands of Water Molecules Trapped in Neutral Matrices

Species	Authors	Strommen et al.[a]	Tursi and Nixon[b]	Van Thiel et al[c]
	ν_{O-H}*	(cm-1)	(cm-1)	(cm-1)
Monomer	ν_3	3737	3725.7	3725
	ν_1	3645	3632.5	3627
	ν_2	1599	1596.9	1600
Dimer			3714.4	
	ν_3	3712		3691
			3697.7	
			3625.6	
	ν_1	3566		3546
			3547.5	
	ν_2	1599	1618.1	1620
Polymer		3704	3688	-
		3642	-	-
		3525	3510	3510[T]
		3378	3355	3355[T,P]
		3337	3320	3318[Te]

* - Frequency of O-H vibration

ν_1 - Symmetric O-H stretching vibration

ν_3 - Antisymmetric O-H stretching vibration

ν_2 - Bending mode

a - Frequency values quoted from reference 142

b - Frequency values quoted from reference 140

c - Frequency values quoted from reference 141

T - Trimer

Te - Tetramer

P - Unspecified Polymer

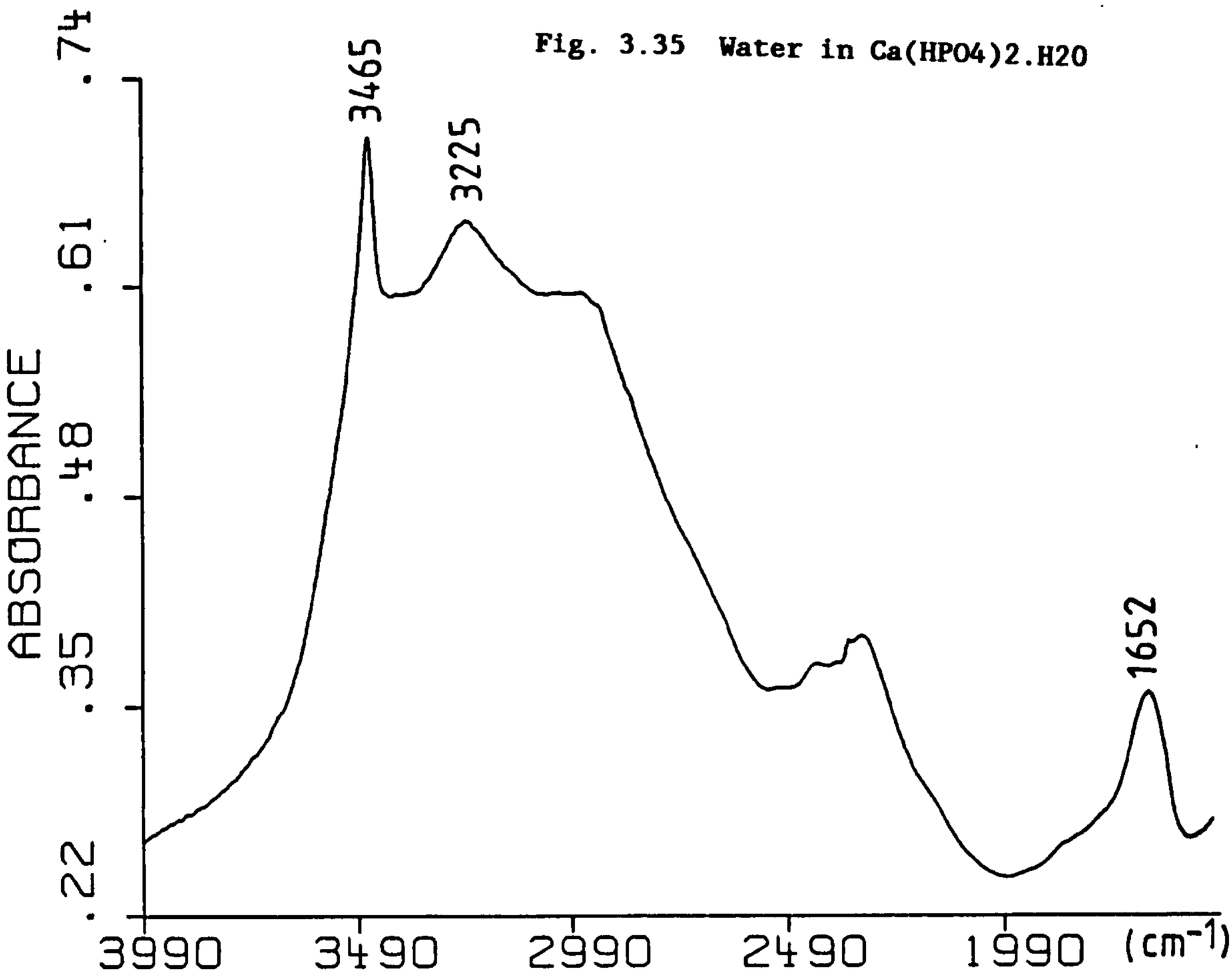

Fig. 3.35 Water in $Ca(HPO_4)_2.H_2O$

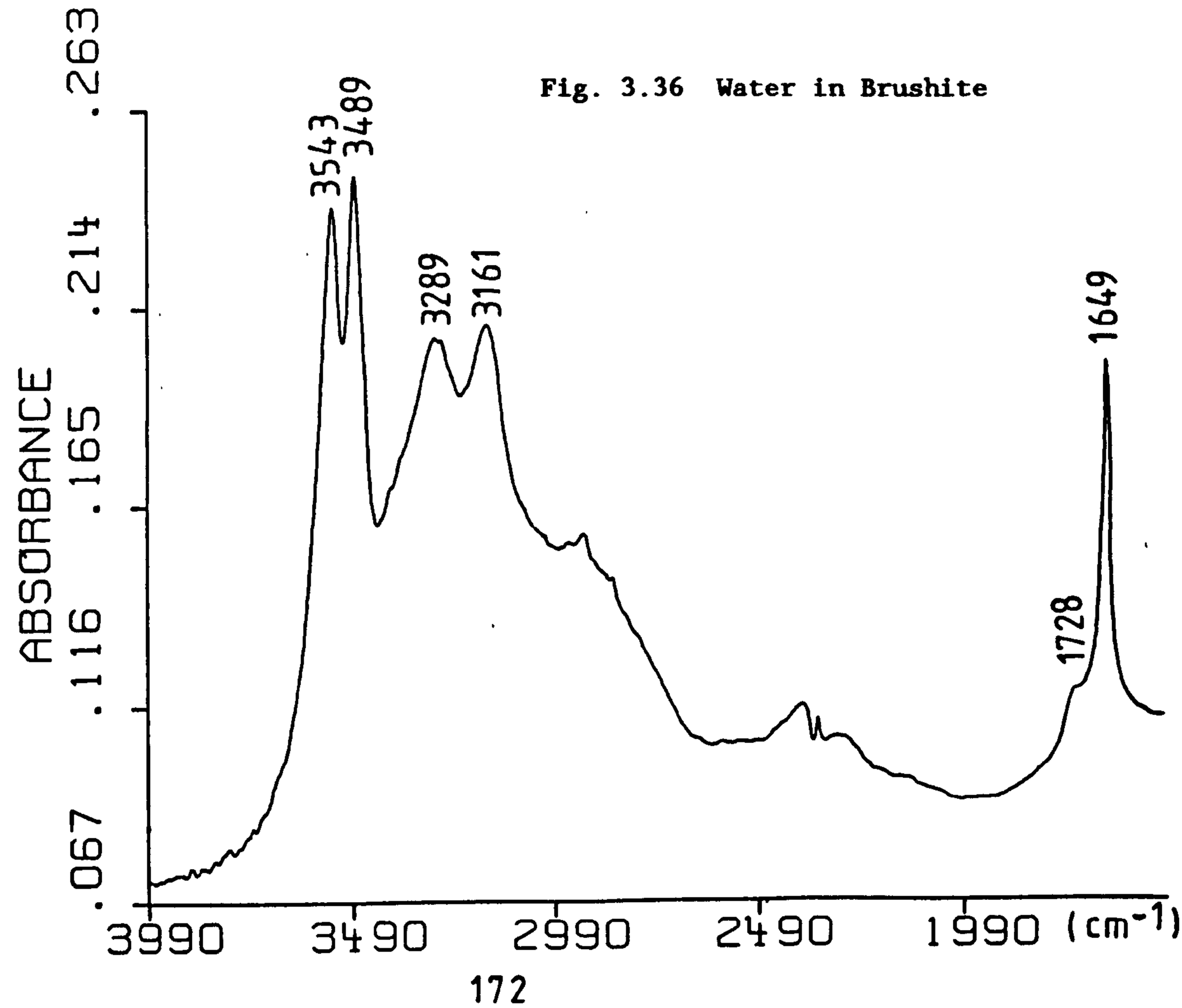

Fig. 3.36 Water in Brushite

Table 3.21 Infrared Bands of Water Molecules and Hydroxyl Ions in Crystals

Crystal	Mode	Frequency (cm^{-1})
Calcium dihydrogen phosphate $[Ca(H_2PO_4)_2.H_2O]$	v_3	3465
	v_1	3225
	v_2	1652
Brushite $[CaHPO_4.2H_2O]$	v_3	3543
		3489
	v_1	3289
		3161
	v_2	1728
		1649
NaCl $(+OH^-)$		3580
NaF $(OH^- + H_2O)$		3737
		3590*
		3573
	v_2	1579
$LiOH^a$ (OH^-)		3678±1
$LiOH.H_2O^a$ (OH^-)		3574±1
$LiOH.H_2O^a$ (H_2O, v_3)		1586±10

* - Denotes cluster of sharp absorption bands

v_1 - Symmetric O-H stretching vibration

v_3 - Antisymmetric O-H stretching vibration

v_2 - Bending mode

a - Values from Jones L.H. (see reference 143)

observed, proving that the four sharp absorption bands were produced by water molecules.

Sharper absorptions than those in a spectrum of liquid can also be observed for water molecules trapped using matrix isolation methods[138]. Tursi and Nixon[140] and others[141,142], trapped water monomer, dimer and higher order oligomers in a solid nitrogen matrix and assigned these species to infrared absorption bands (see table 3.20). This procedure was similar to the situation arising from cooling a quartz crystal to sharpen impurity related peaks. In both cases the environment separates individual trapped species thereby reducing interactions between them.

3.5.2 Hydroxyl Impurities in Crystals

The emphasis in the previous section on the presence of the water bending mode around 1630 cm^{-1} was to distinguish molecular O-H bands from those generated by hydroxyl, $O\text{-}H^-$, species. Absorptions associated with the O-H stretching vibration of an hydroxyl related species occur in the same spectral region as those related to the stretching modes of molecular water. However hydroxyl associated absorptions tend to be sharper than those of molecular water and, as there is no bending mode associated with these species, no absorption around 1630 cm^{-1} is observed. Two crystals known to contain trace quantities of an unspecified hydroxyl species were examined to explore this further.

The first sample which was studied was a sodium chloride

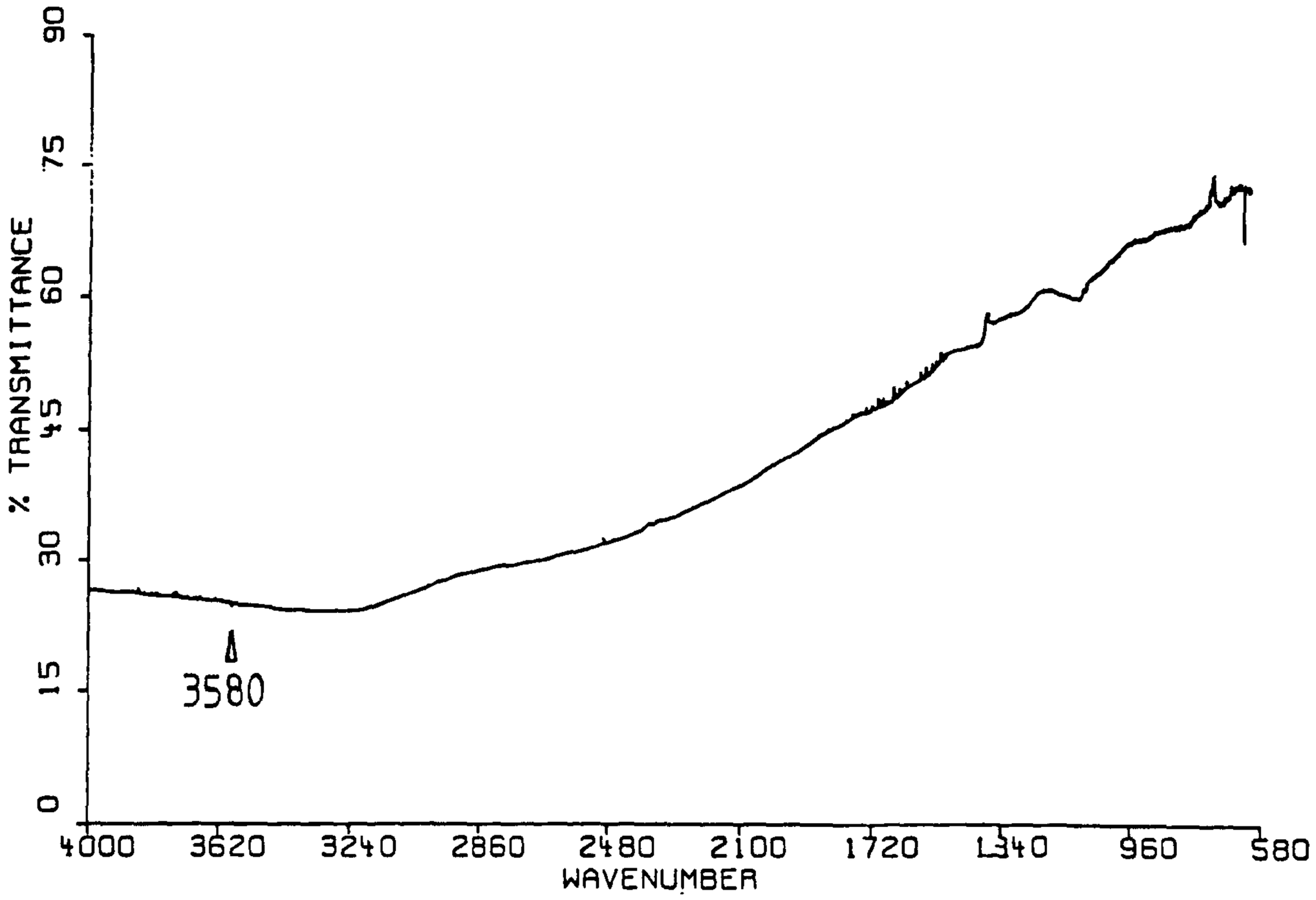

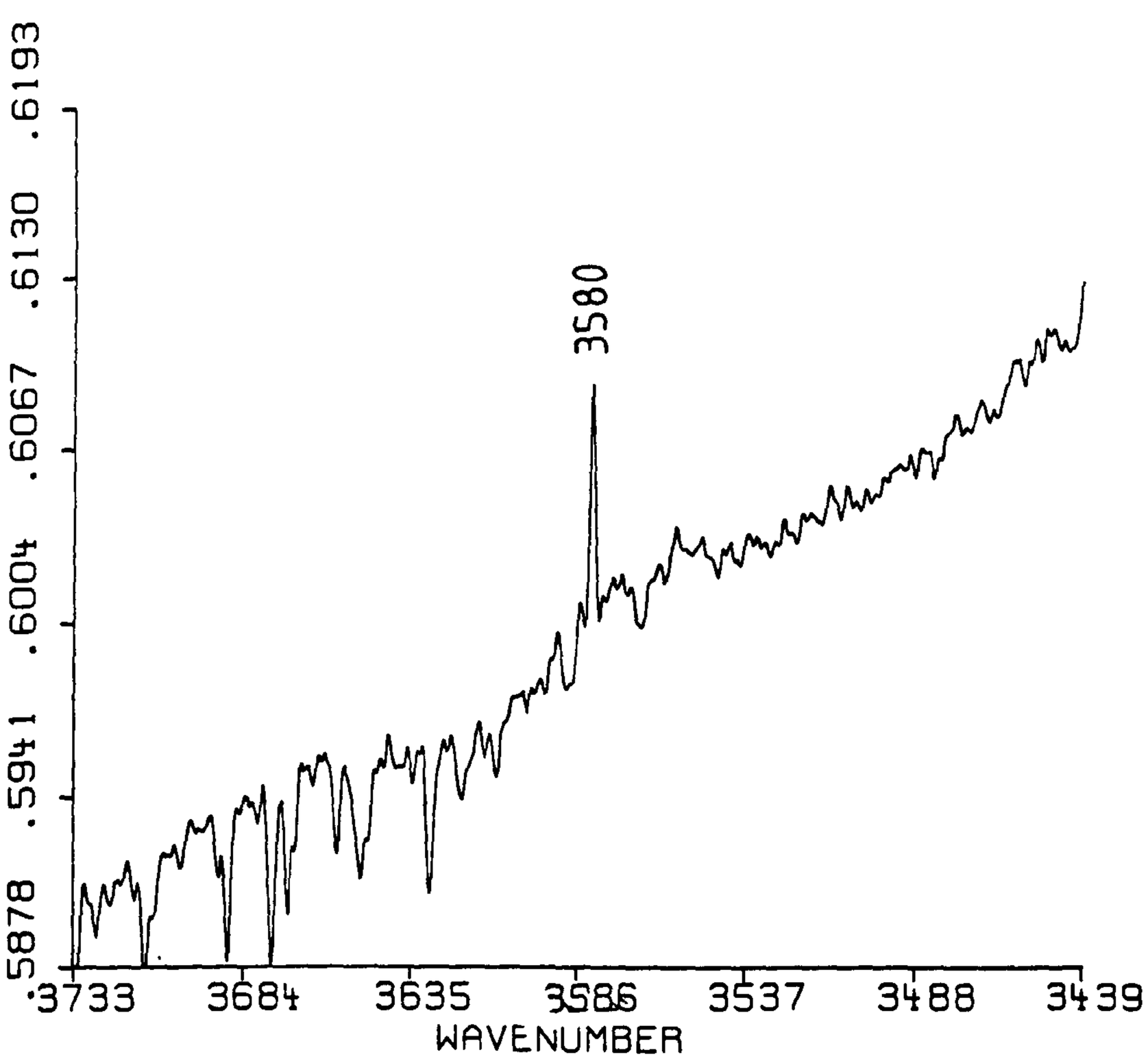

Fig. 3.37 Infrared spectrum of hydrogen impurities in NaCl

crystal. Although this material was transparent to infrared radiation in the spectral region under investigation, ie. 4000-400 cm^{-1}, the hydroxyl impurities present in the crystal absorbed radiation to produce a sharp absorption band at 3580 cm^{-1} on cooling (see fig. 3.37 and table 3.21). This occurred in a region associated with O-H stretching vibrations. No other hydrogen related bands were evident on the spectrum. The absorption was not observed at room temperature. The absence of any additional O-H stretching bands and the bending mode absorption around 1630 cm^{-1} eliminated the possibility that molecular water was present. The hydroxyl ions must be charge compensated in the crystal and so require an association with a positively charged species. An obvious choice of such a species are sodium ions, Na^{+}, which could have become associated with hydroxyl ions during the growth of the crystal. Therefore with this assumption, the absorption band can be assigned to a $Na^{+}OH^{-}$ unit trapped in the sodium chloride matrix. This claim was substantiated by the examination of a sodium fluoride crystal.

In most respects the sodium fluoride crystal was identical to sodium chloride. Again it was transparent to infrared radiation in the region under investigation and was known to possess hydroxyl impurities. However in this case the impurities were suspected to be present in substantially higher levels. The low temperature spectrum revealed a series of much more intense bands in the O-H stretching region of the sample spectrum. The strongest absorptions were observed at

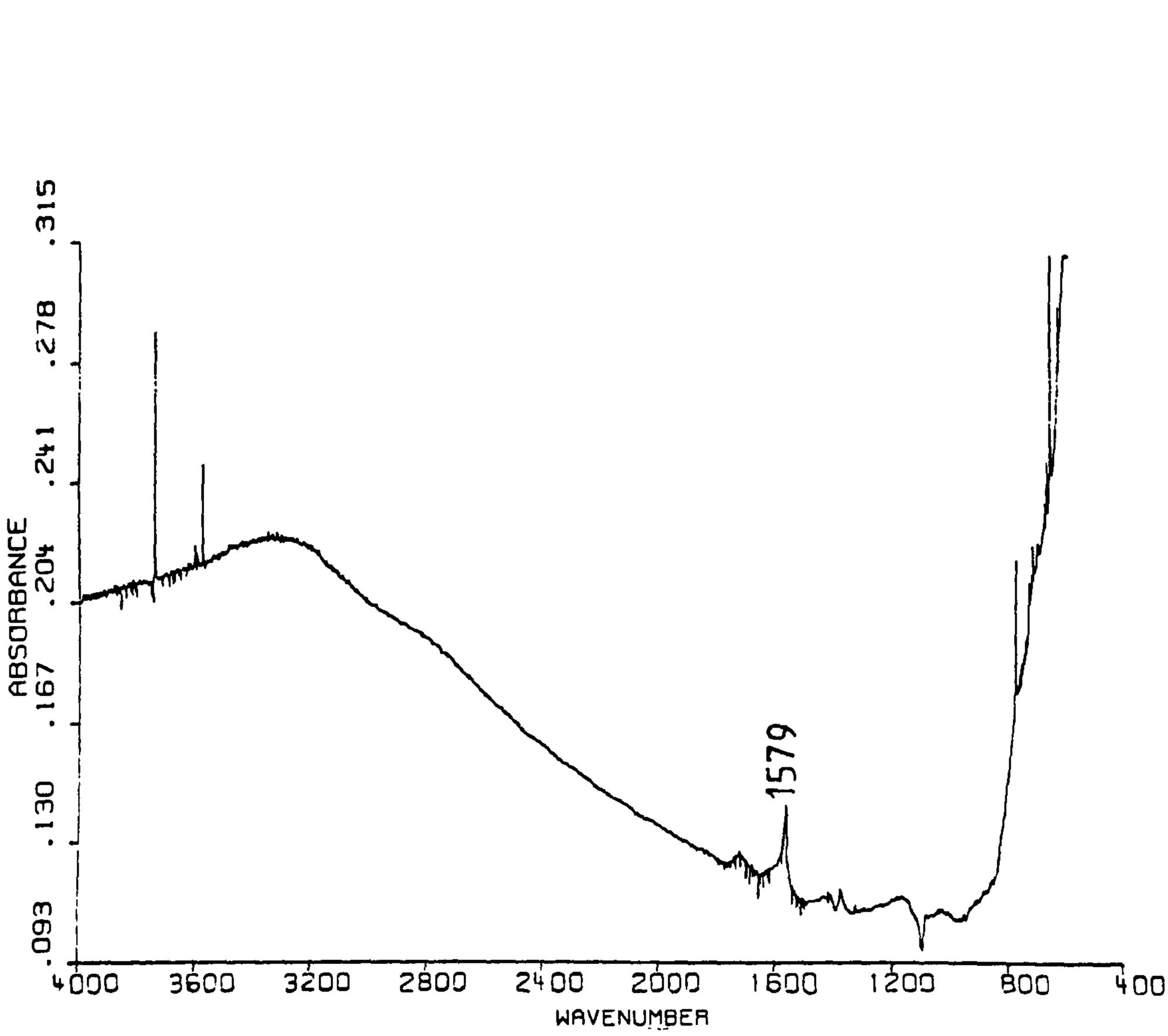

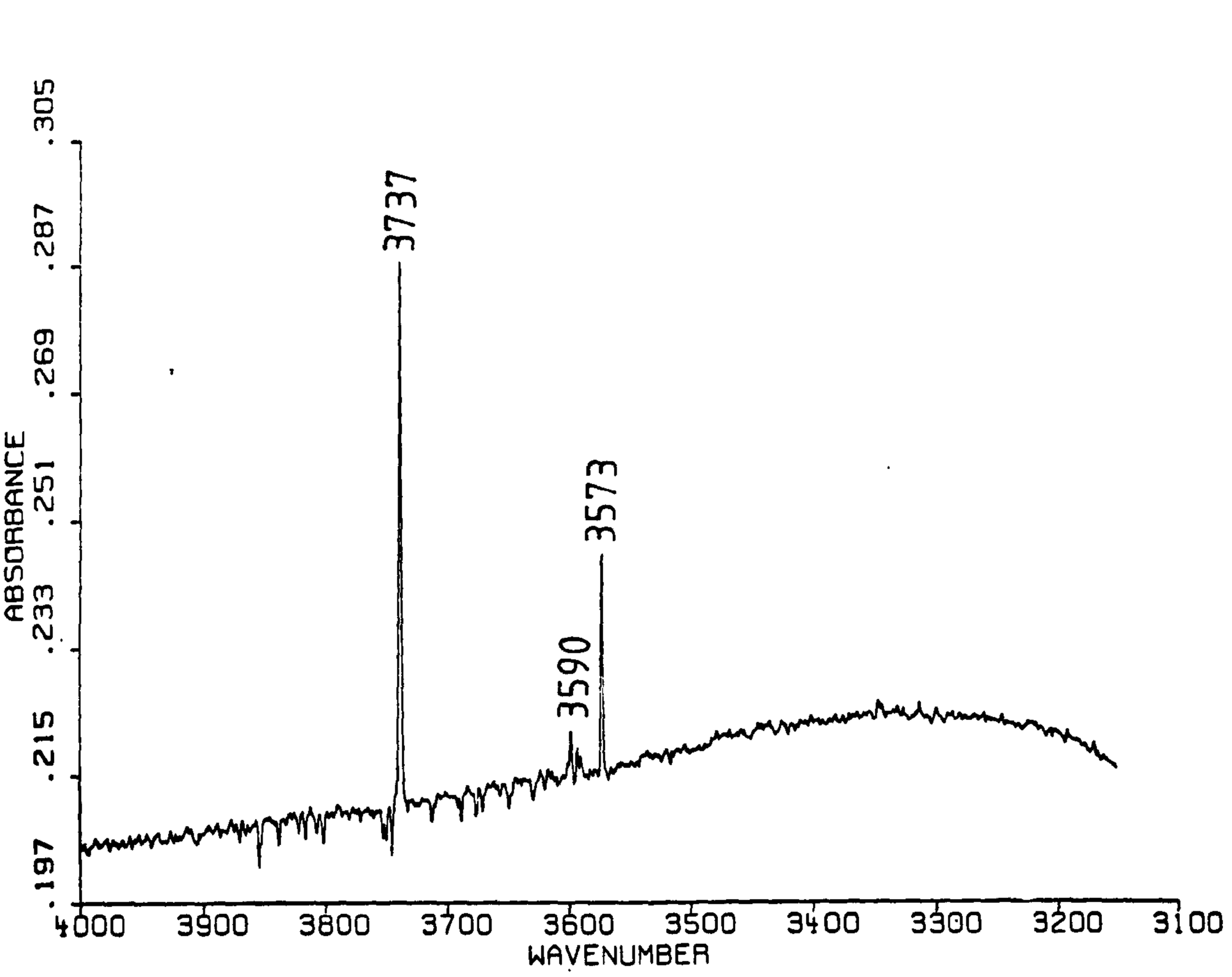

Fig. 3.38 Infrared spectrum of hydrogen impurities in NaF

3737, 3573 and 1564 cm^{-1} (see fig. 3.38 and table 3.21). A small cluster of sharp but weak bands around 3590 cm^{-1} were also in evidence. The 3737 cm^{-1} absorption was broad at room temperature but sharpened greatly on cooling. The 3573 cm^{-1} absorption and 3590 cm^{-1} band cluster were sharp at room temperature and did not change in height or intensity even when cooled to 10 °K. The absorption bands were assigned according to the frequency values reported for isolated water species by Tursi and Nixon[140]. The antisymmetric O-H stretching frequency at 3725.7 cm^{-1} and the bending mode at 1596.9 cm^{-1} of a water monomer compared well with the 3737 cm^{-1} and 1564 cm^{-1} absorptions respectively observed in the sodium fluoride spectrum. The deviation in the case of the bending mode is quite large but can be accounted for by the broadness this peak characteristically shows. Frequency discrepancies between different studies tend to be large in the case of broad absorptions as the exact centre of the absorption is difficult to measure. However, the symmetric stretch of monomeric water at 3632.5 cm^{-1} reported by Tursi and Nixon[140] is not observed on the sodium fluoride spectrum. Therefore the sharp absorption at 3573cm^{-1} could not be assigned if water was considered as the only absorption species. Assignment of this band was possible because of work carried out by Jones on lithium hydroxide[143], which reported the infrared absorption frequencies of the hydrated species $LiOH.H_2O$ (see table 3.21). The values quoted from his paper are comparable with the those observed in sodium fluoride

spectra. The frequency reported for a hydrated hydroxide stretch is 3574 cm^{-1} compared with 3573cm^{-1} in the case of the unassigned band present in the sodium fluoride spectrum. The bending mode absorption band at 1564 cm^{-1} also compared well with the value of 1586 cm-1 reported for the hydrated water bending mode. The bands at 3747 cm^{-1}, 3574 cm^{-1} and 1564^{cm-1} can therefore be assigned to the absorptions associated with hydrated hydroxyl species. However, as there were no lithium impurities in the sample crystals these species could not be hydrated lithium hydroxide units. Therefore the dominant hydrogen species in the sodium fluoride crystal were probably monohydrated $Na^{+}OH^{-}$ units such as $NaOH.H_2O$. This change of ion explains the differences in frequencies between those observed and those reported by Jones. This assignment is relevant to the characterisation of the hydroxyl band present in the sodium chloride sample spectrum. Although the frequency of the assumed sodium hydroxide band at 3580 cm^{-1} does not agree with the O-H stretching frequency of unhydrated lithium hydroxide at 3678 cm^{-1}, it is also obvious that the hydroxyl ions are not hydrated due to the lack of the water absorption peaks that dominate the sodium fluoride spectrum. The only model this leaves is that of an unhydrated sodium hydroxide unit. Differences in frequency can be accounted for by different environments of the unhydrated molecules with respect to host matrices. The good correlation of the hydrated absorption frequency is only an indication that both hydrated species were in similar environments.

3.5.3 Hydrogen in High Purity Quartz

The sharpness shown by O-H stretching absorptions in high purity quartz spectra is the first indication that they are associated with hydroxyl impurities. The absence of the broad absorption characteristic of polymeric hydrogen bonded water shows that no appreciable concentration of molecular water is present. The two most probable hydrogen species are therefore isolated molecules of water and hydroxyl ions. The former species are unlikely because of both the frequency and numbers of absorptions which are present in high purity spectra. A water molecule produces two O-H stretching vibrations. Dimeric water molecules interact with each other to produce two sets of O-H stretching vibrations[140] as does molecular water which forms part of a crystal structure, as shown in the last section. In the case of trimers and higher oligomers, each molecule in the group will interact to produce a set of stretching vibrations. The presence of only four absorption major bands rules out the possibility of any group of water molecules larger than a dimer. The values reported for O-H stretching frequencies produced by water monomers and dimers do not compare well with those observed in high purity quartz spectra[140-143] (see tables 3.2 and 3.20). The differences could be a result of interactions between the quartz crystal lattice and the water molecules since the literature frequencies were recorded for water trapped in various neutral solid gas matrices. However, the good agreement between frequencies of water monomers trapped in the sodium fluoride

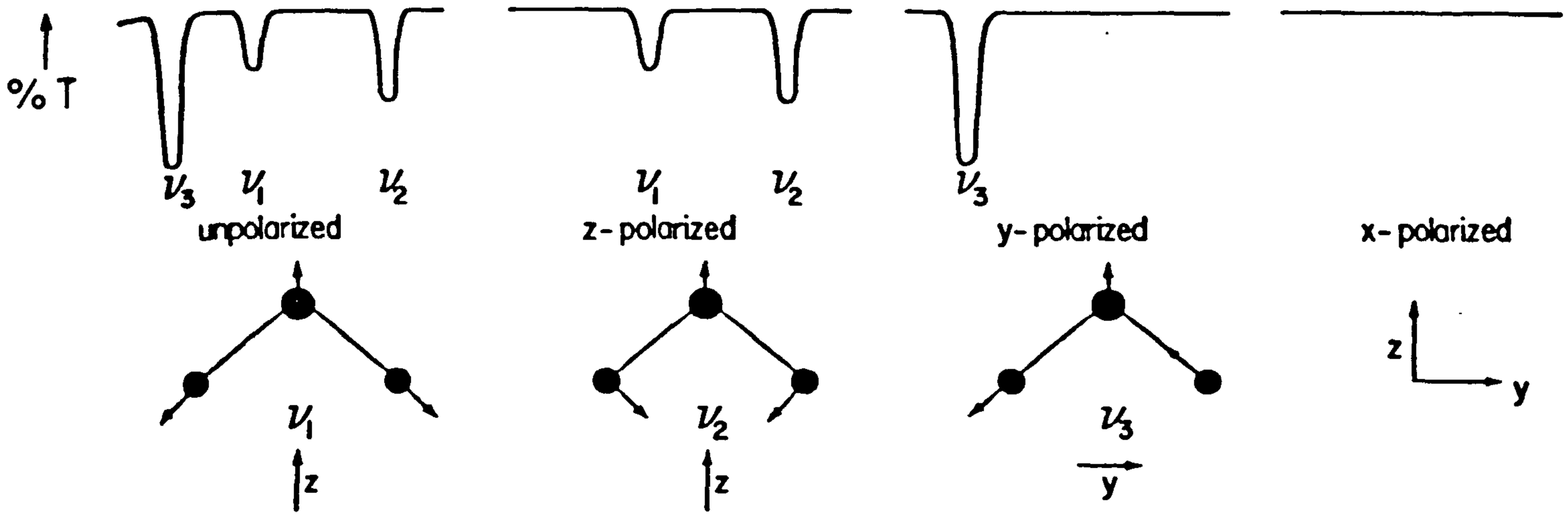

Fig. 3.39 (a) Hypothetical polarized infrared spectra of H_2O. (b) The vibrations ν_1 and ν_2 change only the z component of the dipole moment of H_2O while ν_3 changes only the y component.

(From Ref. 144)

crystal shows that a crystal environment can produce very similar absorptions to those observed in frozen gas matrices. The absence of water molecules is confirmed by considering the polarisation of the absorption bands (see section 3.3). Figure 3.39 shows the theoretical polarised infrared spectrum arising from a hypothetical water molecule[144]. From this spectrum it can be seen that each of the three absorption bands are absent in two of the three polariser configurations. In the case of high purity quartz absorptions, none of the bands are absent in more than one polariser configuration.

The dominant infrared active hydrogen impurities in high purity quartz are therefore hydroxyl species. The nature of these species are strongly suggested by the spectrum of hydroxyl in sodium chloride crystals. The absorption band in that spectrum occurs at the same frequency as the 3580 cm^{-1} absorption in spectra of high purity quartz and both bands are band width temperature dependent and are produced by hydroxyl impurities. Sodium also is the most common impurity in high purity crystals, which is consistent with the proposed model for hydroxyl impurities in the sodium chloride crystal. Therefore, it can be proposed that the hydroxyl impurities in high purity crystals associated with the 3580 cm^{-1} absorption band are sodium hydroxide units, $Na^{+}OH^{-}$.

With this assumption, the other absorption bands in quartz infrared spectra can also be assigned. The hydrogen content of high purity crystals is greater than that observed for the sodium chloride crystal, based on the relative

intensities of bands in the cooled sample spectra. Therefore, the remaining high purity absorptions could be produced by sodium hydroxide units in different environments. This is most probably the case for the 3436 cm^{-1} band which shows polarisation behaviour identical to that observed for the 3580 cm^{-1} band. The O-H bonds of this hydroxyl species are aligned in the same way in the crystal as those associated with the 3580 cm^{-1} band and are most probably produced by the same species. This would indicate the possibility of a sodium hydroxide dimer in the lattice. The polarisation behaviour of the species associated with the 3348 cm^{-1} absorption suggested its assignment to a sodium hydroxide unit aligned directly parallel to the C-axis. The remaining absorption at 3395 cm^{-1} can only be assigned to a hydroxyl species which is randomly distributed throughout a quartz crystal which may also be associated with sodium hydroxide units.

Assignment of absorption bands to sodium hydroxide units is consistent with the known discrepancies between sodium content and aluminium levels in high purity crystals. Atomic absorption analysis of quartz can be used to determine the levels of sodium and aluminium in a quartz crystal. It is normally assumed that all the sodium present in a crystal is used to charge compensate substitutional defect sites[104]. The amount of sodium in a crystal can also be determined from the total charge passed during sweeping since the main charge carriers in quartz are Na^+ ions. Work carried out by Hirst

Table 3.22 Sodium Content in High Purity and Commercial Quartz*

Impurity	Concentration (ppm)[a]		Theoretical Charge[b] ($x10^{-6}F$)		Actual Charge[c] ($x10^{-6}F$)	
	COMQ	HPQ	COMQ	HPQ	COMQ	HPQ
Al	1.0	0.01	-	-	-	-
Na	0.4	0.01	2.40	0.02	2.72	0.59
Li	0.7	<0.005	-	-	-	-
K	0.01	<0.005	-	-	-	-
Fe	0.02	<0.005	-	-	-	-

* - Data for this table quoted from reference 145

a - Measured using atomic absorption spectrometry ($\mu g/g$ SiO2) [Detection limit 0.005 ppm]

b - Charge required to charge compensate every Al^{3+} ion with Na^{+}

c - Actual charge (Na^{+} ions) passed during sweeping

scientists showed that the charge passed by a commercial quartz sample was consistent with the amount of sodium required to exactly charge compensate aluminium defect sites[145] (see table 3.22). However when this was carried out for a high purity crystal, the amount of charge passed was far in excess of the value calculated if the only sodium present was involved in charge compensation of aluminium sites[145] (see table 3.22). Thus, high purity crystals have an excess of sodium ions which could be partly accounted for by the presence of the postulated sodium hydroxide impurities.

Chapter 4. X-Ray Diffraction Studies

Table 4.1 Lang Topographs of Selected Quartz Crystals

Topograph No.	Crystal Title	Crystal Source	Reflection Plane	Film Type
1	R1	Growth Run 1	(02.0)	M3
2	R2	Growth Run 2	(02.0)	M3
3	R15	Growth Run 15	(02.0)	M3
4	R19	Growth Run 19	(02.0)	M3
5*	R13	Growth Run 13	(01.0)	D4
6	R17	Growth Run 17	(02.0)	M3
7*	R6	Growth Run 6	(01.0)	D4
8	R14	Growth Run 14	(02.0)	M3
9	R16	Growth Run 16	(02.0)	M3
10*	R5u	Growth Run 5	(01.0)	D4
11*	R5s	Growth Run 5	(01.0)	D4
12	R8	Growth Run 8	(02.0)	M3

* - Obtained using the white radiation camera at Daresbury

u - Unswept seed s - Swept seed

Notes - The K_α wavelength of Molybdenum radiation, 0.709 Å, was used in Bragg calculations. Exposure times of 24 hours and 30 minutes were employed at Strathclyde University and Daresbury laboratory respectively. All of the above samples were 1mm thick X-slices cut from the crystals detailed in table 2.1.

Chapter 4. X-Ray Diffraction Studies

4.1 Crystal Growth Runs

4.1.1 Crystal Quality

The quality of the quartz crystals discussed in section 3.1 was assessed using conventional Lang transmission x-ray diffraction topography at Strathclyde University. In the context of this section, crystal quality refers to the presence of those imperfections which produce lattice strain that is detectable by x-ray diffraction methods. In general, these include all imperfections discussed in section 1.6 with the exception of point defects. However, the only defects which were observed on the topographs in this section were dislocations and inclusions (see figs. 4.1 - 4.12). Dislocations appeared as dark lines of contrast on topographs, usually lying at $\approx 11^{\circ}$ to the [00.1] growth normal, and are marked by a D. Inclusions were observed as circular dark areas on a topograph and are denoted by an I. A feature common to all of the topographs was a rectangular band which stretched across the centre of each crystal. Each topograph was obtained from an X-slice sample which contained part of the original seed crystal. The rectangular band, S, was produced by and showed the position of the seed in the bulk of the grown crystal. Those features specific to individual crystals will be discussed.

Crystals from growth runs 1, 2, 15 and 19 were grown using heavy water solutions of sodium hydroxide (see figs. 4.1 - 4.4

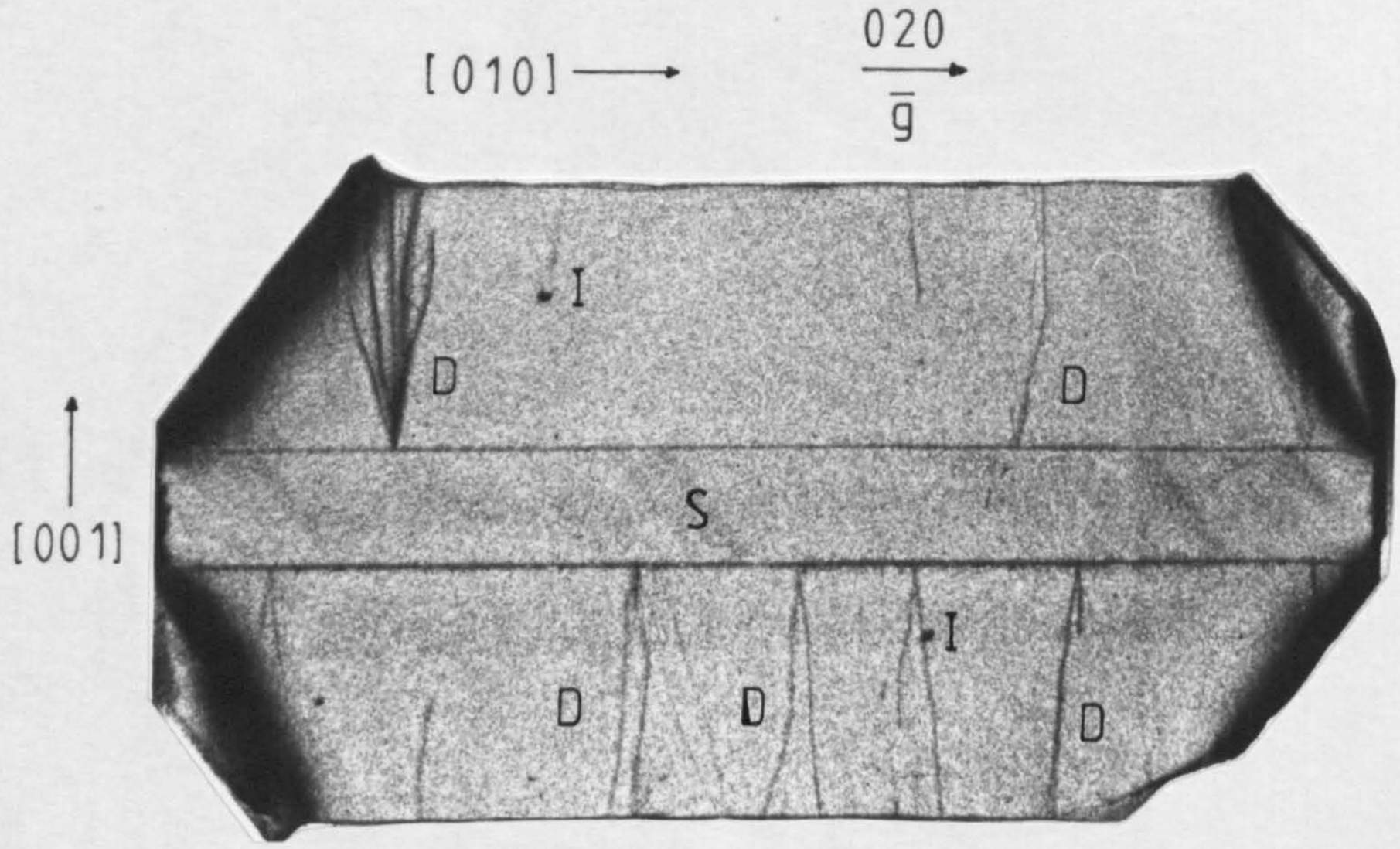

Fig. 4.1 - Topograph 1

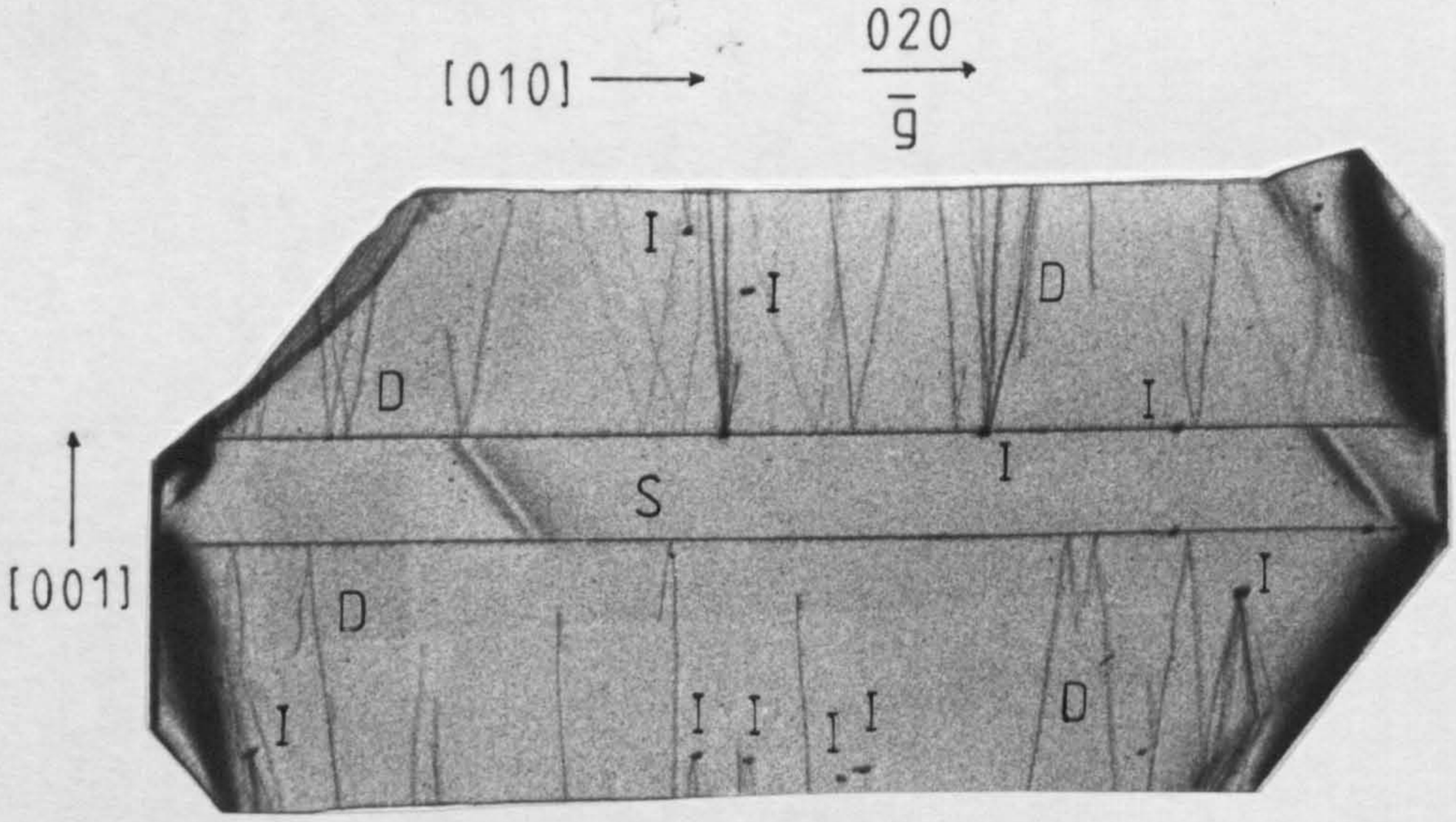

Fig. 4.2 - Topograph 2

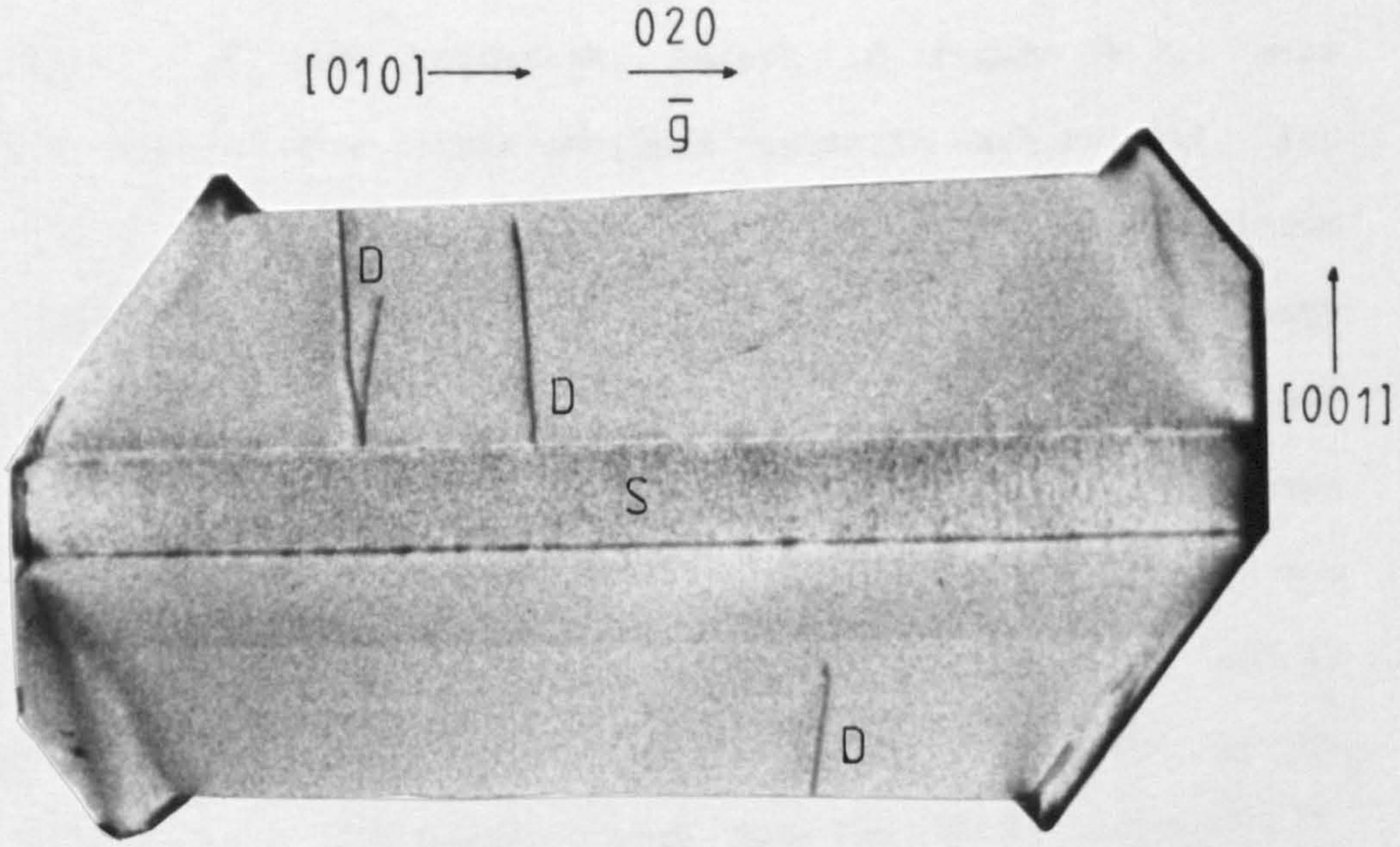

Fig. 4.3 - Topograph 3

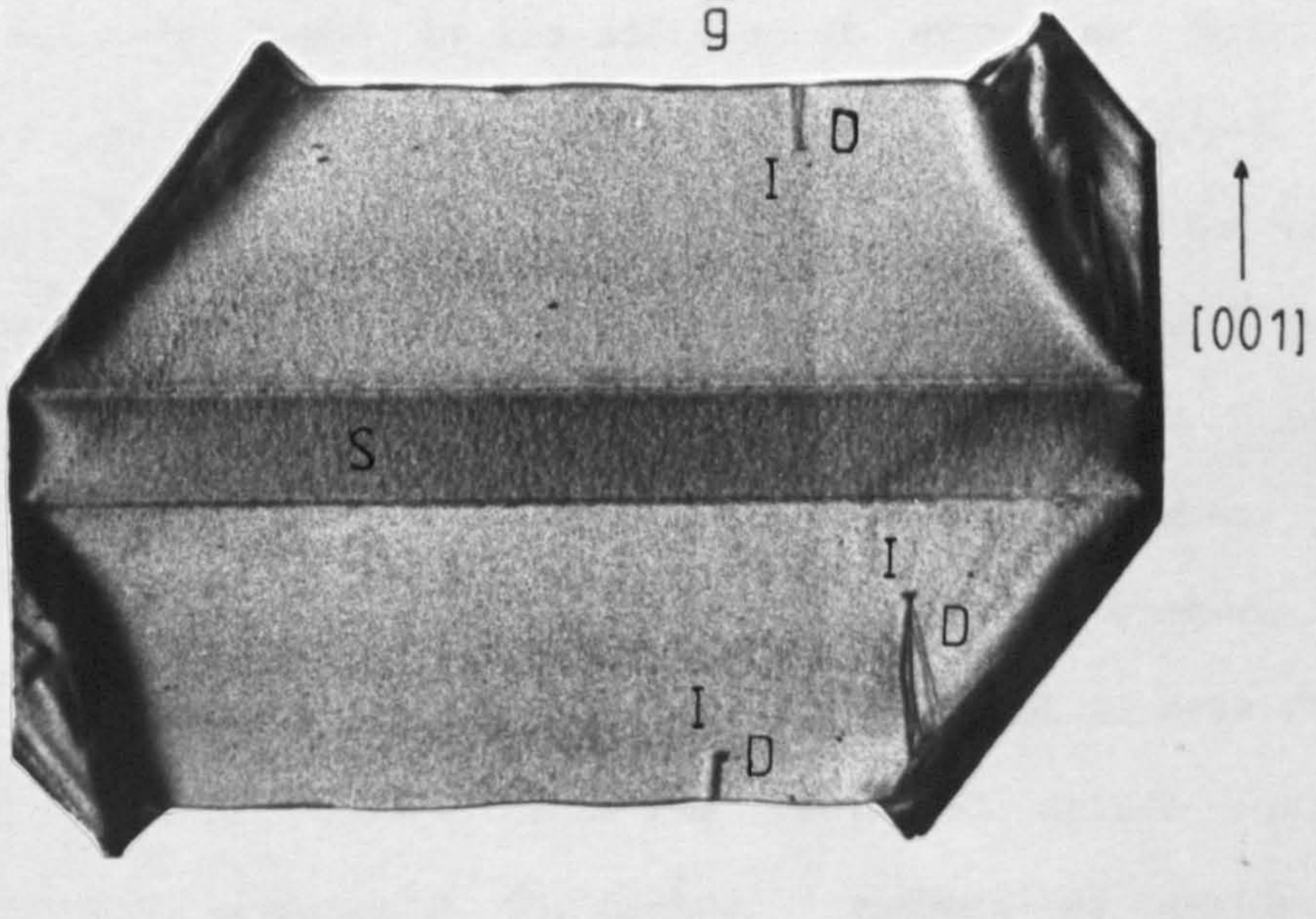

Fig. 4.4 - Topograph 4

and table 4.1). The regions of high contrast near to the edges of each topograph, except in figure 4.3, were indications of a highly strained region in each crystal. The strain was produced by high concentrations of aluminium impurities which were present in rhombohedral growth sectors[145]. Although each crystal was predominantly composed of (00.1) growth sector material, there was always some development of the rhombohedral, {10.1} and {01.1}, and prismatic, {10.0}, growth sectors which border the (00.1) growth sector. Aluminium is incorporated into these growth sectors to a much higher degree than the (00.1) sector[35,93], which was reflected by the strain observed on topographs. The strain in the bordering growth sector material was expected for samples taken from crystals R2 and R19, which had been deliberately doped by the addition of aluminium foil. The appearance of the strain on the topograph of the crystal from growth run 1, R1, which had not been doped, showed the sample to be contaminated with aluminium. Growth run 15 was a repeat of growth run 1 which used high purity quartz as the nutrient (see table 2.1). Run 15 produced a crystal which did not show any signs of strain in the rhombohedral growth sectors (see fig. 4.3). The source of aluminium contaminant in crystal R1 was therefore thought to be the converted silica nutrient which had been used. The higher numbers of particulate inclusions in crystals R1 and R2 compared with R15 and R19 was also thought to be caused by the use of converted silica nutrient (see table 4.2). It could not be established using

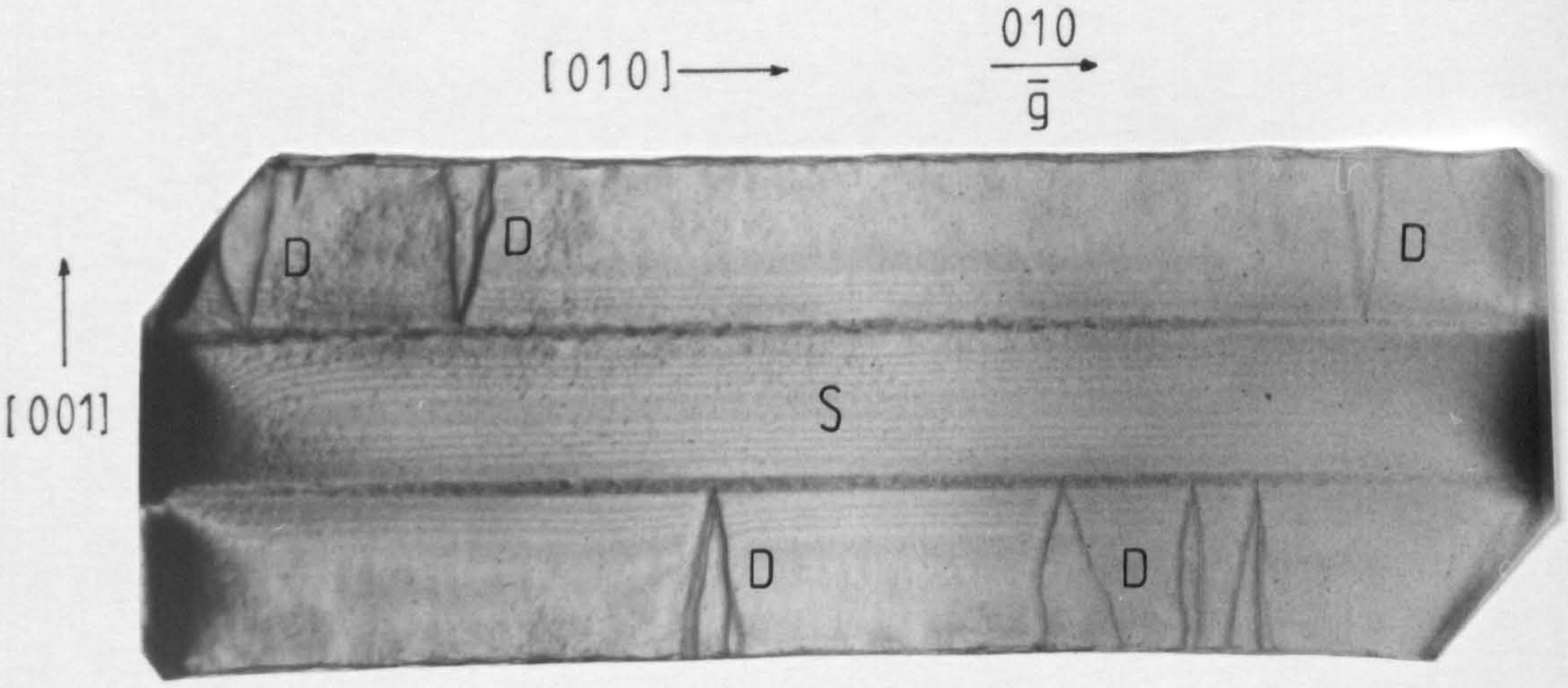

Fig. 4.5 - Topograph 5

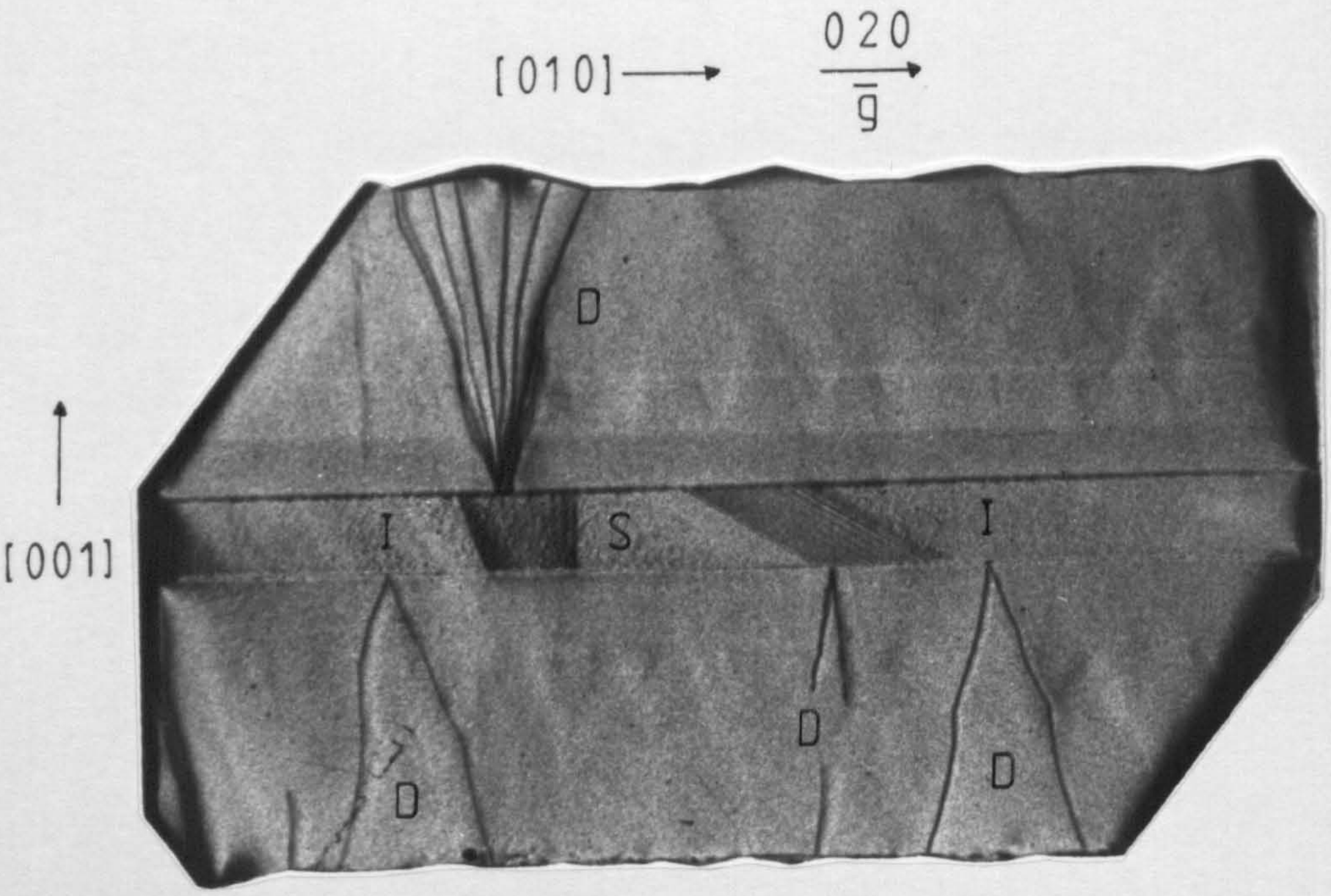

Fig. 4.6 - Topograph 6

topographic methods what caused the formation of these defects or what their exact nature was. However, as there was no cleaning run performed between the convertion of silica and the growth run, the particles were probably acmite.

Crystals R13 and R17 were grown using a heavy water solution but with a sodium carbonate mineraliser (see figs. 4.5, 4.6 and table 4.1). Both crystals were grown using a high purity quartz nutrient and showed similar concentrations of dislocations and no inclusions. The number of dislocations was higher in comparison with those observed in crystals grown using the same nutrient but with a sodium hydroxide mineraliser (see figs. 4.3, 4.4 and table 4.2). The strain in the rhombohedral sectors shows that these crystals are also contaminated with aluminium. The most probable source of this contamination was the mineraliser (see table 2.3).

Growth runs 6 and 14 produced crystals which showed the highest quality (see figs. 4.7, 4.8 and table 4.2). Crystal R6 was defect free and crystal R14 had a very low dislocation density and showed no evidence of inclusions. Both crystals were also free from strain in the rhombohedral growth sectors which was indicative of low aluminium concentrations. Both of these crystals were grown using high purity quartz nutrient. Crystal R16 was produced in the same manner as R6, with the exception that autoclave temperatures were lowered to reduce growth rate. Growth run 16 should therefore have produced a crystal of identical quality to that of run 6. However crystal R16 was of poor quality crystal with a high concentration of

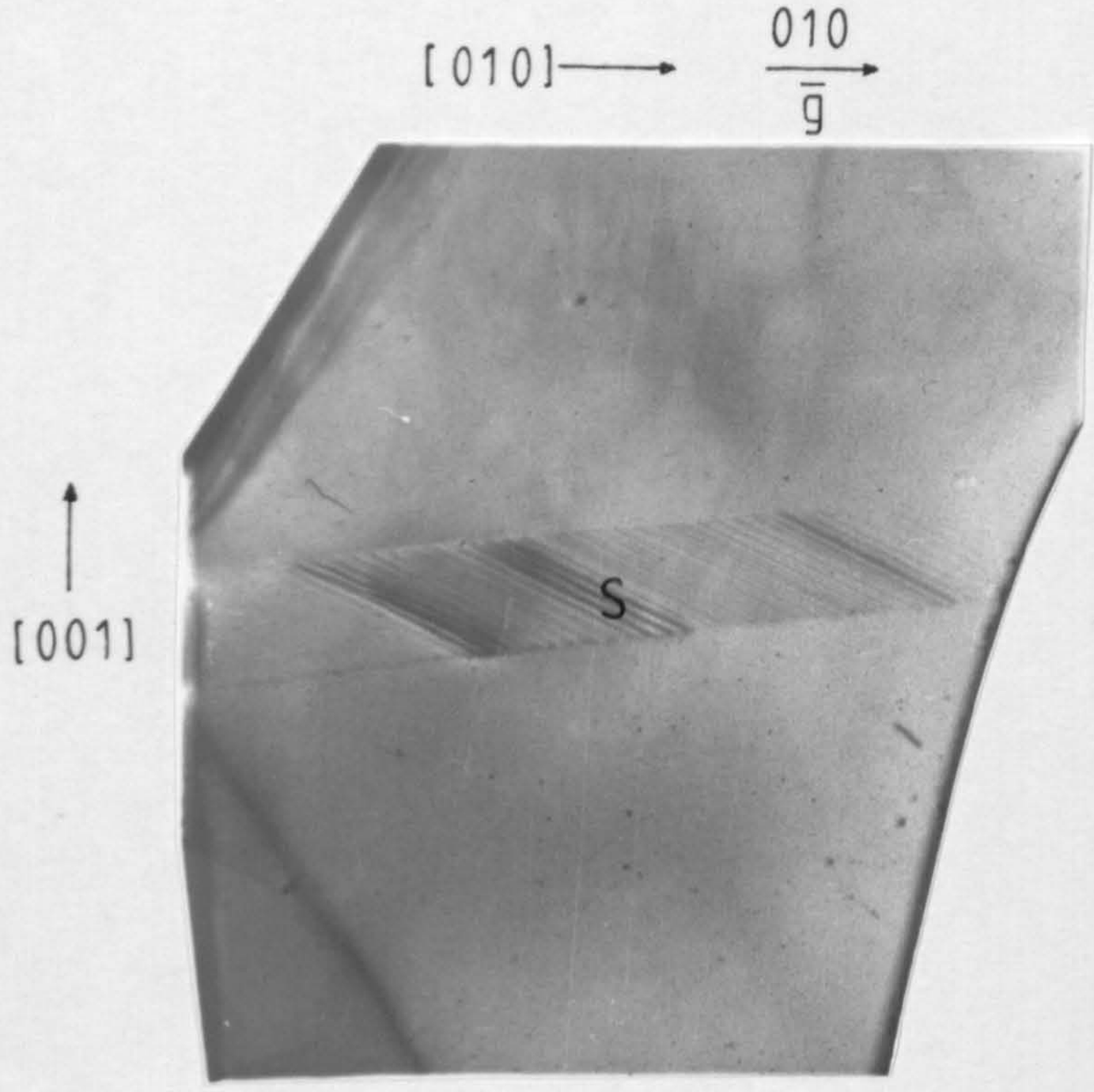

Fig. 4.7 - Topograph 7

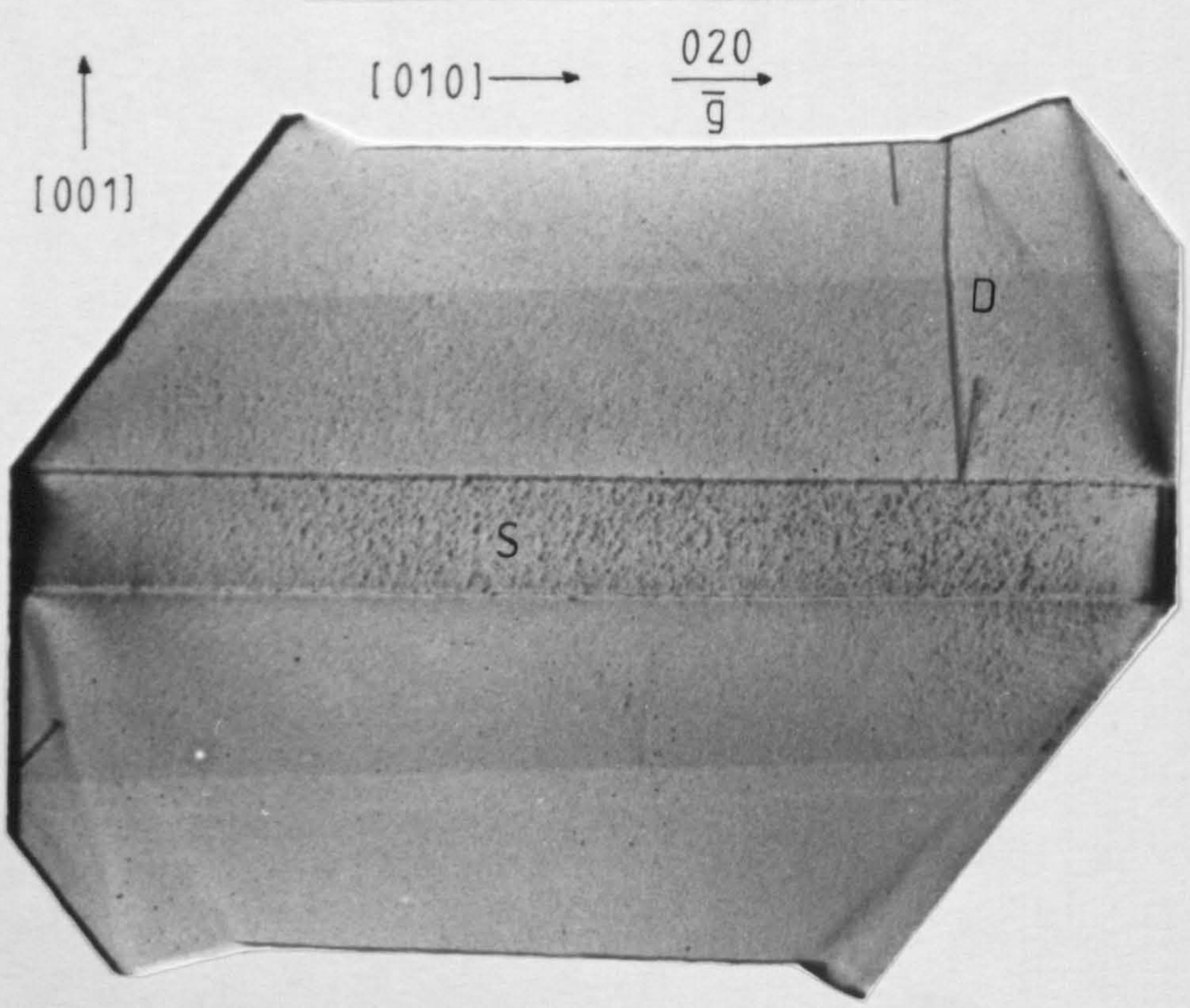

Fig. 4.8 - Topograph 8

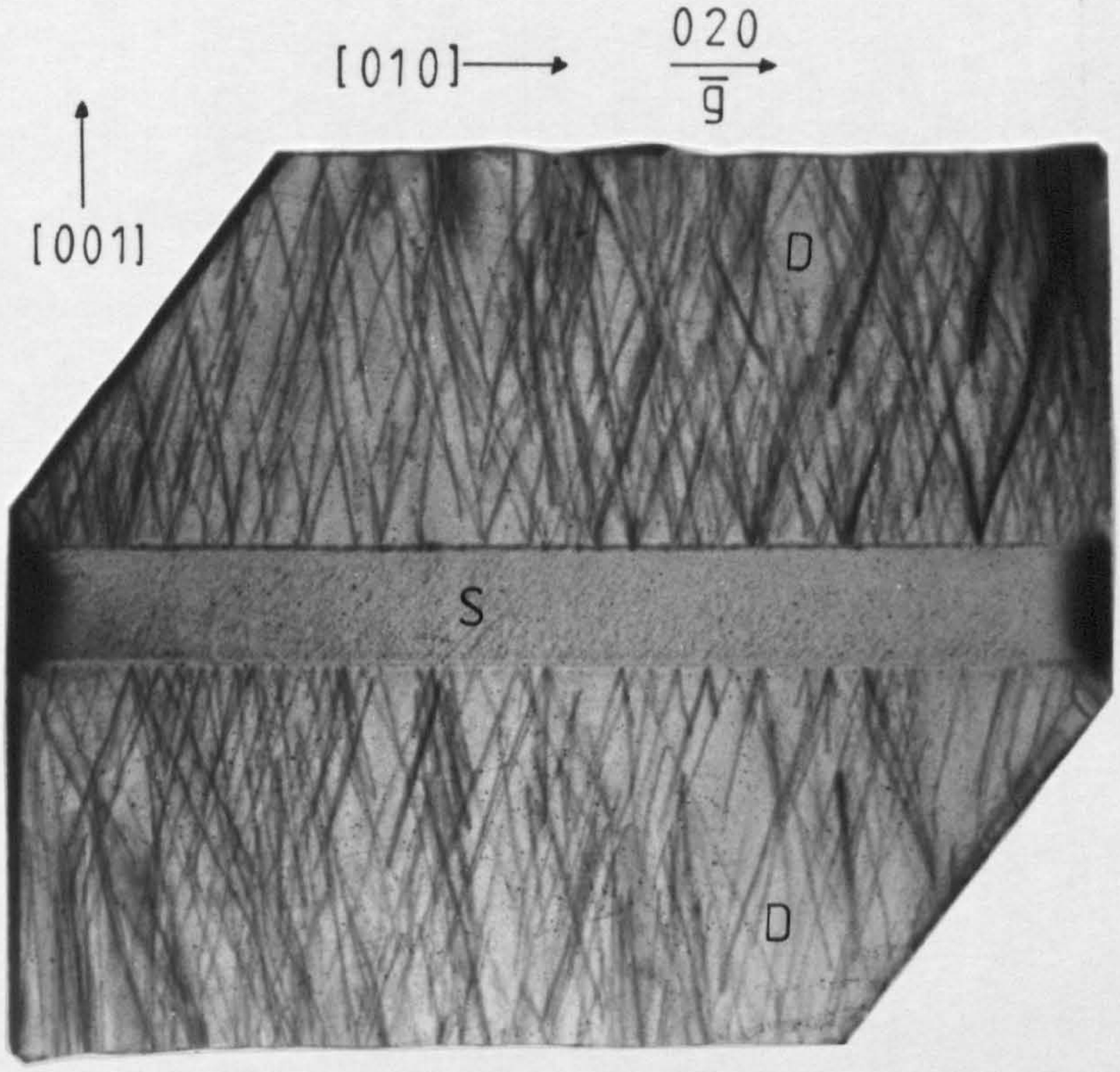

Fig. 4.9 - Topograph 9

Table 4.2 Defect Content of Selected Quartz Crystals

Crystal	No. of Inclusions[a]	Dislocations on Seed[b]	Dislocations from Inclusions[c]	Total No.[a]
R1	3	20	2	22
R2	14	40	20	60
R5u	OD	≈ 300	OD	≈ 300
R5s	OD	≈ 500	OD	≈ 500
R6	0	0	0	0
$R8^T$	4	≈ 300	OD	≈ 300
$R8^B$	0	0	0	0
R13	0	20	0	20
R14	0	1-2	0	1-2
R15	0	4	0	4
R16	0	≈ 140	0	≈ 140
R17	2	10	4	14
R19	3	0	7	7

a - Total number of defects per 1mm thick crystal slice (approximately 1 cm^2 area)

b - Number of dislocations which originate from the seed/crystal boundary

c - Number of dislocations which originate from a particulate inclusion

OD - High density of dislocations obscures any inclusions present

u - Unswept seed

s - Swept seed

T - High dislocation section of crystal R8

B - Dislocation-free section of crystal R8

dislocations (see fig. 4.9 and table 4.2).

The majority of defects was observed in crystals grown using a converted silica nutrient or a sodium carbonate mineraliser. With the exception of the growth run 16, the crystals grown with high purity quartz nutrient and sodium hydroxide mineraliser showed much lower dislocation densities and a lower incidence of particulate inclusions (see table 4.2). Of those crystals grown using a high purity quartz nutrient, only one sample had inclusions present (see fig. 4.4). Inclusions were usually observed on growth from converted silica.

The growth rate of crystals, in the range given in table 2.1, was not thought to influence the generation of dislocations since the fastest grown crystal, R6, also showed the highest perfection (see fig. 4.7). The absence of dislocations in the natural seed crystals used for growth, implied that no dislocations could be formed by continuations of defects from the seed into the growing crystal. Dislocations were formed mainly on the surface of the seed crystal but dislocation generation at particulate inclusions was also observed (see figs. 4.1, 4.2 and 4.6). Generation of dislocations from particles on the seed surface were observed in the topograph of crystal R17 (see fig. 4.6). This observation combined with the fact that the majority of dislocations were generated on the surface of the seed crystal was suggestive that particles were a major source of dislocation generation in high purity quartz (see table 4.2).

The particles which could be observed on topographs were probably acmite inclusions. However, since dislocations were produced in areas of a crystal free from observable particulate inclusions, the presence of other types of particle such as quartz dust could not be ruled out. The increase in the dislocation and inclusion content of a crystal grown using sodium carbonate or converted silica strongly suggests that both of these materials are sources of defect generating particles. Sodium carbonate could achieve this by increasing the deterioration of autoclave walls thereby increasing acmite particle generation. Converted silica nutrient is essentially polycrystalline quartz and is therefore a potential source of quartz dust particles. The majority of dislocations were formed at the seed/crystal interface and were therefore generated during the initial stages of growth. Thus, a possible mechanism for dislocation formation is the deposition of a particle onto a seed crystal during the initial growth of a crystal.

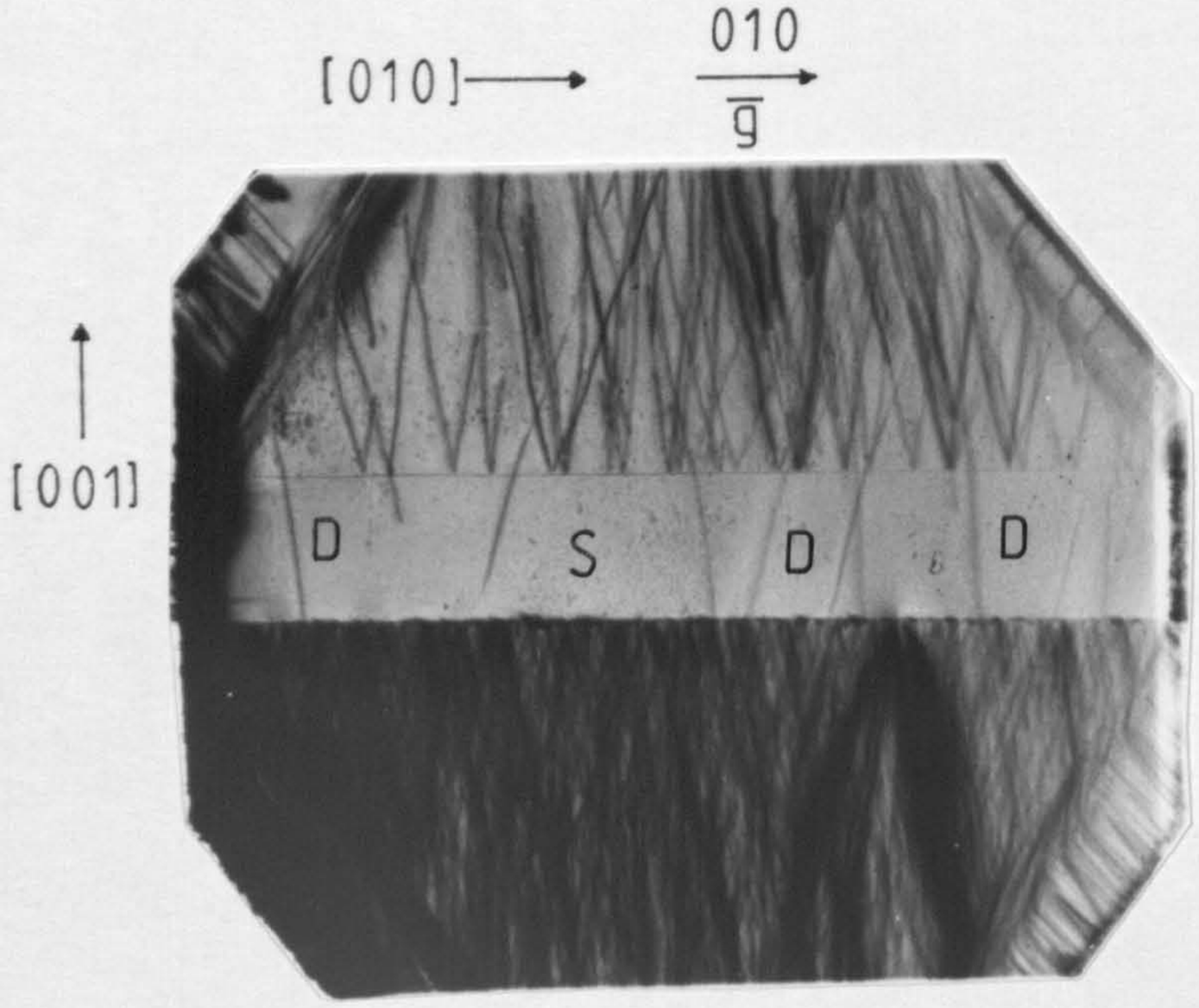

Fig. 4.10 - Topograph 10

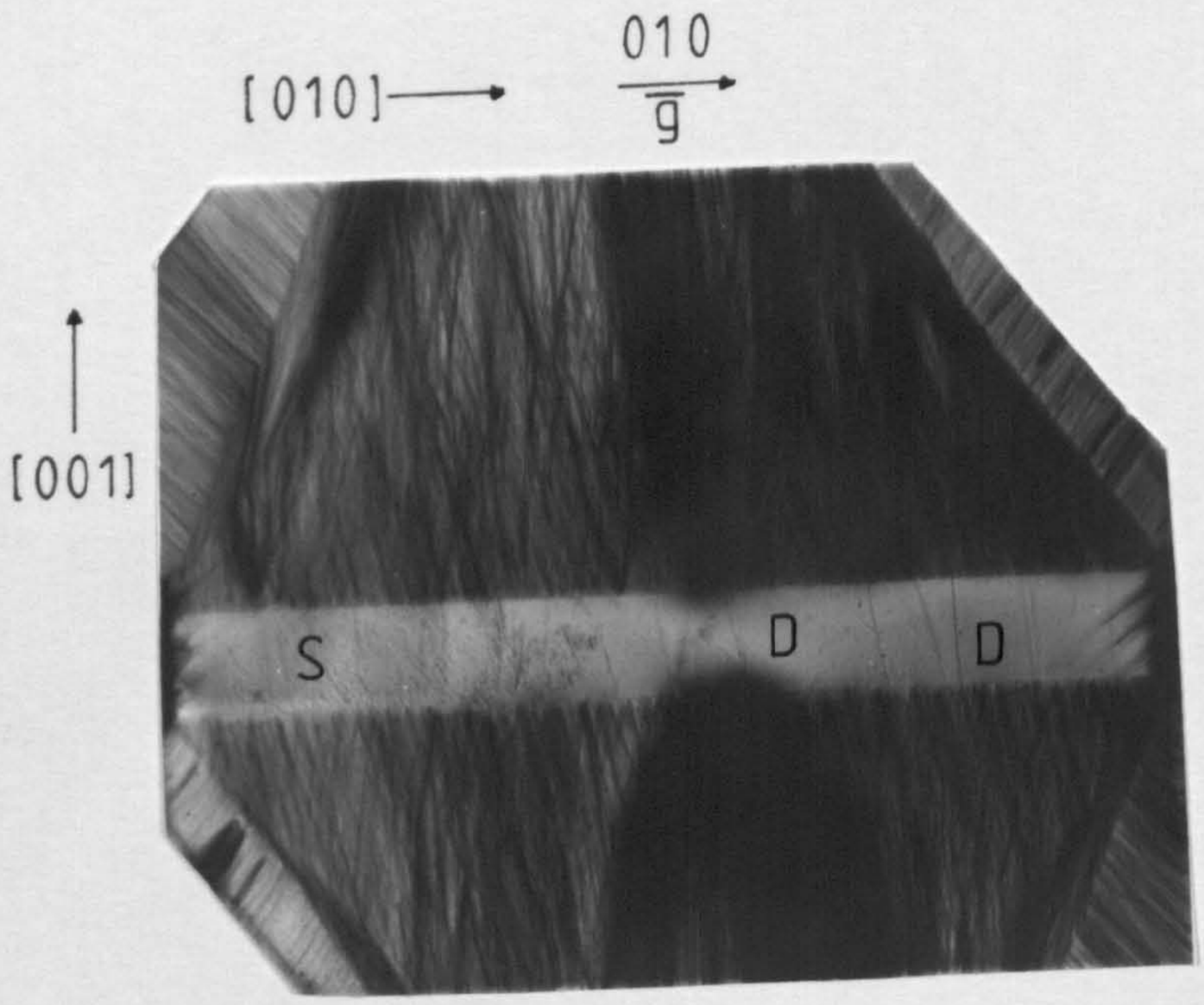

Fig. 4.11 - Topograph 11

4.1.2 Specialised Growth Runs

Growth runs 5 and 8 were carried out using variations to the growth procedures described in section 2.1. For growth run 5, two seed crystals were suspended in the same autoclave. The seeds were cut from high purity synthetic crystals, one of which had been swept to remove alkali metal impurities. The aim of the experiment was to study what effect sweeping would have on the generation of dislocations by continuations of defects present in the seed. Sweeping was known to reduce etch channel formation by the removal of those impurities which concentrate along the core of a dislocation[116,117]. If these impurities were in some way connected with the continuation mechanism of a dislocation then their removal could possibly prevent dislocation formation. A second unswept seed was placed in the same autoclave to act as a control sample.

The growth quality of the two crystals produced by run 5 was very poor (see figs. 4.10, 4.11 and table 4.2). This was thought to be a result of the increased turbulence in the autoclave arising from the presence of two seeds. However the topograph of the crystal grown from the swept seed still showed that dislocations were produced by the continuation mechanism (see fig. 4.11). Sweeping therefore had no effect on the formation of dislocations.

Growth run 8 was designed to produce a crystal which had one region of perfect growth and one which had a very high concentration of dislocations. This was achieved by suspending a seed crystal horizontally in the autoclave instead of

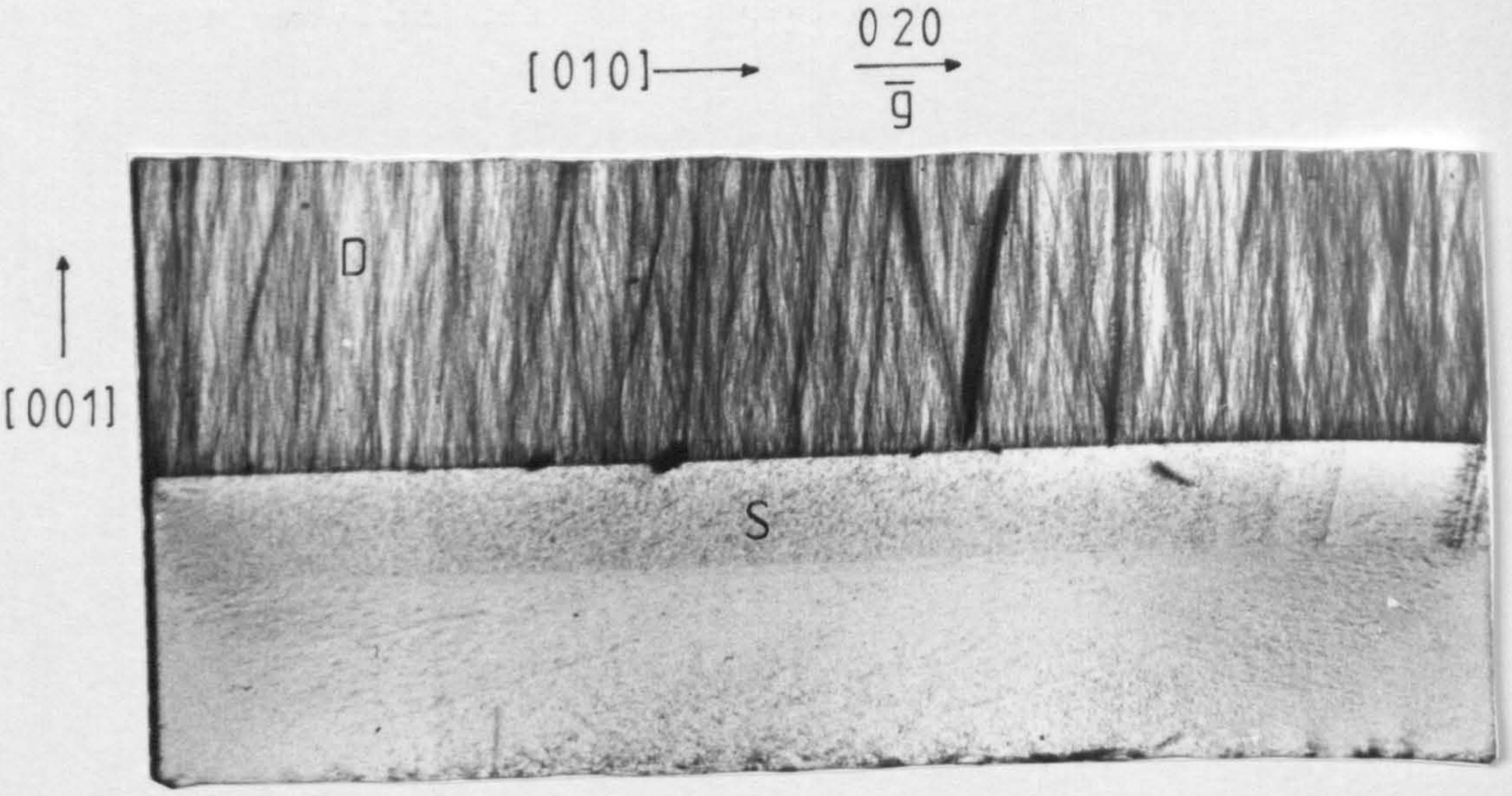

Fig. 4.12 - Topograph 12

vertically. This technique was known to produce good quality growth on the lower seed surface to the detriment of the upper growth layer[136]. The initial aim of the experiment was to provide a crystal which could be used to study the relationship between dislocation concentration and the hydrogen content of quartz (see section 3.1e). However, an additional use of such as sample was the measurement of variations in lattice strain produced by the presence of dislocations. Growth run 6 produced a sample which possessed both extremes of crystal quality and could therefore be used in these studies (see fig. 4.12 and table 4.2). Lattice strain measurements of crystal R6 will be discussed in later sections.

4.2 X-Ray Diffraction Studies of Swept Quartz

4.2.1 Initial Aims and Progress

The main purpose behind the topographic studies carried out during the course of this work was the examination of synthetic quartz crystals which had undergone electrodiffusion. Although this technique has been widely used since its development by King in the 1960's[114], there had been no report of x-ray topographic studies carried out on swept samples prior to the commencement of this project. The sponsoring company, GEC, were especially interested in the possibility that crystal damage occurred as a result of the sweeping process. A series of topographic studies was therefore carried out to examine changes in crystal strain in samples which had undergone sweeping.

The first experiments used conventional Lang transmission x-ray diffraction topography at Strathclyde University to examine crystal strain. Two 1mm thick Y-slice x-ray samples were prepared from a commercial high purity quartz crystal grown at Hirst laboratories. These samples were optically polished to allow infrared examination. Gold electrodes were sputtered onto the (00.1) faces of the crystals to facilitate electrical contact. This was necessary due to the small surface area of the crystals used. Diffraction topographs were obtained from both of the samples before sweeping took place. Only sample SWEPT1 was connected to the platinum electrodes so that sample ANNEAL1 would act as a control to ensure that any features which appeared on topographs could be attributed to

Table 4.3 Single Crystal X-Ray Diffraction Topographs of Swept Crystals

Topograph No.	Sample Title	Reflection Plane	Film Type	Total Exposure (hrs)*	Comments
13	ANNEAL1	(2-1.0)	M3	-	untreated[a]
14	ANNEAL1	(2-1.0)	M3	24	annealed[b]
15	SWEPT1	(2-1.0)	M3	-	untreated[a]
16	SWEPT1	(2-1.0)	M3	-	swept[c]
17	ANNEAL1	(2-1.0)	M3	24	swept[c]
18	ANNEAL1	(2-1.0)	D4	90	retop[d]
19	COMQ	(2-1.0)	M3	21	swept[c]
20	COMQ	(2-1.0)	D7	91	retop[d]
21	COMQ	(2-1.0)	D2	183	retop[d]
27	SWEPT1	(02.-3)	D4	-	WR[e]
28	SWEPT1	(02.-3)	M3	-	etched[f]
29	HPQ	(02.-3)	D4	-	WR[c,e,f]

* - total exposure time of a sample to X-rays directly after sweeping

a - Optically polished

b - Treated under the same conditions as a swept sample but with no potential applied across the sample

c - Swept for 1 week in a Nitrogen atmosphere at 500°C using a potential of 1000 Vcm^{-2}

d - No further treatment, sample retopographed

e - Obtained using the white radiation camera at Daresbury Laboratory

f - Etched in 40% HF to remove surface sweeping damage

Notes - The K_α wavelength of Molybdenum radiation, 0.709Å, was used for all Bragg calculations. All samples were 1mm thick Y-cut crystal slices.

the sweeping process and could be distinguished from features arising from the annealing effect of the high temperatures used. The procedures followed for electrodiffusion were described in detail in section 2.3. The swept samples were then re-topographed and examined for any changes caused by the treatment (see figs. 4.13-4.16 and table 4.3).

Although the pre-treatment topograph 13 obtained from the control sample, ANNEAL1, showed some evidence of surface damage, dislocations were the only type of crystal defect observed (see fig. 4.13). Scratches, SC, appeared as lines of contrast running roughly perpendicular to dislocations. Irregularly shaped contrast "spots", SD, were produced by a chipped crystal surface. Inclusions were not observed on this diffraction image. Topograph 14, which was obtained after annealing, did not show any new features other than those which were consistent with the temperature treatment that the crystal had undergone. An example of this was the marked circular feature, I, on figure 4.14. The lattice strain observed on topograph 14 was produced by the expansion of an inclusion of growth solution upon heating. This caused enough damage to the surrounding crystal to produce the observed increase in lattice strain.

The topograph obtained from the unswept sample, SWEPT1, showed similar features to those observed on topograph 13 (see fig. 4.15). Again the only true crystal defects observed on topograph 15 were dislocations. Images consistent with surface damage, SD, were also present, notably a large scratch

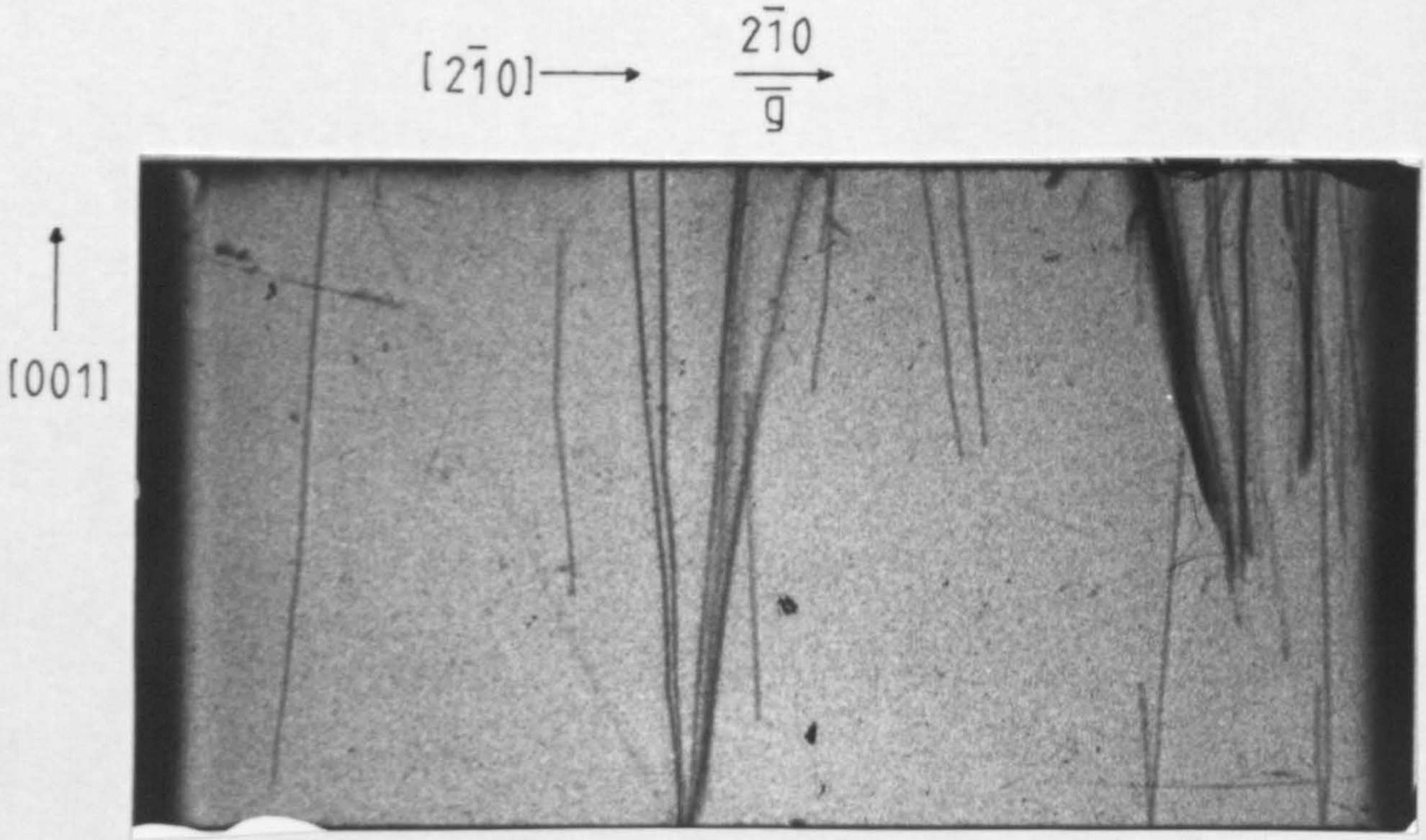

Fig. 4.13 - Topograph 13

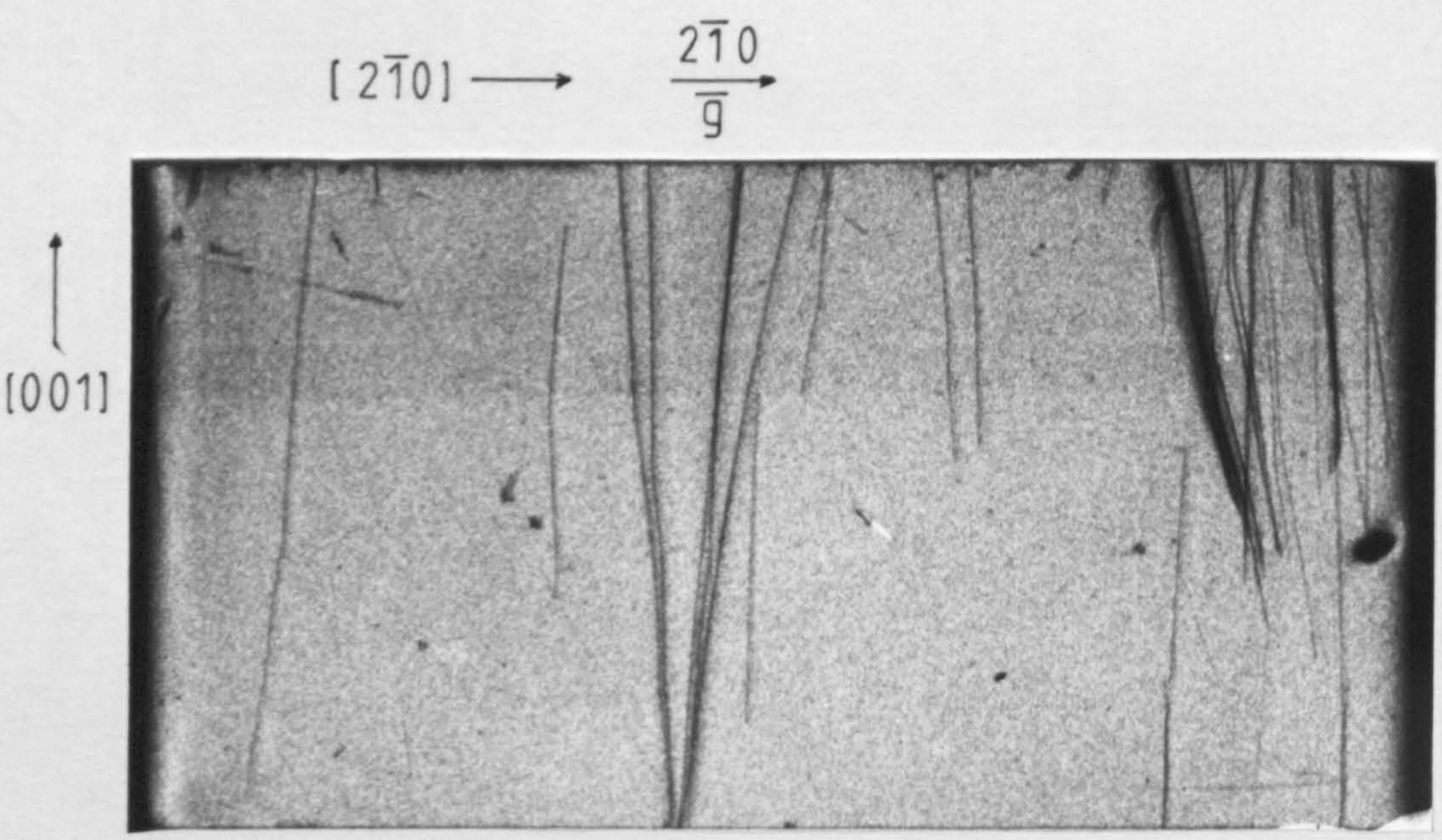

Fig. 4.14 - Topograph 14

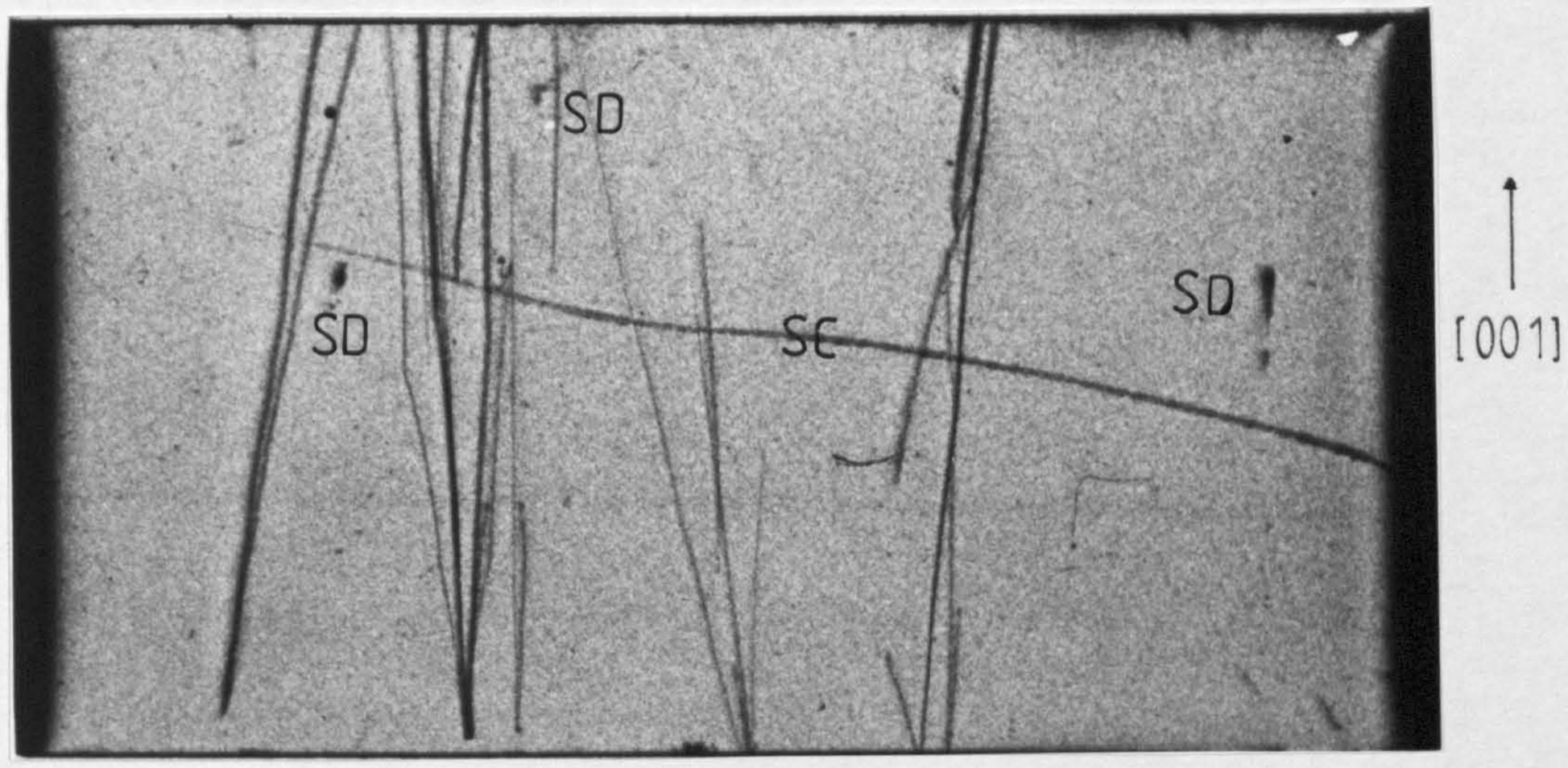

Fig. 4.15 - Topograph 15

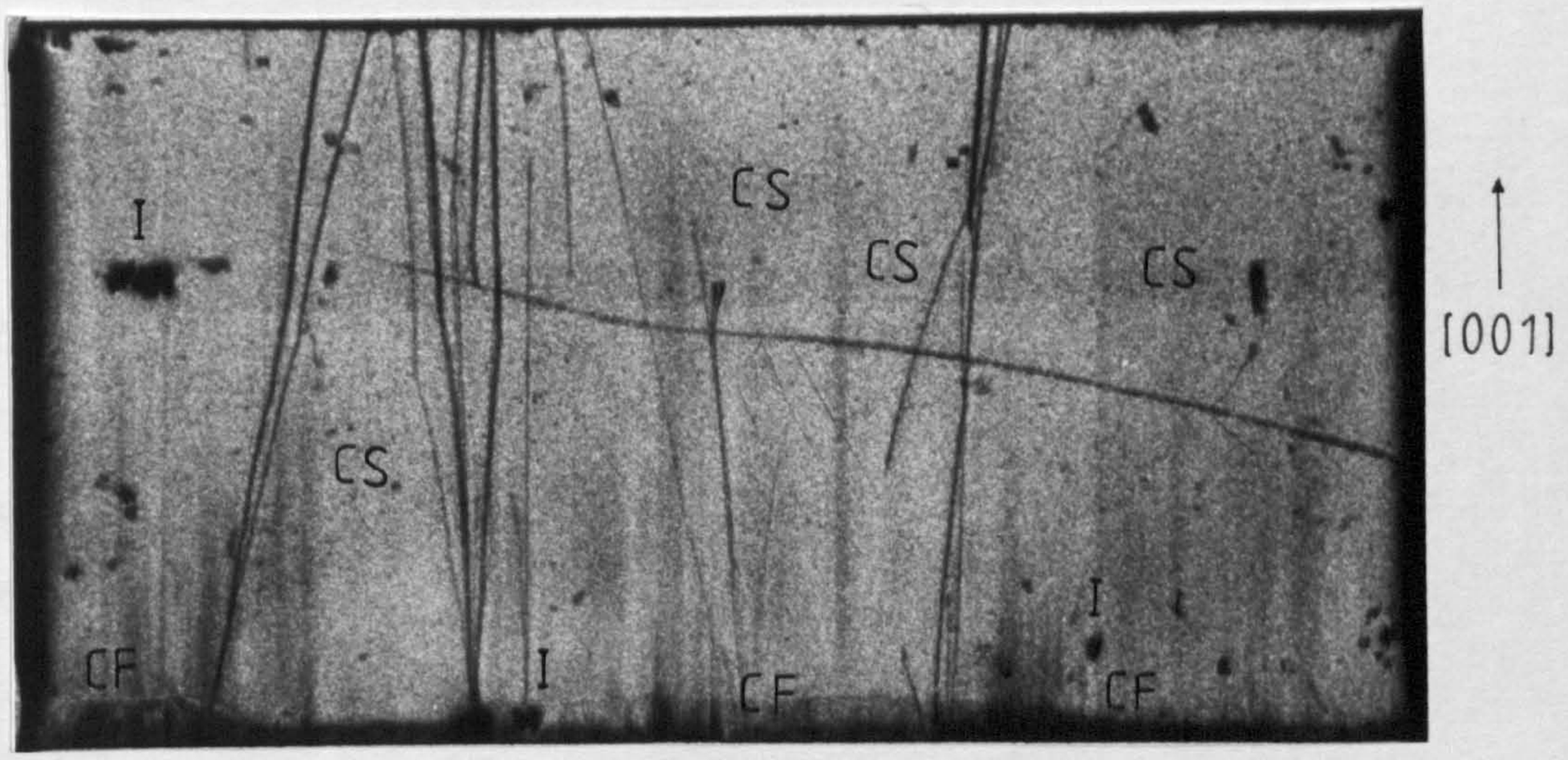

Fig. 4.16 - Topograph 16

stretching horizontally across the topograph, SC (see fig. 4.15). However, the diffraction image obtained after sweeping exhibited a contrast feature not present on the control topograph (see fig. 4.16). This consisted of an uneven band of strain, CF, originating along the face of the crystal which had been attached to the positive electrode. Although the feature was strongest close to this face, strain "streaks", CS, ran across to the other side of the crystal at several places. These "streaks" took the form of lines of strain of various thicknesses running parallel to the Z crystallographic axis and following the direction of the C-channels along which impurity ions were drawn by the sweeping process. The feature was therefore consistent with the damage that might result from the movement of these impurities through the crystal.

4.2.2 Contrast Feature Dependence on Radiation Dosage

To help with the characterisation of the contrast features, CF and CS, it was necessary to improve the resolution of the diffraction image. The easiest way this could be achieved was to use a higher resolution photographic film to image the topograph. The original swept sample, SWEPT1, was being used for experiments discussed later in section 4.3 and so the annealed sample, ANNEAL1, was used as an alternative. After being swept under identical conditions to SWEPT1, the sample was topographed firstly using low resolution AGFA M3 photographic film, to ensure that the

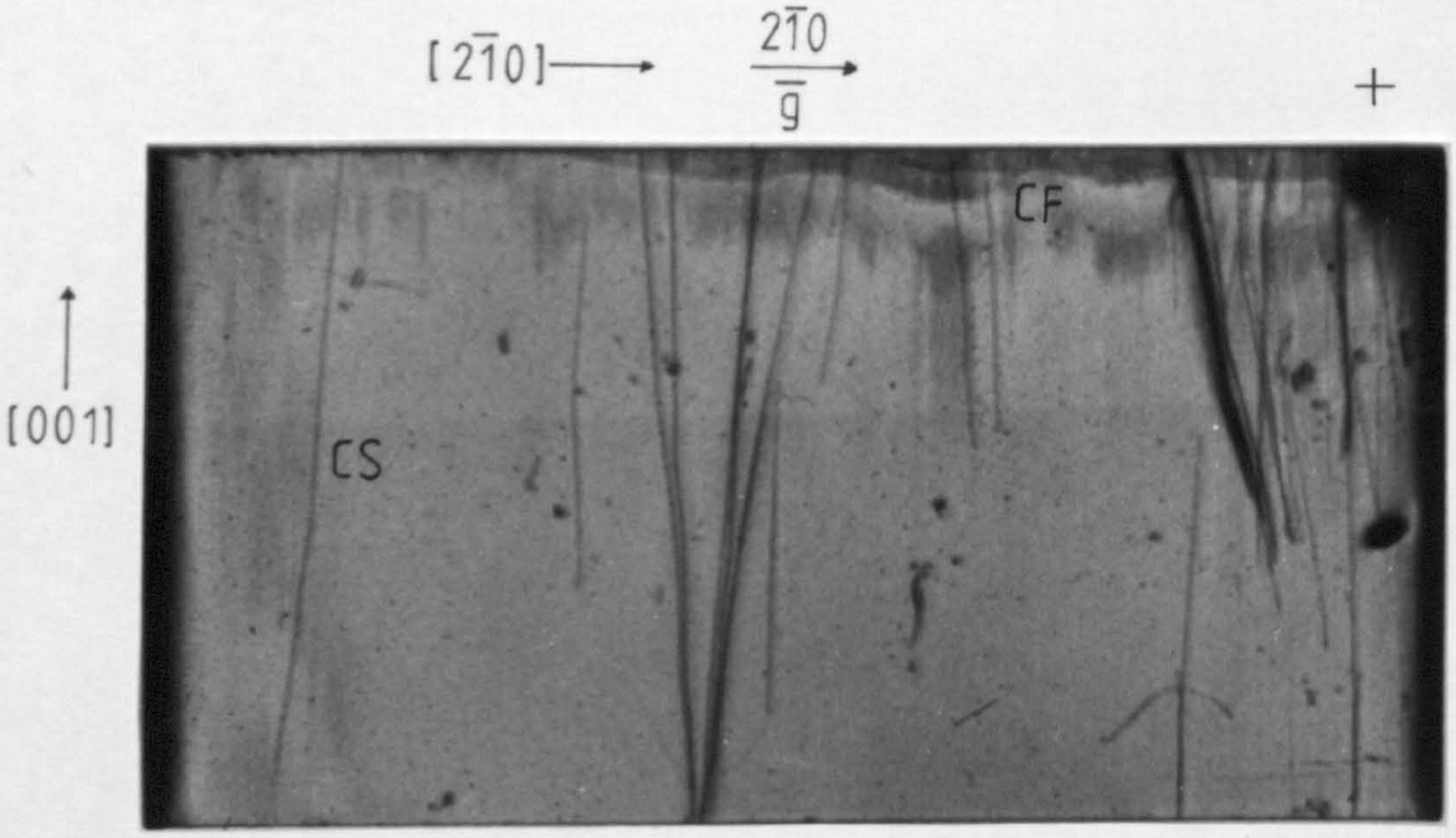

Fig. 4.17 - Topograph 17

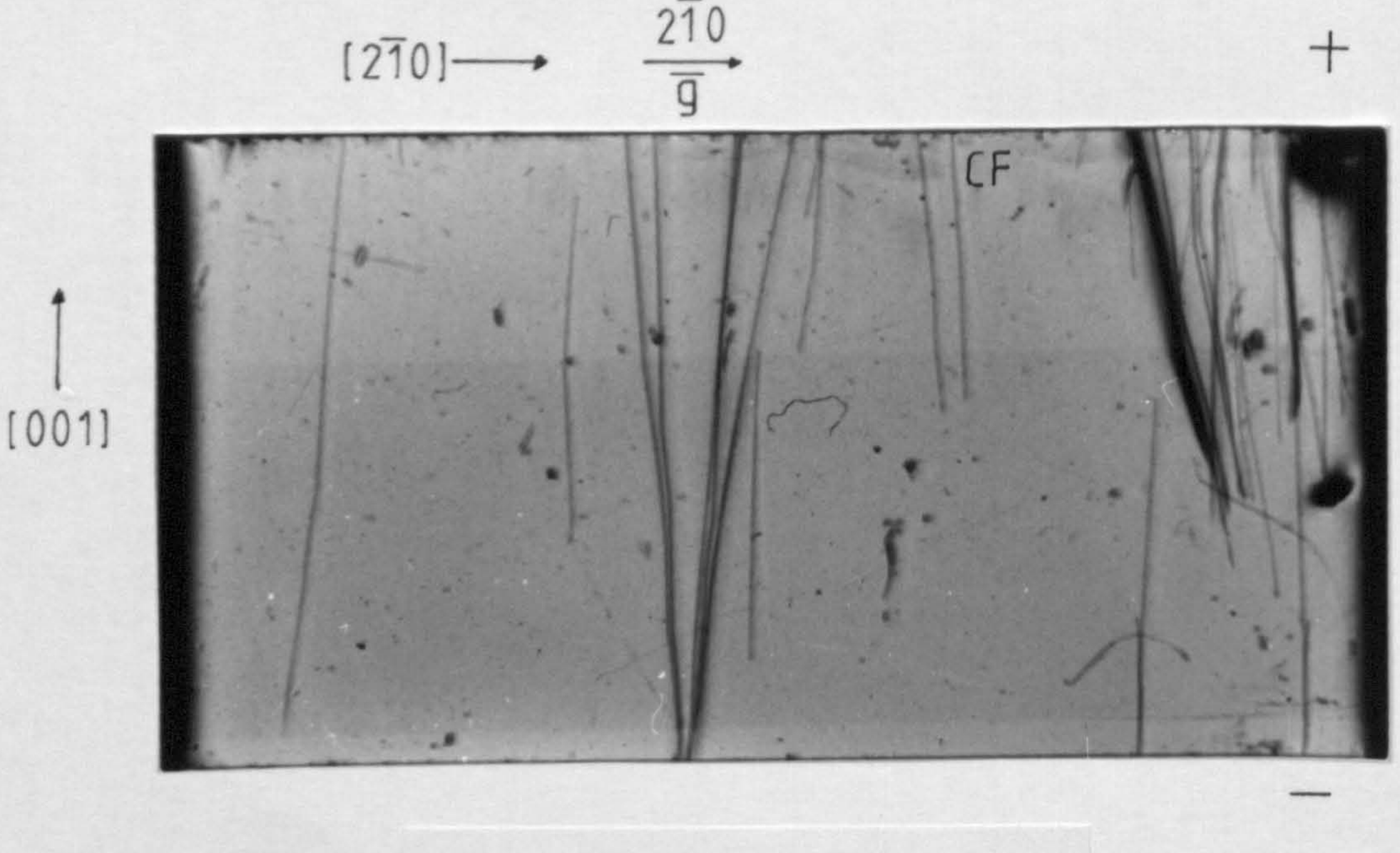

Fig. 4.18 - Topograph 18

contrast feature was present, and then later with higher resolution AGFA D4 film to obtain a better image of the feature. Examination of the resultant diffraction topographs revealed an unexpected property of the contrast feature (see fig. 4.17, 4.18 and table 4.3). The lower resolution topograph 17 shows the contrast feature as expected, concentrated along the anode edge of the sample with a number of strain "streaks" stretching across the crystal from edge to edge. The image of the feature on this topograph was more detailed than in the previous case and clearly showed that the band of strain along the anode became more diffuse with distance from the electrode surface thereby resulting in the streaked appearance observed. However, the contrast feature was virtually absent in the high resolution topograph 18 (see fig. 4.18). The only parts of the contrast feature, CS, that remained were much weaker than observed in the low resolution image and corresponded to the areas of strongest contrast and therefore greatest strain present in the sample. On the whole most of the strain induced into the crystal by the sweeping process had completely disappeared and no strain streaks, CS, were observed. In order to account for this it was necessary to examine any factors that could have caused the loss of strain. Until now it had been assumed that the strain was an indication of crystal damage caused by the forced removal of impurities. If this was indeed the case, the strain was not likely to have been removed by any of the procedures used in recording the topograph. Another possibility that can be ruled

[2$\bar{1}$0] ⟶ $\frac{2\bar{1}0}{g}$ ⟶

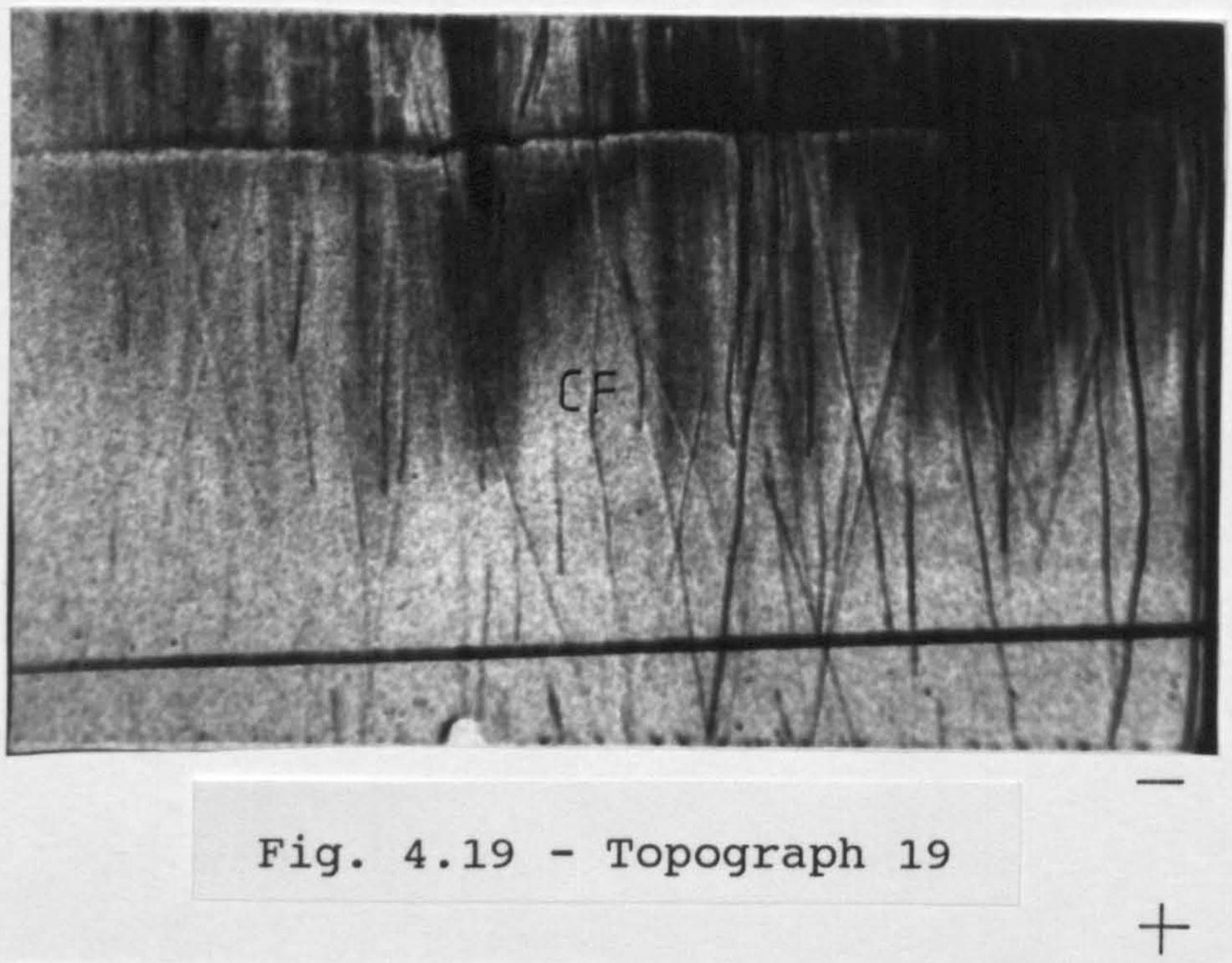

Fig. 4.19 - Topograph 19

[001] ↑

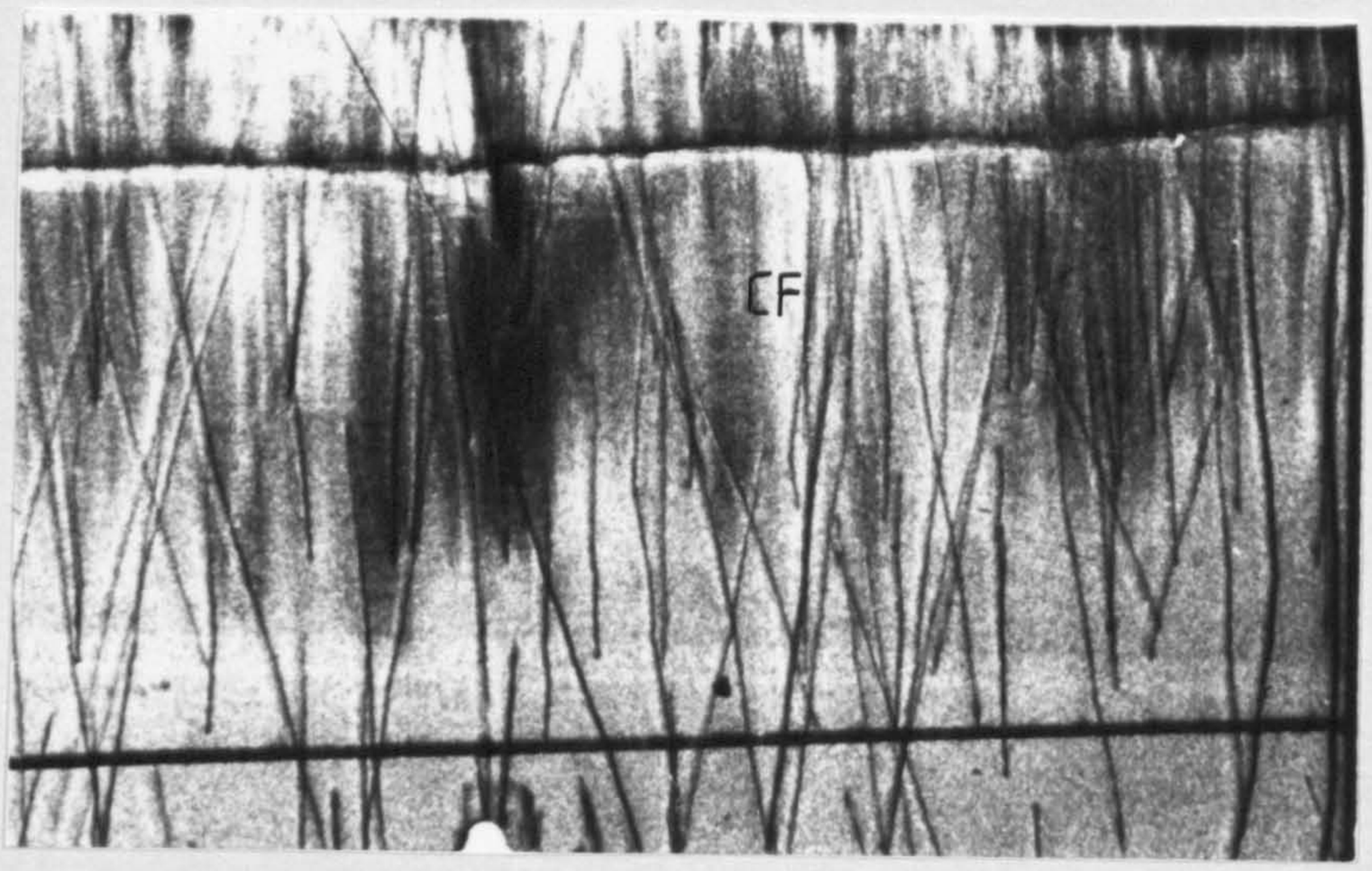

Fig. 4.20 - Topograph 20

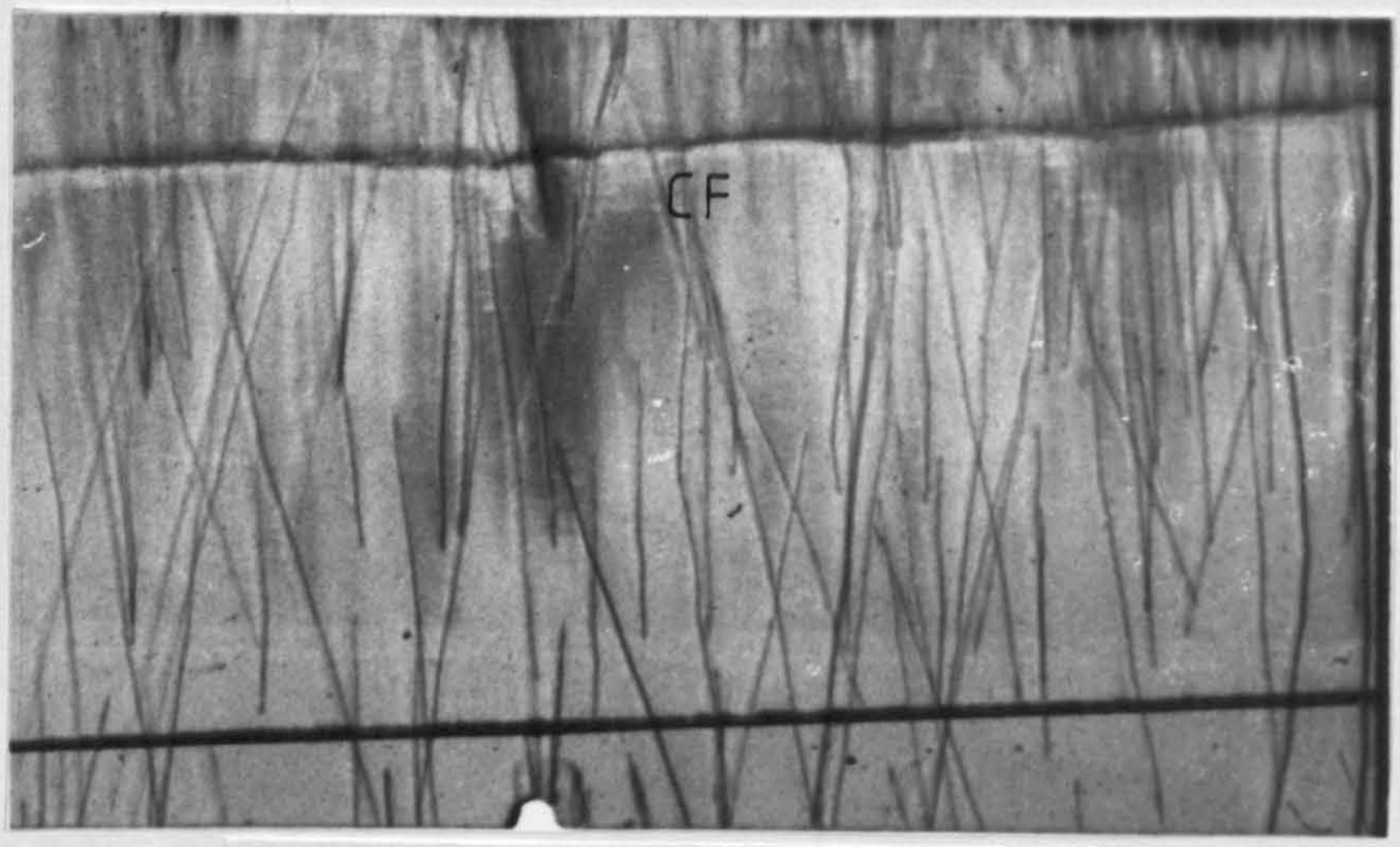

Fig. 4.21 - Topograph 21

out is that the sample may somehow have "healed" itself of crystal damage over a period of time. The first diffraction image of the sample was obtained three weeks after the sweeping process had taken place. In comparison with this period of time, the three days over which the sample was re-topographed to obtain the higher resolution image would have made little difference to the strength of feature even if it had been time dependent.

The only other factor that could have had any influence on the contrast strength of the feature was the duration of the sample's exposure to x-rays (see table 4.3). The total exposure time of ANNEAL1 to irradiation was 24 and 90 hours respectively for the low and high resolution images. After the second more lengthy exposure, the feature had mostly disappeared. A second sample was prepared to investigate this further. The sample was cut from a commercially grown crystal, COMQ, which was not a high purity material. The impurity levels in this material were much higher than those present in the high purity crystals used for the previous sweeping experiments (see table 2.3). COMQ was used because it was suspected that the damage caused by electrodiffusion would be greater in the case of a more impure sample and that the resultant lattice strain would therefore persist for a longer period of time upon exposure to x-rays. The series of topographs obtained from sample COMQ confirmed this suspicion (see figs. 4.19-4.21 and table 4.3).

The first topograph was obtained in the same way as the

initial topographs of SWEPT1 and ANNEAL1 to allow direct comparison with the contrast feature observed on the COMQ topograph (see fig. 4.19). The contrast feature, CF, was much stronger and stretched further across the crystal than observed on previous topographs. Since the sweeping conditions were identical for topographs 16, 17 and 19, the increase in lattice strain induced by the process must have been a consequence of some difference in the properties of the commercial crystal (see table 4.3). The most obvious difference between the three crystals was the higher content of impurities present in COMQ (see table 2.3). This was sensible because the sweeping process involves the removal of impurities and a greater damage should result when more of these species are involved.

The rest of the COMQ topograph series confirmed that the feature was dependent on the amount of radiation the sample was exposed to (see figs. 4.20 and 4.21). These topographs showed a gradual decrease in contrast, and therefore a lowering of lattice strain, with continued exposure to X-rays (see table 4.3). In this case the contrast was still observable even after 183 hours exposure although it was a much weaker feature in comparison with its initial strength.

The gradual relief of lattice strain was a strong indication that the contrast feature was not caused by irreversible damage to the crystal structure. However the strain observed was definitely a consequence of the electrodiffusion process and so was clearly associated with the original impurity content of a treated sample.

4.2.3 The Nature of the Contrast Feature

A possible mechanism for the formation of the contrast feature, CF, is the build up of a negative space charge near to the anode. The only significant charge carriers in quartz are Na^+ ions, which are the main species removed by the sweeping of high purity quartz[145]. These ions not only charge compensate substitutional aluminium impurity sites, but also perform a similar role for the sodium hydroxide impurities postulated in section 3.5. Therefore, their removal from the crystal will result in the production of negatively charged species in the crystal. If no other charge compensator was present, the negative charge in the crystal would build up with prolonged sweeping and could eventually produce an increase in lattice strain in the vicinity of the charged species.

The space charge model is substantiated by the comparison of the contrast observed on topographs obtained from high purity samples, SWEPT1 and ANNEAL1, with that observed on the COMQ series. The high purity samples showed a streaked feature, CS, which was mainly concentrated close to the anode edge and which was removed after only one days exposure to x-rays. The more impure commercial sample gave rise to an intense feature which stretched across more that half way across the crystal and which remained observable even after close to four days irradiation. The major difference between the two crystal types was the much higher levels of aluminium in the commercial material. Therefore, the strength of the

contrast feature is probably related to the number of aluminium defect sites in the crystal.

The streaks of strain that occur far from the anode surface are probably a consequence of the applied electric field being non-uniform across the crystal. Quartz is essentially an electrical insulator and the only charge that can be detected across a crystal is associated with the presence of impurities such as H^+ and Na^+ which are randomly distributed throughout a crystal. Areas of a crystal which have high impurity concentrations will pass current and those which are impurity free will not. This will result in a non-uniform electric field across the crystal. With this assumption, the strain streaks could have been produced in areas of the crystal which were associated with high concentrations of impurities. The higher concentration of charge carriers in impure crystal regions would increase the influence of the electric field in those areas. Therefore, the removal of Na^+ ions would be enhanced.

The removal of the feature after x-irradiation may be explained by the release of hydrogen ions from hydroxyl impurities. As discussed in section 3.1, hydrogen impurities associated with hydroxyl groups replace sodium ions at aluminium sites when a quartz crystal is treated with ionising radiation. Sweeping has been shown to have little effect on the hydrogen content of high purity crystals except to form Al-OH centres (see section 3.1). Therefore exposing a swept sample to x-rays releases H^+ ions from hydroxyl and

other hydrogen related impurities which then migrate to aluminium sites to charge compensate the defect. Over a period of time, this process will neutralise the negative space charge in the crystal to relieve the lattice strain thereby removing the contrast feature. The loss of H^+ ions from hydrogen species will also produce negative charges in the quartz crystal. However, as discussed in chapter 3, hydrogen associated impurities in quartz are mainly incorporated interstitially and are probably located in crystal structure the C-channels. These channels are large enough to accommodate negatively charged species without producing strain in the crystal lattice. Substitutional aluminium impurities form part of the quartz structure as so will cause significant lattice strain when charge compensating Na^+ ions are removed.

N.B.

The investigation of the contrast feature using Lang topography was discontinued at this stage because of the publication of work carried out by Sebastian et al.[146]. Although they had carried out their investigations using vacuum swept material, compared with the nitrogen swept samples studied in this project, they observed a feature identical to that discussed in the previous sections. The model they suggested to account for the feature was in agreement with that proposed in this section. They also proved that the charge build up produced an inhomogeneous distortion of the crystal lattice. This was deduced from the fact that it showed equally strong contrast on topographs obtained from (10.0) and (00.3) reflection planes which suggested that there was no spatial orientation for the charges. However they did not explain by what mechanism the contrast feature was removed after prolonged exposure to x-rays or suggest a relationship between aluminium levels and the strength of the contrast feature.

4.3 Double Crystal Diffraction Studies

4.3.1 Defects in Swept Quartz

Double crystal x-ray diffraction topography was used in a study of lattice strain in swept quartz. This technique was significantly more strain sensitive than Lang topography and so could be used to detect more subtle effects of the sweeping process than was possible using single crystal methods. The swept sample, SWEPT1, was examined in an attempt to obtain a higher resolution image of the contrast feature discussed in section 4.2a. The experiments discussed in this section were carried out before the dependence of this feature on radiation exposure was known.

Sample SWEPT1 was too large to be imaged on one exposure, and so was moved in order to obtain a series of overlapping images which could then be used to construct a composite image of the whole crystal. A beneficial by-product of this procedure was that lattice strain across the crystal could be estimated from the width of the rocking curve recorded at each sample position (see section 2.4c). The position of each strain measurement was marked by exposing a 1mmx1mm section of the crystal to x-rays for twice as long as the rest of the sample section. This produced a dark, rectangular shaped marker area on each topograph. The poor resolution of the diffraction images discussed in this section was a result of using low resolution Agfa M3 photographic film to record topographs. This was unavoidable because of difficulties encountered at Daresbury during that visit.

Table 4.4 Double Crystal Topographic Studies of Swept Crystals

Topograph No.	Sample Title	Reflection Plane Quartz/Silicon	Film Type	Comments
22	SWEPT1*	(02.-3)/(4 0 0)	M3	1st position[a,p]
23	SWEPT1*	"	M3	2nd position[b,p]
24	SWEPT1*	"	M3	3rd position[c,p]
25	SWEPT1*	"	M3	4th position[d,p]
26	SWEPT1*	"	D4	Unetched[w]
30	ANNEAL1*	(02.-3)/(4 0 0)	D4	Optically Polished[w]
31	SWEPT1*	"	D4	Etched[w]
32	HPQ*	"	D4	Etched[e,w]
33	NSW	"	D4	Unswept[w] + Etched[e]
34	NSW	"	D4	Retop[f]

* - Previously used for Lang topography (see table 4.1)

a - Starting position topograph obtained on LHS of rocking curve.

b - Sample moved a total of 1mm downwards, topograph obtained on LHS of rocking curve near 1st position

c - Sample moved a total of 2mm downwards, topograph obtained near top of the rocking curve

d - Sample moved a total of 3mm downwards, topograph obtained near to 1st position on the rocking curve possibly on the RHS

e - Etched in 40% HF to remove surface sweeping damage

f - Sample retopographed to correct for border

p - Sample mounted using a plastic envelope (see 3.4.2i)

w - Sample mounted directly onto stub using a hard wax

Notes The K_α wavelength of Molybdenum radiation, 0.709Å, was used for all Bragg calculations. All samples were 1 mm thick Y-slices cut from high purity quartz crystals.

Table 4.5 Rocking Curve Widths

Topograph No.	Sample Title	Reflection Plane	Theoretical $\theta_{\frac{1}{2}}$ (sec)*	Experimental $\theta_{\frac{1}{2}}$ (sec)*
22	SWEPT1	(02.-3)	0.73	1.43
23	SWEPT1	"	"	1.36
24	SWEPT1	"	"	1.21
25	SWEPT1	"	"	1.50
26	SWEPT1	"	"	0.90
35	R8	(2-1.3)	0.28	3.00
36	R8	"	"	1.90
37	R8	"	"	3.00
38	R8	"	"	1.95
39	R8	(03.0)	0.38	MP
40	R8	"	"	MP
41	R8	"	"	MP

MP - Denotes the appearance of more than one peak on the rocking curve scan

* - Units are seconds of arc

The topographs obtained from SWEPT1 displayed a different range of features at each sample position (see figs. 4.22-25 and table 4.4). This was a result of movement of the sample within its plastic envelope mounting, which was found to be inefficient for double crystal topography. As the sample was being scanned across the diffraction peak, the position of the rocking curve was observed to drift indicating a movement of the quartz crystal. Consequently, each topograph was obtained at a different part of the rocking curve and a variety of contrast features was observed as a result of the associated variation in strain sensitivity. As this movement was random, the position at which the topographs were imaged was not known exactly and could only be estimated using comparisons with results obtained from later studies. The rocking curve widths at each position were approximately double the value expected for a perfect crystal (see table 4.5). However this was acceptable because both the movement of the sample and the differences in interplanar spacings between the two crystals would produce widening of the rocking curve. Therefore, within these limitations, the width at each position was approximately the same and showed that there was no significant lattice strain variation, for the chosen set of reflection planes across the crystal, even near to the anode.

The topograph obtained at the first sample position showed several contrast features (see fig. 4.22). The easiest of these to identify were the dislocations, D, at the centre and towards the right hand side of the image. Also present were a

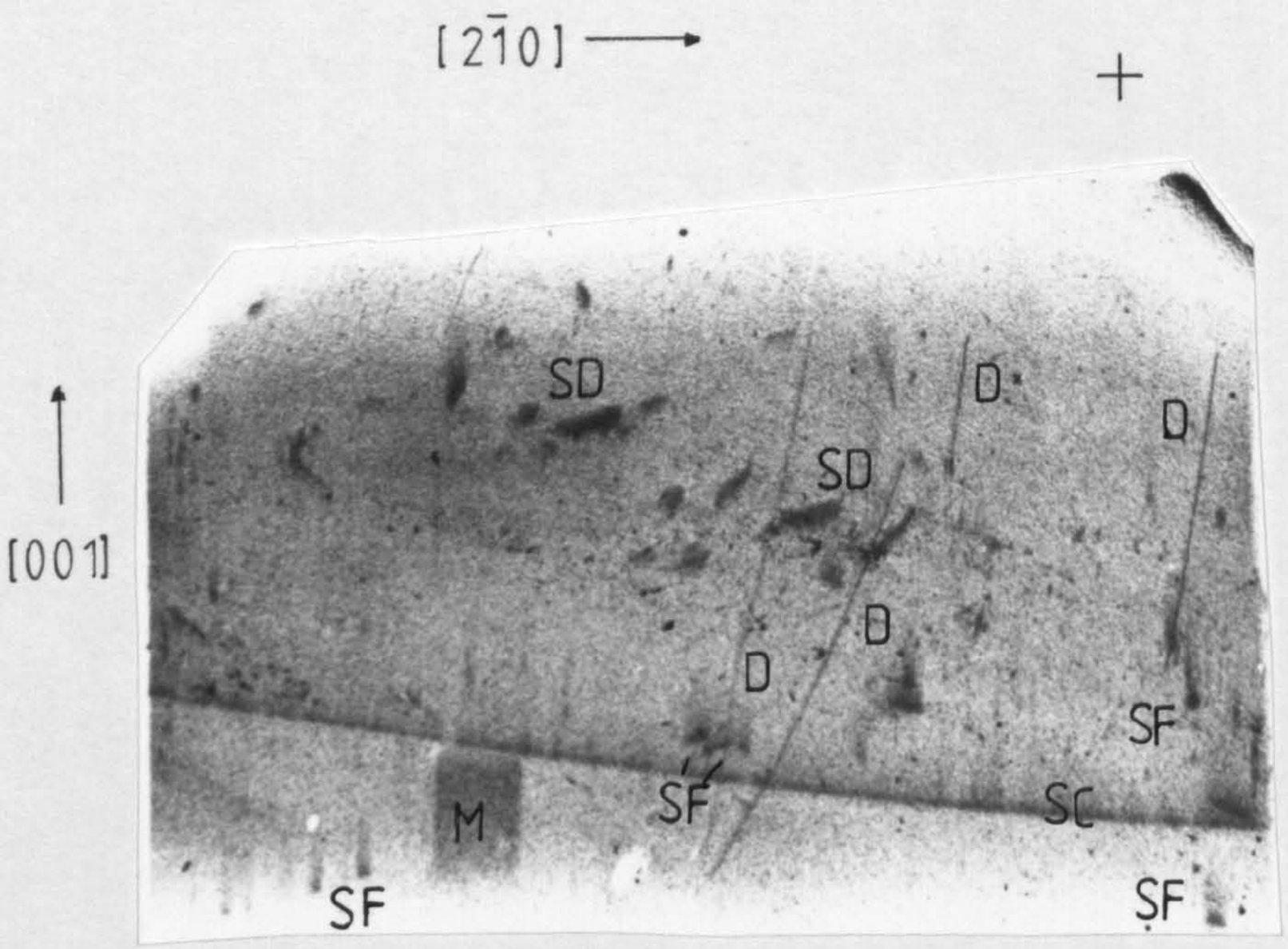

Fig. 4.22 - Topograph 22

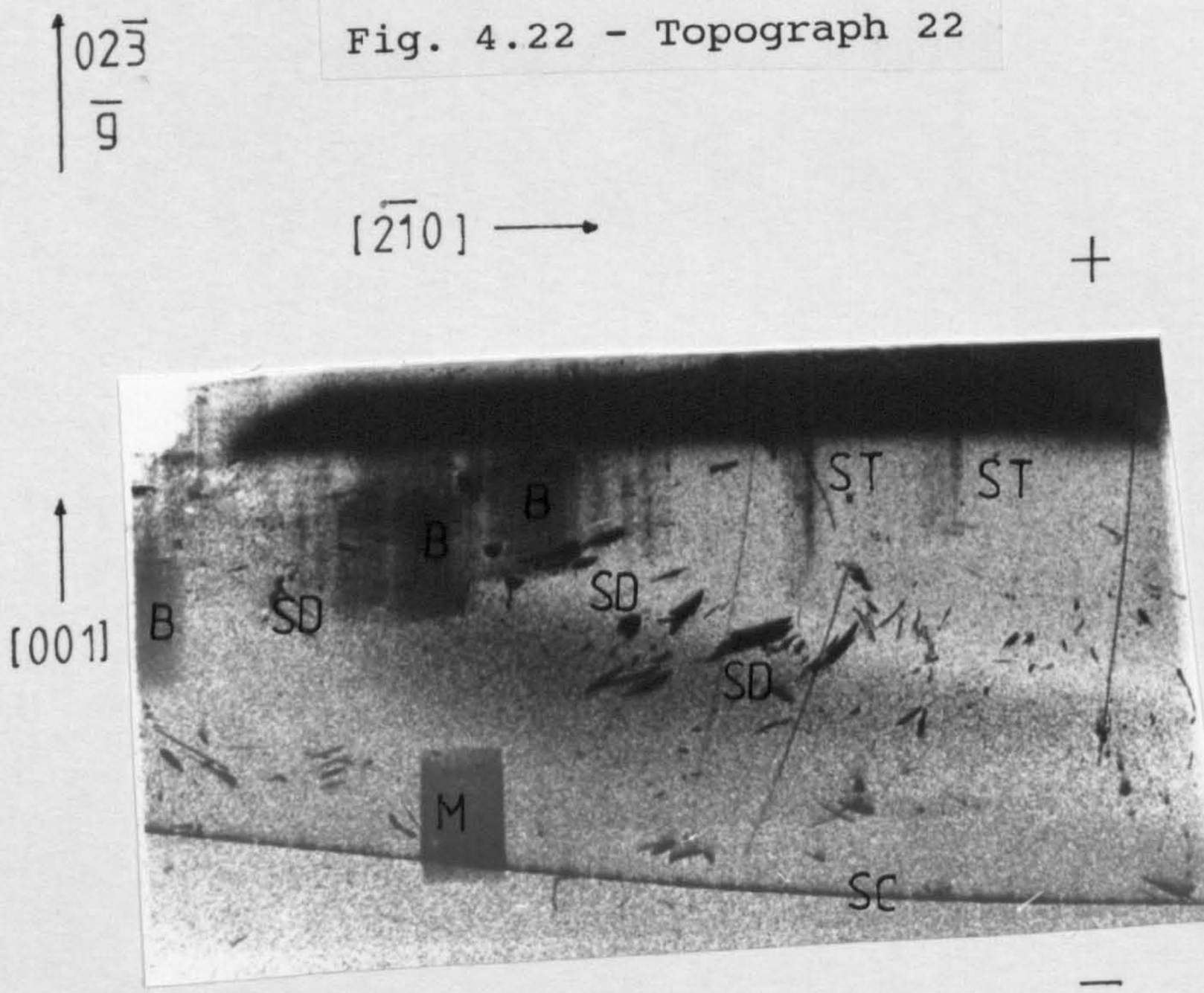

Fig. 4.23 - Topograph 23

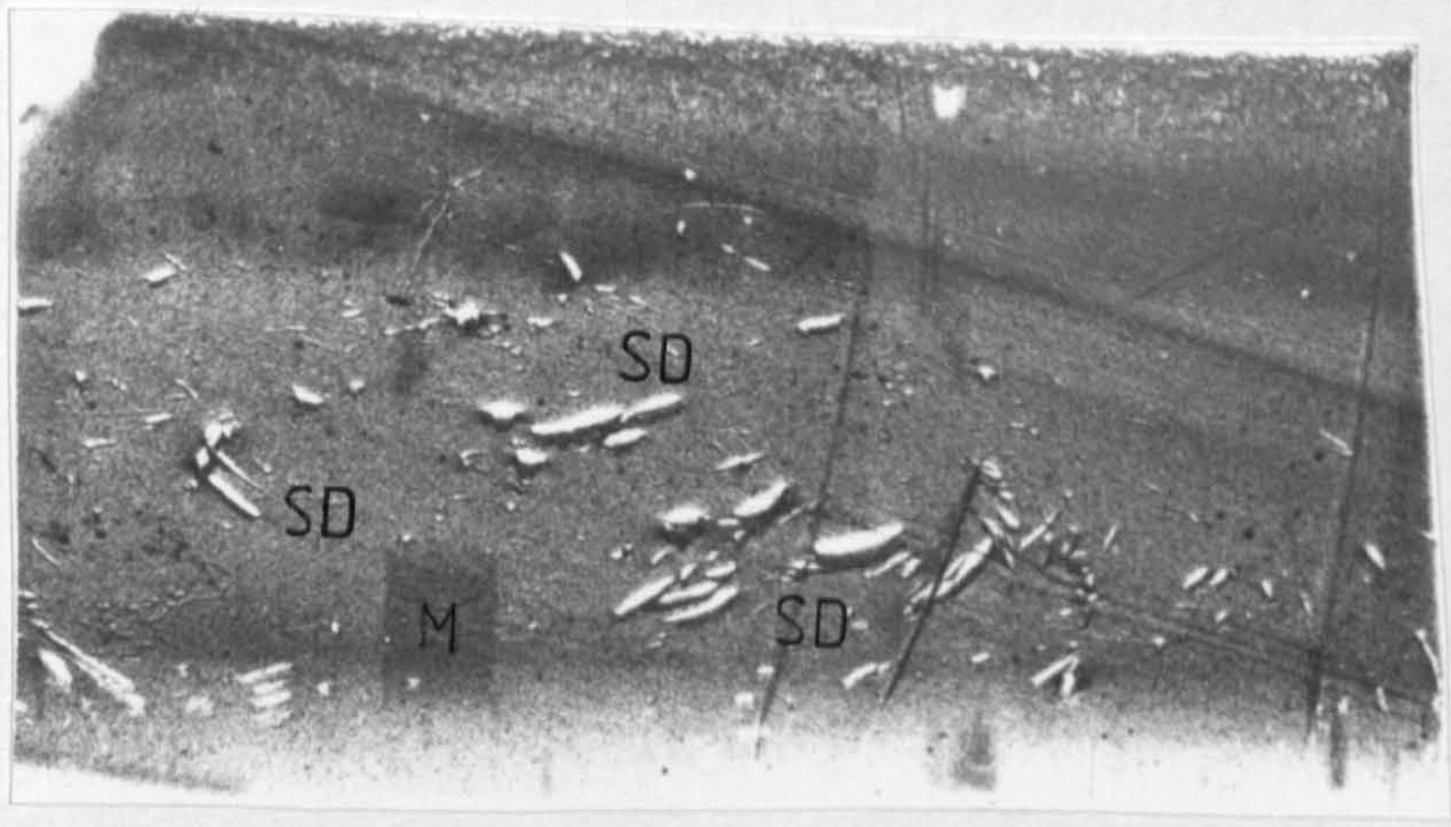

Fig. 4.24 - Topograph 24

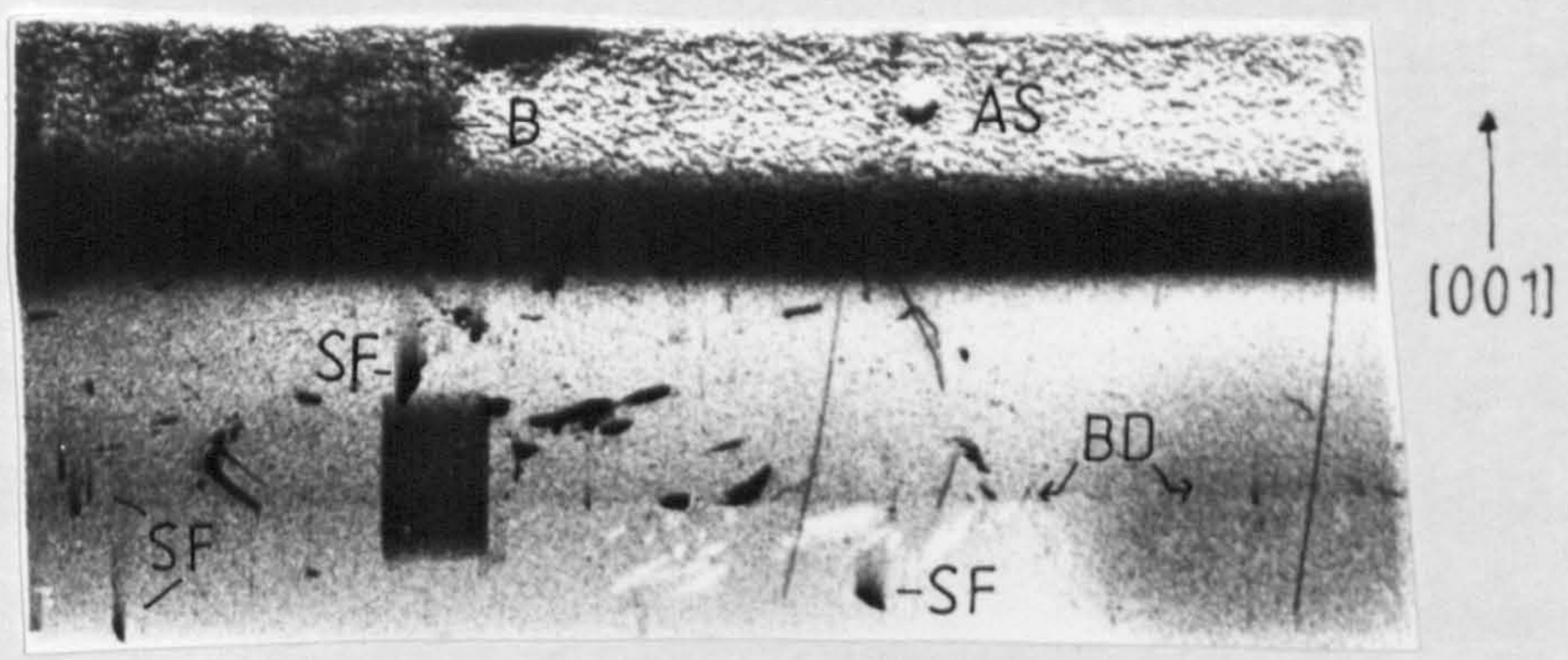

Fig. 4.25 - Topograph 25

number of irregularly shaped dark features, SD, distributed randomly across the topograph. Although these features resembled large defects such as particle conglomerates and fluid inclusions, they were shown on a later topograph to be produced by surface damage in the form of scratches and chips taken out of the polished faces of the crystal (see fig. 4.23). The rectangular feature shown on the lower left hand side of the image, M, was produced by the marker exposure. A scratch, SC, was imaged as a thin black line running from left to right across the middle of the topograph, similar in appearance to a dislocation. However, also present on the topograph was a series of streaked features, SF, aligned parallel to the C-direction. Most of these were distributed randomly across the image but a streaked band originating along the scratch was also observed. Each streak appeared to have similar dimensions in terms of length and thickness. The contrast strength reduced gradually with distance from the most intense end of the feature towards the anode edge of the crystal until a streaked effect was observed.

When the sample was lowered to obtain a second strain measurement and a corresponding topograph, the streaked features disappeared (see fig. 4.23 and table 4.4). However, regular blocks of contrast accompanied by thin lines of strain of varying length originating from the anode edge of the crystal were observed. The irregular shaped surface damage features were still visible as were the dislocations, scratch and marker area. All of these features were sharper

than those observed on the previous image. This was probably due to the topograph being obtained at a more strain sensitive position on the rocking curve, although could have been a consequence of dynamic effects changing diffraction conditions. The block, B, and streak, ST, contrast features stretched away from the anode side towards that of the cathode and were consistent with a higher resolution image of the contrast feature discussed in the previous section.

The movement of the sample to the third position resulted in an almost total loss of resolution (see fig. 4.24 and table 4.4). Although the topograph gave a very clear image of the surface damage and still displayed the dislocations present in the crystal, the strain streaks and blocks seen on the previous two images were absent from the topograph. Also missing from the image was the surface scratch due to that section of the crystal being moved out of the x-ray beam. The white/black contrast of the surface features, SD, showed the topograph to be a dynamic and not a direct diffraction image. As these images were characteristic of defects close to the surface of a crystal, the assignment of the irregular shaped contrast features, SD, was confirmed as surface damage.

When the crystal was moved to its final position, the strain streaks observed on figure 22 were again observed at higher resolution (see fig.4.25 and table 4.4). The rough area, AS, shown on the upper half of the topograph was the anode surface edge of the crystal which was visible because of the orientation of the sample. The block features, B,

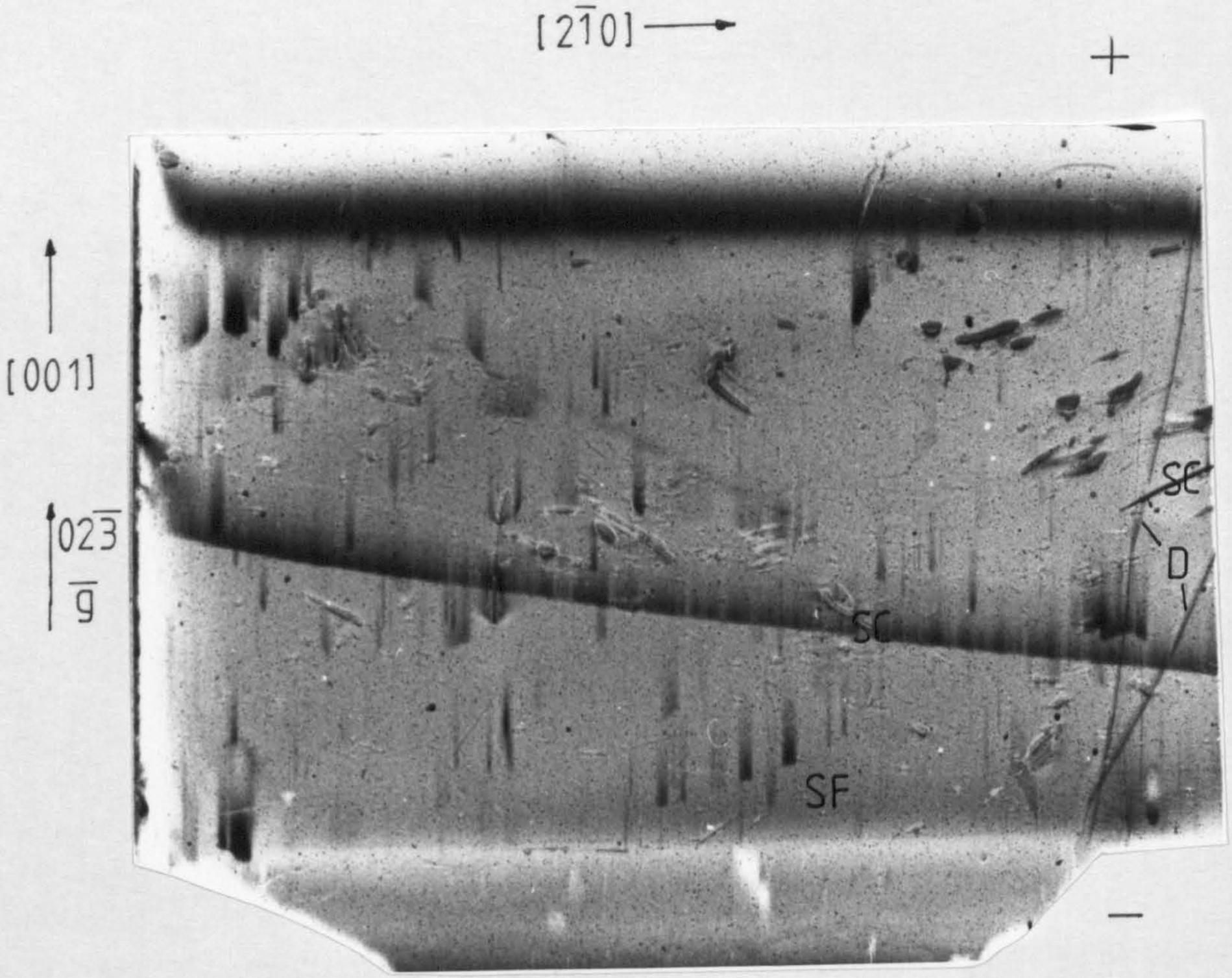

Fig. 4.26 - Topograph 26

observed on figure 4.23 may also have been present, however that feature was obscured by the image of the electrode surface. On the bottom half of the topograph, a boundary line, BD, was observed, over which the contrast of surface damage features was changed from black to white. This indicated that dynamical images were being formed, again characteristic of defects at the surface of a crystal.

This study was repeated in a later set of experiments where SWEPT1 was attached directly onto the sample stub using a mounting wax to prevent unwanted movement while the crystal was being scanned. The effects of this mounting were seen immediately by the observation of a stable rocking curve and a high resolution diffraction image (see fig. 4.26 and tables 4.4 and 4.5). A number of streaked contrast features, SF, identical to those shown on figures 4.22 and 4.25, were observed running parallel to the C-axis of the sample. Individual streaks were shown to be vary in thickness and although all were of similar lengths, none of the features stretched across the image from edge to edge as observed immediately after sweeping for the original contrast feature (see fig. 4.16). The contrast of each streak was tapered, being stronger at the start of the feature and becoming weaker and more diffuse with distance until no longer visible. Contrast was strongest at the straight edge start of each streak and tapered off as the feature stretched towards the anode. From this it was concluded that these features were not the same as those discussed in section 4.1c. There was no

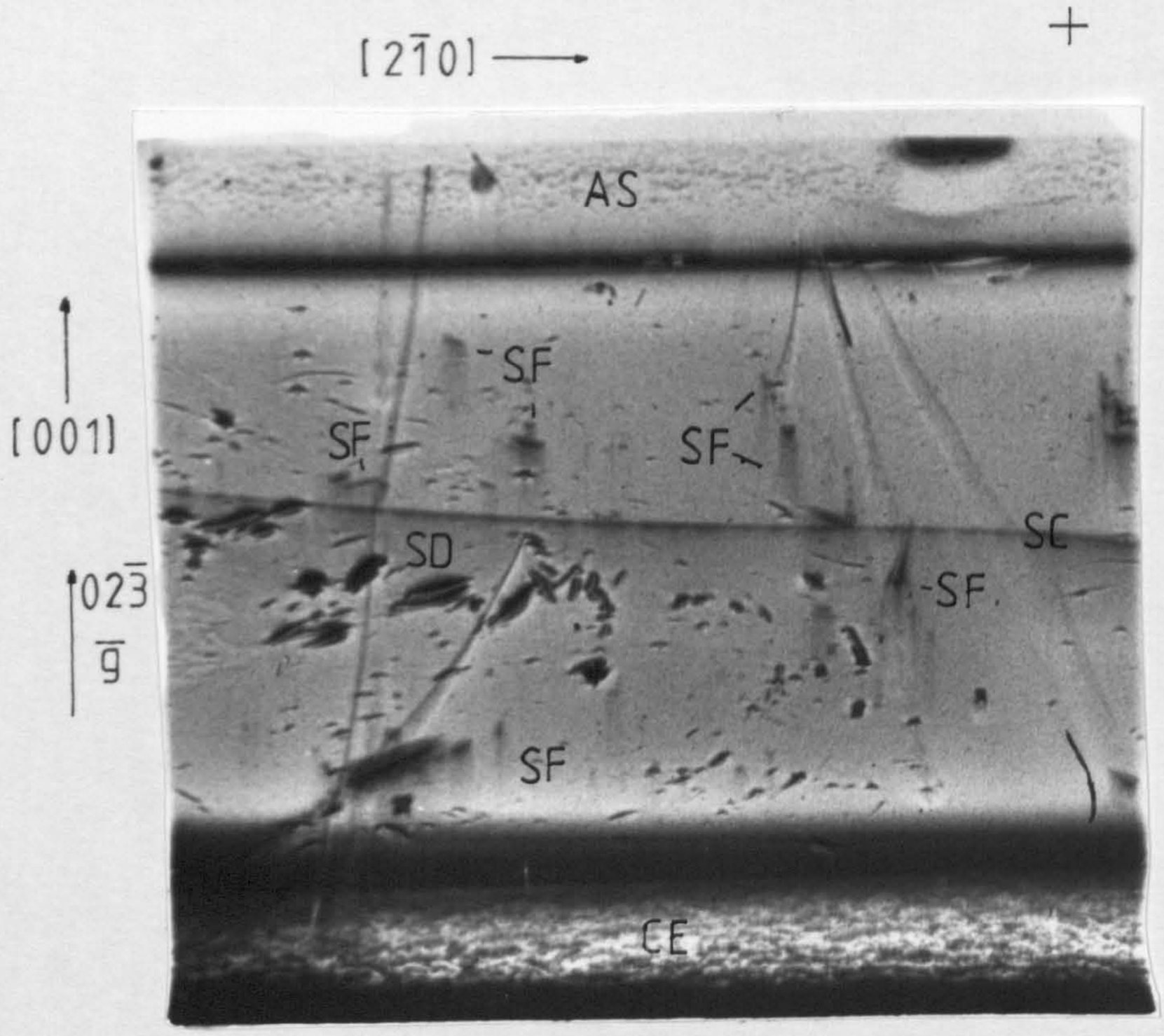

Fig. 4.27 - Topograph 27

apparent change in the diffraction image when the sample was moved and altering the position on the rocking curve only reduced the resolution of direct images, such as dislocations and the streaked features, and produced dynamic images of the chipped surface damage similar to that observed on figure 4.24. The block, B, and streak features, ST, observed on figure 4.23 could not be imaged again.

SWEPT1 was then re-topographed, using the white radiation camera at Daresbury, in an attempt to image the whole crystal and to see if any of the features observed on double crystal topographs could be imaged using single crystal topographic procedures. The diffraction image was obtained using (02.-3) planes of the crystal to allow direct comparison with double crystal topographs (see fig. 4.27 and table 4.3). Features similar to the strain streaks, SF, shown in figures 4.22, 4.25 and 4.26 were observed running parallel to the C-direction. However, the contrast of these streaks became more diffuse with distance towards the cathode and not the anode as was previously the case. The surface damage features, SD, on the crystal was imaged in greater detail than on the original Lang topograph of SWEPT1 as was the rough surface anode edge, AS, as well as the rough cathode edge, CE, of the crystal. Both of these observations were attributed to the use of the asymmetric (02.-3) reflection. No contrast feature was observed along the anode edge of the crystal indicating that accumulated exposure to x-rays had been sufficient to remove the feature shown on figure 4.16. Therefore, the streaked

[2$\bar{1}$0] ⟶

+

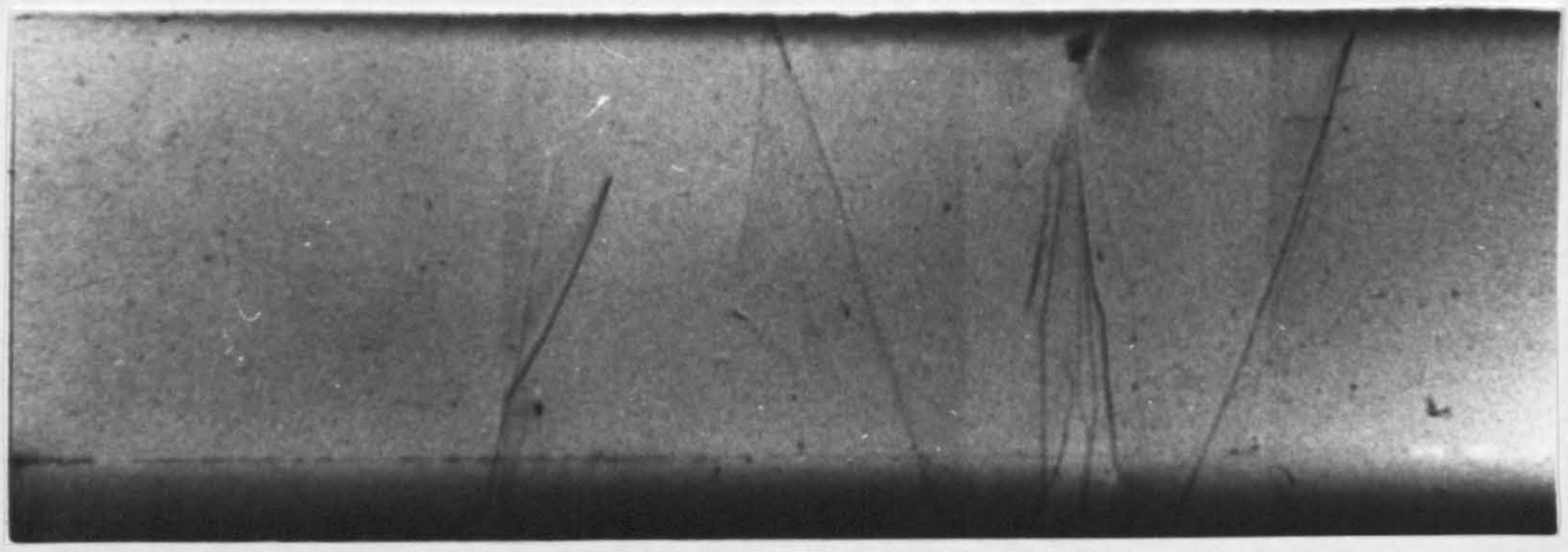

—

Fig. 4.28 - Topograph 28

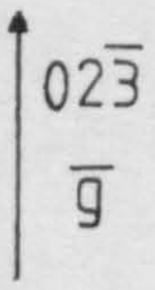

[2$\bar{1}$0] ⟶

+

—

Fig. 4.29 - Topograph 29

features, SF, shown on figures 4.22, 4.25 to 4.27 were independent of the amount of time exposed to x-rays and were a new defect produced in the crystal by the sweeping process.

However, the appearance of some of these features originating along the scratch present on the sample cast doubt on whether these streaks showed bulk crystal damage or were a surface effect. To confirm the nature of the features, SWEPT1 was etched in 40% HF to remove all surface damage and compared with an etched swept sample, HPQ, was examined (see figs. 4.28 and 4.29 and table 4.3). The etching process removed all traces of the surface damage including the scratch, but also removed the streaked features. The control sample HPQ showed no signs of surface damage or streaked features.

The streaks were thought to be a result of the optically polished crystal surface being more susceptible to damaging than a conventional etched surface. This was shown by the abundance of surface scratches on topographs obtained from the optically polished sample and the complete absence of surface damage on the etched finish crystal. Therefore the streaks were caused by the sweeping process but were confined to the surface of the crystal. The crystal strain associated with the presence of the streaks could have been caused by the migration of impurity ions close to the surface of the crystal. Another possibility is that of the migration of gold atoms which had been deposited onto the crystal surface during the sputtering of gold onto the electrode faces of the sample.

The block, B, and streaked features, SF, shown on figure

4.23 feature were still thought to be a higher resolution image of the contrast features, CF and CS, discussed in the section 4.2. As mentioned earlier difficulties had been encountered on the visit to Daresbury at which the topographs discussed in this section were obtained. These difficulties had been associated with technical problems connected with maintaining a high current electron beam in the SRS ring. This resulted in the intensity of the x-ray beam produced by the SRS being much lower than under perfect operational conditions. Consequently, the intensity of the x-rays was not sufficient to remove the contrast features, CF and CS, during that initial study. The disappearance of the feature on figures 4.24 and 4.27 showed that the x-ray exposure was sufficient to eliminate the contrast features. In the later studies the SRS operated at full operational capacity.

4.3.2 Defects in Unswept Quartz

The conclusions discussed in the previous section prompted a repeat series of double crystal topographs to examine etched crystals. This would ensure that any features present on diffraction topographs could be related to bulk crystal damage. To provide a comparison, the optically polished sample, ANNEAL1, was examined along with two etched samples, SWEPT1 and HPQ. This latter sample had not been optically polished prior to being etched and was a control to compare with SWEPT1. An unswept high purity crystal, NSW, was also topographed to ensure that contrast features which appeared on swept crystal topographs were caused by the process and not some artifact associated with sample preparation. Each of the examined crystals had an impurity content similar to that of high purity samples given in table 2.3. Topographs of the sample crystals showed several unexpected features (see figs. 4.30-33 and table 4.4). Firstly, the optically polished swept sample, ANNEAL1, did not show any of the streaked contrast features, SF, observed on figure 4.26 for the analogous polished SWEPT1 sample. The lack of surface damage features on the ANNEAL1 topograph suggested that the sample alignment in this case allowed the imaging of only bulk defects. However, the most important observation was the appearance of a number of rectangularly shaped contrast features, RF, running diagonally from left to right across each topograph. The features were of equivalent lengths but differed in thickness, ranging in appearance from

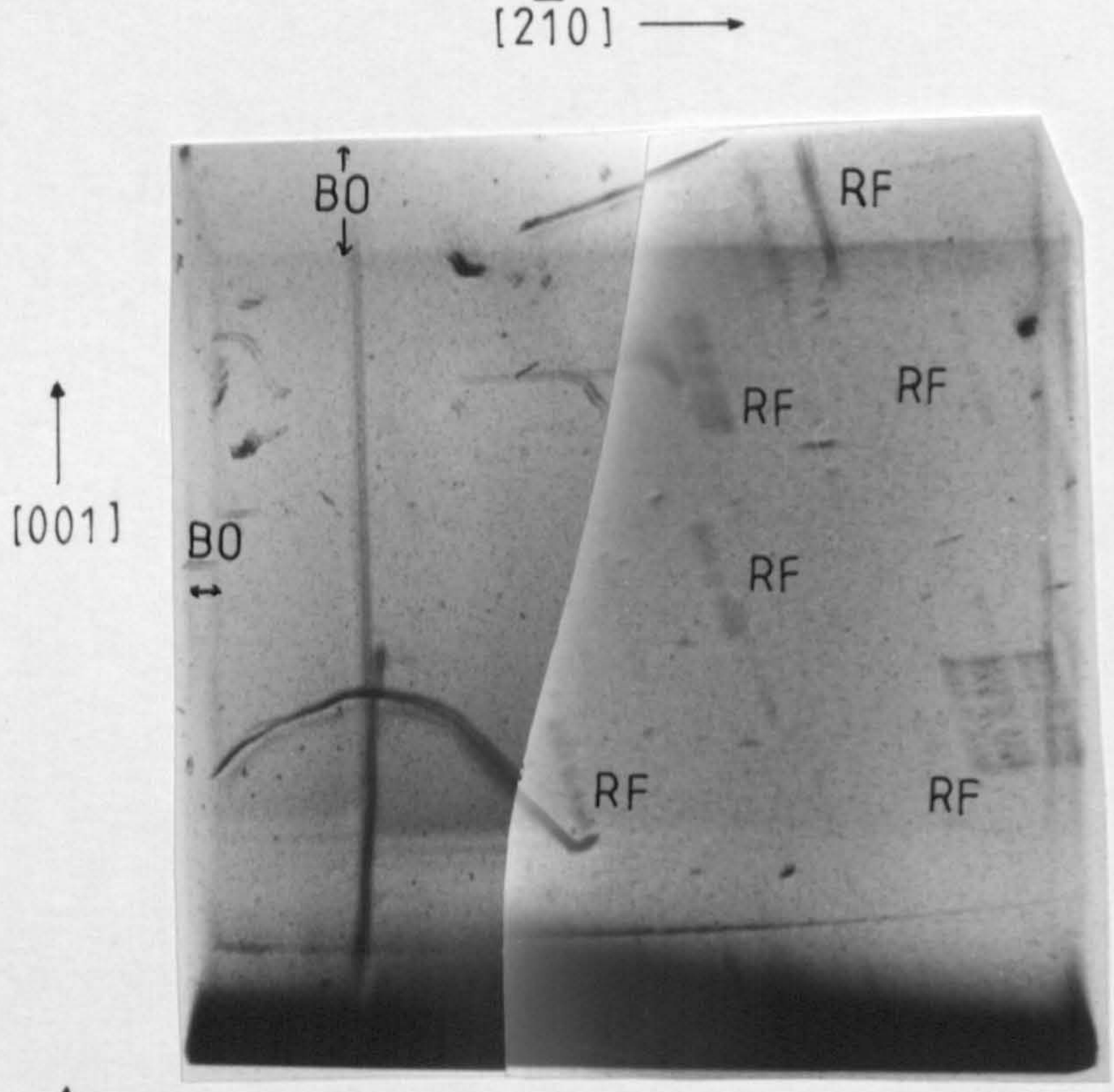

Fig. 4.30 - Topograph 30

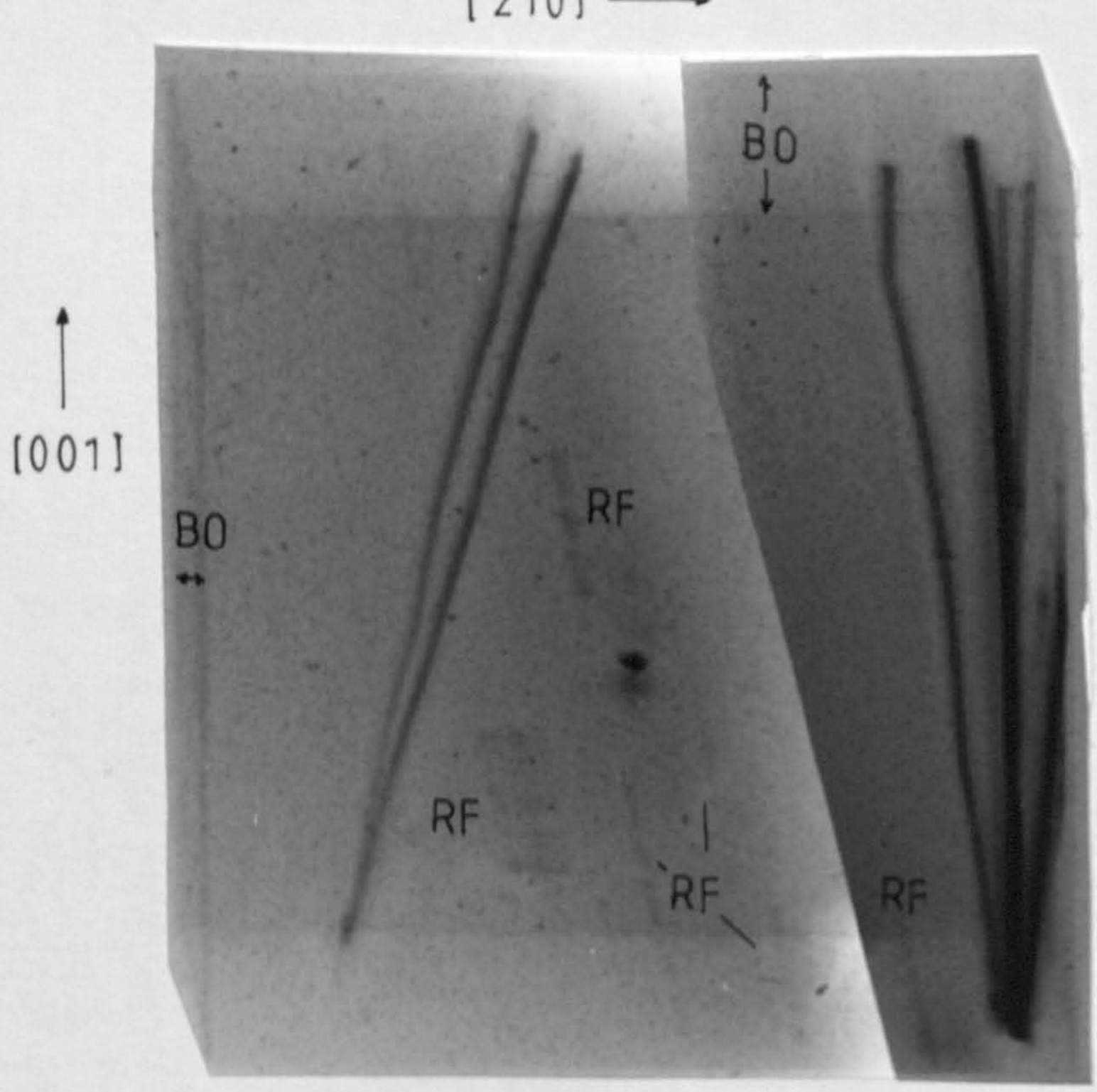

Fig. 4.31 - Topograph 31

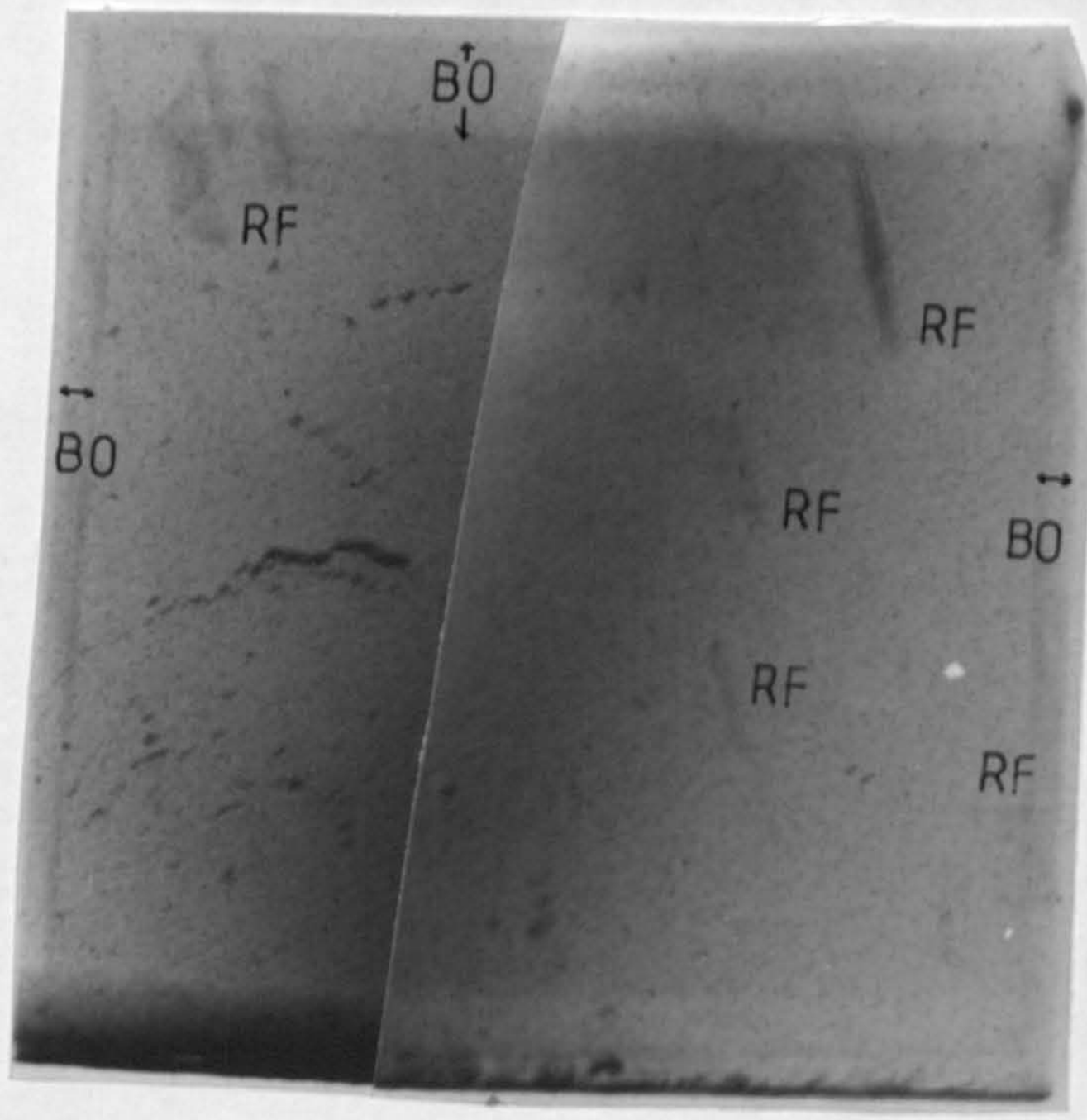

Fig. 4.32 - Topograph 32

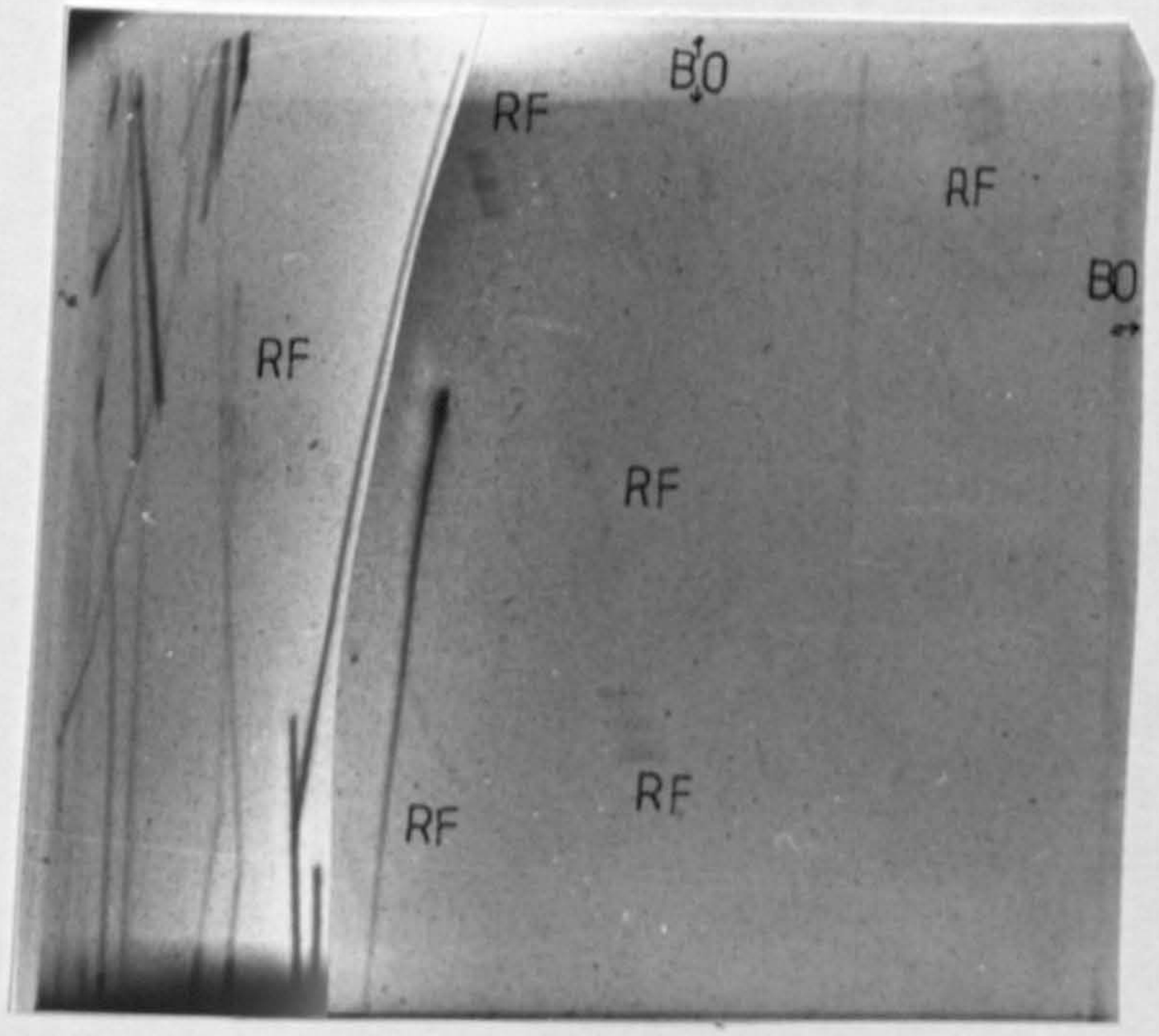

Fig. 4.33 - Topograph 33

Fig. 4.34 Schematic Representation of Border around Double Crystal Topographs

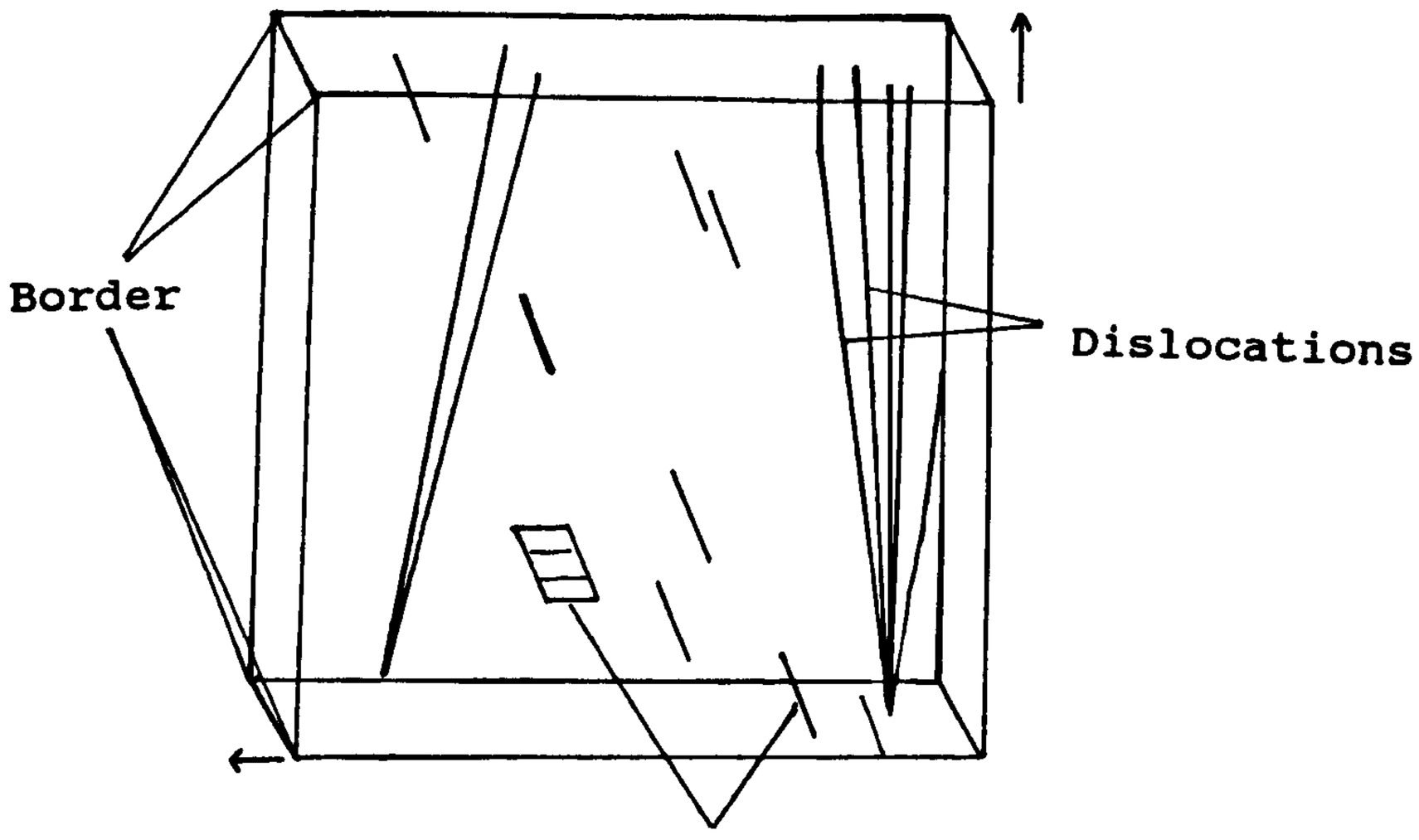

a) Uncorrected

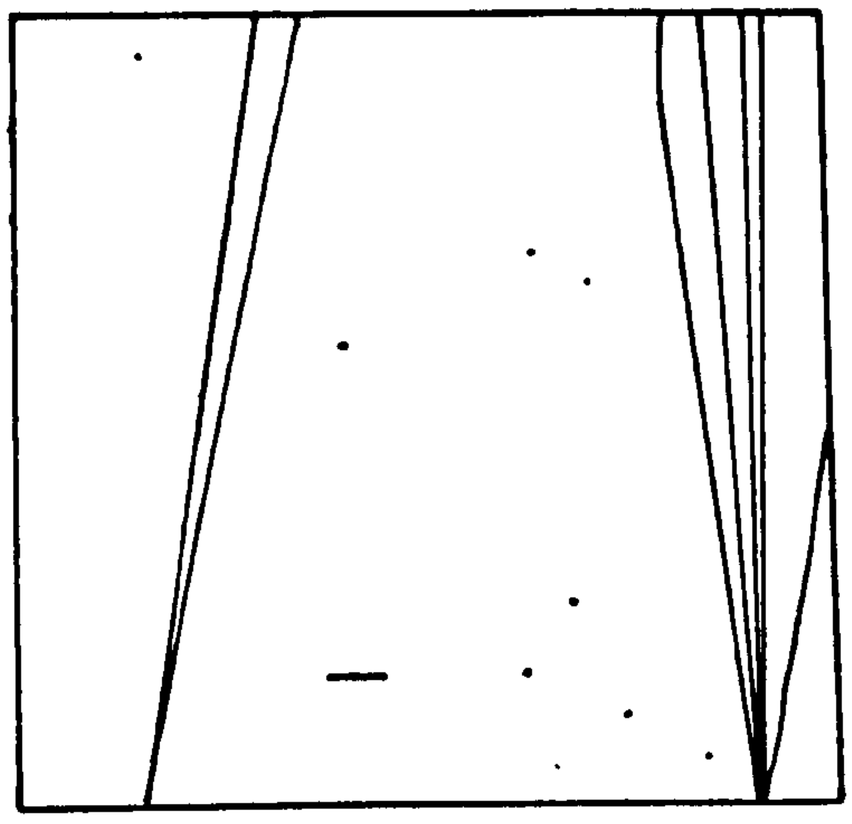

b) Corrected

thin lines to thick blocks. Horizontal banding was present in the block shaped features, which resembled the layered structure normally associated with growth bands. As the features were present on topographs obtained from each of the samples, it could be concluded that the surface finish was not responsible for the features and that they were not caused by the sweeping process. This also suggested that the features were associated with the crystal bulk and were not a surface phenomenon. A rectangular border, BO, surrounding each topograph was also observed which gave a three-dimensional appearance to the images. This was caused by a misalignment of the sample with respect to the diffracted x-ray beam (see fig. 4.34a). This misalignment accounted for the diagonal direction which the contrast streaks followed. If this misalignment was corrected for, the true direction of the strain streaks would be parallel to the Y and X and perpendicular to the Z crystallographic directions respectively (see fig. 4.34b).

To test this theory NSW was re-topographed ensuring that any misalignment of the x-ray beam was corrected prior to the obtainment of a diffraction image. The resultant topograph did not show either the three dimensional border effect or the diagonal streaks characteristic of the previous set of experiments (see fig. 4.35 and table 4.4). This confirmed that the streaks, RF, were rendered visible because of misalignment of x-ray beam and suggested that the features were planar growth defects lying in the X-Y plane and parallel with (00.1) basal planes.

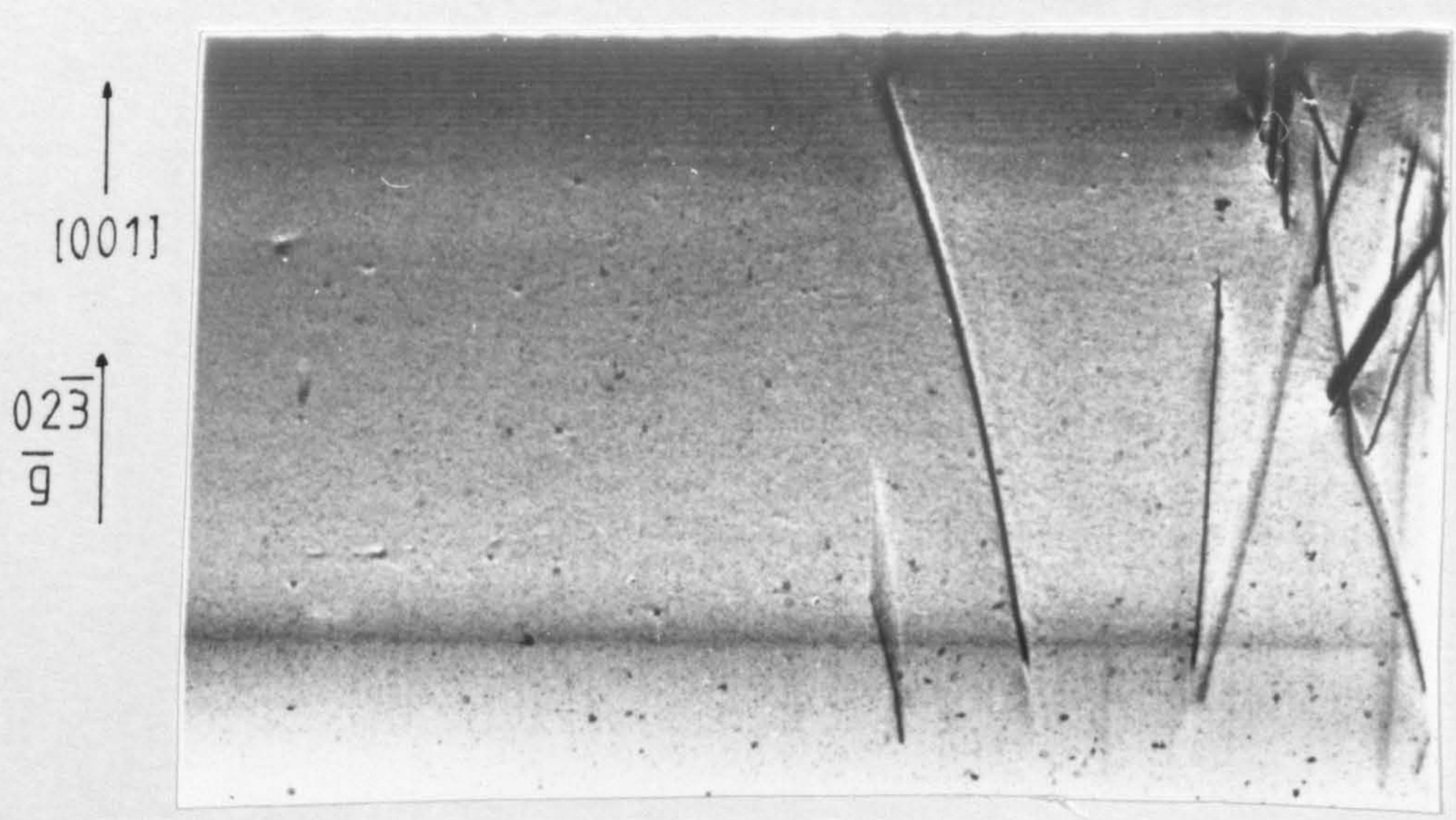

Fig. 4.35 - Topograph 34

Fig. 4.36 Similarities between Contrast Streak Patterns

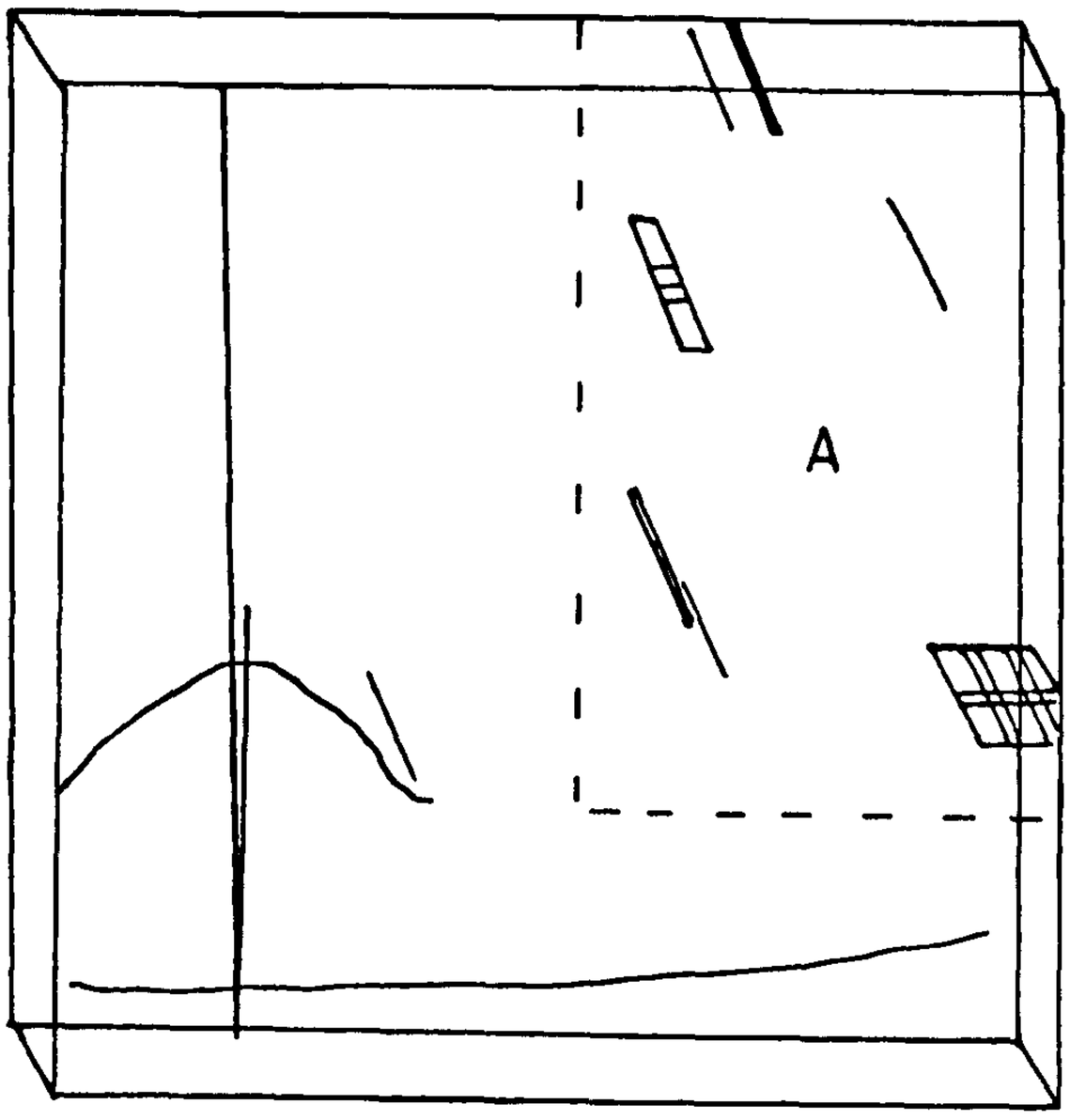

a) Anneal.1

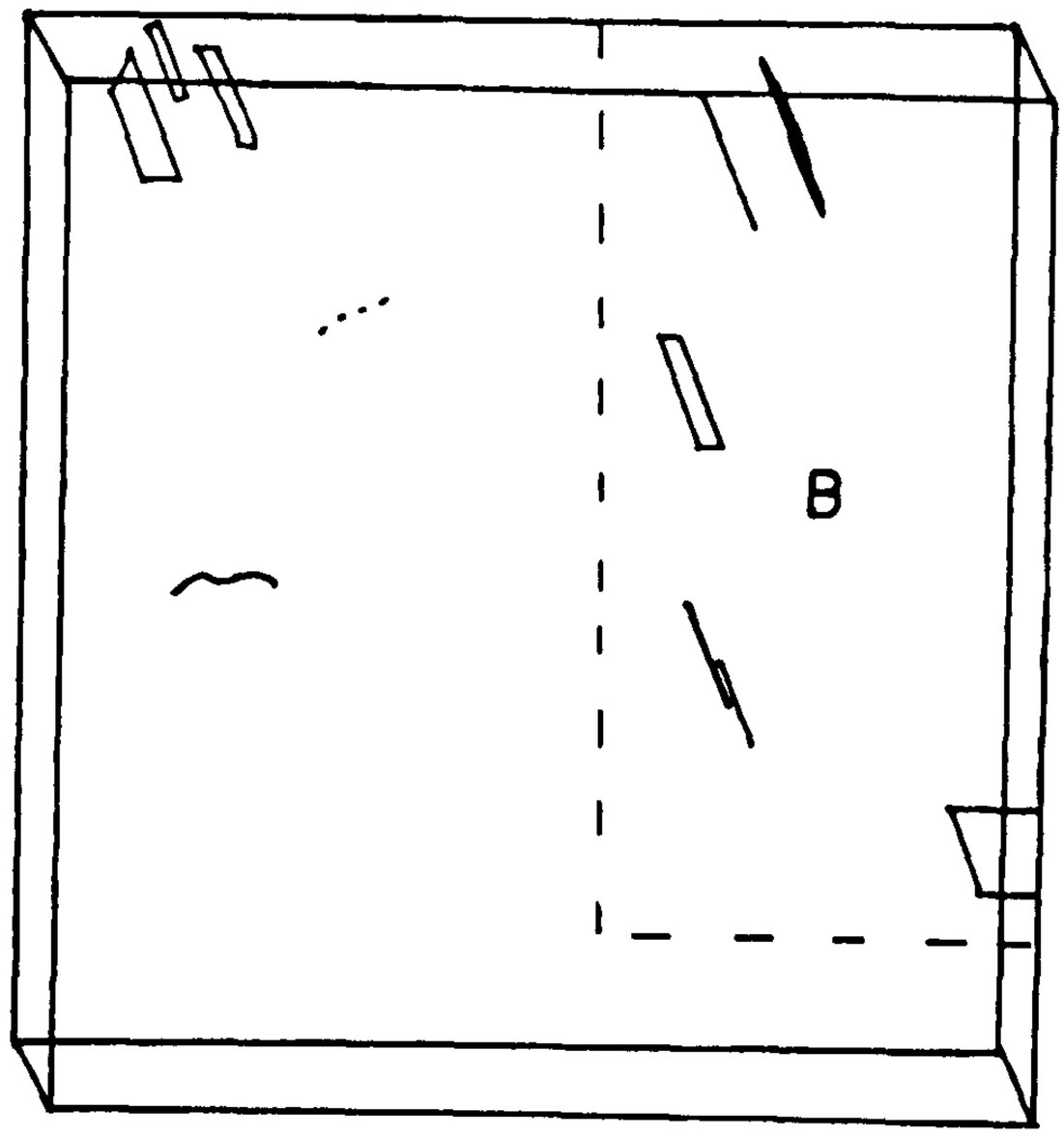

b) HPQ

However, there was some evidence to disprove this planar defect model. Very similar features were present on the diffraction images obtained from ANNEAL1 and HPQ (see fig. 4.30, 4.32 and 4.36). The features observed on the topograph of sample HPQ were not as highly resolved as those present on the ANNEAL1 image and appeared distorted. However the pattern of features on the right hand side of the topograph exactly matched those appearing on the same side of the ANNEAL1 diffraction image. The size and shape of the features which made up this pattern were also identical if allowances were made for the distortion observed on the HPQ topograph. The diagonal contrast feature pattern was different for every sample examined apart from this one case. However, the possibility that samples cut from different Quartz crystals would each have identical defect structures was remote. The validity of the contrast feature, RF, could not be not investigated further due to a shortage of allocated time at Daresbury laboratory.

4.3.3 Case Study of Defects in Crystal R8

The remaining allocation of Daresbury beam time was used to investigate defects in the crystal produced by growth run 8, which discussed earlier in section 4.1b. Three distinct regions were present in the crystal, namely, an imperfect growth region possessing a very high concentration of dislocations, a dislocation free region of perfect growth and an area corresponding to the dislocation free natural quartz seed. The original aim of the R8 study was to map lattice strain across the three regions of the crystal through the seed/crystal boundary. Unfortunately the sample slice which was cut from crystal R8 to be used for this purpose, although adequate for single crystal studies, was bent. The distortion of the reflection planes caused by this warping resulted in only a small area of the crystal being in the correct orientation to produce Bragg diffraction. Each double crystal topograph was dominated by an intense horizontal contrast band in the centre of the image which corresponded to the maximum diffracted intensity. The only useful diffraction images of the crystal appeared on either side of the intense band, however the intensity of the contrast decreased with distance and so only a small area of the sample could be imaged at a time. The bend in the crystal also increased the width of the rocking curve, rendering it unsuitable for the original purpose of strain mapping (see table 4.5). Therefore the study concentrated on the contrast features present on the topographs. The sample was moved into a number of

Table 4.6 Details of Topographs Obtained from Crystal R8

Topograph No.	Reflection Plane Sample / Silicon	Comments
35	(2-1.3) / (4 0 0)	1st position[a], RHS
36	" "	2nd position[b], RHS
37	" "	3rd position[c], RHS
38	" "	4th position[d], LHS
39	(03.0) / (4 0 0)	5th position[e], LHS
40	" "	6th position[f], LHS
41	" "	As 40, MP, ALL

RHS - Imaged on right hand side of rocking curve
LHS - Imaged on left hand side of rocking curve
MP - Multiple peaks
All - Imaged over whole rocking curve

a - Initial diffraction position of sample crystal
b - Sample moved 2mm down from a) to image perfect area
c - Sample moved 4mm down from a) to image imperfect area
d - Sample moved 6mm down from a) to image imperfect area
e - Sample moved through 90°
f - Sample moved down from e) by 2mm

Note - The K_α wavelength of Molybdenum radiation, 0.709Å, was used for all Bragg calculations. Topographs were imaged using Agfa D4 photographic film. The sample was a 1mm thick X-Slice cut from the crystal produced by growth run 8 (see table 2.1).

positions to enable the defects across the whole of the crystal to be studied. Experimental details concerning the topographs obtained for this study are given in table 4.6. A summary of sample positions is given at the end of this chapter (see figure 4.44).

The first diffraction image was obtained near to the edge of the crystal in the dislocation free region (see fig. 4.37). All that could be observed was a series of approximately horizontal parallel bands which had the appearance of a number of layers. These were similar in appearance to both crystal growth layers or to Pendellösung interference fringes. The remainder of the topograph was obscured by the intense horizontal contrast band caused by the bend in the crystal.

When the crystal was moved to the second position, a number of interesting contrast features were observed (see fig. 4.38 and table 4.6). The topograph showed a collection of interpenetrating rectangular blocks, BF, whose vertical edges ran parallel to the Z-crystallographic direction. These blocks had a horizontally layered structure similar to the diagonal features, RF, observed on figures 4.30-4.33 and varied in thickness but not in depth. A spiral feature, SP, was also observed to the right of these blocked structures. This was composed of a series of vertical lines which terminated in a very strongly contrasted rectangular feature near to the seed/crystal interface. Only those features in the immediate vicinity of the intense bending band were imaged, although intense features such as large fluid inclusions, I, were observed away from this band. The marker exposure, used

[010]

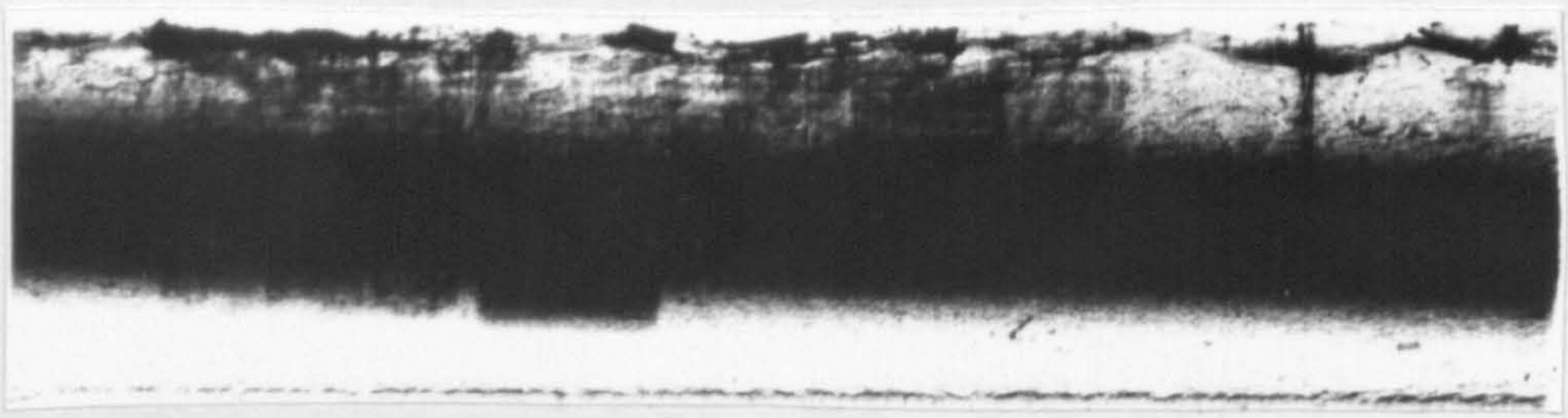

[001]

Fig. 4.37 - Topograph 35

$2\bar{1}3$
$\bar{g}$

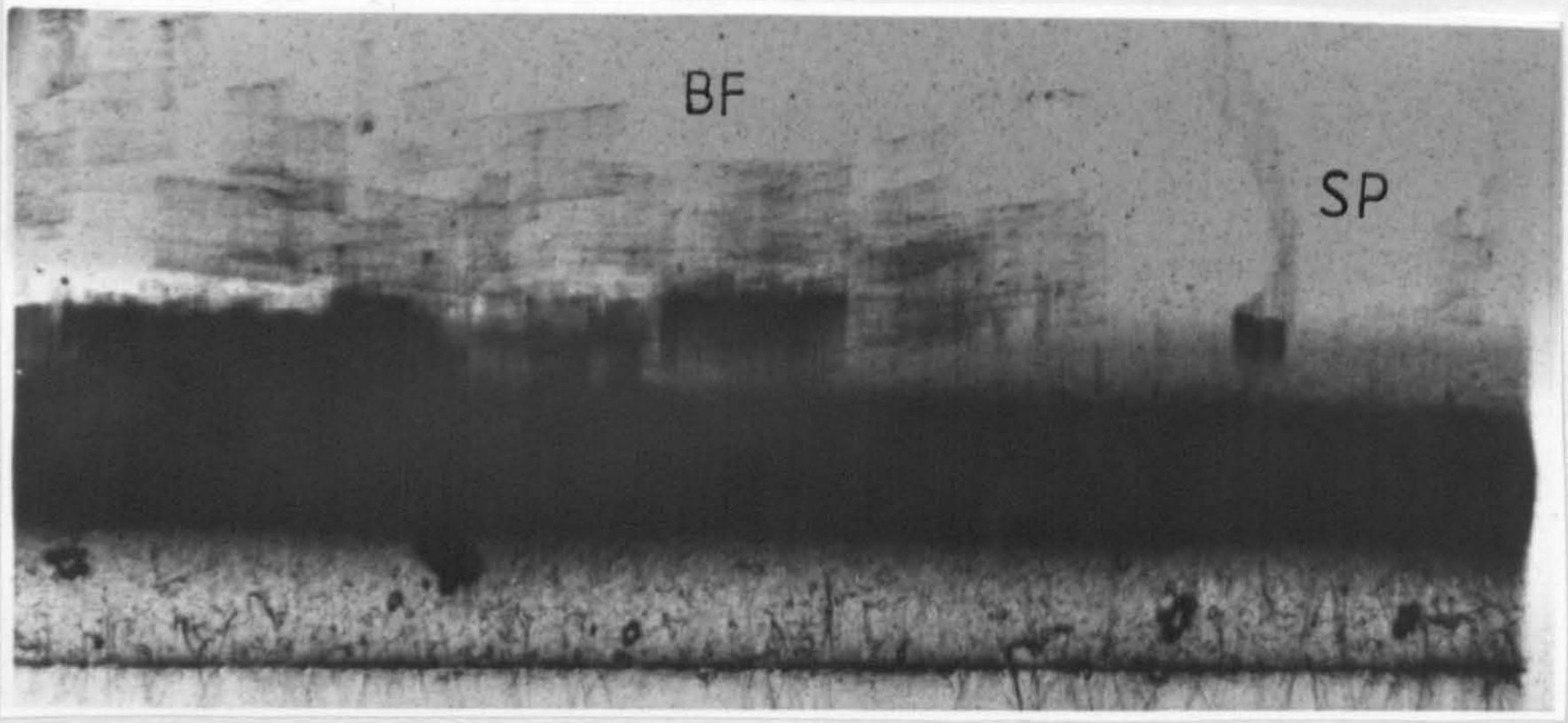

Fig. 4.38 - Topograph 36

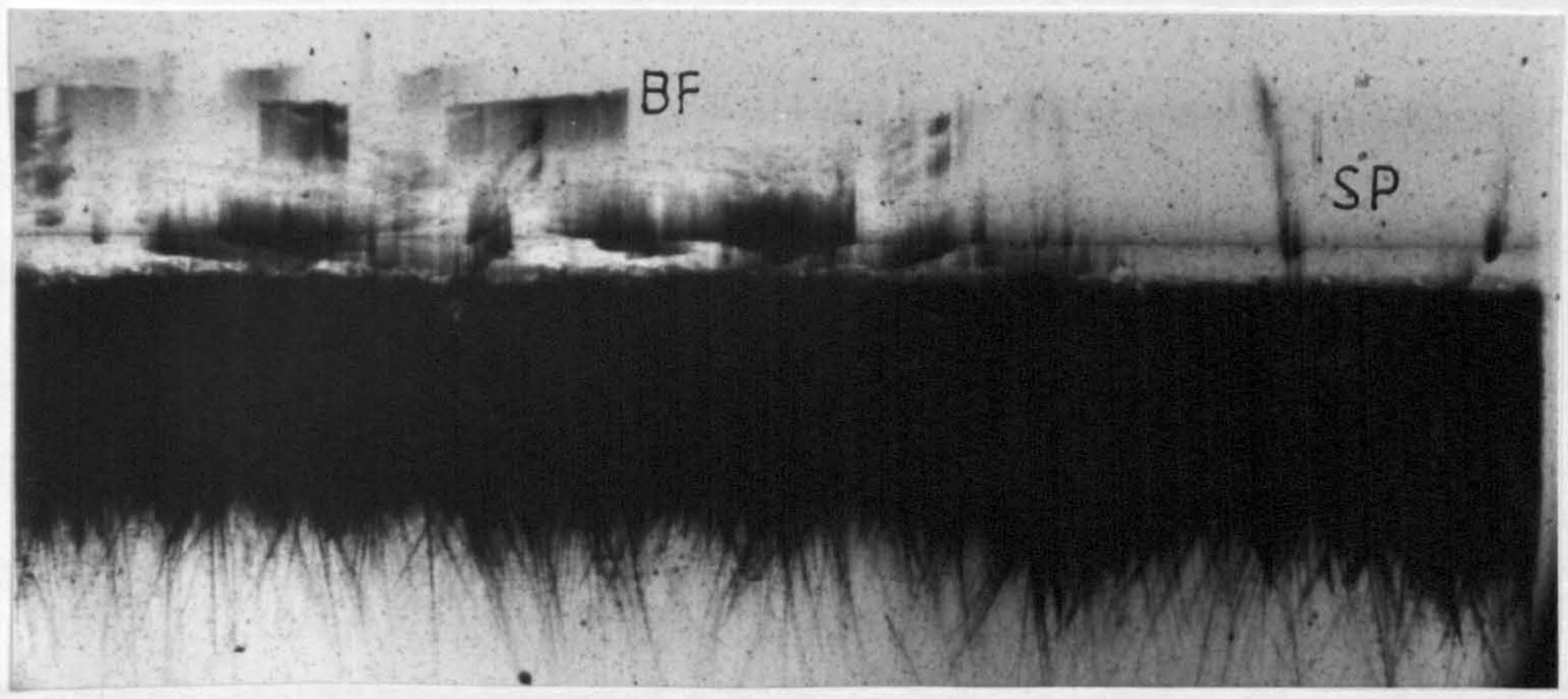

Fig. 4.39 - Topograph 37

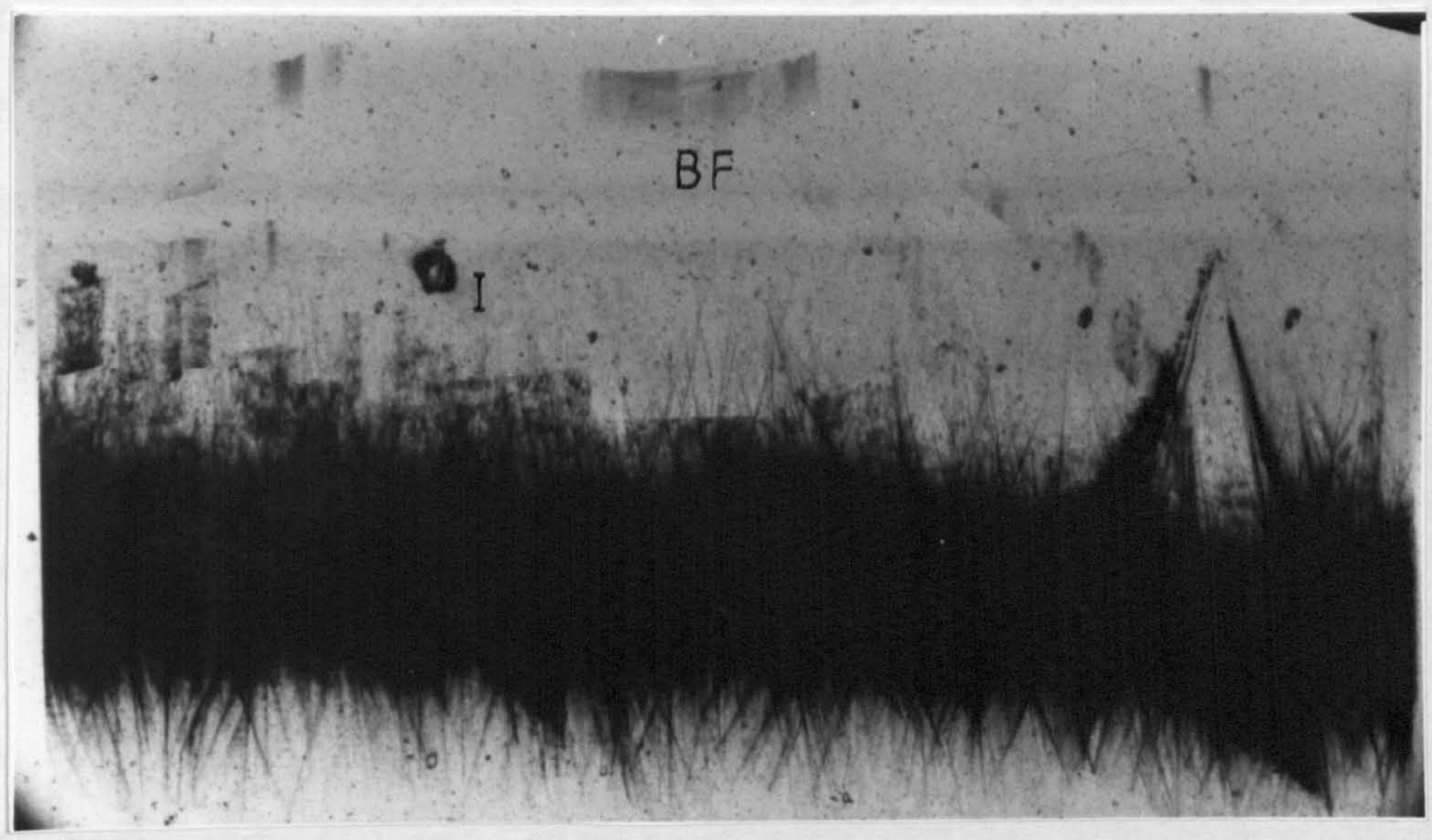

Fig. 4.40 - Topograph 38

to indicate the position of strain measurement, was not observed and was therefore positioned somewhere in the intense horizontal seed strain band.

The crystal was then moved to image the vicinity of the seed (see fig. 4.39 and table 4.6). In this topograph, the blocked features, BF, became streaked and appeared to be composed of a number of thin vertical components similar to those observed for the spiral feature, SP, observed in figure 4.38. Those features near to the seed/crystal interface appeared to originate at the seed surface and became streaked with distance. The block terminus of the spiral feature was not observed on this topograph. The spiral feature itself was distorted, which was probably a result of only a part of the feature being imaged in this position of the sample. Similarly, the streak appearance of the blocked feature was also probably a result of only part of the feature being imaged in this sample position.

The final sample position imaged the high dislocation section of the crystal (see fig. 4.40 and table 4.6). A series of blocked features, BL, similar to those shown on figure 4.38 were observed. Unfortunately, The high concentration of dislocations combined with the bend in the crystal obscured most of the detail in these features. Also observed were several streaked features in the dislocation free sector of the crystal, BF. These were thought to be the more intense of the blocked features observed in figure 3.38.

To confirm the validity of the blocked features, the

sample was then moved through 90° and a series of topographs taken in that orientation using the symmetric (03.0) reflection planes instead of the asymmetric (2-1.3) planes which were used to obtain the previous set of R8 topographs (see figs. 4.41-43 and table 4.6). At the first sample position, features very similar to the blocked features, B, appeared in the dislocation free sector. The spiral feature, SP, observed on fig.4.38 was observed. Unfortunately this feature had not moved with the sample and remained in the same orientation as observed previously, thereby proving that it was not a quartz crystal defect. When the crystal was moved to image the blocked features, these features also did not move with the crystal (see fig. 4.42 and table 4.6). This was shown by the relative positions of the blocks and spiral with regard to a large fluid inclusion, I. When the crystal was repositioned, the inclusion moves with it to appear near the top of the topograph. The block and spiral features were positioned opposite the inclusion on figure 4.41, but appeared below that defect in figure 4.42 after the crystal had been moved. If the contrast features had been genuine crystal defects they would have moved with the inclusion. To eliminate the possibility that there were two fluid inclusions present and that the movement of the crystal had placed the marker inclusion in the horizontal contrast band, a topograph was taken by scanning the sample over the whole rocking curve. This procedure lowered the strain sensitivity of the technique to eliminate the bending contrast band (see fig.

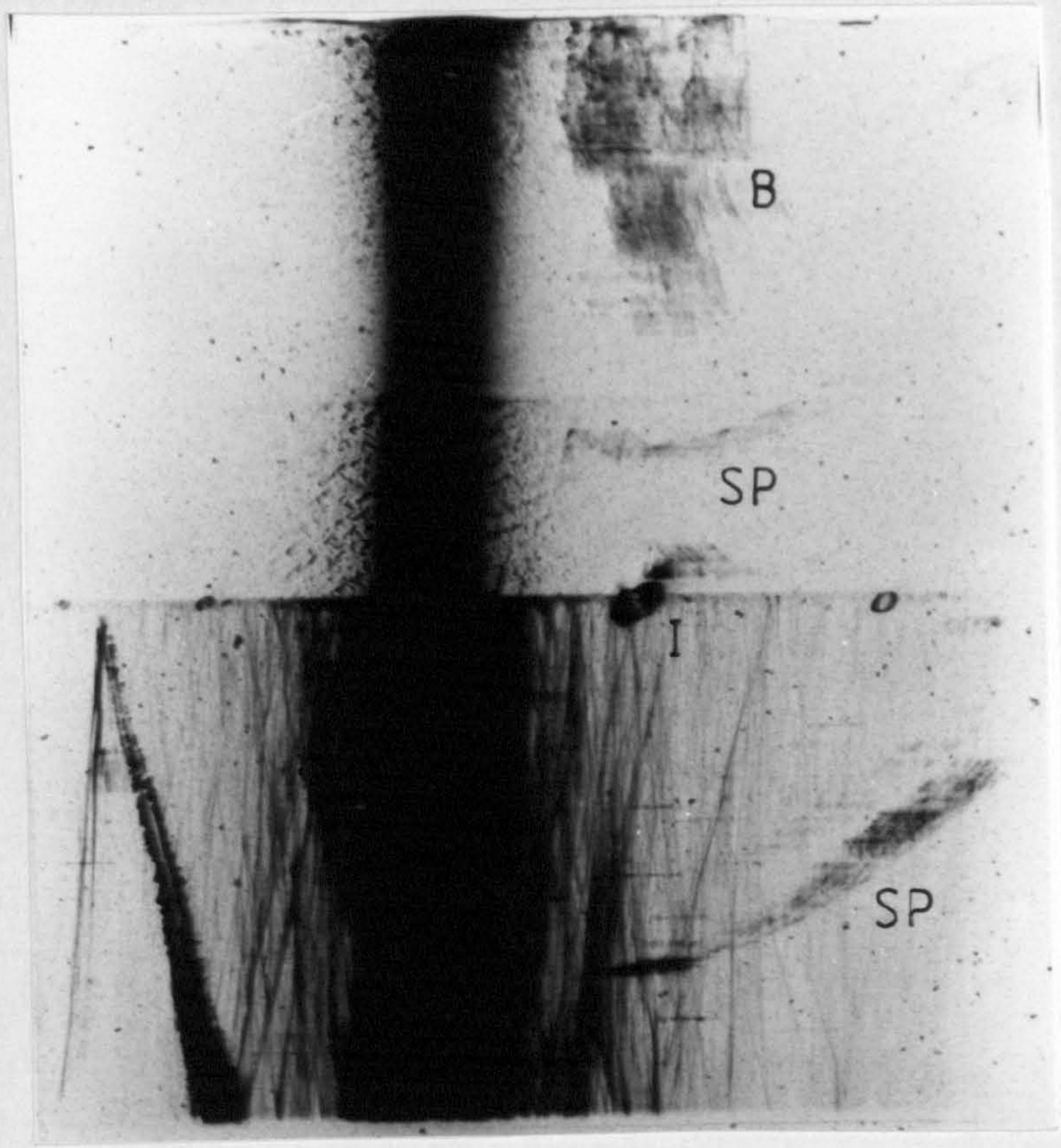

221a

Fig. 4.41 - Topograph 39

[001]

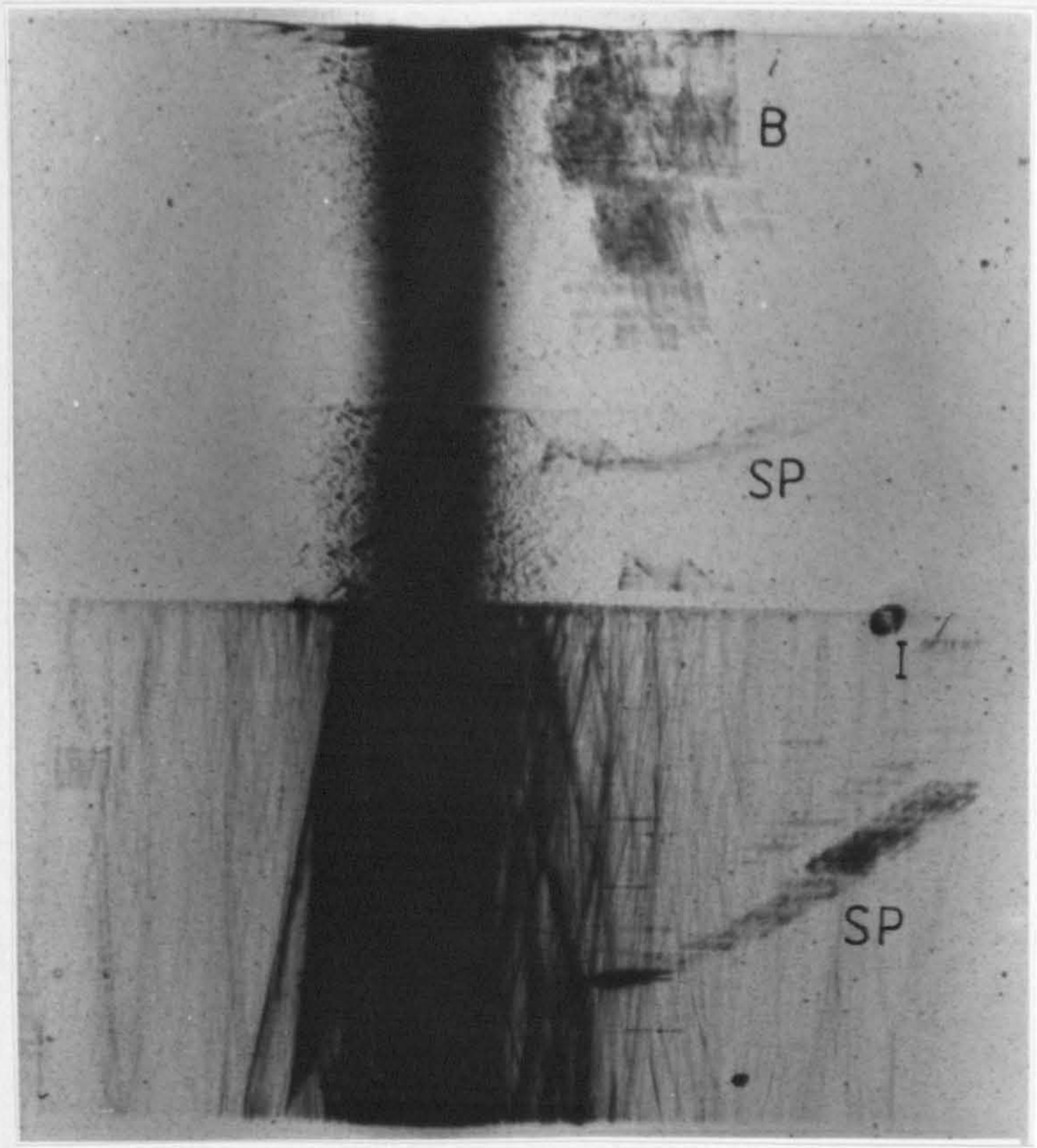

Fig. 4.42 - Topograph 40

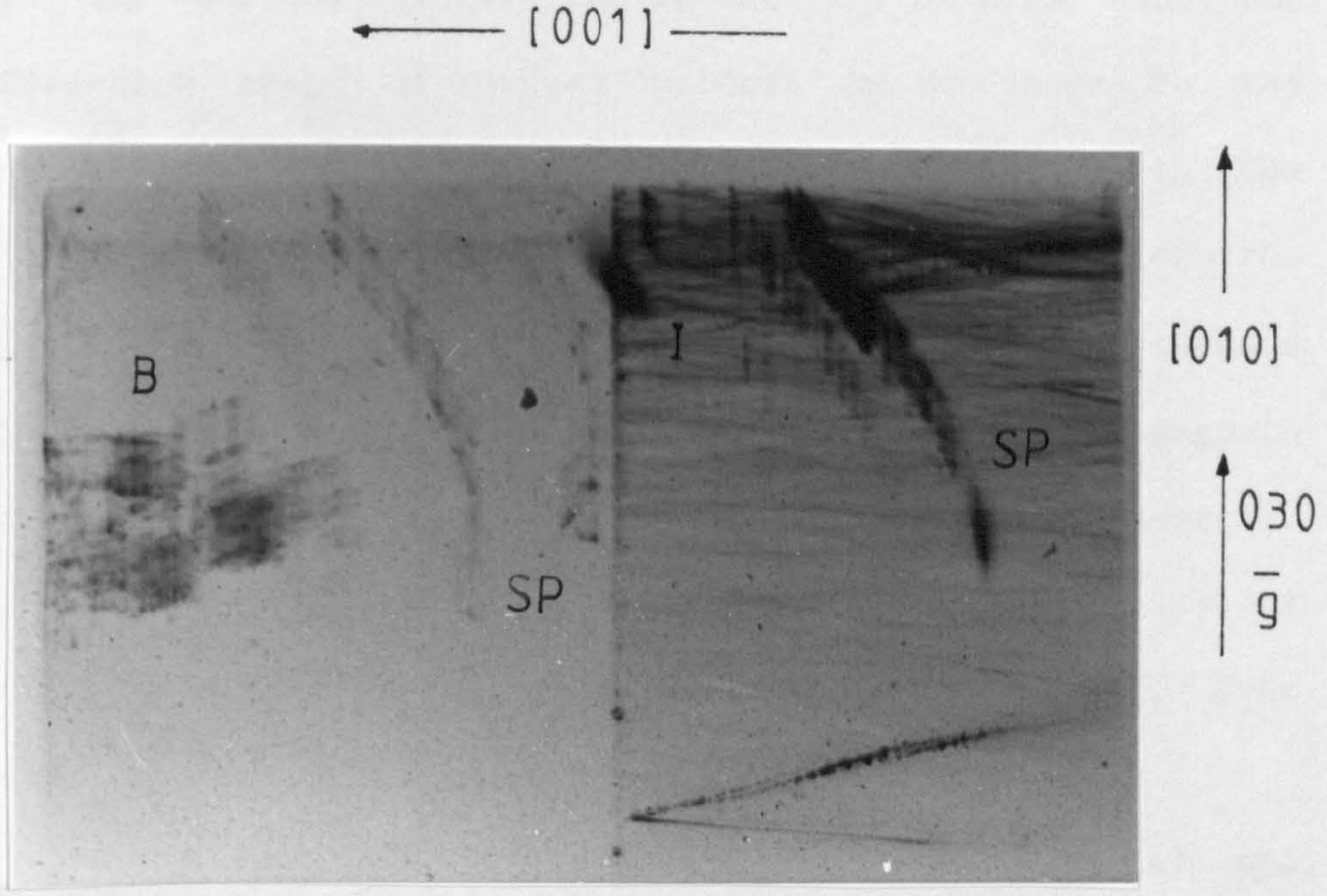

Fig. 4.43 - Topograph 41

4.43 and table 4.6). The major contrast features are still present in the topograph but are much weaker. Since there is no inclusion opposite the contrast blocked features, it is probable that they are not quartz crystal defects.

This led to the problem of identifying the blocked and spiral contrast features. Since the x-ray beam was diffracted from the silicon crystal, the possibility existed that the diffraction image of defect features on or near to the surface of the monochromator would be transmitted with the diffracted x-ray beam. The internal defect structure of the crystal bulk would not be transmitted since only surface diffraction from the Silicon was involved. However a topograph obtained from the silicon crystal did not show any features. This did not mean that the features were not some property of the Silicon, only that they could not be imaged directly from the crystal.

Examination of the right hand portion of figures 4.41 and 4.42 showed a series of very thin lines and thicker blocks that were similar to those features observed on figures 4.30-4.33 with the exception that they did not run diagonally across the crystal. Therefore the possibility exists that the diagonal contrast features, RF, could be attributed to an artifact of defects on the silicon monochromator crystal.

From observations discussed in this section it can be concluded that the block and spiral features observed on figures 4.41-4.43 were produced by defects on silicon monochromator crystal. However, some doubt remains to the

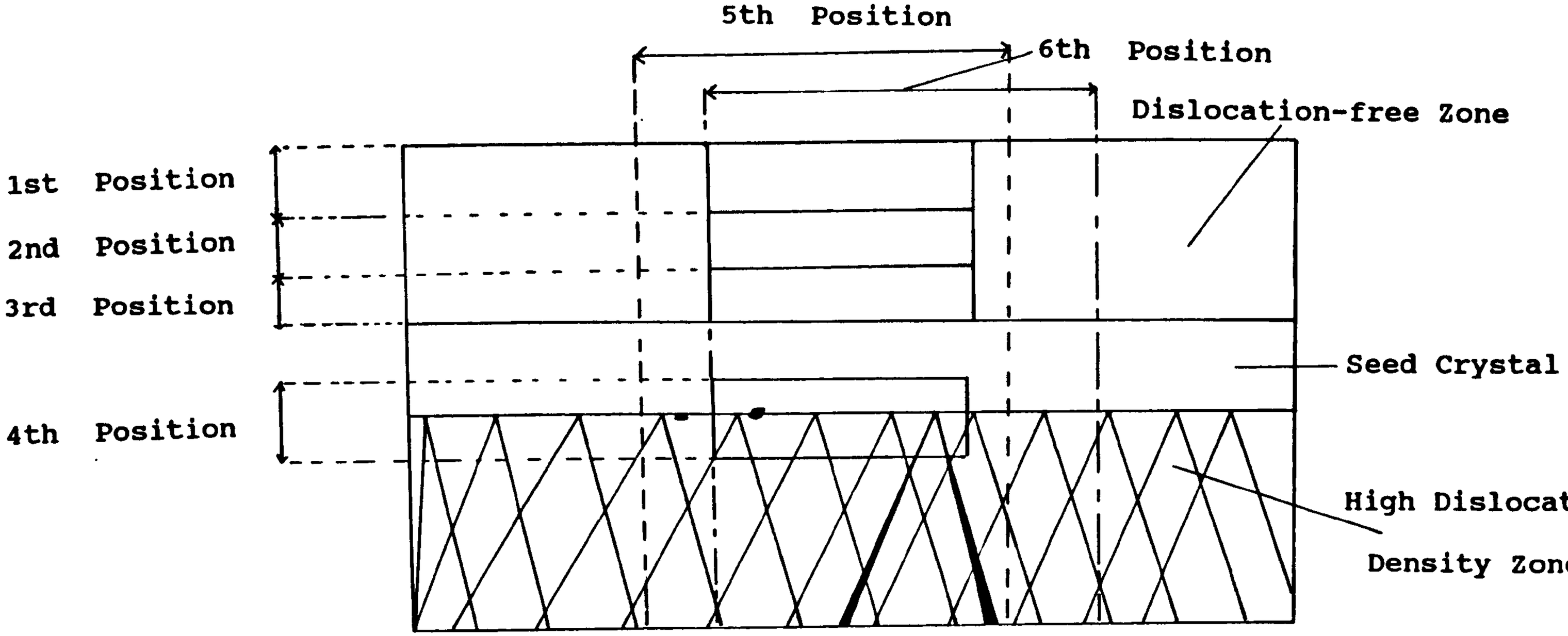

Fig. 4.44 Positions at which Topographs were Obtained from Crystal R8

nature of the blocked contrast features observed on figures 4.38-4.40. These featuresbehaved as expected for a crystal defect, moving with the crystal and losing contrast when the sample position was changed. If these features are genuine defects they could be attributed to the planar defects produced by lattice mismatch at the cellular growth walls that produce the cobbled structure on the (00.1) quartz crystal faces[54]. These defects can be observed using diffraction topography only if reflection planes parallel to (00.1) planes are employed. only be visible to diffraction topography using reflection planes parallel to the (00.1) planes. This would explain why the contrast features in the original R8 topographic series behave and look differently to those obtained when the crystal was moved through 90°. The blocked features may still be artifacts of the silicon crystal but to prove this requires further investigation.

Chapter 5. Summary, Conclusions and Future Work

Chapter 5. Summary, Conclusions and Future Work

5.1 Crystal Growth

Deuterated quartz was successfully grown using both a sodium hydroxide and a sodium carbonate mineraliser. Growth conditions were found which enabled the production of deuterium analogues of high purity quartz crystals. Growth rate, dislocation content and impurity concentrations of the deuterated crystals studied in this thesis were found to be comparable to their respective hydrogen analogues. The deuterium content of deuterated crystals was always lower than the comparative hydrogen content of the analogue crystal, which indicated that deuterium did not incorporate into the quartz lattice as easily as hydrogen. However, with this exception, deuterated quartz samples behaved as would be expected for undeuterated crystals. The frequency ratios of analogous O-D and O-H infrared absorption bands were not constant but rose asymptotically with wavenumber. Aluminium impurities were observed to preferentially incorporate into the rhombohedral growth sectors which bordered the dominant (00.1) sector of the studied crystals. Aluminium incorporation was indicated in x-ray diffraction topographs by an increased lattice strain in the rhombohedral areas of a crystal.

Sweeping a seed prior to quartz growth did not prevent dislocations propagating into the growing crystal. Growth using a horizontally mounted seed resulted in the production of an upper growth layer which possessed a very high dislocation concentration and a lower protected growth layer

which was dislocation free. Infrared studies on this type of crystal showed no relationship between the dislocation concentration and the hydrogen content of quartz. Similarly, no relationship could be found between dislocation content and impurity concentrations in quartz crystals.

5.2 Effects of Irradiation and Electrodiffusion

High purity synthetic quartz differed from conventionally produced synthetic material in several important ways. Electrodiffusion, or sweeping, did not introduce hydrogen species into a high purity crystal even when the procedure had taken place in an air atmosphere. Sweeping did produce a weak absorption band at 3365 cm^{-1} in the infrared spectrum of high purity quartz which indicated the formation of Al-OH defects in the crystal. The appearance of the aluminium associated absorption band was accompanied by a marked reduction in intensity of the 3580 cm^{-1} and 3436 cm^{-1} bands and a significant intensity increase in the 3348 cm^{-1} absorption. The overall hydrogen content of swept samples did not change significantly from that observed in the unswept sample spectra, indicating that the process did not remove hydrogen ions from the crystal but merely rearranged them. The formation of the 3365 cm^{-1} absorption band was a consequence of the removal of charge compensating Na^+ ions from Al-Na^+ defect sites by the sweeping process. The reduction of the 3580 cm^{-1} and 3436 cm^{-1} absorption bands indicated that H^+ ions from the infrared active hydroxyl species associated with

these bands preferentially replaced Na^+ ions in the charge compensation process to produce Al-OH sites. Sweeping Na^+ ions through a high purity quartz sample did not alter the infrared spectra from those observed by conventional sweeping in either a nitrogen or an air atmosphere. In each case the same infrared spectrum was obtained.

Irradiation of high purity quartz samples of aluminium content less than 0.01 ppm did not alter the infrared spectrum from that observed in the pre-irradiated case. At aluminium levels in excess of 0.01 ppm, the intensity of all as-grown hydrogen associated absorption peaks was reduced and two Al-OH absorptions at 3365 cm^{-1} and 3304 cm^{-1} were produced. At levels of 0.5 ppm aluminium, irradiation virtually eliminated all as-grown hydrogen associated absorption bands from the spectrum. The lack of preferential absorption band reduction shows the formation of Al-OH sites during irradiation to follow a different mechanism to formation during the electrodiffusion process.

5.3 Impurities in Synthetic Quartz

In general, the addition of dopants during the growth of high purity synthetic quartz produced samples which displayed identical infrared spectra, in terms of the absorption bands present, irrespective of what the dopant impurity species was. The only difference between individual doped sample spectra was the intensity of the absorption bands, the frequencies at which they occurred were the same. The only exceptions to this

observation, where aluminium and iron had been used as dopants, had been reported in the literature to incorporate substitutionally into the quartz lattice[52,100,101]. The two Al-OH absorption bands at 3365 cm^{-1} and 3304 cm^{-1} were well documented however, prior to this thesis, no infrared absorption bands had been attributed to substitutional iron impurities in synthetic quartz crystals. Absorption bands characteristic to the spectrum of iron doped samples were observed at 3576, 3546 and 3456 cm^{-1} respectively. These could be assigned with some confidence to substitutional iron impurities. The lack of characteristic absorption bands corresponding to the other impurities studied, combined with the similarities in sample spectra lead to the conclusion that, with the exceptions already stated, the impurities which were studied were all incorporated interstitially. Since the only difference between individual doped sample spectra was the amount of hydrogen which had been introduced into the crystal by the dopant, it could be concluded that there was a relationship between impurity content and hydrogen concentration. The existence of this relationship was further substantiated by the presence of a broad intense band centred around 3200 cm^{-1} in the spectrum of each doped sample. This band was characteristic of synthetic crystals which had been grown at a fast rate and was associated with a large intake of hydrogen impurities into the crystal. Doped crystals were grown at a rate which would not normally have produced the broad absorption. Therefore, the addition of the dopant

caused large amounts of hydrogen impurities to be introduced into a doped crystal. This suggested hydrogen impurities were incorporated along with and associated to impurities in a quartz crystal. The sharp absorption bands in doped sample infrared spectra were produced by the O-H stretching vibration of hydroxyl ions which probably acted as charge compensators for the impurity ions. Doped samples were shown to produce an ice absorption band which was superimposed upon the broad 3200 cm^{-1} absorption in the infrared spectrum after a sample had been heated above 500°C. After this treatment, a doped sample changed from clear and transparent in appearance to milky and slightly opaque. This was a consequence of the release of water from the quartz lattice upon heating to form fluid inclusion bubbles. From these observations it was concluded that the broad absorption band on doped sample spectra was associated with hydrogen bonded water molecules interstitially incorporated in the quartz lattice. The absence of the ice band upon cooling an untreated sample was attributed to the quartz lattice intruding between individual water molecules to prevent the formation of the regular water structure which produced the ice absorption band. Water molecules were thought to form a hydration sphere around impurity ions and thus be introduced into quartz when these ions were incorporated into the crystal lattice. The variation in hydrogen content between doped samples was thought to indicate the different levels of impurity in each crystal, with hydrogen content increasing with impurity concentration.

Each of the absorption bands observed in the spectra of doped and impure synthetic quartz crystals displayed polarisation behaviours identical to one of the four characteristic high purity quartz absorption bands. In general the O-H bonds were aligned preferentially along the X and Y axes. The O-H bond associated with the Al-OH absorption at 3365 cm^{-1} was shown to be preferentially aligned along the Z-axis.

5.4 Hydrogen in High Purity Quartz

The four impurity related absorptions in high purity synthetic quartz infrared spectra at 3580, 3436, 3395 and 3348 cm^{-1} respectively were found to each show a different polarisation behaviour. The O-H bonds of the hydrogen species associated with the 3580 cm^{-1} and 3436 cm^{-1} absorption bands were shown to be preferentially aligned along the X and the Y-axes, with a 10% and a 40 % component along the Z-axis respectively for the two absorption species. The O-H bonds associated with the 3348 cm^{-1} absorption species were shown to be preferentially aligned almost 100% along the Z-axis. There was no observed preferential alignment for the 3395 cm^{-1} absorption species.

Deuteration studies of high purity crystals showed that hydroxyl ions were not incorporated directly from sodium hydroxide mineralisers, but came from the water solvent. Irradiation removed all as-grown O-D associated absorption bands to produce deuterium analogues of Al-OH associated

absorptions. Sweeping after irradiation regenerated the as-grown O-D absorption bands and was shown to preferentially increase the intensities of the deuterium analogues of the four absorption bands characteristic of high purity quartz infrared spectra. It was concluded from the sweeping studies that deuterium was present in the crystal lattice at sites which were not infrared active as well as in the infrared active O-D species. In comparison with a swept sample spectrum, the intensity of the Al-OD absorption bands in the spectrum of a crystal which had been irradiated prior to sweeping was greater, indicating a more efficient conversion of Al-M^+ centres to Al-OH sites. From this observation it was concluded that swept quartz which had been pre-irradiated was better able to resist the effects of future irradiation than crystals which had not undergone the treatment. As the deuterated crystals were good analogues of non-deuterated quartz, the above observations could be applied equally for high purity quartz crystals.

The major hydrogen species in high purity synthetic quartz was hydroxyl ions. No detectable molecular water was observed in sample infrared spectra. Levels of hydroxyl ions in high purity quartz crystals was always less than 1 ppm. From the infrared studies of hydroxyl impurities in non-quartz crystal systems, it was concluded that the hydrogen species which produced the 3580 cm^{-1} absorption band could be assigned to an Na^+OH^- unit aligned preferentially along the X and the Y axes, depending on the chosen orientation of the sample

slice. Similarly the species associated with the 3348 cm^{-1} was assigned to a sodium hydroxide unit aligned along the Z-axis, probably lying in the C-channels. The 3436 cm^{-1} associated hydrogen species was also thought to be a sodium hydroxide unit but one which was aligned at approximately 45% to the X-Y plane along the X and the Y axes. The 3395 cm^{-1} absorption band was tentatively suggested to be associated with sodium hydroxide units which were randomly orientated throughout the quartz lattice. Sodium hydroxide units were thought to be a source of the Na^{+} ion excess which was present in high purity quartz crystals.

5.5 Defects in Swept Quartz Crystals

Electrodiffusion induced the formation of a negative space charge near to the anode edge of a swept quartz crystal, which gave rise to inhomogeneous strain in the quartz lattice. This was a consequence of the removal of Na^{+} ions from Al-M^{+} defect sites to leave negatively charged aluminium impurity ions in the crystal lattice. This feature was observed on diffraction topographs as a streaked band of contrast mainly concentrated along the anode edge of a crystal, but which also stretched across the whole of the crystal from anode to cathode in several places. From the streaked appearance of the feature and its variations in distance across the crystal along the anode edge, it was concluded that the electric field which had been applied across swept samples was inhomogeneous and the effects of sweeping across a crystal were therefore

intrinsically variable. The strain in the crystal was related to the concentration of aluminium impurities, with the lattice strain increasing with impurity concentration. The lattice strain was independent of time and persisted in the crystal. Prolonged exposure to x-rays relieved the lattice strain. The mechanism by which this was achieved was thought to be the release of H^+ ions from binding sites in quartz, upon irradiation, followed by migration of these ions to negatively charged aluminium impurities. The hydrogen ions form Al-OH centres thereby removing the negative space charge and relieving the lattice strain.

Double crystal diffraction studies showed that optically polished quartz samples were subject to surface damage by the sweeping process. This was observed on topographs as weak contrast streaks aligned along the Z-axis parallel with the C-channel direction. Crystals which had been chemically polished using hydrofluoric acid were not subject to this damage. No other new contrast feature induced by the sweeping process was observed using double crystal topography.

Comparison of x-ray topographs obtained from pre- and post-swept sample crystal slices showed that sweeping did not alter dislocation contrast. The process therefore did not reduce the lattice strain at the core of a dislocation.

In conclusion, dislocations in high purity α-quartz crystals were virtually unaffected by the sweeping process. Essentially the process only resulted in the removal of alkali metal ion impurities from a treated sample combined with the

rearrangement of hydrogen impurities throughout the quartz crystal lattice. No irreversible bulk crystal damage occurred as a result of the process, although a build up of negative space charges and the possibility of surface damage in a crystal were disadvantages of electrodiffusion.

5.6 Bulk Defects in Quartz

Two possible crystal defects in the bulk of quartz were observed using double crystal topographic methods. The first of these was a planar defect which was parallel with the X-Y plane of quartz and was observed as a consequence of the misalignment of a sample crystal with respect to the diffracted x-ray beam. This feature appeared as regularly shaped diagonal blocks of contrast on diffraction topographs which disappeared when sample were corrected for the misalignment. No planar defect has been reported as lying in the X-Y plane direction and so, if the features are genuine, is a new quartz defect. The only evidence against the validity of the feature was the observation of very similar contrast streak patterns on two different quartz samples.

The second bulk defect appeared on diffraction images as a series of regularly shaped interlocking contrast blocks. The edges of the blocked features were parallel to the direction of the C-channels in the quartz structure and were horizontally banded. The features were similar in appearance to the planar defect reported by Lang and Muiscov, which was attributed to lattice mismatch between cellular growth cells

in the (00.1) growth sector of quartz[54]. The contrast features moved as the crystal was moved when imaged using an asymmetric (2-1.3) reflection. The evidence against the contrast feature was that similar features on topographs obtained using an orthogonal symmetric reflection were proven to be artifacts of the silicon monochromator. Therefore, either the original contrast feature was a monochromator artifact or that it could not be imaged using a symmetric reflection. The validity of this feature and the horizontal planar defect could not be categorically established using the data available.

5.6 Future Work

The most pressing work that has to be carried out concerns establishing the validity or not of the two defect features discovered using double crystal topography. This could be accomplished by repeating the x-ray diffraction experiments detailed in section 4.3 using a quartz crystal monochromator which had a known defect structure. This would allow unambiguous identification of defects in the sample crystal. Another option would be to carry out a series of section topographs on quartz crystals, which would determine what features on diffraction images were produced by defects in the crystal bulk.

A useful set of experiments would be to repeat the polarisation studies carried out in this thesis using two polarisers. This would ensure that the irregularity of increased band intensity upon polarisation which was observed

during this project could be eliminated. The orientation of the impurity related O-H bonds in quartz crystals could be further characterised by polarisation studies of crystal cuts at various angles to the X, Y and Z growth axes.

The relationship between hydrogen content and impurity concentration must be investigated further. This could be accomplished by growing doped quartz crystals of sufficient size that impurity analysis could be carried out in addition to infrared studies. In this way, the efficiency of various impurities in introducing hydrogen into a quartz crystal could be assessed and an accurate correlation between impurity concentration and hydrogen content could be established. The substitutional iron impurities discussed in this thesis warrant further study. EPR studies such as those carried out by Lehmann[101] would confirm the validity of the substitutional nature of the iron impurities and provide further information on how they were incorporated into the quartz lattice.

Further investigations into the effects of sweeping on quartz crystals could also be profitable. In particular, the determination of whether the production of space charges in quartz is an unavoidable consequence of the sweeping process. Space charge production may only occur as an undesirable result of sweeping a crystal for a longer period of time than is necessary for the removal of alkali metal impurities. Excessive sweeping may remove hydrogen ions from charge compensation sites in a crystal to produce space charges. To substantiate this claim requires the examination, using x-ray

diffraction topography, of a series of swept crystals of known aluminium content. By altering the duration of a sweeping run and the size of the applied voltage across a crystal, the relationship between space charge formation with duration, voltage and aluminium concentration could be obtained. This would give information which could possibly be used to alter the conditions under which sweeping is carried out so that space charge formation may be reduced or even eliminated completely. At the very least, such a study would provide data which would enable better understanding of the sweeping process.

Appendix A and References

Appendix A

Specimen Calculations

1. Calculation of Bragg Angle

Example Reflection Plane - (02.-3)

Formula Required - Bragg's Law - $n\lambda = 2d \sin\theta$

Required Variable = Bragg Angle θ

$n = 1$, $\lambda = K_\alpha$ Mo = 0.709Å , d = Unknown

Calculate interplanar spacing, d, from the following formula

$$d^2_{hkl} = \frac{1}{(h^2 + k^2 + hk).a^{*2} + l^2 c^{*2}}$$

where,

$$a^* = \frac{1}{a./3} \qquad c^* = \frac{1}{c}$$

$h = 0$, $k = 2$, $l = -3$, $a = 4.913$ Å , $c = 5.404$ Å

substituting for a and c, $a^* = 0.235$ $c^* = 0.185$

substituting for h, k, l, a^* and c^*

$$d^2_{(02.-3)} = \frac{1}{(0 + 2^2 + 0)(0.235\ Å)^2 + (-3)^2(0.185\ Å)^2}$$

$$= 1.891\ Å^2$$

$$d_{(02.-3)} = 1.357\ Å$$

Rearranging Bragg's Law

$$\sin \Theta = \frac{n \tau}{2 d}$$

Substitution for n, τ and d

$$\sin \Theta = \frac{0.709 \text{ Å}}{2.(1.357 \text{ Å})}$$

$$\sin \Theta = 0.261$$

Therefore, the Bragg angle for the (02.-3) reflection of quartz is 15°.

Calculation of Solution Volume in an Autoclave

Cleaning Run

Example Autoclave - K31

Autoclave Volume - 107 ml

Average Autoclave Temperature During Run - 360 °C

Required Internal Autoclave Pressure - 1500 atm

Volume of solution required to produce 1500 atm at 360 °C = Unknown

Free Volume of Autoclave, FV = 107 ml

Specific volume of water at 1500 atm and 360 °C,

S = 1.2545 (Specific volume values from reference 147)

Volume of solution required to produce required temperature and pressure conditions, V is calculated as follows,

$$V = \frac{FV}{S}$$

$$= \frac{107 \text{ ml}}{1.2545}$$

$$= \mathbf{85.3 \text{ ml}}$$

Conversion Run

Example Autoclave - K34

Autoclave Volume - 86.7 ml

Average Autoclave Temperature During Run - 360 °C

Required Internal Autoclave Pressure - 1500 atm

Volume of solution required to produce 1500 atm at 360 °C = Unknown

Weight of Unconverted Silica = 30g

Density of Silica = 2.00 g cm^{-3}

Volume of Silica = 15ml

Free Volume of Autoclave, FV = (86.7 - 15)ml

= 71.7 ml

Specific volume of water at 1500 atm and 360 °C,

S = 1.2545 (Specific volume values from reference 147)

Volume of solution required to produce required temperature and pressure conditions, V is calculated as follows,

$$V = \frac{FV}{S}$$

$$= \frac{71.7 \text{ ml}}{1.2545}$$

$$= 57.2 \text{ ml}$$

Growth Run

Example Autoclave - K33

Autoclave Volume - 92 ml

Average Autoclave Temperature During Run - 360 °C

Required Internal Autoclave Pressure - 1500 atm

Volume of solution required to produce 1500 atm at 360 °C = Unknown

Weight of Quartz Nutrient = 30g

Density of Quartz = 2.65 g cm^{-3}

Volume of Quartz = 11.3 ml

Free Volume of Autoclave, FV = (92 - 11.3)ml

= 80.7 ml

Specific volume of water at 1500 atm and 360 °C,

S = 1.2545 (Specific volume values from reference 147)

Volume of solution required to produce required temperature and pressure conditions, V is calculated as follows,

$$V = \frac{FV}{S}$$

$$= \frac{80.7 \text{ ml}}{1.2545}$$

$$= 64.3 \text{ ml}$$

References

1. Singer F., Z. Elektrochem 32 382 (1926)
2. Frondel C., "Dana's System of Mineralogy" 7th Ed. Vol.III Wiley (New York) (1962)
3. Cady W.G., "Piezoelectricity" 1st Ed. McGraw-Hill (1946)
4. Cady W.G, Proc. I.R.E. 10 83 (1922)
5. Brice J.C., Reviews of Modern Physics 57 (1) 105 (1985)
6. Mason W.P., " Piezoelectric Crystals and Their Applications to Ultrasonics" 1st Ed. Von Nonstrand (1950)
7. Croxall D.F., Christie I.R.A., Holt J.M., Todd A.G. Isherwood B.J., Proc. 36th Ann. Freq. Con. Symp. (1982)
8. Weiss, Abh. Ak. Wiss. Berlin p318 (1816)
9. Biot, Mem. cl. sci. math. phys. inst. imp. France 1 241 (1814)
10. Cullity B.D., "Elements of X-Ray Diffraction" 2nd Ed. Addison-Wesley (1978)
11. Bravais, J. école polytechn. 20 117 (1851)
12. Cady W.G., Van Dyke, Proc. I.R.E. 30 495 (1942)
13. Proc. I.R.E. 37 1378 (1949)
14. Wyckoff, "Crystal Structures" Vol.11 p312 Wiley (New York) (1963)
15. Evans R.C., "An Introduction to Crystal Chemistry" Cambridge University Press (1952)

16. Kirkaldy J.F. "Minerals and Rocks" 2nd Ed.
Blanford Press (London) (1972)

17. Kraus H.E., Walter F.H., Ramsdell L.S., "Mineralogy"
5th Ed. McGraw Hill (1959)

18. Iddings J.P., "Rock Minerals" 2nd Ed. Wiley (1911)

19. Spezia G., Atti. Accad. Sci. Torino 40, 254 (1905)

20. Nacken R., captured German reports RDRC/13/18
Feb. 28 (1946)

21. Nacken R., Chemiker-Z, 74 (50) 745 (1950)

22. Wooster N., Wooster W.A., Nature 157 297 (1946)

23. Thomas L.A., Wooster N. and Wooster W.A
Disc. Faraday Soc. 5 341 (1949) [M.A. 10-104]

24. Kohman G.T., Final report Bell Telephone Laboratories
U.S. Army Signal Corps contract DA-36-039 SC-64493 p1
Aug. (1955)

25. Hale D.R., 2nd quarterly progress report , Brush
Development Co., U.S. Signals Corps contract
W-36-039 SC-32093 p7 1946

26. Hale D.R., Science 107 393 (1948)

27. Hale D.R., 3rd, 5th, 6th and 7th quarterly reports
U.S. Army Signals Corps, contract W-36-039 SC-32093
Jan, July, Aug and Oct 1947 and Jan 1948 respectively

28. Bueller E., Walker A.C., Bell Telephone Lab. Record
26 384 (1948)

29. Bueller E., Walker A.C., Ind. Eng. Chem. 42 1369
(1950)

30. Kohman G.T., U.S. Patent 2,895,812 (1959)

31. Franke I., Delongchamp M.H., Compt. rend. acad. sci. 228 1136 (1949)

32. Nagy J., Tarjan I., Acta Phys. Acad. Sci. Hung. 6 485 (1957)

33. Brown C.S., Kell R.C., Thomas L.A., Wooster N. and Wooster W.A., Mineral Mag. 29 858 (1952)

34. Hale D.R., Ceramic Age 56 22 (1950)

35. Laudise R.A., Nielsen J.W., Solid State Physics 12 149 (1961)

36. Brown C.S., Thomas L.A., J. Phys. Chem. Solids 13 337 (1960)

37. Flickstein J., Schieber M., J. Cryst. Growth 8 157 (1971)

38. Flickstein J., Schieber M., J. Cryst. Growth 24/25 603 (1974)

39. Yamashita S., Shinomiya A., Kumasaki H. J. Cryst. Growth 30 27 (1975)

40. Kolb E.D., Nassau K., Laudise R.A., Simpson E.E. and Kroupa K.M., J. Cryst. Growth 36 93 (1976)

41. Baughman R.J., Proc. 36th Ann. Freq. Con. Symp. 82 (1982)

42. Gordienko L.A., Muiskov V.F., Khoaz V.E. and Tsinober L.I., Soviet Phys. Cryst. 14 454 (1969)

43. Barns R.L., Freeland P.E., Kolb E.D., Laudise R.A. and Patel J.R., J. Cryst. Growth 43 676 (1978)

44. Armington A.F., Larkin J.J., J. Cryst. Growth 71 799 (1985)

45. Kopp O.C., Clark G.W., J. Cryst. Growth 2 308 (1968)

46. Kopp O.C., Staats P.A., J. Phys. Chem. Solids 31 2469 (1970)

47. Hosaka M., Taki S., J. Cryst. Growth 51 640 (1981)

48. Hosaka M., Taki S., Proc. Ann. Freq. Con. Symp. 304 (1981)

49. Hosaka M., Taki S., J. Cryst. Growth 52 837 (1981)

50. Hosaka M., Taki S., J. Cryst. Growth 53 542 (1981)

51. King J.C., Wood D.L., Dodd D.M., Phys. Rev. Lett. 4 500 (1960)

52. Kats A., Philips Res. Repts. 17 133 (1962)

53. Chernov A.A., Khadzhi V.E., J. Cryst. Growth 3, 4 641 (1968)

54. Lang A.R., Muiscov V.F., J. Appl. Phys. 38 2477-2483 (1967)

55. Read W.T., "Dislocations in Crystals" McGraw-Hill (1953)

56. Hull D., "Introduction to Dislocations" 2nd Ed. Permagon (1975)

57. Griggs D., Journal of Geophysical Research 79 (11) 1655 (1974)

58. McClaren A.C., Cook R.F., Hyde S.T., Tobin R.C. Phys. Chem. Minerals 9 79 (1983)

59. Johnson G.R., Irvine R.A., Proc. 41st Ann. Freq. Con. Symp. 175 (1987)

60. Vondeling J.K., Journal of Materials Science 18 304 (1983)

61. Iwasaki F., J. Cryst. Growth 39 291-298 (1977)

62. Yip K.L., Fowler W.B., Phys. Rev. B 11 2327 (1975)

63. Isoya J., Weil J.A., Halliburton L.E., J. Chem. Phys. 74 5436 (1981)

64. Weeks R.A., Abraham M.M., Bull. Min. Phys. Soc. 44 374 (1965)

65. Nielson J.W., Foster F.G., Amer. Min. 45 299 (1960)

66. Halliburton L.E., Markes M.E., Martin J.J., Brown R.N. Doherty S.P., Koumvakalis N., Sibley W.A. Armington A.F., IEEE Trans. on Nuc. Sci. NS-26 (6) 4851 (1979)

67. Lipson H.G., Kahan A., IEEE Trans. on Nuc. Sci. NS-31 (6) 1223 (1984)

68. Doherty S.P., Morris S.E., Andrews D.C., Croxall D.F. Rad. Eff. 74 145 (1983)

69. Kato N., Lang A.R., Acta Cryst. 12 787-793 (1959)

70. Lang A.R., J. Appl. Phys. 29 597-598 (1958)

71. Lang A.R., Acta Cryst. 12 249-250 (1959)

72. Lang A.R., J. Appl. Phys. 30 (11) 1768-1755 (1959)

73. Lang A.R., Appl. Phys. Lett. 7 (6) 168-170 (1965)

74. Spencer W.J., Haruta K., J. Appl. Phys. 37 (2) 549-553 (1966)

75. King J.C., Bell Syst. Tech. J. 38 573 (1959)

76. McClaren A.C., Osborne C.F., Saunders L.A. Phys. Stat. Sol. (a) 4 235-247 (1971)

77. Homma S., Iwata M., J. Cryst. Growth 19 125-132 (1973)

78. Takagi M., Mineo H., Sato M., J. Cryst. Growth 24/25 541-543 (1974)

79. Young R.A., Wagner C.E., J. Appl. Phys. 37 4070-4076 (1966)

80. Yamashita S., Kato N., J. Appl. Cryst. 8 623-627 (1975)

81. Epelboin Y., Patel J.R., J. Appl. Phys. 53 (1) 271-275 (1982)

82. Michot G., Weil B., George A., J. Cryst. Growth 69 627-630 (1984)

83. Zarka A., Lin L., J. Cryst. Growth 61 397-405 (1983)

84. Yoshimura J., Kohra K., J. Cryst. Growth 33 311-323 (1976)

85. Yoshimura J., Miyazaki T., Wada T., Kohra K. and Hosaka M., Ogawa T., Taki S., J. Cryst. Growth 46 691-700 (1979)

86. Zarka A., Lin L., Sauvage M., J. Cryst. Growth 62 409-424 (1983)

87. Dreisch T., Z. Phys. 42 426 (1927)

88. Plyler E.K., Phys Rev. 33 48 (1929)

89. Saskena B.D., Proc. Ind. Acad. Sci. 12A 93 (1941)

90. Arnold G., J. Chem. Phys. 22 1259 (1954)

91. Drummond D.G., Proc. Roy. Soc. A153 328 (1936)

92. Mitchell E.W.J., Ridgen J.D., Phil. Mag. 2 941 (1957)

93. Wood D.L., J. Phys. Chem. Solids 13 326 (1960)

94. King J.C., Phys. Rev. 109 1552 (1958)

95. Bambauer H.U., Schweiz. Min. Petr. Mitt. 41 335 (1961)

96. Bambauer H.U., Brunner G.O., Laves F., Schweiz Min. Petr. Mitt. 43 259 (1963)

97. Dodd D.M., Fraser D.B., J. Phys. Chem Solids 26 673 (1965)

98. Brown R.N., Kahan A., J. Phys. Chem Solids 36 467 (1975)

99. Chakraborty D., Lehmann G., J. Solid State Chem. 17 305 (1976)

100. Chakraborty D., Lehmann G., Phys. Stat. Solidi (a) 34 467 (1976)

101. Lehmann G., Z. Naturf. 22a 2080 (1967)

102. Walrafen G.E., Luongo J.P., The Spex Speaker 20 (3) 1 (1975)

103. Lipson H.G., Euler F., Armington A.F. 32nd Ann. Proc. Freq. Con. Symp. 11 (1978)

104. Halliburton L.E., Koumvakalis N., Markes M.E., Martin J.J., J. Appl. Phys. 52 (5) 3565 (1980)

105. Lipson H., Kahan A., J. Appl. Phys. 58 (2) 963 (1985)

106. Brunner G.O., Wondratschek H., Laves F. Z. Electrochem 65 735 (1961)

107. Perlson B.D., Weil J.A., Journal of Magnetic Resonance 15 594 (1974)

108. Nuttall R.H.D., Weil J.A., Solid State Communications 33 99 (1980)

109. Markes M.E., Halliburton L.E., J. Appl. Phys. 50 (12) 8172 (1979)

110. O'Brien M.C.M., Proc. Roy. Soc. (London) A231 404 (1955)

111. Aines R.D., Kirby S.H., Rossman G.R. Phys. Chem. Mineral. 11 204 (1984)

112. Stenina N.G., Mineral. Zh. 9 (5) 59 (1987)

113. DryBurgh P.M., Cockayne B., Barraclough K.G. "Advanced Crystal Growth" Sixth International Summer School on Crystal Growth (ISSCG6) 6-11th July (1986) Prentice Hall International UK Limited (1987)

114. King J.C., "Electrolysis of Quartz", U.S. Patent No. 3,113,224

115. King J.C., "Vacuum Electrolysis of Quartz" U.S. Patent No. 3,932,777 (1976)

116. Gualtieri J.G., Vig J.R., 38th Ann. Freq. Con. Symp. 42 (1984)

117. Bernot A.J., 39th Ann. Freq. Con. Symp. 271 (1985)

118. Milne E.L., Gibbs P., J. Appl. Phys. 35 (8) 2364 (1964)

119. White S., Nature 219 1248 Sept. (1968)

120. Griffiths P.R., de Haseth J.A., " Fourier Transform Infrared Spectrometry", Chemical Analysis Vol. 83 (1986) Wiley

121. Ambrose E.J., Elliot A., Temple R.B. Proc. Roy. Soc. (London) A206 192 (1952)

122. Angell C.L., "Polarised Infrared Spectroscopy" in "Progress in Infrared Spectroscopy" Vol. 2 Editor Szymanski H.A. Plenum Press (1964)

123. "Max Von Laue - Historical Introduction" International Tables of Crystallography 1 1-5

124. Lang A.R., Acta. Met. 5 358 (1957)

125. Tanner B.K., "X-Ray Diffraction Topography" Oxford Press (1976)

126. Lang A.R., in "Modern Diffraction and Imaging Techniques in Materials Science" Ed. Amelinckx North Holland

127. Kelly A., Groves G.W., "Crystallography and Crystal Defects" Reading Mass., Addison-Wesley (1970)

128. Hart in Reference 126

129. Authier A., "Advances in X-Ray Analysis" Vol.9 Plenum Press, New york (1976)

130. Authier A. in Reference 126

131. Jones G.R., Young I.M., Cockayne B., Brown G.T. Inst. Phys. Conf. Ser. No. 60 : Section 5 265 (1981)

132. Kulipanov G.N., Skinskii A.N., Sov. Phys. Usp. 20 (7) 559 July (1977)

133. Lea K.R., Munro I.H., "The Synchrotron Source at Daresbury Laboratory", Daresbury publication (1978)

134. Bowen D.K., "Applications of Synchrotron Radiation to Problems in Materials Science", Proceedings of the Daresbury Study Weekend DL-SCI-R19 14th Nov. (1982)

135. "LAUE", computer program, Dept. of Pure and Applied Chemistry, Physical Chemistry Group, University of Strathclyde

136. Butuzov V.P., Gordienko L.A., Tsinober L.I., Khadzhi V.E., "Method of Producing Single Crystals" British Patent No. 1,443,835

137. Kekulawala K.R.S.S., Paterson M.S., Boland J.N. Geophyiscal Monograph, Mechanical Behaviour in Crustal Rocks 49 (1981)

138. "Structure of Water and Aqueous Solutions", Editor Luck W.A.P., Verlag Chemie, Physik Verlag (1974)

139. Koumvakalis N., Markes M., J. Appl. Phys. 51 (6) 3431 (1980)

140. Tursi A.J., Nixon E.R., J. Chem. Phys. 52 (3) 1521 (1970)

141. Strommen D.P., Greun D.M., McBeth R.L., J. Chem. Phys. 58 (9) 4028 (1973)

142. Van Thiel M., Becker E.D., Pimentel G.C. J. Chem. Phys. 27 (2) 486 (1957)

143. Jones L.H., J. Chem. Phys. 22 (2) 217 (1954)

144. Harris D.C., Bertolucci M.D., "Symmetry and Spectroscopy", Oxford (1978)

145. Private communication, Croxall D.F., G.E.C. Hirst Research Laboratories

146. Sebastian M.T., Zarka A., Capelle B. J. Appl. Cryst. 21 326 (1988)

147. American Journal of Science 248 540 (1950)